

MIMO digital signal processing for optical spatial division multiplexed transmission systems

Citation for published version (APA):

Uden, van, R. G. H. (2014). *MIMO digital signal processing for optical spatial division multiplexed transmission systems*. [Phd Thesis 1 (Research TU/e / Graduation TU/e), Electrical Engineering]. Technische Universiteit Eindhoven. <https://doi.org/10.6100/IR780927>

DOI:

[10.6100/IR780927](https://doi.org/10.6100/IR780927)

Document status and date:

Published: 01/01/2014

Document Version:

Publisher's PDF, also known as Version of Record (includes final page, issue and volume numbers)

Please check the document version of this publication:

- A submitted manuscript is the version of the article upon submission and before peer-review. There can be important differences between the submitted version and the official published version of record. People interested in the research are advised to contact the author for the final version of the publication, or visit the DOI to the publisher's website.
- The final author version and the galley proof are versions of the publication after peer review.
- The final published version features the final layout of the paper including the volume, issue and page numbers.

[Link to publication](#)

General rights

Copyright and moral rights for the publications made accessible in the public portal are retained by the authors and/or other copyright owners and it is a condition of accessing publications that users recognise and abide by the legal requirements associated with these rights.

- Users may download and print one copy of any publication from the public portal for the purpose of private study or research.
- You may not further distribute the material or use it for any profit-making activity or commercial gain
- You may freely distribute the URL identifying the publication in the public portal.

If the publication is distributed under the terms of Article 25fa of the Dutch Copyright Act, indicated by the "Taverne" license above, please follow below link for the End User Agreement:

www.tue.nl/taverne

Take down policy

If you believe that this document breaches copyright please contact us at:

openaccess@tue.nl

providing details and we will investigate your claim.

MIMO Digital Signal Processing for Optical Spatial Division Multiplexed Transmission Systems

PROEFSCHRIFT

ter verkrijging van de graad van doctor aan de
Technische Universiteit Eindhoven, op gezag van de
rector magnificus prof.dr.ir. C.J. van Duijn, voor een
commissie aangewezen door het College voor
Promoties, in het openbaar te verdedigen
op dinsdag 30 september 2014 om 16:00 uur

door

Roy Gerardus Henricus van Uden

geboren te Oss

Dit proefschrift is goedgekeurd door de promotoren en de samenstelling van de promotiecommissie is als volgt:

voorzitter:	prof.dr.ir. A.C.P.M. Backx
1 ^e promotor:	prof. ir. A.M.J. Koonen
copromotor:	dr. C.M. Okonkwo
leden:	prof.dr. P. Poggiolini (Politecnico di Torino) prof. M. Karlsson PhD (Chalmers Tekniska Högskola) Prof.Dr.-Ing. N. Hanik (Technische Universität München) prof. dr. A.G. Tijhuis
adviseur:	Dr.-Ing. S. Randel (Alcatel-Lucent Bell Laboratories)

A catalogue record is available from the Eindhoven University of Technology library.

MIMO Digital Signal Processing for Optical Spatial Division Multiplexed Transmission Systems

Author: Roy Gerardus Henricus van Uden
Eindhoven University of Technology, 2014
ISBN: 978-90-386-3688-7
NUR: 959

Keywords: Optical fiber communication / Space division multiplexing / Digital signal processing / Modulation.

The work described in this thesis was performed in the Faculty of Electrical Engineering, Eindhoven University of Technology, and was financially supported by the European Commission funded 7th framework project MODE-GAP (grant agreement 258033).

Copyright © 2014 by Roy Gerardus Henricus van Uden

All rights reserved. No part of this publication may be reproduced, stored in a retrieval system, or transmitted in any form or any means without prior written consent of the author.

I invented nothing new. I simply assembled the discoveries of
other men behind whom were centuries of work ...

progress happens when all the factors that make for it are
ready and then it is inevitable.

Henry Ford

Summary

MIMO Digital Signal Processing for Optical Spatial Division Multiplexed Transmission Systems

Over the past decades, optical communications has established itself as the indispensable network technology for societal IP-driven traffic, resulting in a dependence of our society on this network technology. This network is based on single mode fibers (SMFs) to transport all data. It enables the throughput demand to grow each year, the compounded annual growth rate (CAGR). The predicted CAGR is converging to 25-40%. To accommodate it, wavelength division multiplexing (WDM), polarization division multiplexing (PDM) enabled by high-speed 2×2 multiple-input multiple-output (MIMO) digital signal processing (DSP), and higher order modulation formats exploiting both quadrature signal components, have been exploited. By employing all these dimensions simultaneously, laboratory transmission systems have achieved a throughput of beyond 100 Tbit s⁻¹ using SMFs. It is shown that the theoretical throughput limit of SMF-based optical transmission systems corresponds to this bits s⁻¹ order of magnitude. Considering the predicted traffic growth, it is estimated that the throughput demand surpasses the theoretical SMF throughput limit between the year 2020 and 2030. A straightforward method for increasing the transmission system's throughput is by employing a number of SMFs in parallel, which scales the costs per bit linearly. However, it is mandatory that the single fiber throughput is to be substantially increased in a cost-effective manner. Spatial division multiplexing (SDM) is envisioned to do exactly that by exploiting multiple modes, multiple cores, or both, as transmission channels in an optical fiber. These SDM transmission cases extend the high-speed 2×2 MIMO DSP to higher computational complexities. Therefore, this thesis focuses on the analysis, design, and implementation of efficient DSP techniques, which optimize optical transmission performance and support fiber design, whilst minimizing computational complexity.

Accordingly, the first part of this thesis describes the MIMO transmission system, and theoretical limits with respect to linear and non-linear tolerances. The MIMO transmission system description is started with the transmitter side, where the generation of two dimensional and four dimensional constellations is detailed. Then, the optical fiber medium is described, which allows for scaling the number of transmitted channels. To insert and extract these channels into and out of the fiber, mode multiplexers (MMUXs) are employed. For the optical component characterization, digital least-squares (LS) and minimum mean square error (MMSE) channel state information (CSI) estimation algorithms are used. The

power difference between received channels is denoted as mode dependent loss (MDL). It is demonstrated that the LS and MMSE CSI estimation is similar for a large optical signal-to-noise ratio (OSNR) regime, which is important as both methods provide similar insight in the theoretical transmission system capacity.

The second part of this thesis focuses on the receiver-side DSP, where the lion's share of the signal processing is performed. First, conventional building blocks are described which are used in conventional SMF transmission systems, which are inphase/quadrature (IQ) imbalance compensation, group velocity dispersion (GVD) compensation, adaptive rate conversion, MIMO equalization, and carrier phase estimation (CPE). The MIMO equalizer is the heart of the receiver-side DSP. In conventional PDM transmission systems, the MIMO equalizer is a $2 \times 2L$ MMSE time domain equalizer (TDE). Here, L denotes the number of transmission channel impulse response length samples. The TDE provides the starting point for investigating equalizer convergence properties, which quantify transmission system tracking capabilities. To minimize the convergence time, a varying adaptation gain MIMO equalizer is proposed. It is shown that the convergence time can be reduced by 50% with respect to conventional fixed adaptation gain MIMO equalization using the proposed equalizer. In addition, as laboratory setups use offline-processing using 64-bit floating point processors, a bit-width reduced TDE with 12 bit floating point operations is investigated as a first investigation step towards hardware implementation. It is shown that there is potential for low-complexity real-time implementation with smaller bit width floating point operations. Furthermore, it is shown that the computational complexity of the TDE scales linearly with the number of transmitted channels, and linearly with the impulse response length. Therefore, an MMSE frequency domain equalizer (FDE) MIMO equalizer is introduced with IQ-imbalance compensation. Again, convergence properties are investigated, and the varying adaptation gain is applied to reduce the convergence time by 30%. The convergence time gain difference with respect to the TDE is caused by the block updating properties of the FDE. Furthermore, it is shown that the computational complexity of the FDE scales linearly with the number of transmitted channels, and logarithmically with the impulse response length.

After MIMO equalization, CPE is performed per independent transmitted channel. To minimize the CPE stage computational complexity, a joint CPE algorithm is proposed, which compensates all transmitted channels simultaneously. It is demonstrated that the proposed joint CPE scheme has a performance penalty of < 0.5 dB OSNR for 28 GBaud 6×32 quadrature amplitude modulation (QAM) transmission at the 20% soft-decision forward error correcting (SD-FEC) limit with respect to the conventional 6 independent CPE blocks. For quadrature phase

shift keying (QPSK), 8, and 16 QAM, the observed penalty was smaller. To further reduce the CPE stage computational complexity, a novel phase detector (PD) is introduced, which did not show any performance penalty with respect to conventional PDs. Finally, a time domain multiplexed SDM (TDM-SDM) receiver is proposed for research activities to experimentally verify the transmission performance of SDM transmission systems. This TDM-SDM receiver allows for the reception and offline processing of >1 mode per dual-polarization (DP) coherent receiver and corresponding 4-port analog-to-digital converter (ADC).

The final part of this thesis focuses on the experimental verification of the proposed algorithms, and investigates coding schemes. First, a 41.7 km three mode fiber (3MF) is investigated, where the number 3 refers to the SMF throughput multiplier. The 3MF has been used to transmit the following two dimensional constellations: QPSK, 8, 16, 32 QAM. In addition, the 3MF has been used to quantify the performance of 3 four dimensional constellations: time shifted QPSK, 32, and 128 set-partitioned (SP) QAM. Furthermore, space-time coding is proposed, which demonstrates that a 3MF can achieve a transmission performance better than theoretically possible in a SMF. This however, comes at the cost of additional receivers and computational complexity in the MIMO equalizer. Finally, the 3MF has been used to demonstrate a first investigation towards a 3MF network, where 3 independent locations are emulated, combined, and transmitted over the 3MF. This gives an OSNR penalty up to 2 dB with respect to conventional MIMO transmission. The second experimental fiber investigated is the 0.95 km 19-cell hollow-core photonic bandgap fiber (HC-PBGF), which guides the transmitted signal predominantly in air (99%). Here, due to the experimental nature of the fiber, CSI is applied to investigate the polarization dependent loss (PDL). An average PDL of 1.1 dB was noticed over a wavelength range from 1537.4 nm to 1562.23 nm. Here, 32 WDM channels have been used to demonstrate a gross aggregate throughput of 8.96 Tbit s^{-1} , which denotes the highest capacity \times distance product, and the longest transmission distance at the time of the experiment. Finally, a 1 km 7-core step-index fiber is investigated, where each core allows the co-propagation of 3 spatial modes. This fiber type is denoted as the few mode multicore fiber (FM-MCF). Accordingly, 21 SMF channels are guided into the FM-MCF, where $7 \times (6 \times 6)$ FDE MIMO equalization is employed to equalize the $5.1 \text{ Tbit s}^{-1} \text{ carrier}^{-1}$ spatial superchannels. Combined with 50 wavelength carriers on a 50 GHz grid, a gross aggregate throughput rate of 255 Tbit s^{-1} is demonstrated. This work demonstrates the MIMO computational complexity scaling when multimode transmission is combined with multicore transmission.

This work was financially supported by the European Commission 7th framework project MODE-GAP (grant agreement 258033).

Contents

CHAPTER 1	INTRODUCTION.....	5
1.1	MOTIVATION OF THE WORK	5
1.2	WIRELESS AND OPTICAL MIMO TRANSMISSION.....	13
1.3	THESIS STRUCTURE	16
1.4	THESIS CONTRIBUTIONS.....	19
CHAPTER 2	MIMO TRANSMISSION SYSTEM CAPACITY	21
2.1	LINEAR 1×1 CHANNEL MODEL.....	22
2.2	LINEAR MIMO CHANNEL MODEL.....	24
2.3	CHANNEL STATE INFORMATION.....	25
2.3.1	<i>Least squares estimation</i>	<i>25</i>
2.3.2	<i>Minimum mean square error estimation</i>	<i>27</i>
2.4	TRANSMISSION CAPACITY	28
2.5	MAXIMIZING THROUGHPUT	30
2.5.1	<i>Generalized QAM transmitter.....</i>	<i>30</i>
2.5.2	<i>Constellations.....</i>	<i>32</i>
2.6	CONSTELLATION SEQUENCES	35
2.6.1	<i>CAZAC sequence.....</i>	<i>36</i>
2.6.2	<i>Pseudo random bit sequence</i>	<i>36</i>
2.6.3	<i>De Bruijn sequence.....</i>	<i>37</i>
2.7	CONVERTING CONSTELLATIONS TO THE OPTICAL DOMAIN.....	37
2.8	TRANSMITTER DIGITAL FILTERS.....	40
2.8.1	<i>Digital predistortion filters.....</i>	<i>40</i>
2.8.2	<i>Digital pulse shaping filters.....</i>	<i>41</i>
2.9	SUMMARY.....	42
CHAPTER 3	SCALING IN THE OPTICAL FIBER MEDIUM.....	45
3.1	SPATIAL DIVISION MULTIPLEXING IN OPTICAL FIBERS	46
3.2	THE WAVE EQUATION	47
3.3	LINEARLY POLARIZED MODES	51
3.4	FIBER IMPULSE RESPONSE	57
3.4.1	<i>Differential mode delay.....</i>	<i>58</i>

3.4.2	<i>Fiber splices</i>	59
3.5	FADING CHANNELS	60
3.5.1	<i>Flat fading</i>	60
3.5.2	<i>Rician fading</i>	61
3.6	PROPAGATION EFFECTS	62
3.6.1	<i>Attenuation</i>	64
3.6.2	<i>Amplification</i>	64
3.6.3	<i>Group velocity dispersion</i>	66
3.7	SCALING USING MULTIPLE CORES	68
3.8	SUMMARY	69
CHAPTER 4	DSP AIDED OPTICAL MODE MULTIPLEXER DESIGN AND OPTIMIZATION	71
4.1	SSMF DUAL POLARIZATION TRANSMISSION	72
4.2	BINARY PHASE PLATE CHARACTERIZATION	73
4.2.1	<i>Mode conversion</i>	73
4.2.2	<i>Mode crosstalk</i>	74
4.3	SPOT LAUNCHING	76
4.4	THREE DIMENSIONAL WAVEGUIDE	79
4.5	PHOTONIC LANTERN	80
4.6	SCALING NUMBER OF MULTIPLEXED CHANNELS.....	81
4.7	SUMMARY	82
CHAPTER 5	MIMO RECEIVER FRONT-END	85
5.1	OPTICAL QUADRATURE RECEIVER	86
5.1.1	<i>Optical mixer</i>	86
5.1.2	<i>Optical quadrature receiver</i>	88
5.1.3	<i>Generalized quadrature receiver</i>	89
5.2	DUAL-POLARIZATION QUADRATURE RECEIVER	91
5.3	TIME-DOMAIN MULTIPLEXED MIMO RECEIVER.....	91
5.3.1	<i>The TDM-SDM scheme</i>	92
5.3.2	<i>Scaling the TDM-SDM MIMO receiver</i>	95
5.4	OPTICAL FRONT-END IMPAIRMENT COMPENSATION	96
5.4.1	<i>Gram–Schmidt orthonormalization</i>	96
5.4.2	<i>Löwdin orthonormalization</i>	98
5.4.3	<i>Blind moment estimation</i>	98
5.5	DIGITAL INTERPOLATION FILTERS	100
5.5.1	<i>Interpolation filter design</i>	101
5.5.2	<i>Timing recovery</i>	103

5.6	GROUP VELOCITY DISPERSION COMPENSATION.....	105
5.6.1	<i>GVD estimation</i>	105
5.6.2	<i>GVD compensation</i>	107
5.7	SUMMARY.....	107
CHAPTER 6	MIMO EQUALIZATION.....	109
6.1	ZERO-FORCING EQUALIZATION.....	111
6.2	TIME DOMAIN MMSE EQUALIZATION	113
6.2.1	<i>The steepest gradient descent method</i>	116
6.2.2	<i>SGD convergence and stability</i>	117
6.2.3	<i>Least mean squares algorithm</i>	119
6.2.4	<i>Decision-directed least mean squares</i>	120
6.2.5	<i>Constant modulus algorithm</i>	121
6.2.6	<i>Segmented MIMO equalization</i>	122
6.2.7	<i>Varying adaptation gain algorithm</i>	124
6.3	MMSE FREQUENCY DOMAIN EQUALIZATION.....	127
6.3.1	<i>Updating algorithm</i>	128
6.3.2	<i>FDE convergence</i>	132
6.3.3	<i>Varying adaption gain FDE</i>	132
6.4	MIMO EQUALIZER COMPUTATIONAL COMPLEXITY	133
6.4.1	<i>TDE computational complexity</i>	134
6.4.2	<i>FDE computational complexity</i>	135
6.4.3	<i>Computational complexity comparison</i>	136
6.5	OFFLINE-PROCESSING IMPLEMENTATION	136
6.6	TOWARDS HARDWARE IMPLEMENTATION	138
6.6.1	<i>Advanced equalization</i>	138
6.6.2	<i>Bit-width reduced floating point operations</i>	139
6.6.3	<i>MIMO DSP scaling</i>	141
6.7	SUMMARY.....	143
CHAPTER 7	CARRIER PHASE ESTIMATION	145
7.1	FREQUENCY OFFSET ESTIMATION.....	146
7.2	PHASE OFFSET ESTIMATION	148
7.2.1	<i>nth order Viterbi-Viterbi phase estimator</i>	148
7.2.2	<i>Costas loop</i>	149
7.2.3	<i>2D maximum-likelihood phase detector</i>	150
7.2.4	<i>Argument-based phase detector</i>	150
7.2.5	<i>2×1D phase detector</i>	151
7.3	JOINT CPE.....	152

7.4	CYCLE SLIPPING	155
7.5	SUMMARY	156
CHAPTER 8	EXPERIMENTAL TRANSMISSION SYSTEM RESULTS.....	157
8.1	SOLID-CORE 3MF TRANSMISSION.....	158
8.1.1	<i>41.7 km 3MF transmission setup.....</i>	<i>158</i>
8.1.2	<i>Space-time diversity</i>	<i>163</i>
8.1.3	<i>Multipoint-to-point 3MF aggregate network.....</i>	<i>167</i>
8.2	HOLLOW-CORE PHOTONIC BANDGAP FIBER	169
8.3	FEW-MODE MULTICORE FIBER.....	173
8.4	SUMMARY	178
CHAPTER 9	CONCLUSIONS AND FUTURE OUTLOOK	181
9.1	CONCLUSIONS	181
9.1.1	<i>Mode multiplexers.....</i>	<i>182</i>
9.1.2	<i>MIMO digital signal processing.....</i>	<i>184</i>
9.1.3	<i>CPE digital signal processing</i>	<i>185</i>
9.1.4	<i>Higher order modulation formats and coding.....</i>	<i>185</i>
9.1.5	<i>Experimental fiber characterization and DSP validation.....</i>	<i>186</i>
9.2	FUTURE OUTLOOK	187
9.2.1	<i>Multimode or multicore for capacity scaling.....</i>	<i>187</i>
9.2.2	<i>Hollow-core photonic bandgap fibers</i>	<i>188</i>
9.2.3	<i>Optical components.....</i>	<i>188</i>
9.2.4	<i>Transmission formats and equalization.....</i>	<i>189</i>
BIBLIOGRAPHY	191	
LIST OF ACRONYMS	206	
LIST OF SYMBOLS.....	210	
LIST OF OPERATORS.....	214	
LIST OF PUBLICATIONS.....	215	
ACKNOWLEDGEMENTS	221	
CURRICULUM VITAE.....	223	

Chapter 1

Introduction

...a true creator is necessity, which is the mother of our invention.

Plato

This chapter introduces currently employed optical transmission systems and gives a motivation of the contributed work to society based on a brief overview on the history of optical transmission systems and the current state-of-the art to highlight the necessity of the contributed work. Finally, the structure of this thesis is outlined and the original contributions of this work are summarized.

1.1 Motivation of the work

Since ancient times, people have required communication over long distances, which is necessary for defending their territory against invasion or wild animals. Such communication was implemented by lighting up wooden beacons, using smoke signals, and later the usage of semaphore lines. In fact, all these communication types can be considered optical communication systems. However, before reaching modern communication systems using fibre optics, first, the use of cables guiding electricity and electrical telegraphs were predominant. Especially since the transmitter and receiver side consisted of electrical components. Hence, the semaphore line acted as the precursor of the electrical telegraph line. From the early 1800s, communication systems became electrical where a single serial channel was transmitted over copper cables. In the electrical domain, many key developments for increasing the throughput have been exploited. First, time domain multiplexing (TDM) was introduced in the late 1800s, where several low speed serial channels are time slotted to fully occupy the available throughput a high speed serial channel offers, as shown in Fig. 1.1(a). TDM was mainly exploited in telephony. Then, the frequency domain multiplexing (FDM) technique was introduced in the early 1900s, which allowed multiple baseband signals to be converted to parallel frequency bands using independent electrical local oscillators (LOs), as shown in Fig. 1.1(b). An electrical oscillator signal is generally provided by a highly stable quartz crystal. FDM allows a larger portion of the bandwidth

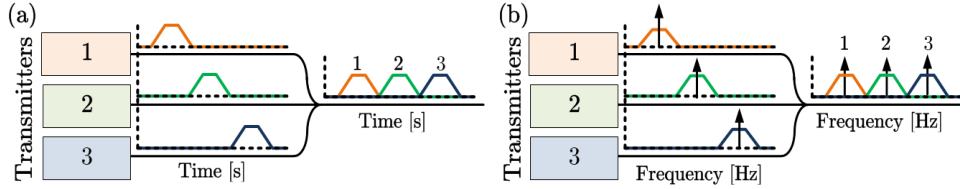


Fig. 1.1 Orthogonal dimensions for increasing the throughput, (a) time domain multiplexing, and (b) frequency domain multiplexing.

the electrical cable offers to be better utilized. The attenuation of an electrical cable increases as the frequency increases, effectively resulting in a bandwidth limited channel. During the 1960s, the coaxial cable attenuation figure of 5-10 dB km⁻¹ for employed transmission channels limited the potential transmission distance [1].

Due to two key developments in the optical domain, the 1960s mark the introduction of the optical transmission systems which now form the backbone of the worldwide communication network. One of these developments was the development of the laser in 1960 [2]. This achievement was quickly followed by the demonstration of the first Gallium Arsenide (GaAs) semiconductor laser in 1962 [3], and was particularly important, as it was the first coherent optical frequency oscillator. Accordingly, this demonstration showed the optical equivalent of the electrical oscillator. The second key development was the fiber medium, which has a long history of achievements. A key moment was 1965, when C.K. Kao and G.A. Hockham posed the idea that the optical fiber attenuation could be reduced <20 dB km⁻¹, the ocular attenuation figure, by reducing impurities [4]. At that time, the attenuation figure of optical fibers was >1000 dB km⁻¹, which were used for medical applications [5]. Among other contributions, the proposal of using optical fibers for telecommunications resulted in C.K. Kao receiving the Nobel Prize in Physics in 2009. In 1970, engineers at the Corning Glass Works (now Corning Inc.) developed the first single mode fiber (SMF) with an attenuation figure <20 dB km⁻¹ [1]. The theoretical model of the SMF was first described by E. Snitzer in 1961 [6], which could minimize the attenuation figure. Over the following years, the SMF drawing, and purity were optimized to decrease the medium's attenuation. Currently, commercial SMFs approach the fundamental attenuation figure of ~0.148 dB km⁻¹ at 1550 nm [7], where the measured attenuation is ~0.2 dB km⁻¹. This attenuation was reached in 1978 [8]. The SMF attenuation curve $\alpha(\lambda)$ is depicted in Fig. 1.2, where the attenuation graphs represent standard single mode fibers (SSMFs), or G.652 fibers, according to the ITU-T G.652 standardization specification. The attenuation graphs in Fig. 1.2 are the result of the combined attenuation due to

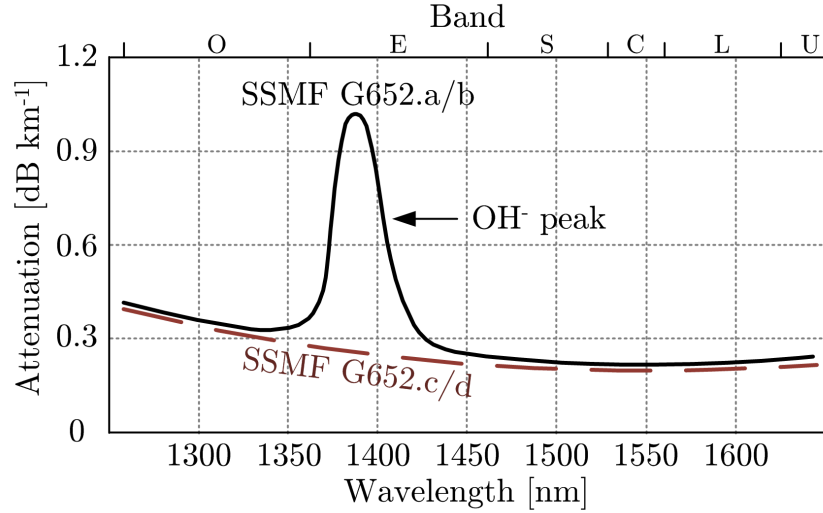


Fig. 1.2 SSMF (ITU G652) attenuation graph [10].

Rayleigh scattering, Brillouin scattering, water peak (OH^-) absorption, and siliciumdioxide (SiO_2) absorption [9, 10]. From Fig. 1.2 it can be observed that there is a large wavelength window optimum for transmission. Accordingly, the wavelength region is subdivided into transmission windows, further detailed in Table 1.1. As lasers are optical oscillators, they allow for the subdivision of the wavelength region for FDM in the optical domain, termed wavelength division multiplexing (WDM). WDM was first demonstrated in the laboratory in 1978 [11], and is currently standardized in the ITU G.694.1 standard to account for a channel spacing of 12.5, 25, 50, and 100 GHz [12]. As WDM is the optical equivalent of FDM, optical TDM (OTDM) was also proposed for optical transmission systems. However it was never widely adopted. Due to its implementation simplicity, WDM transmission became the standard for optical transmission systems. However, the transmission distance remained short before optical-electrical-optical conversion

Band	Abbreviation	Wavelength boundaries [nm]	
Original	O	1260	1360
Extended	E	1360	1460
Short	S	1460	1530
Conventional	C	1530	1565
Long	L	1565	1625
Ultra-long	U	1625	1675

Table 1.1 ITU standard wavelength bands [10].

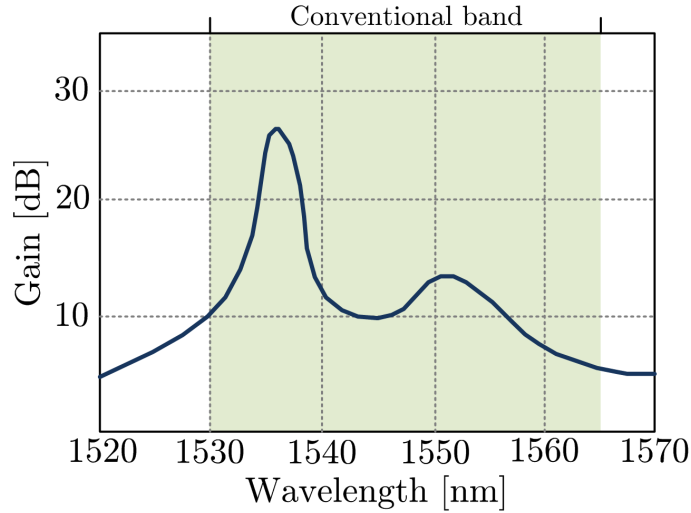


Fig. 1.3 Amplification window of the first EDFA, corresponding with the conventional band [15].

repeaters were required. Nevertheless, this transmission distance was substantially longer than copper based solutions could achieve. Coherent transmission and detection was proposed in the 1980s to extend the transmission distance [13]. However, the solution for increasing the transmission distance without requiring OEOC repeaters came with the invention of the low-noise erbium doped fiber amplifier (EDFA) by R.J. Mears et al. in 1986 [14], and the EDFA demonstration in 1987 by R.J. Mears et al. and E. Desurvire et al. [15]. This demonstration caused the development of coherent transmission to be halted as the EDFA allows low-noise optical amplification of the transmitted signal in the wavelength region shown in Fig. 1.3, thereby matching the SSMF's conventional transmission band. Fig. 1.3 shows the first demonstration of the EDFA gain spectrum, before gain flattening filters (GFFs) were introduced. GFFs ensure similar amplification over the entire C-band, where the signal-to-noise ratio (SNR) varies over the C-band. The development of the EDFA is the reason the conventional band is designated as such. By changing the wavelength of the pump laser, the long band can be amplified instead of the conventional band. The working of the EDFA is further discussed in section 3.6.2.

Since the EDFA made long-haul transmission possible, the limiting factor in transmission distance in the 1990s was group velocity dispersion (GVD), a linear transmission impairment. GVD causes transmitted pulses to widen as further detailed in section 3.6.3. To compensate the GVD in the optical domain, the

Network	Transmission distance [km]	Network structure
Access	<100	Tree
Metro	<300	Ring/Mesh
Regional	300 – 1,000	Mesh
Long-haul	1,000 – 3,000	Mesh
Ultra long-haul	> 3,000	Point-to-point

Table 1.2 Networks with corresponding transmission distances and structures.

development of dispersion-shifted (DS) SMFs was a key research interest in the 1990s. In addition, this decade marks the commercial exploitation of optical transmission networks, where the networks are subdivided into transmission distance categories, as denoted in Table 1.2 [16]. Combined with the rapid increase in internet communications, the SSMF based network have consequently become a backbone of the modern society.

Initially, Physics research for understanding the materials and phenomena was the main aspect in optical transmission systems development. However, around the late 1990s engineering became the predominant form of research as the conventional band was rapidly being occupied by WDM transmission channels. Consequently, the available bandwidth in SSMFs quickly became sparse. Therefore, the spectral efficiency (SE) [$\text{bits s}^{-1} \text{Hz}^{-1}$] needed to increase. To achieve this, initially, the serial channel symbol rate increased. However, as the ITU specifications denote standardized channel spacings, the serial rate cannot increase indefinitely as two neighbouring channels start overlapping in the frequency domain. In the late 1990s, all transmission systems were direct-detection, i.e. the received power denotes the binary values being transmitted. To increase the SE, coherent receivers were reintroduced in 2004 [17], and were combined with powerful digital signal processing (DSP) techniques to compensate for linear transmission impairments. Coherent transmission exploits the amplitude and phase dimensions, and can therefore increase the SE over direct-detection transmission systems. This was a common transmission technique for radio communications, denoted as quadrature amplitude modulation (QAM), further detailed in section 2.5. However, the optical component structures are substantially different, which is further discussed in section 2.7. Soon after the reintroduction of coherent receivers, it was proposed to exploit the two linear polarization dimensions of the SSMF [18], which is denoted as polarization division multiplexing (PDM). The two modulated channels mixed during transmission, and were unravelled at the receiver side using 2×2 multiple-input multiple-output (MIMO) equalization. Note that both polarization channels

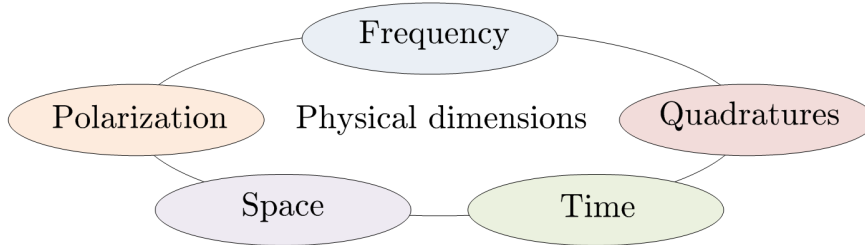


Fig. 1.4 Optical transmission system orthogonal dimensions [19].

use the same frequency spectrum. Accordingly, the SE is doubled with respect to single polarization transmission. In 2010, the first real-time $\geq 100 \text{ Gbit s}^{-1} \text{ carrier}^{-1}$ employing 2 information channels using PDM was demonstrated using prototype equipment [19]. In this thesis, a channel denotes an independently transmitted signal. Henceforth, information theory and DSP became popular topics in optical transmission systems to maximize the throughput in SSMFs by compensating linear and nonlinear transmission impairments [19]. Currently, GVD compensation in coherent transmission systems is performed in the digital domain using DSP without a penalty with respect to dispersion shifted SMFs [19]. Therefore, DS SMFs are no longer commonly used in long-haul transmission systems. For clarity, all orthogonal dimensions available in optical transmission systems are shown in Fig. 1.4 [19]. By using WDM and direct-detection receivers, a throughput of 10

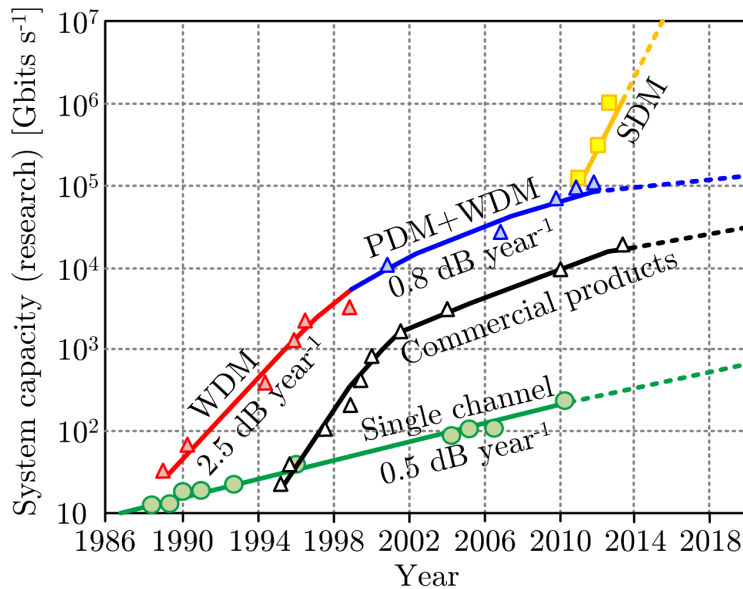


Fig. 1.5 Serial, WDM, PDM combined with WDM, and SDM with WDM transmission system capacity with respect to commercially operating products [19].

Tbit s^{-1} was achieved, as shown in Fig. 1.5 [19].

Using coherent transmission with higher order modulation formats and simultaneously exploiting the 2 available polarizations in an SSMF, a throughput of ~ 100 Tbit s^{-1} was achieved [20]. Here, all possible orthogonal dimensions are exploited simultaneously, corresponding to a theoretical throughput limit of the SSMF. As shown in Fig. 1.4, to further increase the throughput of a single fiber only one option is left unexploited: space. Therefore, the optical transmission systems exploiting the spatial dimension are termed SDM [19]. Earlier SDM work using direct-detection referred used the terminology mode group diversity multiplexing (MGDM) due to the usage of multimode fibers (MMFs) [21, 22].

Through the aforementioned technologies, the SSMF throughput has increased substantially for research systems over the recent decades, as shown in Fig. 1.5. However, since the mid-1980s, rapid growth in capacity demand has also been observed from the commercialization of optical telecommunication networks and IP driven traffic, where modern commercial products already exploit PDM and WDM transmission. From Fig. 1.5 it can be observed that the throughput in commercial products closely follows the throughput increase achieved in research systems. However, it was previously noted that ~ 100 Tbit s^{-1} was the theoretical limit of SSMFs [20], and it is expected that commercial products will reach the theoretical SSMF throughput limit. The growth in capacity demand is denoted as the compounded annual growth rate (CAGR), and is shown in Fig. 1.6 for the total

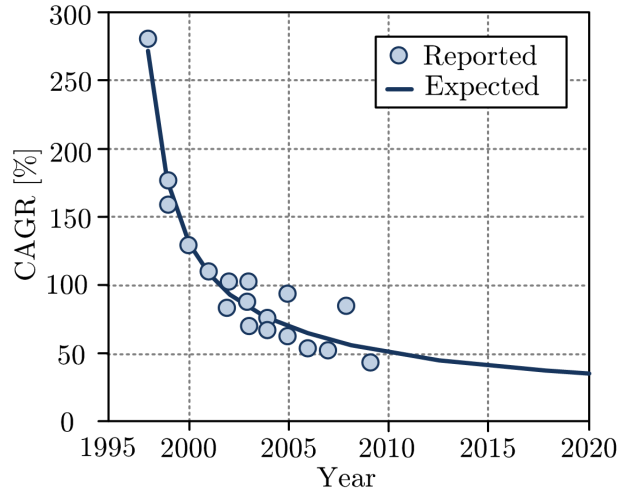


Fig. 1.6 Exponentially decreasing CAGR for the total backbone traffic, converging to an estimated 25-40% per year [23].

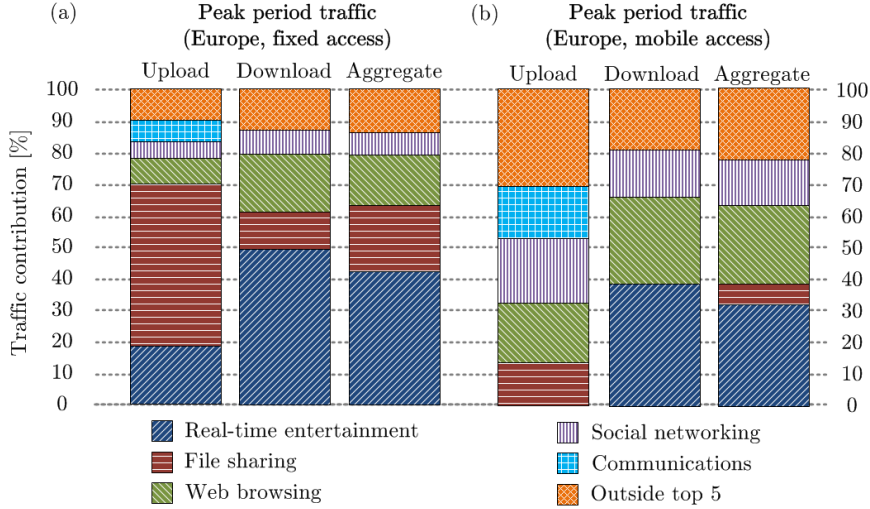


Fig. 1.7 Peak period traffic in Europe for (a) fixed and (b) mobile access [24].

backbone traffic. The lion's share of the data transfer (fixed access numbers shown in brackets) is contributed by real-time entertainment (40.78%), file sharing (20.16%), web browsing (15.15%), and social networking activities (6.95%), as shown in Fig. 1.7 [24]. Modern examples of these contributors are Netflix and Youtube (real-time entertainment), cloud storage applications and bittorrent traffic (file sharing), Facebook (social networking), and voice over IP (VoIP) using Skype and text messages through Whatsapp (communications). Among others, these contributions lead to a persistent exponential growth in Internet driven traffic. From Fig. 1.6, it can be observed that the CAGR is exponentially decreasing, and is predicted to converge to 25 to 40% in the future [23]. It was previously noted that the theoretical capacity limit of SSMFs is $\sim 100 \text{ Tbit s}^{-1}$, where all orthogonal dimensions are exploited. Note that the available bandwidth in an SSMF is limited to the transmission window of choice, where the EDFA amplification window is generally considered to be the determinative factor. However, considering the CAGR, this fundamental capacity limit is predicted to be surpassed by the capacity demand between the year 2020 and 2030. Independently of prediction philosophy, the impending capacity crunch is inevitable, which implies that network carriers are lighting up dark fibers at an exponentially increasing rate to support societal capacity demands [25]. This scaling method keeps the cost per bit equal. Combining this fact with the exponentially increasing capacity demand, results in an economical difficulty for future optical transmission links and networks. Therefore, a cost effective, and energy effective method for substantially increasing the capacity of a single fiber needs to be found [19].

With the demonstration of 100 Gbit s⁻¹ carrier⁻¹ PDM-based transmission systems employing SMFs [26], initial 2×2 MIMO algorithms have already been employed in optical telecommunication systems. In addition, in wireless communications, MIMO transmission systems are widely used in research and real-time transmission systems providing knowledge spanning nearly 2 decades. These two aspects are the deciding factors for suggesting MIMO transmission in the conventional band. Here, optical amplifiers can be developed based on conventional EDFA technology. In wireless communications, MIMO transmission was originally proposed by G.J. Foschini in 1996, and was denoted as Vertical-Bell Laboratories Layered Space-Time (V-BLAST). The working of V-BLAST is further detailed in Chapter 2. As previously mentioned, in optical communications MIMO transmission is termed SDM. Here, SDM can exploit multiple modes, multiple cores, or a combination thereof, in a single fiber. Note that PDM is a form of SDM, where SDM in fibers is further discussed and detailed in Chapter 3. For the SDM paradigm to truly fulfil its promise, it is envisioned that the capacity of a single fiber increases by at least two orders of magnitude [27]. This is mandatory, to accommodate the CAGR. To employ the emerging SDM fibers, carriers are required to overhaul their entire network, including the installation of new SDM components. The installation of SDM fibers and components is therefore accompanied by high installation costs. Consequently, these SDM fibers need to have the capacity capabilities to provide enough transmission capacity for carriers to last many years without the requirement of installing a new generation of SDM fibers and components. At the moment, these SDM fibers, optical components, and DSP are being heavily investigated by the research community. This heavy investigation has led to several single fiber throughput records, as shown by the yellow squares in Fig. 1.5. Subsequently, these records were achieved by J. Sakaguchi et al. in 2011 using a 7-core fiber resulting in 109 Tbit s⁻¹ throughput [28]. This record was broken by the same group using a 19-core fiber early 2012 achieving 305 Tbit s⁻¹ throughput [29]. Then, late 2012 two groups transmitted over 1 Pbit s⁻¹ in a single fiber independently [30, 31]. This is still the current record.

1.2 Wireless and optical MIMO transmission

As previously mentioned, the field of wireless transmission provides nearly two decades of knowledge on key optimisations required to substantially increase transmission capacity. Therefore, an interesting starting point for using MIMO transmission in optical communication systems is the comparison between wireless and optical communications. This comparison is shown in Table 1.3, which an extended version of [32].

	Wireless transmission	Optical transmission
Carrier frequency	0.8-6 GHz	185-196 THz
Transmitters	Antennas	Optical modulators
Receivers	Antennas	Photodetectors
Noise source	Thermal noise	Distributed ASE noise
Spatial diversity	1, 2, 3, 4, 5, 6, ...	1, 2, 6, 10, 12, 16, 20, 24, ... (modes) 1, 2, 3, 4, 5, 6, ... (cores)
Signal fading	Multipath propagation	Optical amplifier mode dependent gain, fiber mode dependent loss
Distortion and interference	Cochannel interference, electromagnetic interferers	Nonlinear inter- and intrachannel
Symbol rate	tens of MBaud	tens of GBaud
Transmission format	OFDM	Single-carrier
Medium	Air, no control	Optical fibers, designable medium
Channel tracking	Order of milliseconds	Order of microseconds
Receiver feedback	Available (closed-loop)	Not available (open-loop)

Table 1.3 Key differences in optical and wireless transmission systems.

First, the carrier frequency for wireless communications is between 0.8-6 GHz, generated by highly stable electrical oscillators. For optical communications, the carrier frequencies range from 185 to 196 THz, and are generated using lasers which tend to drift. Therefore, digital frequency and phase tracking is required, which is detailed in Chapter 7. Antennas act as transmitters and receivers in wireless communications, where thermal noise a key source of noise, other noise sources are electromagnetic interferers. The received power determines the system's SNR. For optical communications, EDFAs add amplified spontaneous emission (ASE) noise, and since there can be multiple EDFAs in a transmission link, the ASE noise is distributed over the link. Furthermore, individual antennas can be added to increase the spatial diversity at the transmitter or receiver side, where the surroundings cause multipath propagation, resulting in a Rayleigh fading channel with an unknown delay spread. To maximize transmission throughput, orthogonal frequency division multiplexing (OFDM) is used, with a symbol rate of tens of MBauds. However, optical transmission systems work in the order of tens of GBauds. Here, the digital-to-analog converters (DACs) and analog-to-digital (ADCs) are limited in effective number of bits (ENOBs), adding substantial amounts of quantization noise and greatly limiting the signal generation quality. Therefore, single-carrier transmission is the predominant transmission format in

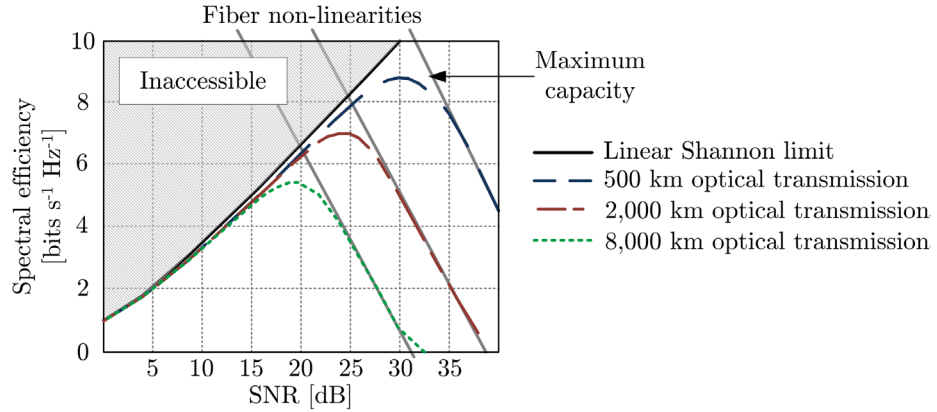


Fig. 1.8 Linear and non-linear capacity limits, where the fiber non-linearity influence scales with the transmission distance [36].

optical transmission systems [19], although OFDM is still regularly proposed [33, 34]. The conversion from electrical signals to the optical domain is further detailed in Chapter 2. The spatial diversity in optical communications is achieved within the fiber medium, where multiple cores, or modes, can be employed as channels. Naturally, a linear combination of these two can be made in which the delay spread can be engineered. The coupling parameters in the fiber medium cause the channel fading to be dependent on the amplifier mode dependent gain, and fiber mode dependent loss (MDL). Furthermore, a fiber is a non-linear medium [35], unlike air for wireless communications, and further constraints the theoretical linear Shannon transmission capacity, as shown in Fig. 1.8 [36]. This constrained transmission capacity limit is often referred to as the non-linear Shannon limit [37]. The linear Shannon limit is detailed in Chapter 2, and the fiber medium characteristics are further addressed in Chapter 3.

Channel tracking in wireless systems is generally in the order of milliseconds, which results in slow changing channels. The transmission distance depends on the application (such as satellite, WiFi, or mobile applications). Generally for short distance, receivers give feedback to the transmitter to optimize the transmission performance [38]. This transmission system type is considered a closed-loop system. In optical communications however, the channel changes in the order of microseconds. The latency of SSMF is $\sim 4.9 \mu\text{s km}^{-1}$ at 1550nm, and for long-haul transmission (≥ 1000 km) it results in receiver feedback being out-dated for optimizing transmission performance. Due to this delay, coherent optical transmission systems are open-loop, i.e. the receiver does not provide channel information feedback to the transmitter.

Clearly, there are many key differences between the field of wireless and optical transmission systems. However, there are also similarities, providing interesting considerations for optimizing optical SDM transmission systems. Therefore, this thesis focuses on the following aspects:

- The characterization and estimation of the optical transmission channel.
- Digital signal processing building blocks, which focus on the unraveling of mixed transmission channel using MIMO equalizers.
- The corresponding tracking capabilities of the transmitted channels.
- Minimizing the DSP computational complexity.
- Scaling to many-fold SSMF throughput.

1.3 Thesis structure

This thesis addresses the challenges of the optical transmission MIMO transmission system in the following 9 chapters, where each chapter (with exception of introduction and conclusion) addresses a particular part of the optical MIMO transmission system.

Chapter 2 provides the linear band-width limited MIMO transmission system description, where first a simple 1×1 transmission system is detailed, and next is extended to an arbitrary linear MIMO transmission system. Using this system description, two transmission channel estimation algorithms are detailed, the least-squares (LS) algorithm, and the minimum mean square error (MMSE) algorithm, which has been proposed for optical communication systems in [r25]. Note that references [r#] denote co-authored work. Accordingly, from a known channel, the transmission channel capacity can be computed. This allows for estimating the maximum theoretical throughput. To approach this theoretical limit as closely as possible, QAM based constellations are proposed, which can maximize the throughput depending on the SNR. Multiple symbols carrying these constellations form sequences, which are converted from the electrical domain to the optical domain using a Mach-Zehnder-Modulator (MZM) structure. Finally, digital filters are shown to optimize the optically transmitted symbol sequences.

Chapter 3 details the optical fiber medium, which is particularly important as it provides the spatial diversity, and hence potential to perform MIMO transmission, in the optical domain. The focus of this chapter is the description of the linear transmission impairments, as they can be efficiently compensated by digital signal processing algorithms. In this thesis, spatial diversity in optical fibers is primarily achieved by exploiting the solutions of the wave equation, called modes, as

transmission channels. Here, a heavily simplified fiber model is assumed which results in the description of the linearly polarized (LP) modes. Alternatively, multiple cores can be used as separate transmission channels as well. From these modes, it is shown that propagation parameters and fiber splices impact the MIMO equalizer complexity heavily, and accordingly fiber designs are discussed. As multiple transmission channels mix during transmission, a fading channel is created, which reduces the potential throughput. Finally, the origin of attenuation and amplification, and GVD effects are detailed.

Chapter 4 discusses the launch conditions for exploiting the spatial diversity the optical fiber offers. These components are the mode multiplexers (MMUXs), and four generations are detailed. First, the phase plate based MMUX, which excites individual modes, is discussed and performance tolerances are investigated [r17]. Then, the spot launcher is detailed, which ensures the mixing of all transmitted channels to exploit the spatial diversity, and to minimize the power differences between transmitted channels during transmission [r3]. Based on the same spot launching concept, a three dimensional waveguide (3DW) is proposed, which has the advantage of a substantial smaller footprint [r34], [r36]. Finally, details are given of the currently emerging in-fiber photonic lantern.

Chapter 5 provides insight in the optical and digital receiver side front-end (FE), before MIMO equalization is performed. First the received mixed MIMO transmission signals are separated by the mode demultiplexer (MDMUX) and guided to dual-polarization (DP) coherent receiver FEs. The receivers are quadrature receivers and allow the reception of QAM constellations. Conventionally in a laboratory environment, for every received DP transmission channel, one DP coherent receiver and a 4-port oscilloscope is required. The proposed time domain multiplexed spatial division multiplexing (TDM-SDM) receiver allows for the reception of multiple DP transmission channels using only one DP coherent receiver and a 4-port oscilloscope [r13], [r37]. Each of these two optical FEs gives digitized received signals, where first FE compensation is performed. Then adaptive rate conversion is performed to achieve a 2-fold oversampling. Finally, the GVD is removed before going into the MIMO equalizer.

Chapter 6 details the heart of the receiver side digital signal processing, the MIMO equalizer. The two most influential updating algorithms in optical transmission systems are detailed, the zero-forcing and MMSE updating algorithm, which correspond to the LS and MMSE channel estimation algorithms detailed in Chapter 2, respectively. Current state-of-the-art 100 Gbit s⁻¹ SSMF transmission

systems use a time domain equalizer (TDE). MMSE equalization is based on the steepest gradient descent method for adaptive tracking of the transmission channel. To track the transmission channel, a convergence time, or learning time, is required. The downside of the TDE is that the computational complexity scales linearly. From this point, several contributions have been made to this scheme, such as segmented MIMO equalization, a varying adaptation gain [r27], and bit-width reduction of floating point operations [r35]. All these extended schemes either reduce the computational complexity or improve the convergence properties. Additionally, a frequency domain equalizer (FDE) is proposed which allows for compensating imbalances within the QAM symbols [r11]. This equalizer scales logarithmically in computational complexity with impulse response length. The proposed varying adaptation gain is also applied to the FDE scheme. Other equalizers are briefly discussed, and are not considered for implementation due to their computational complexity and stability properties. Finally, the offline-processing peer-to-peer distributed network implementation which supported the laboratory measurements is described.

Chapter 7 discusses the carrier phase estimation (CPE) algorithms, comprising frequency offset estimation and phase offset estimation algorithms. Due to the heavy channel mixing effects during transmission, frequency offset estimation is limited to data-aided estimation, as blind estimation cannot guarantee similar accuracy. For phase estimation, two schemes are described, the n^{th} order Viterbi-Viterbi (V-V) scheme and the Costas loop. As the Costas loop theoretically outperforms the V-V scheme, the proposed joint CPE scheme is based on the Costas loop [r7], [r21]. Furthermore, a low complexity phase estimator is shown for decision directed phase estimation [r12].

Chapter 8 combines all previous chapters in an experimental setup, where the transmission performance of three experimental fibers is investigated. First, the transmission performance of a 41.7 km three mode fiber (3MF) is investigated for the transmission of 2D and 4D QAM symbols [r3], [r4]. Also, it is shown that the receiver side DSP allows for detailed investigation of the transmission channel. Furthermore, two transmission cases are considered. The first is where space-time coding is applied [r30], which allows for adding a new dimension in potential future flex-grid applications, and additionally shows that 3MFs can achieve an optical-to-signal ratio (OSNR) tolerance better than SSMFs can offer in theory. Furthermore, the 3MF is used to investigate a multipoint-to-point link with respect to a point-to-point link [r29]. The second experimental fiber investigated is the hollow-core photonic bandgap fiber [r32]. This fiber allows the propagation of modes mainly in

air, and hence reduced the fiber transmission latency. Finally, the last experimental fiber is investigated, the few-mode multicore fiber, which allows for combining multimode, multicore, and advanced modulations formats [r36].

Finally, in **Chapter 9** conclusions are drawn from the contributions, and a future outlook is given for further work necessary for SDM systems to become a reality.

1.4 Thesis contributions

The author is solely responsible for the selection, offline-processing structure, and verification of all digital domain algorithms demonstrated in this thesis. These algorithms primarily aim to aid the optical component and fiber performance analysis, and optimize transmission performance. To this end, a MMSE based channel estimation information (CSI) algorithm was proposed for optical transmission systems. Conventional SSMF transmission systems employ a TDE, however as the computational complexity scales linearly with the number of transmitted MIMO channels and impulse response length, therefore an FDE with inphase/quadrature (IQ) imbalance compensation is proposed. Furthermore, to minimize the convergence time, a varying adaptation gain MIMO TDE and FDE were proposed. As all implemented algorithms were based on offline-processing, a first performance investigation step towards real-time implementation is made, where the performance of a bit-width reduced MIMO equalizer was demonstrated. Finally, in the digital domain, the usage of reduced complexity phase detectors (PDs) in the CPE algorithm is proposed, and combined this with a novel joint CPE scheme for optical MIMO transmission systems. For laboratory use, the digital domain offline-processing algorithms have been implemented on a distributed cloud platform to minimize computation time. The distributed cloud platform was implemented by Roel van Uden and Maikel van de Schans. Here, technical assistance with respect to the algorithms and performance analysis was provided by the author.

All the proposed algorithms were demonstrated with the aid of a laboratory setup. The experimental work in chapter 8 was performed by the author, where the component selection, assembly, and transmission system characterization are contributions of the author himself. The spot launcher MMUX is built and aligned by dr. H. Chen and F.M. Huijskens. In addition, a novel TDM-SDM receiver is proposed, which allows the reception of multiple MIMO channels with a reduced number of receivers. This greatly reduces the required financial investment to verify the performance of the MIMO transmission system. Three experimental

fibers have been characterized using the experimental MIMO transmission system, a 3MF, a hollow-core photonic bandgap fiber (HC-PBGF), and a few mode multicore fiber (FM-MCF). Furthermore, higher order modulation formats in four dimensions, and space-time coding, is demonstrated for 3MF transmission. Moreover, using an experimental setup, the potential of a mesh network is investigated where three SSMFs are guided into the 3MF for MIMO transmission. The latter fiber, the FM-MCF, demonstrates potential scaling capabilities in optical SDM fibers, where multiple modes, multiple cores, and multi-level modulation formats can be employed to maximize the throughput.

Chapter 2

MIMO transmission system capacity

If I have seen further than others, it is by standing upon the shoulders of giants.

Isaac Newton

From the previous chapter¹ it is clear that the available bandwidth in currently employed single mode fibers is rapidly being exhausted, and hence there is an ongoing investigation into techniques to substantially increase the capacity of a single fiber. The most suitable band for low-loss optical transmission over optical fibers uses the conventional band (1530-1565 nm), as discussed in Chapter 1. This wavelength band is the operating window of the commonly available erbium doped fiber amplifier, therefore it is a practical choice to continue operating in this region. However, a technique to increase the capacity within a limited bandwidth needs to be found. The same bandwidth limitation challenge has arisen in the field of wireless transmission, and a viable option was found: MIMO transmission.

This chapter firstly provides the basic description of a linear 1×1 transmission system, and the scaling towards the linear MIMO case is addressed. Corresponding to the MIMO case, the system capacity is determined. For the MIMO case, it is exceptionally important to understand the transmission medium, and this can be better understood by obtaining the CSI, i.e. the transmission coupling between the transmitters and receivers. A method for obtaining the CSI is proposed [r25], based on the MMSE receiver scheme. Note that transmission capacity is always limited by noise, which originates from active components such as amplifiers. To minimize the system capacity throughput difference, constellation symbols have to be chosen, where each constellation has its respective theoretical limits. Finally, this chapter investigates how these chosen constellations can be generated and optimized in the optical domain.

¹ This chapter incorporates results from the author's contributions [r15] and [r25].

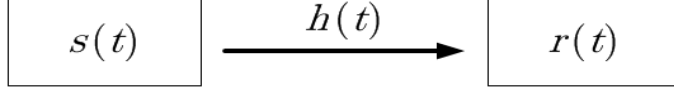


Fig. 2.1 Functional diagram of a general 1x1 transmission system without noise [39].

2.1 Linear 1×1 channel model

Every transmission system, whether it is wired or wireless, can be described by three main modules [39]; a transmitter source s , a link, and a receiver r , as depicted in Fig. 2.1. In the simplest case, there is only 1 transmitter source, and 1 receiver. Initially, the impact of noise is omitted for simplicity, which results in the 1×1 transmission system description in the time domain as [40]

$$r(t) = h(t) \otimes s(t) = \int_{-\infty}^{+\infty} h(t - \tau) s(\tau) d\tau \quad (2.1)$$

where $s(t)$ and $r(t)$ represent the transmitted and received signal, respectively, and $h(t)$ is the impulse response of the link. The convolution operation is denoted by \otimes . The transmitted signal $s(t)$ is assumed to be a sequence of uncorrelated zero-mean symbols with variance $\text{var}[s(t)] = E\{s^2(t)\} = \sigma_s^2$ and symbol time T_{sym} . Here, $E\{\cdot\}$ represents the expected value. Eq. (2.1) describes the transmission system in the time domain. However, in optical communication systems, binary information is transmitted and received by digital processors. Therefore, it is important to rewrite Eq. (2.1) in the (digital) sampled domain. Any time domain signal can be digitized without aliasing by sampling at, or above, two times the signal bandwidth B , which is the Nyquist sampling rate [41]. The discrete-time linear transformation of Eq. (2.1) therefore is [42]

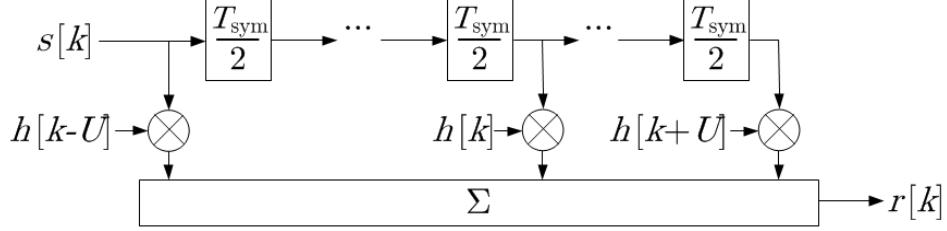
$$r(kT_{\text{sr}}) = \sum_{u=-\infty}^{+\infty} h(kT_{\text{sr}} - uT_{\text{st}}) s(uT_{\text{st}}), \quad (2.2)$$

where T_{st} and T_{sr} represent the sampling times of the transmitter and receiver, respectively. For clarity, let the simplified notation be

$$\begin{aligned} r[k] &= r(kT_{\text{st}}), \\ s[u] &= s(uT_{\text{sr}}). \end{aligned} \quad (2.3)$$

For further simplicity, the sampling times are assumed to be $T_{\text{st}} = T_{\text{sr}} = T_{\text{sym}} / 2$. Hence, by substituting Eq. (2.3) in Eq. (2.2) yields

$$r[k] = \sum_{u=-\infty}^{+\infty} h[k - u] s[u]. \quad (2.4)$$

Fig. 2.2 $T_{\text{sym}}/2$ system transmission model.

Note that u ranges from $-\infty$ to $+\infty$. As this is not a realistic case, a finite impulse response (FIR) channel is introduced which limits the range of u as

$$r[k] = \sum_{u=-U}^U h[k-u]s[u]. \quad (2.5)$$

The assumed FIR length L is $2U+1$, which is particularly important for adaptive equalizers, further detailed in Chapter 6. Each discrete multiplication in Eq. (2.5) is called a tap. Fig. 2.2 illustrates Eq. (2.5) for the finite impulse response. Note that the aforementioned transmission system description does not take noise into account. In reality however, no transmission system is free from noise which is the primary limiting factor in transmission distance. In optical transmission systems, noise is generally modeled as additional white Gaussian noise (AWGN) in the linear transmission regime [43]. Thereby, due to the transmission link consisting of multiple fiber spans with corresponding erbium doped fiber amplifiers, the noise should be considered distributed noise. However, in a simplified model, generally the noise is added at the receiver side [36, 44]. Extending Eq. (2.5) to account for the impact of noise, gives

$$r[k] = \sum_{u=-U}^U h[k-u]s[u] + n[k], \quad (2.6)$$

where $n[k]$ represents the zero-mean AWGN with variance σ_n^2 . Alternatively, Eq. (2.6) can be written in vector form for time instance k

$$r[k] = \mathbf{h}\mathbf{s} + n[k], \quad (2.7)$$

where $\mathbf{h} = \{h[k+U], \dots, h[k], \dots, h[k-U]\}$ and $\mathbf{s} = \{s[k-U], \dots, s[k], \dots, s[k+U]\}^T$. Note that Eq. (2.7) provides a basis for the MIMO transmission model based on matrices, often found in the literature. The implications of scaling from a 1×1 channel model to a MIMO transmission model is further detailed in the next section.

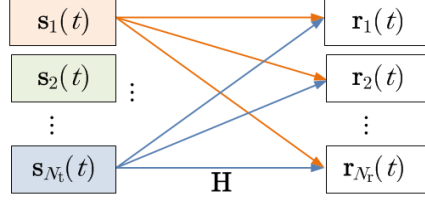


Fig. 2.3 V-BLAST architecture for increasing capacity within a fixed bandwidth.

2.2 Linear MIMO channel model

As WDM is widely applied in optical core transmission links based on single mode fibers, bandwidth is becoming scarce. Therefore, finding methods for increasing the available transmission system capacity is an area of on-going research. Fortunately, such scaling method exists and is widely being applied in wireless communications. Instead of adding more parallel transmission channels in terms of wavelengths, parallelization is performed in space, using the same carrier frequency [Hz]. Fig. 2.3 illustrates the well-known V-BLAST architecture, where multiple transmitters exploit parallel spatial paths to multiple receivers [45]. First, for clarity, the transmission model from Eq. (2.7) is extended to single-input multiple-output (SIMO) where N_r receivers are employed as

$$\mathbf{R} = \mathbf{H}\mathbf{s} + \mathbf{N}, \quad (2.8)$$

where

$$\begin{aligned} \mathbf{R} &= \{ \mathbf{r}_1[k], \dots, \mathbf{r}_j[k], \dots, \mathbf{r}_{N_r}[k] \}^T, \\ \mathbf{N} &= \{ \mathbf{n}_1[k], \dots, \mathbf{n}_j[k], \dots, \mathbf{n}_{N_r}[k] \}^T, \\ \mathbf{H} &= \{ \mathbf{h}_1, \dots, \mathbf{h}_j, \dots, \mathbf{h}_{N_r} \}^T, \end{aligned} \quad (2.9)$$

and j represents the j^{th} receiver. Extending Eq. (2.8) to account for N_t transmitters, requires restructuring both \mathbf{H} and \mathbf{s} . Therefore, the generalized $N_t \times N_r$ MIMO transmission system can be described by

$$\mathbf{R} = \mathbf{H}\mathbf{S} + \mathbf{N}, \quad (2.10)$$

where the vector $\mathbf{S} = \{ \mathbf{s}_1 \dots \mathbf{s}_j \dots \mathbf{s}_{N_t} \}^T$, and the transmission matrix

$$\mathbf{H} = \begin{Bmatrix} \mathbf{h}_{11} & \dots & \mathbf{h}_{1N_t} \\ \dots & \mathbf{h}_{ji} & \dots \\ \mathbf{h}_{N_r1} & \dots & \mathbf{h}_{N_rN_t} \end{Bmatrix}. \quad (2.11)$$

The matrix representation in Eq. (2.10) allows for a three dimensional multiplication (N_t , N_r , and impulse response length L) to be written in a two

dimensional matrix equation, where the size of \mathbf{H} is $[N_t \times N_r L]$. The elements \mathbf{h}_{ji} of \mathbf{H} denote the transmission impulse response from transmitter i to receiver j . Note that the impulse response length L has to be equal for all elements of \mathbf{H} . Note that Eq. (2.11) is not in tensor calculus. In order to unravel all parallel transmitted channels, $N_t \leq N_r \leq N_s$ for Gaussian elimination to be performed, assuming that sufficient transmission diversity is achieved in the transmission channel such that $\text{rank}(\mathbf{H}) = N_t$. Note that N_s represents the spatial channel diversity, i.e. spatial mode channels further detailed in Chapter 3, and to minimize the outage probability, $N_t = N_r = N_s$ is generally used [46].

2.3 Channel state information

MIMO transmission has been recently introduced in the field of optical communications, and therefore many new optical components and sub-systems are currently being developed such as fibers, (de)multiplexers, filters, and amplifiers. As these recently introduced components are not mature and developed, it is important to verify their respective performances. Digital signal processing provides accurate characterization of these components through the acquisition of the channel state information. CSI represents the known transmission properties of \mathbf{H} . Two main methods for obtaining the CSI are well known, namely LS [44], and MMSE estimation [r25]. The former relies on the transmission of a known training sequence \mathbf{S} , and the latter can make use of either known transmitted sequences, or blind estimation. As mentioned before, many components and sub-systems are being developed. Therefore, known transmitted sequences are used for both the LS and MMSE method, as they provide a higher reliability.

2.3.1 Least squares estimation

The transmission matrix \mathbf{H} can be estimated by the transmission of a known sequence \mathbf{S}_T for a received signal \mathbf{R} . The LS estimation method then optimizes [42]

$$\mathbf{H} \approx \mathbf{H}_{LS} = \min_{\mathbf{H}} \{\mathbf{R} - \mathbf{H}\mathbf{S}_T\}. \quad (2.12)$$

Using the autocorrelation method, the LS solution is readily given as [47]

$$\mathbf{H}_{LS} = \mathbf{R}\mathbf{S}_T^H(\mathbf{S}_T\mathbf{S}_T^H)^{-1} = \mathbf{R}\mathbf{S}_T^\dagger, \quad (2.13)$$

where † is the Moore–Penrose pseudo inverse, and in this particular case, the right inverse. From Eq. (2.13), it is implied that $\mathbf{S}_T^\dagger = \mathbf{S}_T^H(\mathbf{S}_T\mathbf{S}_T^H)^{-1}$, and Eq. (2.13) represents a correlation between the received signal and the known transmitted signal. The correlation method averages the result over a symbol sequence with length F_L . Note that a large F_L can increase the accuracy, under the assumption

of a stable channel. The cross correlation of vector signals \mathbf{a} and \mathbf{b} is

$$C_{\text{ab}}(i) = \sum_{j=0}^{J-1} \mathbf{a}_j \mathbf{b}_{j+i}^*, \quad (2.14)$$

where i is the lag, and J is the correlation length. Autocorrelation is the case where $\mathbf{a} = \mathbf{b}$. At the receiver side, 2-fold oversampling is used for the received signal. Therefore, the known training sequence is also 2-fold oversampled. This is achieved by zero-padding, i.e. between two consecutive known training symbols one zero is added. Hence, the pseudo-inverse of the training sequence matrix \mathbf{S}_T^\dagger is the concatenation of N_t toeplitz matrices $\mathbf{S}_{T_i}^\dagger$ as

$$\mathbf{S}_T^\dagger = [\mathbf{S}_{T_1}^\dagger, \mathbf{S}_{T_2}^\dagger, \dots, \mathbf{S}_{T_{N_t}}^\dagger]. \quad (2.15)$$

The Toeplitz matrices \mathbf{S}_{T_i} are generated by [48]

$$\begin{aligned} & \{s_i[k], s_i[k+1], \dots, s_i[k+L-1]\}, \\ & \{s_i[k], s_i[k+1], \dots, s_i[k+F_L-1]\}, \end{aligned} \quad (2.16)$$

representing the first row and column, respectively. F_L denotes the number of samples taken into account. The received matrix

$$\mathbf{R} = \begin{pmatrix} \mathbf{r}_1 \\ \vdots \\ \mathbf{r}_{N_r} \end{pmatrix} = \begin{pmatrix} r_1[k] & \dots & r_1[k+F_L-1] \\ \vdots & \ddots & \vdots \\ r_{N_r}[k] & \dots & r_{N_r}[k+F_L-1] \end{pmatrix}. \quad (2.17)$$

The Toeplitz matrix multiplication performs a convolution between receiver j and transmitter i , as can be understood from section 2.2. Therefore, for large F_L , Eq. (2.13) can be computed more efficiently in the frequency domain as proposed in [r25]. Let

$$\begin{aligned} \mathbf{r}_j(f) &= \mathcal{F}\{\mathbf{r}_j\}, \\ \mathbf{s}_i(f) &= \mathcal{F}\{(s_i[k], s_i[k+1], \dots, s_i[k+F_L-1])^\dagger\}, \end{aligned} \quad (2.18)$$

where $\mathcal{F}\{\cdot\}$ denotes the discrete Fourier transformation (DFT), which uses a power of 2 size for efficient implementation. By performing an element-wise autocorrelation in the frequency domain and selecting the correct section of the outcome, the frequency domain methods yields the same results as the time domain equivalent in Eq. (2.13), where

$$\mathbf{h}_{\text{LS},ji}(f) = \mathcal{F}^{-1}\{\mathbf{r}_j(f) \odot \mathbf{s}_i(f)\}. \quad (2.19)$$

The main challenge for estimating \mathbf{H}_{LS} in optical communications is that Eq. (2.13) does not account for the carrier frequency offsets between the transmitter and LO lasers. For accurate LS channel estimation, the carrier frequency offset must be first removed. This aspect is further detailed in Chapter 7.

2.3.2 Minimum mean square error estimation

A second method for estimating the channel transmission matrix \mathbf{H} is based upon MMSE estimation, and is proposed for optical transmission systems in [r25]. It exploits the MMSE MIMO equalizer's weight \mathbf{W}_{MMSE} response (see Chapter 6). In the receiver DSP, carrier frequency offset is compensated by CPE algorithms (see Chapter 7). Therefore, this method does not require additional frequency offset compensation. MMSE estimation using the MIMO equalizer's weight is particularly interesting for optical communications, as MMSE equalizers are widely employed. The corresponding estimated transmission matrix can then be denoted as

$$\mathbf{H}_{\text{MMSE}} = \mathbf{W}_{\text{MMSE}}^{\dagger} \quad (2.20)$$

The main difference between MMSE and LS is that MMSE takes noise into account, and therefore $\mathbf{H}_{\text{MMSE}} \neq \mathbf{H}_{\text{LS}}$. However, both transmission matrices are approximations of the true transmission matrix \mathbf{H} , and are not exact solutions. The MMSE method has been experimentally compared with the LS method [r25], as shown in Fig. 2.4 for an impulse response estimation of an 80 km quadrature phase shift keying (QPSK) 3MF transmission experiment [r19]. Here, the elements in the figure represent the elements of \mathbf{H} , where the impulse response length L is shown on the horizontal axis of the elements. The maximum eigenvalue discrepancy between the two methods was only 0.3 dB over an OSNR region from 13 to 19 dB. Therefore, it can be concluded that both methods perform similarly and provide good CSI insight.

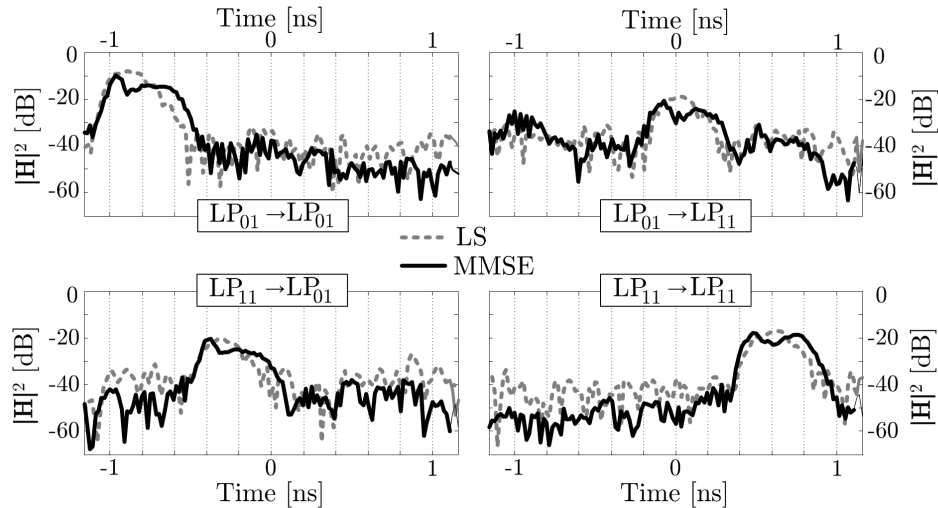


Fig. 2.4 Channel estimation comparison between the LS and MMSE method [r25].

2.4 Transmission capacity

As the transmission matrix \mathbf{H} can be readily estimated, important information from \mathbf{H} can be deduced about the transmission system. Most probably, the most important parameter are the eigenvalues, as they provide insight into the mutual information, and hence, the potential transmission system capacity [44]. In this section, the singular values of the transmission matrix \mathbf{H} are first computed, before the capacity equations are introduced. In communication research, the most commonly used method for computing eigenvalues of a matrix is the singular value decomposition (SVD) [49]. Therefore, let

$$\mathbf{H} = \mathbf{U}\mathbf{\Sigma}\mathbf{V}^H \quad (2.21)$$

and substitute in Eq. (2.10), which results in

$$\mathbf{R} = \mathbf{U}\mathbf{\Sigma}\mathbf{V}^H\mathbf{S} + \mathbf{N}, \quad (2.22)$$

where \mathbf{U} and \mathbf{V}^H are unitary matrices of size $[N_r \times N_r]$ and $[N_t \times N_t]$, respectively. The columns of \mathbf{U} and \mathbf{V} are orthonormal vectors, which can be considered as basis vectors. Note that the Hermitian transpose of \mathbf{V} is unitary. $\mathbf{\Sigma}$ is a diagonal matrix of size $[N_r \times N_t]$, where the singular values σ_m are on the diagonal entries, and are real-valued and positive, where $1 \leq m \leq N_t$. Now, to further simplify Eq. (2.22), assume transmission of [50]

$$\mathbf{S}' = \mathbf{V}^H\mathbf{S}, \quad (2.23)$$

and the reception of

$$\mathbf{R}' = \mathbf{U}^H\mathbf{R}. \quad (2.24)$$

By substituting Eq. (2.23) and Eq. (2.24) into Eq.(2.22), the transmission system is

$$\mathbf{R}' = \mathbf{\Sigma}\mathbf{S}' + \mathbf{U}^H\mathbf{N}. \quad (2.25)$$

Note that by performing a unitary rotation of \mathbf{N} , the AWGN properties remain unaffected. Therefore, for simplicity, introduce

$$\mathbf{N}' = \mathbf{U}^H\mathbf{N}, \quad (2.26)$$

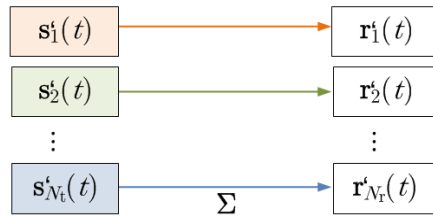


Fig. 2.5 Transmission relation of the rotation of \mathbf{S} and \mathbf{R} through the diagonal matrix $\mathbf{\Sigma}$.

and substitute \mathbf{N}' in Eq. (2.25), to result in a new transmission system model

$$\mathbf{R}' = \mathbf{\Sigma}\mathbf{S}' + \mathbf{N}'. \quad (2.27)$$

This is a very elegant formula, graphically represented in Fig. 2.5, as it directly relates to Eq. (2.10) and clearly indicates the dominance of the singular values of the diagonal entries of $\mathbf{\Sigma}$ for the transmission system performance. Therefore, the singular values provide greater insight into potential transmission system performance. For example, the rank of \mathbf{H} is immediately visible from the number of singular values of $\mathbf{\Sigma}$, and hence, the number of addressable spatial channels for potential parallel information streams employing the same bandwidth is known. Thereby, the potential performance of each parallel stream is indicated. In the optimum case, the condition number of $\mathbf{\Sigma}$ is 1, meaning that the transmission channel matrix \mathbf{H} is statistically well-conditioned. The condition number κ of matrix \mathbf{H} is computed as [51]

$$\kappa(\mathbf{H}) = \frac{\max[|\sigma_m(\mathbf{H})|]}{\min[|\sigma_m(\mathbf{H})|]}. \quad (2.28)$$

If \mathbf{H} is well-conditioned, a high transmission capacity can be realized. However, if the condition number is large, \mathbf{H} is ill-conditioned, resulting in a potentially low transmission capacity [52].

Thus far, the singular values have been used for channel state information purposes. As the main goal of MIMO transmission is to spatially increase the open-loop transmission capacity, the eigenvalues of \mathbf{H} require to be computed. As introduced in Chapter 1, open-loop transmission is currently the only form of transmission in optical core networks, where the receiver does not provide feedback to the transmitter. Therefore, in optical transmission systems the term transmission capacity is used for the open-loop transmission capacity. The eigenvalues λ_m can directly be obtained from the singular values as $\lambda_m = \sigma_m^2$, readily allowing the MDL to be determined as [44]

$$\text{MDL}(\mathbf{H}) = 10 \cdot \log_{10} \left(\frac{\max[\lambda_m(\mathbf{H})]}{\min[\lambda_m(\mathbf{H})]} \right). \quad [\text{dB}] \quad (2.29)$$

Therefore, a large MDL indicates a lower potential transmission capacity. Note that the MDL does not correspond to a spatial mode (see Chapter 3), but to a transmitted spatial channel which during transmission becomes mixed with other spatial channels. The Shannon-Hartley theorem for capacity states that the transmission rate R_T is equal to, or smaller than, the maximum transmission

capacity as [38, 44, 52]

$$R_T \leq C = B \sum_{m=1}^{N_t} \log_2(1 + \lambda_m \text{SNR}_{\text{pol}}), \quad [\text{bits s}^{-1}] \quad (2.30)$$

where

$$\text{SNR}_{\text{pol}} = \sigma_s^2 / \sigma_n^2 \quad (2.31)$$

is the common SNR in one channel (in optical transmission this is a single polarization) and B represents the used bandwidth. The transmission rate R_T denotes the system throughput. Therefore, Eq. (2.30) provides an upper bound for throughput, where the total system transmission throughput rate is the summation of the independent channel rates as

$$R_T = \sum_{m=1}^{N_t} R_m. \quad (2.32)$$

With every transmission system, the initial transmission system design focuses on throughput. When the capacity C is smaller than the designed R_T , the system is considered to be in outage [46]. Finally, an additional important parameter in optical transmission systems is the spectral efficiency SE, and is defined as

$$\text{SE} = R_T / B. \quad [\text{bits s}^{-1} \text{ Hz}^{-1}] \quad (2.33)$$

2.5 Maximizing throughput

As has been well established in theory [39], system throughput is limited by the Shannon capacity, resulting in the aim by system designers to minimize the capacity, where the throughput difference is $C - R_T$. In order to maximize the throughput, the transmitted signal consists of constellations. A constellation is a representation of a modulated signal pulse at the center symbol sampling instant in the complex plane. In this thesis, the employed transmitted signal constellations range from QPSK to higher order QAM symbol sequences. In the following subsections, the generation of these constellations is addressed.

2.5.1 Generalized QAM transmitter

A QAM symbol consists of two orthogonal components, the inphase $I_{\text{QAM}}(t)$ (real) and quadrature $Q_{\text{QAM}}(t)$ (imaginary) component, where both occupy the same bandwidth. To this end, a transmitted QAM symbol sequence can be represented in the perfect case as

$$\begin{aligned} s_{\text{QAM}}(t) &= [I_{\text{QAM}}(t) + jQ_{\text{QAM}}(t)] e^{j2\pi f_0 t} \\ &= I_{\text{QAM}}(t) \cos(2\pi f_0 t) - Q_{\text{QAM}}(t) \sin(2\pi f_0 t), \end{aligned} \quad (2.34)$$

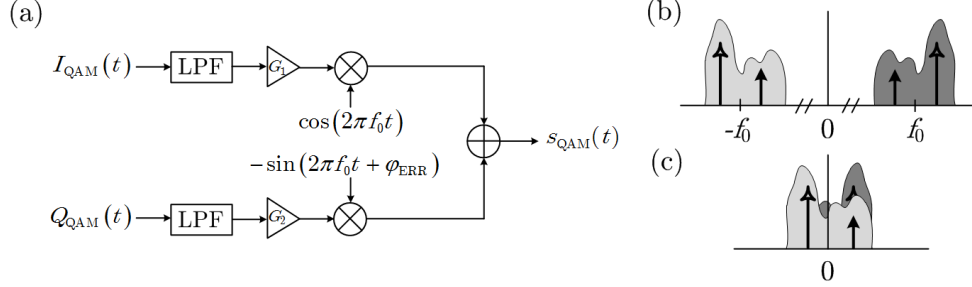


Fig. 2.6 (a) QAM symbol transmitter scheme. Effects of IMRR for (b) the modulated carrier signal and (c) the baseband signal [53].

where f_0 is the carrier onto the QAM signal is modulated. The orthogonality between the two components can easily be proven by

$$\int_0^{1/f_0} \cos(2\pi f_0 t) \sin(2\pi f_0 t) dt = 0, \quad (2.35)$$

when $I_{QAM}(t)$ and $Q_{QAM}(t)$ are constant. However, in reality the QAM transmitter is not perfect. Fig. 2.6(a) shows the generalized QAM transmitter scheme, where an incorrect phase offset between the two mixers is present. This effect is known as the image rejection ratio (IMRR) in [dB], which represents the ratio of the desired frequency to the image frequency [53]. The effect of IMRR is graphically represented in Fig. 2.6 (b) Fig. 2.6 (c) for carrier and baseband signal, respectively. A large negative IMRR_{dB} corresponds to a well performing transmitter. Additionally, in the transmitter two amplifiers are inserted. The gains G_1 and G_2 are also unequal, and contribute to reducing the IMRR. Finally, low pass filters (LPFs) are inserted in each branch. For the experimental work further described in Chapter 8, the low pass filter 3 dB bandwidth was large enough to be considered flat in the signal bandwidth. The transmitter IMRR is defined as [54]

$$\text{IMRR}_{\text{dB}} = 10 \log_{10} \left[\frac{G_1^2 + G_2^2 - 2G_1 G_2 \cos(\varphi_{\text{err}})}{G_1^2 + G_2^2 + 2G_1 G_2 \cos(\varphi_{\text{err}})} \right]. \quad [\text{dB}] \quad (2.36)$$

This equation can be simplified when introducing the gain ratio $G_R = G_1 / G_2$ and $G = G_R - 1$ and by studying two cases. First, assume that the phase offset is 0. In addition, assume that G_R is close to 1. Then the IMRR becomes

$$\text{IMRR}_{\varphi_{\text{err}}=0} = \frac{G_R^2 + 1 - 2G_R}{G_R^2 + 1 + 2G_R} = \frac{(G_R - 1)^2}{(G_R + 1)^2} \approx \frac{G^2}{4}. \quad (2.37)$$

For the second case, assume that there is no gain difference, which results in

$$\text{IMRR}_{G_R=1} = \frac{1 - \cos(\varphi_{\text{err}})}{1 + \cos(\varphi_{\text{err}})} = \tan^2 \left(\frac{\varphi_{\text{err}}}{2} \right) \approx \frac{\varphi_{\text{err}}^2}{4}. \quad (2.38)$$

As these two cases are independent, Eq. (2.36) can be approximated as the summation of the two separate cases as

$$\text{IMRR}_{\text{dB}} \approx 10 \log_{10} \left(\frac{G^2 + \varphi_{\text{err}}^2}{4} \right). \quad (2.39)$$

2.5.2 Constellations

In the experiments in Chapter 8 four standard two dimensional (2D) QAM constellations have been used; QPSK, 8, 16, and 32 QAM. The available laboratory equipment was limited to generating 32 QAM symbols, and hence constellations beyond 32 QAM have not been investigated. Each constellation carries $\log_2(N_{\text{const}})$ bits, where N_{const} represents the number of constellation points. Note that QPSK and 16 QAM are rectangular QAM constellations, and 8 and 32 QAM are non-rectangular constellations. Rectangular constellations have the advantage of bits being modulated in either $I_{\text{QAM}}(t)$ or $Q_{\text{QAM}}(t)$, whereas non-rectangular QAM constellations have a dependence on both dimensions. This is shown in Fig. 2.7, where the respective numbers decimally represent the bit sequence. Theoretically, arbitrary bit mappings can be chosen. However, for optimal performance, the square transmitted constellations are Gray coded, where the bit mapping is shown in Fig. 2.7 [55]. Note that the non-square constellations are not Gray coded.

Recently in optical transmission systems, based on the two dimensional QAM constellations, higher order constellations are considered to be employed. The main motivation for this is the readily available electronic capabilities and the available bandwidth which is being occupied by the transmission channels. Four dimensions are formed by using two consecutive 2 dimensional QAM constellations. A technique was introduced in the early 80's by Ungerboeck to use symbols carrying a number of bits in redundant signal sets [56]. The transmitted signal sets were set-

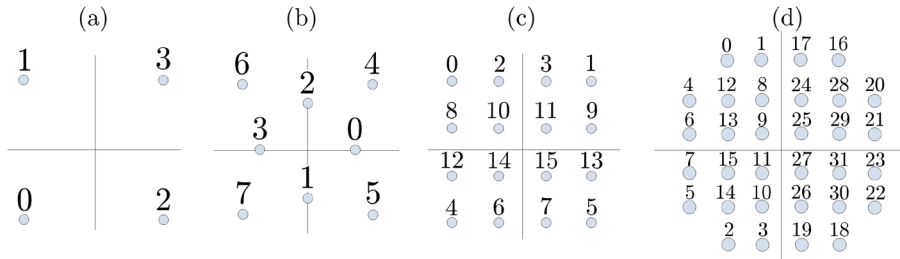


Fig. 2.7 Transmitted QAM constellations in this work: (a) QPSK, (b) 8, (c) 16, and (d) 32 QAM. The numbers decimally represent the bit allocations [55].

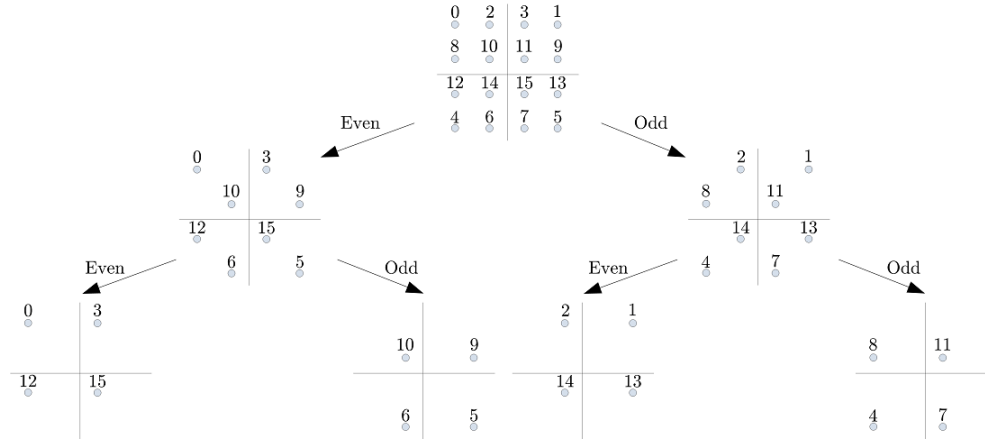


Fig. 2.8 Two-step set partitioning of the 16 QAM constellation on even or odd parity.

partitioned (SP) to maximize the Euclidian distance. Note that, by performing set partitioning, the number of transmitted bits per symbol is reduced. Effectively, the same methodology can be applied in 4D constellations, where the 4 dimensional Euclidian distance between constellation points is increased. This method was first introduced in optical transmission systems in 1990 [57]. However, it wasn't widely adopted. For approximately 20 years there was little interest in constellation coding. With optical transmission systems currently being aided by high speed digital signal processing electronics, there is a resurgence in the use of higher order modulation format coding [58, 59]. This represents the first four dimensional (4D) constellation transmission over a 3MF, further detailed in Chapter 8. The transmission of three 4D constellations has been investigated in this thesis, namely time-shifted (TS) QPSK (3 bits), 32-SP-QAM (5 bits), 128-SP-QAM (7 bits). TS-QPSK is based on two QPSK symbols, and the latter two are based on two 16 QAM symbols. In two 2D constellations $2 \cdot \log_2(N_{\text{const}})$ bits can be transmitted, which is 4 and 8 bits for the QPSK and 16 QAM basis, respectively. TS-QPSK can easily be generated by adding one parity bit to 3 data bits which are being transmitted. The same methodology is applied to 128-SP-QAM, where 7 data bits and one parity bit are transmitted. A slightly more difficult constellation to generate is 32-SP-QAM. First, both the first and second 16 QAM constellations are SP once, as depicted in Fig. 2.8. This reduces the throughput to 6 bits per 4D symbol. Finally, the last bit is used as parity bit, similarly to previously mentioned 4D constellations. This results in the transmission of 5 bits per four dimensions. Note that, by further increasing the dimensionality of the constellations, increased gains in SNR tolerances could potentially be achieved [56]. To investigate the theoretical performance limits of all the transmitted constellations, the bit error rate (BER) for each SNR is computed. Therefore, the 2D and 4D constellations are

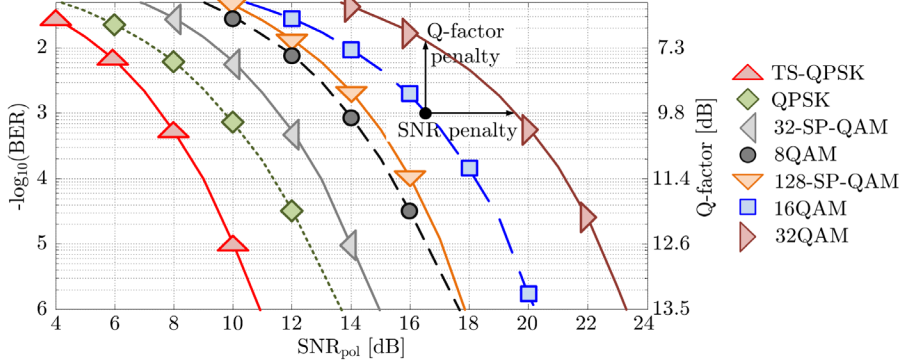


Fig. 2.9 BER and Q-factor versus SNR_{pol} for all transmitted constellations in Chapter 8.

noise loaded per SNR value, and Monte-Carlo simulations are performed such that $>10,000$ errors are counted. For all constellations, a maximum-likelihood (ML) decoder is used to maximize the BER performance. The resulting BER curves for all constellations are depicted in Fig. 2.9, and are used for system characterization in Chapter 8. BER versus SNR characterization is the only true system performance measure available. However, for historical reasons, occasionally research groups and carriers prefer to use the quality factor, or Q-factor Q . The Q-factor can be computed from the BER in linear units using [60]

$$\text{BER} = \frac{1}{2} \text{erfc} \left(\frac{Q}{\sqrt{2}} \right) \approx \frac{\exp(-Q^2/2)}{Q(2\pi)^{1/2}}, \quad (2.40)$$

where erfc represents the complementary error function as

$$\text{erfc}(x) = \frac{2}{\sqrt{\pi}} \int_x^{\infty} e^{-v^2} dv, \quad (2.41)$$

and the Q-factor in dB is $Q_{\text{dB}} = 20 \log_{10}(Q)$. Note that an SNR penalty is the primary performance indicator of a system penalty and is defined on the horizontal axis for a set BER, and the Q-factor penalty is defined on the vertical axis for a set SNR, as depicted in Fig. 2.9. Clearly, for all transmitted constellations, SNR is the main limiting factor in transmission capacity and throughput [61]. SNR has been previously defined in Eq. (2.31), however, in optical transmission systems, the term OSNR is more commonly used. OSNR can be directly computed from SNR as [36]

$$\text{OSNR} = \frac{N_{\text{pol}}}{2T_{\text{sym}} B_{\text{ref}}} \text{SNR}_{\text{pol}}, \quad (2.42)$$

where B_{ref} is 0.1 nm reference bandwidth (12.5 GHz at 1550 nm wavelength), and N_{pol} is the number for transmitted polarizations. Note that in the denominator the symbol time is used, therefore OSNR is dependent on the serial data rate. In this work, N_{pol} is always assumed to be 2, corresponding to DP transmission. The 0.1

nm reference bandwidth is commonly chosen for measurement purposes [36]. In decibel, OSNR is a linear shift of SNR_{pol} as

$$\text{OSNR}_{\text{dB}} = 10\log_{10}\left(\frac{N_{\text{pol}}}{2T_{\text{sym}}B_{\text{ref}}}\right) + \text{SNR}_{\text{pol,dB}}. \quad (2.43)$$

For further transmission performance characterization in the experiments discussed in Chapter 8, OSNR_{dB} is used.

2.6 Constellation sequences

The previous section described how constellations are formed with a number of bits. However, the transmitted signals consist of constellation sequences. For real data, these constellation sequences are continuous zero-mean uncorrelated bit sequences, as previously defined in section 2.1. However, in the laboratory, the length of these sequences is bound by the laboratory equipment memory. Therefore, constellation sequence lengths are generally of length 2^n , and are cyclically repeated. In order to emulate multiple channels, delayed copies of one sequence are transmitted. This is a cheap methodology for emulating multiple transmitters. Therefore, it is key that the transmitted constellation sequences have very good autocorrelation features, i.e. no correlation is allowed with itself. As constellations are formed by multiple bit sequences, it is important to note that the used bit sequences should be independent and uncorrelated. For completeness, the three main sequence generators often used are explained [62], namely polyphase constant amplitude zero autocorrelation (CAZAC) sequences, binary pseudo random bit sequences (PRBSs), and non-binary De Bruijn sequences. The transmitted sequences in the experimental work in Chapter 8 are based on PRBSs, and the resulting autocorrelation of the full sequence length for the various 2D

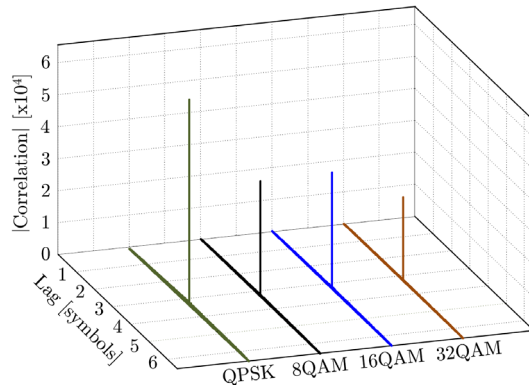


Fig. 2.10 Autocorrelation of the transmitted 2^{15} length QPSK, 8, 16, and 32 QAM symbol sequences, based on independent PRBSs.

constellations is shown in Fig. 2.10. The autocorrelation is defined in Eq. (2.14). Note that the correlation peaks are different in height, which is attributed to the average amplitude in the constellation. The maximum amplitude was set to 1 per dimension. Therefore, it can be concluded that for all QAM constellations truly uncorrelated sequences are transmitted.

2.6.1 CAZAC sequence

The CAZAC sequence was initially proposed by Frank and Zadoff [63], and improved by Chu [64]. Therefore, this polyphase sequence type is also known as the Frank-Zadoff-Chu sequence, and is used in long-term evolution (LTE) wireless networks. The CAZAC sequence is defined as [64]

$$s[k] = \begin{cases} e^{j\frac{i\pi k^2}{N_{\text{CAZAC}}}} & \text{for even } N_{\text{CAZAC}}, \\ e^{j\frac{i\pi k(k+1)}{N_{\text{CAZAC}}}} & \text{for odd } N_{\text{CAZAC}} \end{cases}, \quad (2.44)$$

where i and N_{CAZAC} are relatively prime, i.e. the greatest common divider is 1, and N_{CAZAC} denotes the desired sequence length. The main benefit of using CAZAC sequences are the constant amplitude and autocorrelation properties. Therefore, this type of sequence is mainly interesting for phase shift keying (PSK) modulation formats. To this end, sequences with good autocorrelation features that do not necessarily have to satisfy constant amplitude are preferred.

2.6.2 Pseudo random bit sequence

From the bit sequence generators, the most commonly used is the deterministic PRBS generator. Its popularity is mainly attributed to its simplicity in employing a linear feedback shift register (LFSR) of length n , to generate a 2^{n-1} cyclic pseudo random sequence. Constellations based up PRBSs have been used in this work. Currently known maximum length shift registers go beyond $n=168$ [65]. Using $n=168$ results in a sequence substantially longer than commonly used laboratory instruments memory can hold. Generally, a LFSR of length 15, 21, or 31 is used. Unless otherwise noted, the LFSR length used in this work is 15, and the employed

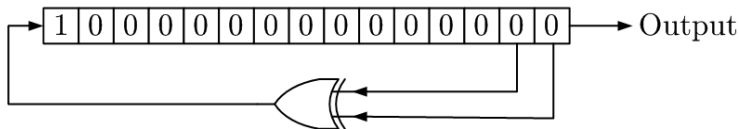


Fig. 2.11 LFSR of length 15, which generates a $2^{15}-1$ PRBS.

LFSSR is shown in Fig. 2.11. The initial values in the shift register are the seed values, which cannot be all zeros as the exclusive-or will not generate 1's. Note that using the same PRBS for constellation sequences carrying multiple bits results in loss of the autocorrelation properties [66]. However, as n increases, >1 PRBS solution exists for each value of n , where each solution uses a different LFSSR. Consequently, the creation of multiple independent and uncorrelated bit sequences can be exploited to generate symbols with good autocorrelation features carrying multiple bits, as depicted for all transmitted constellation sequences in Fig. 2.10.

2.6.3 De Bruijn sequence

The last sequence type is the non-binary De Bruijn sequence, which is also a cyclic sequence. Unlike PRBSs however, De Bruijn sequences are not limited to binary solutions, but are formed by an alphabet (the constellation points), and a subsequence length. Unfortunately, they are more difficult to generate than PRBSs [67], as each constellation type with N_{const} , requires new De Bruijn sequences to be generated. The main advantage of De Bruijn sequences is that they satisfy the occurrence of each subsequence in the total constellation sequence once. This is not true for PRBS, as the $0\dots 0$ subsequence is not visited. In terms of autocorrelation, both have good performance.

2.7 Converting constellations to the optical domain

Previous sections have focused on the linear theoretical limits and generation of constellation sequences. Thus far, the generation of constellation sequences is performed analytically in the digital domain. To convert the digital domain sequences to the optical domain, first the sequences are transformed to analog electrical sequences. This conversion is performed using a DAC. The DAC is a key component for increasing and optimizing the serial channel data rate and performance, shown in Fig. 1.5. Each DAC has a number of analog levels available, the quantization levels, which correspond to the number of precision bits. This is also true for the ADC. However, the ENOB is not equal to the number of precision bits and can be computed by generating sine wave patterns, where the number of cycles is relatively-prime to the number of points in the pattern [68]. Fig. 2.12 depicts the record ENOB figures of commercially available ADCs up to 2008 [69], which experience a similar trend as DACs. From the figure can be observed that the ENOB decreases as the frequency increases. The performance is theoretically limited by the 50 ohms thermal noise, and to overcome this limit, the usage of photonic ADCs is proposed [70]. The ENOB figure of the commercial DAC used in this work, the Micram Vega DAC II, limited the constellation size to 32 QAM in 2

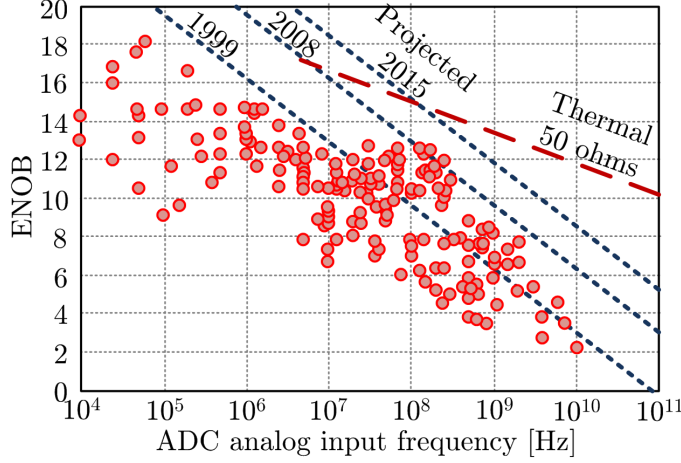


Fig. 2.12 Analog-to-digital converter ENOB scaling with frequency, limiting the signal generation performance [69].

dimensions, as denoted in section 2.5. Due to a non-disclosure agreement with the manufacturer, this figure cannot be shown with respect to the output baud rate.

After the digital domain sequence has been converted to the analog domain, there are three fundamental techniques for the implementation of an analog-to-optical converter [71]: direct modulation of a laser, laser external modulation, and external modulation through a Mach-Zehnder modulator (MZM). The latter technique is the most preferred method, as chirp-free constellation generation can be achieved [72], and is the technique used throughout this work. Note that this is also the most expensive analog-to-optical converter method. The MZM scheme is shown in Fig. 2.13(a), where in each arm a phase modulator is present. Without considering insertion loss and assuming a correct bias point, the transfer function from an analog electrical signal to optical signal is [72]

$$\frac{\mathcal{E}_{\text{out}}(t)}{\mathcal{E}_{\text{in}}(t)} = \frac{1}{2} \left(e^{j\varphi_1(t)} + e^{j\varphi_2(t)} \right), \quad (2.45)$$

where for simplicity $\mathcal{E}_{\text{in}}(t)$ and $\mathcal{E}_{\text{out}}(t)$ represent the MZM input and output optical carrier independent of Cartesian coordinates, respectively, and the phase

$$\varphi_i = \frac{s_i(t)}{V_{\pi,i}} \pi. \quad (2.46)$$

Note that $s(t)$ has been previously defined as the transmitted signal, and V_{π} denotes the driving voltage required to achieve a π -phase shift in one arm. Typical V_{π} driving voltages range from 3 to 6 Volt. To achieve chirp-free constellation

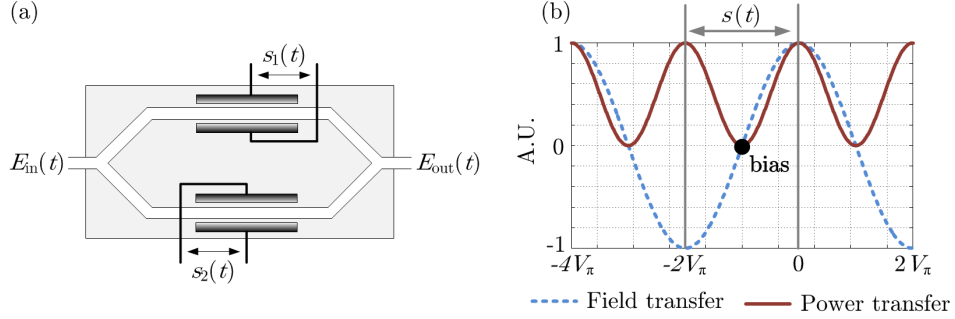


Fig. 2.13 (a) Mach-Zehnder modulator scheme, (b) field and power transfer function of the Mach-Zehnder modulator [72].

generation, the arms are driven in a push-pull configuration, this means that the transmitted signals are generated as

$$s_1(t) = -s_2(t) = s(t)/2. \quad (2.47)$$

Inserting Eq. (2.46) and Eq. (2.47) in (2.45) gives

$$\frac{\mathcal{E}_{\text{out}}(t)}{\mathcal{E}_{\text{in}}(t)} = \cos \left[\frac{s(t)\pi}{2V_\pi} \right]. \quad (2.48)$$

The field transfer function is shown in Fig. 2.13(b), where the bias Voltage is set at $-V_\pi/2$. Operating the MZM with the bias Voltage at $V_\pi/2$ results in a sign change of the modulated field with respect to the $-V_\pi/2$ bias Voltage. The power transfer function between the input P_{in} and output P_{out} can be obtained by squaring the electrical field output of Eq. (2.48), resulting in

$$\frac{P_{\text{out}}(t)}{P_{\text{in}}(t)} = \cos^2 \left[\frac{s(t)\pi}{2V_\pi} \right] = \frac{1}{2} + \frac{1}{2} \cos \left[\frac{s(t)\pi}{V_\pi} \right]. \quad (2.49)$$

The power transfer function is illustrated in Fig. 2.13(b). Note that the MZM allows only one analog electrical input to be converted to the optical domain. Therefore, for generating QAM constellations, two MZMs are required. This element is often referred to as a double nested MZM or an IQ-modulator. The IQ-modulator scheme is shown in Fig. 2.14. In the lower arm, an optical $\pi/2$ phase shift is introduced to generate the real and imaginary axis of the QAM constellation. The transfer function can be extended from Eq. (2.48) as

$$\mathcal{E}_{\text{out}}(t) = \left\{ \cos \left[\frac{s_I(t)\pi}{2V_\pi} \right] + j \cos \left[\frac{s_Q(t)\pi}{2V_\pi} \right] \right\} \frac{\mathcal{E}_{\text{in}}(t)}{2}, \quad (2.50)$$

where s_I and s_Q represent the transmitted inphase and quadrature signal,

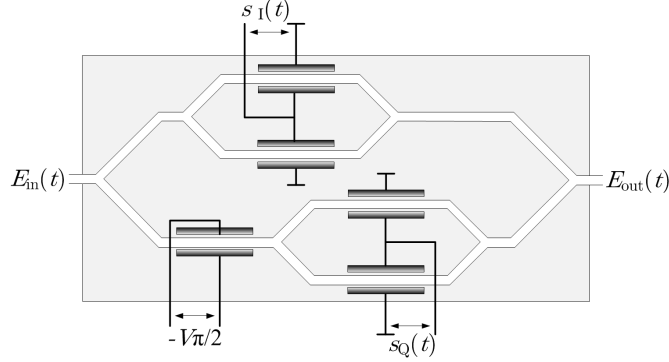


Fig. 2.14 IQ-modulator scheme consisting of two MZMs, where one is phase shifted by $\pi/2$.

respectively. Note that Eq. (2.50) is directly related to Eq. (2.34), where

$$\begin{aligned}
 I_{QAM}(t) &= \cos\left[\frac{s_I(t)\pi}{2V_\pi}\right], \\
 Q_{QAM}(t) &= \cos\left[\frac{s_Q(t)\pi}{2V_\pi}\right], \\
 \mathcal{E}_{in}(t) &= 2e^{j2\pi f_c t}.
 \end{aligned} \tag{2.51}$$

The IQ-modulator used in this work is implemented on a Lithium Niobate (LiNbO3) platform. IQ-modulators can also be implemented in Gallium Arsenide (GaAs) or Indium Phosphide (InP) [72].

2.8 Transmitter digital filters

The goal of digital domain filters is to optimize the transmitted signal, and hence, improve the transmission system performance. This section first focuses on digital predistortion filters, followed by pulse shaping filters.

2.8.1 Digital predistortion filters

In Eq. (2.51) it was shown that I_{QAM} and Q_{QAM} are related to s_I and s_Q through a Cosine function. Obviously, it is clear that the digital to optical transfer function is not linear. As the transfer function is known, a simple digital predistortion filter can be introduced to obtain a linear digital to optical transfer function. Therefore, let

$$\begin{aligned}
 \hat{s}_I(t) &= \frac{2V_\pi}{\pi} \arccos[s_I(t)], \\
 \hat{s}_Q(t) &= \frac{2V_\pi}{\pi} \arccos[s_Q(t)].
 \end{aligned} \tag{2.52}$$

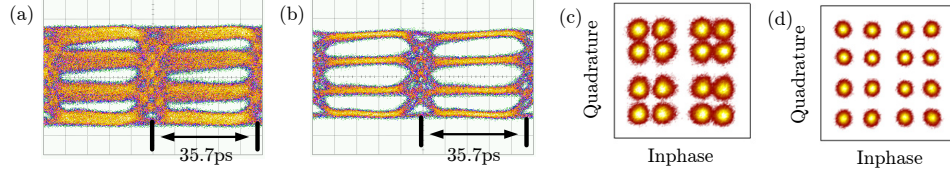


Fig. 2.15 Experimental demonstration of the arccos and overshoot predistortion filters. 28 GBaud 4 PAM electrical driving signal (a) without, and (b) with overshoot filter. 28 GBaud 16 QAM optical constellation (c) without, and (d) with arccos and overshoot filter.

when inserting Eq. (2.52) in Eq. (2.50), the linear transfer function

$$\mathcal{E}_{\text{out}}(t) = \left\{ \hat{s}_I(t) + j \hat{s}_Q(t) \right\} \frac{\mathcal{E}_{\text{in}}(t)}{2} \quad (2.53)$$

is obtained. Hence, the desired analog signal to be transmitted is $\hat{s}_I(t) + j \hat{s}_Q(t)$. This conversion can be achieved by a single-tap amplitude filter.

In addition, in the QAM constellation generation figure (Fig. 2.6), a low pass filter is inserted in the signal paths. The primary sources of the low pass filter are the DAC and electrical cable bandwidth limitations, which have to be taken into account. As bandwidth limitations are inevitable in practice, a signal amplitude change results in a non-zero rise and fall time. The amplitude difference between the current and next transmitted symbol is

$$\Delta s = s[k] - s[k+1]. \quad (2.54)$$

Now, a simple single-tap digital filter can be applied through which Δs can be altered, either in a linear or nonlinear fashion. Employing such digital filter can result in overshoot. However, when implemented correctly, the overshoot effect is smaller than the rise and fall time penalty. To indicate the filter performance, an experimental 28 GBaud 16 QAM consisting of two 4 pulse amplitude modulation (PAM) electrical driving signals with and without digital overshoot filter is shown in Fig. 2.15. This figure depicts an experimental 16 QAM constellation measured in a back-to-back (BTB) setup where (c) no filters are applied, and (d) both the overshoot and Arccosine filter are applied.

2.8.2 Digital pulse shaping filters

The previous two digital filters focused on optimizing the constellation by predistorting the s_I and s_Q signals. However, a second type of digital filter can be applied as well: the pulse shaping filter. By performing digital pulse shaping, the intersymbol interference (ISI) can be minimized, and the signal frequency spectrum response can be altered [r15]. It is important to note that the maximum system capacity in Eq. (2.30) assumes a limited bandwidth B . When transmitting a signal

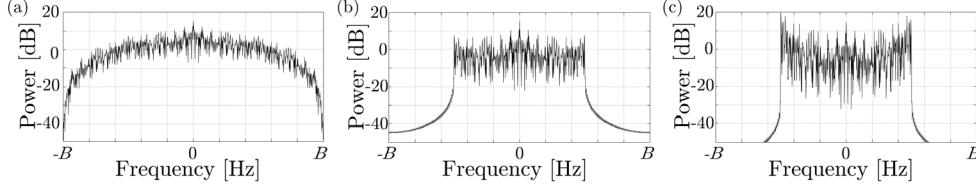


Fig. 2.16 Transmission spectrum (a) without digital pulse shaping filter, (b) with Nyquist filter, and (c) with Nyquist and spectral pre-emphasis filter.

without signal shaping, a wide bandwidth is used as shown in Fig. 2.16(a). Usually, this bandwidth is considered to be approximately $2B$. The wide bandwidth can be reduced to B by employing a raised-cosine filter $H_{rc}(f)$. In the frequency domain, this filter is defined as [71]

$$H_{rc}(f) = \begin{cases} T_{\text{sym}} & |f| \leq \frac{1 - \beta_R}{T_{\text{sym}}} \\ \frac{T_{\text{sym}}}{2} \left[1 + \cos\left(\frac{\pi T_{\text{sym}}}{\beta_R} |f| - \frac{1 - \beta_R}{2T_s}\right) \right] & \frac{1 - \beta_R}{2T_s} < |f| \leq \frac{1 + \beta_R}{2T_{\text{sym}}} \\ 0 & \text{otherwise} \end{cases}, \quad (2.55)$$

where $0 \leq \beta_R \leq 1$ is the roll-off factor. The simulated resulting spectrum for a BTB transmission is shown in Fig. 2.16(b) for $\beta_R = 0$. For this case, the raised cosine filter is considered to be a Nyquist filter, which corresponds to a Sinc function in the time domain. Theoretically, this digital filter provides a minimized signal bandwidth B , and thus maximizes the SE. To implement a perfect Nyquist raised cosine filter, 2-fold signal oversampling is required. However, the required oversampling rate is often limited by availability of a high-speed DACs, resulting in roll-off factors being chosen which are larger than 0 at the cost of bandwidth. Furthermore, for completeness, a digital spectral pre-emphasis filter can be employed to compensate the analog bandwidth roll-off, as shown in Fig. 2.16(c).

2.9 Summary

This chapter has introduced the general linear transmission system, and has discussed the implications in scaling from a regular one transmitter and one receiver system to a MIMO transmission system. Through employing V-BLAST, it is shown that the system capacity can be increased, without requiring additional bandwidth. Channel state information has been introduced for estimating the MIMO transmission matrix, and is particularly important for understanding the coupling parameters and maximum capacity achievable by the MIMO transmission

system. As the capacity is the upper limit of the throughput, the QAM constellation format has been introduced, which exploits the inphase (real) and quadrature (imaginary) phase components. However, for low BER performance, the chosen QAM constellation is always limited by the signal-to-noise ratio performance of the transmission system. Therefore, depending on the transmission system's signal-to-noise ratio, a suitable QAM constellation has to be chosen. Furthermore, the generation of the QAM constellation sequence by a number of independent bit sequences has been explained, and the electrical to the optical domain conversion has been detailed. Finally, digital filters are introduced for compensating for transmitter impairments and for optimizing the chosen transmission constellation.

Chapter 3

Scaling in the optical fiber medium

Study the past, if you would divine the future.

Confucius

In the previous chapter, a linear transmission model was established for MIMO systems exploiting the spatial domain to increase the transmission system capacity for a fixed bandwidth. This chapter provides a detailed description to create and exploit the spatial dimension in optical fibers through recently introduced fiber types such as few-mode fibers, multi-mode fibers, multi-core fibers, and potential combinations between multi-mode and multi-core fibers. These SDM fibers are introduced in section 3.1. The key difference between SDM fibers and conventional SSMFs is that the latter only allows for the guidances of one spatial mode in a single core. Therefore, the primary focus of this chapter is to provide a fundamental basis for scaling and managing the digital signal processing equalizer computational complexity in Chapter 6, and experimental results obtained in Chapter 8. As the majority of the contributions is based on employing multiple modes as spatial transmission channels, first, the origin of a mode is described. To this end, section 3.2 focuses on Maxwell's equations, to obtain the transverse wave equation. The transverse wave equations allows for establishing the field modes, which are approximated by the LP mode basis in section 3.3. In section 3.4 the linear description of the fiber impulse response is obtained. Therefore, section 3.4 gives great insight in digital equalization requirements. Unfortunately, due to mode coupling in the fiber, and coupling at fiber splice points, the optical transmission channel becomes a fading channel. This is detailed in section 3.5. Finally, optical propagation effects are described in section 3.6. There are three primary propagation effects, namely attenuation, linear impairments such as GVD, and nonlinear impairments. Attenuation can be compensated by optical amplifiers, which add ASE noise, degrading the OSNR. GVD can be considered an all-pass filter, and can therefore be compensated by digital filters. Then, a brief description is outlined of the origin of nonlinear behaviour. The primary equalization task is to mitigate linear impairments, and therefore the transmission system is generally operated in a region where the nonlinear effects are small. Finally, scaling channels through multi-core transmission is detailed.

3.1 Spatial division multiplexing in optical fibers

In Chapter 2 it was noted that the transmission system's capacity can be increased through MIMO transmission, where all transmitted channels occupy the same bandwidth. However, the key requirement for MIMO transmission to work is spatial diversity, i.e. the condition number of the transmission matrix \mathbf{H} has to be low (near 1 to maximize transmission capacity). A key advantage of optical transmission systems is that transmission medium, the optical fiber itself, can be engineered to the designer's liking for increasing the number of spatial transmission channels. The most obvious and simplest method of spatial diversity is by employing multiple SSMFs, as shown in Fig. 3.1(a). The main advantage of this approach is that all components are readily available, and accordingly, no research is required, and the capacity crunch can be alleviated. However, employing single mode fibers scales the cost per transmitted bit linearly. As Chapter 1 introduced, the capacity demand is increasing exponentially, and therefore linear scaling is not commercially viable in the long term. Key to reducing costs is the sharing of components in a transmission system. To this end, multiple solutions have been proposed over the last few years [25]:

- Few-mode fibers (FMFs) [73-75].
- Multimode fibers [76].
- Multi-core fibers (MCFs) [30, 77].
- Coupled-core fibers (CCFs) [78].
- Hollow-core photonic bandgap fibers [79-81].

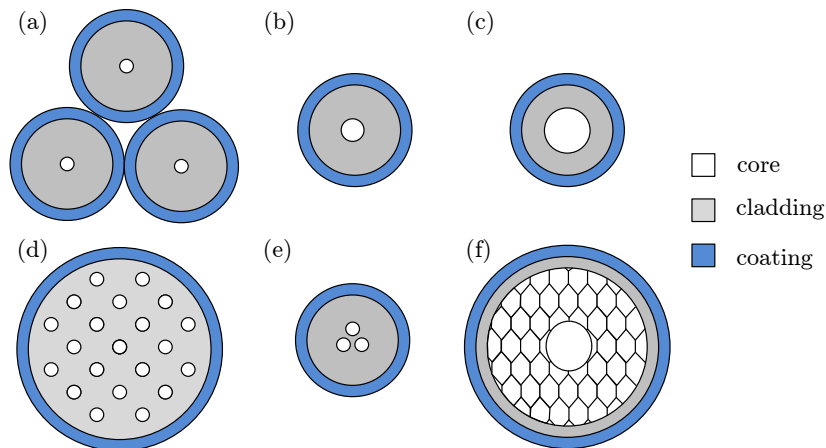


Fig. 3.1 Schematic representation of the suggested optical fiber types for SDM. (a) multiple single mode fibers. (b) few-mode fiber. (c) multimode fiber. (d) multicore fiber. (e) coupled-core fiber. (f) photonic bandgap fiber.

Currently, the best spatial multiplexing solution is unknown. Further research is required, and will not depend on the fiber medium only, but also on optical components such as (de)multiplexers, amplifiers, optical filters, and switches. There are two approaches for subdividing the above fiber types, namely multimode and multicore, where either the orthogonal fiber modes or orthogonal spatial cores are used as transmission channels. The former fiber type comprises the FMF, MMF, and HC-PBGF, and the latter fiber type comprises the remaining two fibers in Fig. 3.1. Alternatively, a second approach to subdivide the above fibers is by separating them in the solid core and hollow core fiber types, where the latter type only consists of the HC-PBGF.

Note that any linear combination of the aforementioned fibers can also be made. In Chapter 8, a 3MF is characterized [r3], HC-PBGF [r32], and the linear combination of a few mode and a multi core fiber; the FM-MCF [r36]. In this work, the primary focus is achieving SDM through mode multiplexing. Note that all aforementioned fiber types described are experimental fibers, and can be considered non-optimal for commercial application. They are to be further optimized for increased transmission performance in the future. Therefore, in the next sections, first the optical fiber wave equation is described, followed by the weakly guiding approximation to arrive at a basis describing the spatial mode equations [82]. This description is based on the conventional solid core fibers. Note that similar results can be obtained for the HC-PBGF. However, the theoretical analysis of the HC-PBGF is considered to be outside the scope of this thesis.

3.2 The wave equation

To explain the concept of employing guided orthogonal spatial optical eigenmodes, or fiber modes, as transmission channels the fundamental basis of light propagation is explained in this section. In short, an optical mode is a particular solution to the Maxwell equations, and in one spatial dimension is generally explained as a vibrating string in a two-dimensional plane. When solving the wave equation, the vibrations result in a set of harmonic oscillating standing waves. In fact, a similar analogy can be applied to optical modes. As propagating light in an optical fiber is an electromagnetic wave, the fundamental starting point to explaining the nature

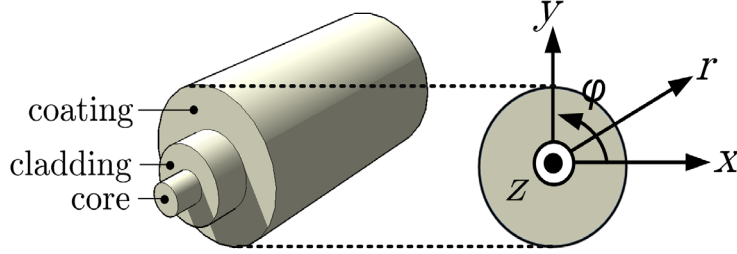


Fig. 3.2 Optical fiber description in Cartesian and Cylindrical coordinates, where the z -axis denotes the direction of propagation.

of fiber modes are Maxwell's equations in the space-time domain, as [83]

$$\nabla \times \mathcal{E}(\mathbf{p}, t) = -\partial_t \mathcal{B}(\mathbf{p}, t), \quad (3.1)$$

$$\nabla \times \mathcal{H}(\mathbf{p}, t) = \partial_t \mathcal{D}(\mathbf{p}, t), \quad (3.2)$$

$$\nabla \cdot \mathcal{D}(\mathbf{p}, t) = 0, \quad (3.3)$$

$$\nabla \cdot \mathcal{B}(\mathbf{p}, t) = 0. \quad (3.4)$$

The partial derivative with respect to time is denoted by ∂_t , and ∇ is the three dimensional gradient operator. Accordingly, $\nabla \times \mathbf{A}$ and $\nabla \cdot \mathbf{A}$ denote the curl and divergence of the three dimensional vector \mathbf{A} , respectively. The vectors \mathcal{E} [V m^{-1}] and \mathcal{H} [A m^{-1}] represent the electric and magnetic field, respectively, and \mathcal{D} [A s m^{-2}] and \mathcal{B} [V s m^{-2}] describe the corresponding flux densities. All previously mentioned vectors are dependent on the three dimensional Cartesian position vector $\mathbf{p} = [x, y, z]^T$, as shown in Fig. 3.2, and time t . Note that the electric field $\mathcal{E}(t)$ defined in Eq. (2.45) is extended to the spatial domain in Eq.(3.1). Therefore,

$$\mathcal{E}(\mathbf{p}, t) = \mathcal{E}(\mathbf{p}) \mathcal{E}(t) = \begin{bmatrix} \mathcal{E}_x \\ \mathcal{E}_y \\ \mathcal{E}_z \end{bmatrix} e^{j\omega_0 t}. \quad (3.5)$$

Through Eq. (3.5) it is obvious that the angular frequency ω_0 can be converted to the carrier frequency f_0 , to relate Eq. (3.5) to Eq. (2.51), by

$$\omega = 2\pi f. \quad [\text{rad}] \quad (3.6)$$

For simplicity, assume that the optical fiber is a linear, time-invariant, isotropic, and inhomogeneous medium. In fact, optical fibers are not a linear transmission medium. However, for the computation of the spatial modes, the non-linear behaviour of the fiber can be neglected for simplicity. Assuming a time invariant system, the constitutive relation between the electric field and flux is given by [84]

$$\mathcal{D}(\mathbf{p}) = \varepsilon(\mathbf{p}) \mathcal{E}(\mathbf{p}) + \mathcal{J}(\mathbf{p}), \quad (3.7)$$

and the constitutive relation between the magnetic field and flux is

$$\mathcal{B}(\mathbf{p}) = \mu_0 [\mathcal{H}(\mathbf{p}) + \mathcal{K}(\mathbf{p})]. \quad (3.8)$$

$\mathcal{J}(\mathbf{p})$ [A m⁻²] and $\mathcal{K}(\mathbf{p})$ [V m⁻²] represent the induced electric and magnetic current density. μ_0 ($= 4\pi \times 10^{-7}$ V s A⁻¹ m⁻¹) denotes the permeability in vacuum. The absolute permittivity

$$\varepsilon(\mathbf{p}) = \varepsilon_0 \varepsilon_r(\mathbf{p}), \quad (3.9)$$

where ε_0 ($= 8.854 \times 10^{-12}$ A s V⁻¹ m⁻¹) and $\varepsilon_r(\mathbf{p}, t)$ denote the permittivity in free space and the relative permittivity in the optical fiber. Note that the propagation speed in vacuum $c_0 = (\varepsilon_0 \mu_0)^{-1/2}$ [m s⁻¹]. Now that the material parameters have been introduced, the optical fiber can be considered for further reducing the complexity of Maxwell's equations. The above equations can be further simplified as optical fibers are source free regions, and hence

$$\mathcal{J}(\mathbf{p}) = \mathcal{K}(\mathbf{p}) = 0, \quad (3.10)$$

which is true for the purely linear transmission region, where fiber non-linear behavior is fully neglected. To obtain the wave equation, the first step is to convert the time-domain Maxwell equations of Eq. (3.1)-(3.4) to the frequency domain as

$$\nabla \times \mathcal{E}(\mathbf{p}, \omega) = -j\omega \mathcal{B}(\mathbf{p}, \omega), \quad (3.11)$$

$$\nabla \times \mathcal{H}(\mathbf{p}, \omega) = j\omega \mathcal{D}(\mathbf{p}, \omega), \quad (3.12)$$

$$\nabla \cdot \mathcal{D}(\mathbf{p}, \omega) = 0, \quad (3.13)$$

$$\nabla \cdot \mathcal{B}(\mathbf{p}, \omega) = 0. \quad (3.14)$$

Note that the only time dependence in the time-domain Maxwell equations is the multiplication by $e^{j\omega t}$, and therefore a time derivate results in a multiplication by $j\omega$. By substituting Eq. (3.10) in the constitutive relations of Eq. (3.7) and Eq. (3.8), and transferring them to the frequency domain yields

$$\mathcal{D}(\mathbf{p}, \omega) = \varepsilon(\mathbf{p}, \omega) \mathcal{E}(\mathbf{p}, \omega) = \varepsilon_0 \varepsilon_r(\mathbf{p}, \omega) \mathcal{E}(\mathbf{p}, \omega), \quad (3.15)$$

$$\mathcal{B}(\mathbf{p}, \omega) = \mu_0 \mathcal{H}(\mathbf{p}, \omega). \quad (3.16)$$

From observing Eq. (3.15), it is clear that the permittivity is dependent of frequency, meaning that the optical fiber medium is dependent on frequency. Now, an important material parameter can be introduced, namely

$$n(\mathbf{p}, \omega) = [\varepsilon_r(\mathbf{p}, \omega)]^{1/2}, \quad (3.17)$$

which represents the refractive index of the optical fiber. Eq. (3.17) is particularly important, as it indicates that the refractive index can vary in the fiber over all three dimensions. Generally, in the transverse plane with respect to the direction in which light propagates, a circle symmetric refractive index profile is assumed. In

the longitudinal direction, $n(\mathbf{p}, \omega)$ in theory is assumed to be constant in the z -direction. However, for the experimental fibers presented in Chapter 8, this is not the case due to perturbations during the manufacturing process. Though, after optimization of the fiber drawing process, a close-to-constant refractive index profile over the length could be achieved.

In this section, the main definitions have been established to obtain the wave equation from Maxwell's equations, and understand the refractive index $n(\mathbf{p}, \omega)$ dependence. First, take the curl of Eq. (3.11), and substitute the constitutive relations in Eq. (3.12) and to obtain

$$\begin{aligned}
\nabla \times [\nabla \times \mathcal{E}(\mathbf{p}, \omega)] &= -j\omega [\nabla \times \mathcal{B}(\mathbf{p}, \omega)] \\
&= -j\omega\mu_0 [\nabla \times \mathcal{H}(\mathbf{p}, \omega)] \\
&= -j\omega\mu_0 [j\omega\mathcal{D}(\mathbf{p}, \omega)] \\
&= -j\omega\mu_0 [j\omega\varepsilon_0 n^2(\mathbf{p}, \omega) \mathcal{E}(\mathbf{p}, \omega)] \\
&= \omega^2 \mu_0 \varepsilon_0 n^2(\mathbf{p}, \omega) \mathcal{E}(\mathbf{p}, \omega).
\end{aligned} \tag{3.18}$$

The curl of the curl on the left hand side of Eq. (3.18) can be substituted using the curl identity equation by

$$\nabla \times [\nabla \times \mathcal{E}(\mathbf{p}, \omega)] = \nabla [\nabla \cdot \mathcal{E}(\mathbf{p}, \omega)] - \nabla^2 \mathcal{E}(\mathbf{p}, \omega). \tag{3.19}$$

To simplify Eq. (3.19), the weakly guiding approximation (WGA) is introduced [82], and it states that the variations in $\varepsilon_r(\mathbf{p}, \omega)$ are very small and can be considered constant. The WGA was first used by A.W. Snyder and W.R. Young [85], and was later named as such by D. Gloge [82]. By using the WGA, the first term on the right hand side of Eq. (3.19) disappears, as is implied by Eq. (3.13) in combination with the constitutive relation in Eq. (3.15) [9, 83]. Therefore, the linear transmission regime wave equation for the electric field is

$$\nabla^2 \mathcal{E}(\mathbf{p}, \omega) + \omega^2 \mu_0 \varepsilon_0 n^2(\mathbf{p}, \omega) \mathcal{E}(\mathbf{p}, \omega) = 0. \tag{3.20}$$

Effectively, the same method can be performed for the magnetic field, where the starting point is taking the curl of Eq. (3.12). Performing similar steps results in the wave equation for the magnetic field as

$$\nabla^2 \mathcal{H}(\mathbf{p}, \omega) + \omega^2 \mu_0 \varepsilon_0 n^2(\mathbf{p}, \omega) \mathcal{H}(\mathbf{p}, \omega) = 0. \tag{3.21}$$

Note that Eq. (3.20) and Eq. (3.21) are the same, with exception of the field description. Therefore, the wave equations for both the electric and the magnetic fields are known and are ready to be solved. This is performed in the next section. For clarity, first introduce the constant

$$k_0 = \omega(\mu_0 \varepsilon_0)^{1/2} = \omega c_0^{-1} = 2\pi\lambda_0^{-1}, \text{ [m}^{-1}\text{]} \tag{3.22}$$

to reduce the symbols used in Eq. (3.20) and Eq. (3.22), where k_0 denotes the free-space wave number, and λ_0 [m] the wavelength in vacuum. Note that c_0 denotes the propagation speed of light in vacuum.

3.3 Linearly polarized modes

The previous section has established the wave equations in the optical fiber. These provide the basis for the orthogonal eigenmodes, which can be employed as spatial transmission channels within the fiber core to construct a transmission matrix \mathbf{H} . Note that the wave equations for the electrical and magnetic fields can be written in a general form as

$$\nabla^2 \Psi(\mathbf{p}, \omega) + k_0^2 n^2(\mathbf{p}, \omega) \Psi(\mathbf{p}, \omega) = 0, \quad (3.23)$$

where Ψ can either be \mathcal{E} or \mathcal{H} . Thus far, the Cartesian basis is assumed. However, as optical fibers are cylindrical, it makes more sense to use the cylindrical coordinates. To this end, let the separation of variables be

$$\Psi(\mathbf{p}) = \Psi(r, \varphi, z) = R(r) \Phi(\varphi) Z(z), \quad (3.24)$$

which introduces three functions, depending on the radius r , the azimuth φ , and the direction of propagation z , respectively. In addition, assume that the optical fiber is symmetrical, and cylindrical, which simplifies the refractive index to be only dependent on the radius $n(r, \omega)$. This variable is called the refractive index profile (RIP) of the optical fiber. The first term on the left hand side of Eq. (3.23) contains a Laplacian operator, which can be rewritten in cylindrical coordinates as

$$\begin{aligned} \nabla^2 \Psi &= \left[r^{-1} \partial_r (r \partial_r) + r^{-2} \partial_\varphi^2 + \partial_z^2 \right] \Psi \\ &= \left[\partial_r^2 + r^{-1} \partial_r + r^{-2} \partial_\varphi^2 + \partial_z^2 \right] \Psi. \end{aligned} \quad (3.25)$$

Substituting Eq. (3.25) in Eq. (3.23) yields three distinct ordinary differential equations (ODEs). The first ODE is dependent on the propagation direction z , and is defined as

$$\left[\partial_z^2 + \beta^2 \right] Z(z) = 0, \quad (3.26)$$

which is a standard ODE, and results in the solution

$$Z(z) = C_1 e^{j\beta z} + C_2 e^{-j\beta z}, \quad (3.27)$$

where C_1 and C_2 are constants. Note that the newly introduced variable β represents the propagation constant. It was earlier assumed that the direction of propagation is in the positive z -direction, which implies that C_1 has to be 0. Now, we can rewrite Eq. (3.27) with respect to the propagation direction and time as

$$Z(z) e^{j\omega t} = C_2 e^{j[\omega t - \beta z]}, \quad (3.28)$$

which denotes the most basic plane wave in the z -direction. Eq. (3.28) is important for section 3.6, as propagation parameters are dependent on the longitudinal axis. The second ODE is defined in the azimuthal domain as

$$\left[\partial_\varphi^2 + l^2 \right] \Phi(\varphi) = 0, \quad (3.29)$$

where l is an integer ≥ 0 , as the field is periodic in the azimuthal domain, with a period of 2π . Accordingly, the two possible answers are readily given as [86]

$$\Phi(\varphi) = \begin{cases} \cos(l\varphi) \\ \sin(l\varphi) \end{cases}, \quad (3.30)$$

for even and odd symmetry, respectively. From Eq. (3.30) can be observed that if l is larger than 0, two orthogonal π/l -shifted azimuthal degenerates exist. Alternatively, the azimuth can be described by $e^{jl\varphi}$. Now, the fields have been described in the propagating direction z , and the azimuthal direction φ . Therefore, the remaining ODE, which has to be solved, is defined in the radial direction as

$$\left\{ \partial_r^2 + r^{-1} \partial_r + k_0^2 n^2(r, \omega) - \beta^2 - l^2 r^{-2} \right\} R(r) = 0. \quad (3.31)$$

This solution cannot be solved analytically for any arbitrary refractive index. Note that two conventional fiber RIPs are step-index (SI), and graded-index (GI), as shown in Fig. 3.3. As the WGA is used, both RIPs will result in similar solutions. Eq. (3.31) can be analytically solved for the SI fiber, therefore, we continue with this fiber. The SI fiber corresponds to the conventional SSMF, where the RIP is homogeneous in the core, and cladding. Accordingly, let

$$n(r, \omega) = \begin{cases} n_{\text{co}}(\omega) & r \leq r_0 \\ n_{\text{cl}}(\omega) & r > r_0 \end{cases}, \quad (3.32)$$

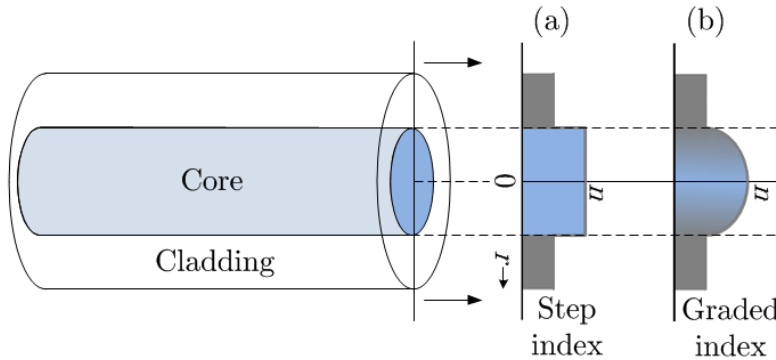


Fig. 3.3 Conventional refractive index profiles of optical fibers: (a) step-index, and (b) graded-index.

where n_{co} and n_{cl} correspond to the core and cladding refractive index, respectively, and r_0 represents the core radius. For completeness, the refractive index profile of a generalized GI fiber is [87]

$$n^2(r, \omega) = \begin{cases} n_{\text{co}}^2(\omega) \left[1 - 2 \left(\frac{r}{r_0} \right)^p \Delta_{\text{GI}} \right] & r \leq r_0 \\ n_{\text{cl}}^2(\omega) & r > r_0 \end{cases}, \quad (3.33)$$

where p represents the grade profile parameter, which is approximately 2 for GI fibers. The refractive index at $r = 0$ is denoted by n_{co} , and [10]

$$\Delta_{\text{GI}} = \frac{n_{\text{co}}^2(\omega) - n_{\text{cl}}^2(\omega)}{2n_{\text{co}}^2(\omega)}. \quad (3.34)$$

Note that no refractive index profile wavelength dependence is assumed in Eq. (3.33) for simplicity. Fig. 3.3(b) gives a graphic representation of the GI fiber. Through manipulating p , n_0 , and r_0 , the modal propagation constants can be modified. Also note that Eq. (3.33) can be used to describe the SI fiber by using $p = \infty$. Alternatively, a low refractive index trench can be added before the cladding region, to further confine the modal field distribution [88].

As the SI RIP can be solved analytically, Eq. (3.31) results in ordinary Bessel functions as [89]

$$R(r) = \begin{cases} C_3 J_l \left(\frac{ur}{r_0} \right) + C_4 Y_l \left(\frac{ur}{r_0} \right) & r \leq r_0 \\ C_5 K_l \left(\frac{wr}{r_0} \right) + C_6 I_l \left(\frac{wr}{r_0} \right) & r > r_0 \end{cases}, \quad (3.35)$$

where $C_{3,6}$ are constants, J , Y , K , and I are types of Bessel functions, and the newly introduced variables [82]

$$u = r_0 \left[k_0^2 n_{\text{co}}^2(\omega) - \beta^2 \right]^{1/2}, \quad (3.36)$$

$$w = r_0 \left[\beta^2 - k_0^2 n_{\text{cl}}^2(\omega) \right]^{1/2}. \quad (3.37)$$

In addition, let

$$V = u^2 + w^2 = r_0 k_0 \left[n_{\text{co}}^2(\omega) - n_{\text{cl}}^2(\omega) \right]^{1/2} \quad (3.38)$$

be the normalized frequency, which is used in optical communications to describe the modal guiding properties of a fiber. In addition, it is interesting to introduce

$$b_{\text{SI}} = w^2 V^{-2} = 1 - u^2 V^{-2}, \quad (3.39)$$

which is the normalized propagation constant for the SI fiber. When $b_{\text{SI}} \rightarrow 0$ for a certain mode, it is no longer guided along the optical fiber.

The wave function in Eq. (3.35) can be simplified by assuming that the field cannot extend to infinity, and therefore when $r \rightarrow \infty$ the field value has to go to 0. By taking this assumption into account, Eq. (3.35) reduces to

$$R(r) = \begin{cases} C_3 J_l(ur) & r \leq r_0 \\ C_5 K_l(wr) & r > r_0 \end{cases}. \quad (3.40)$$

Therefore, the general form of the wave equation solution is

$$\begin{aligned} \Psi(r, \varphi, z) &= R(r)\Phi(\varphi)Z(z) \\ &= \begin{cases} \begin{cases} C_3 J_l(ur) \cos(l\varphi) e^{-j\beta z} & r \leq r_0 \\ C_5 K_l(wr) \cos(l\varphi) e^{-j\beta z} & r > r_0 \end{cases} & l \text{ even} \\ \begin{cases} C_3 J_l(ur) \sin(l\varphi) e^{-j\beta z} & r \leq r_0 \\ C_5 K_l(wr) \sin(l\varphi) e^{-j\beta z} & r > r_0 \end{cases} & l \text{ odd} \end{cases} \end{aligned} \quad (3.41)$$

Boundary conditions imply that the two solutions per l need to be continuous at r_0 . Note that it particularly important to realize that Eq. (3.41) can either be the electric or magnetic field. As these two fields are related through Maxwell's equations, the boundary conditions need to be applied on r_0 for all solutions in Eq. (3.1)-(3.4). Therefore solving Eq. (3.41) on the boundary results in

$$\frac{u}{n_{\text{co}}(\omega)} \left[\frac{J_{l-l}(u)}{J_l(u)} \right] = - \frac{w}{n_{\text{cl}}(\omega)} \left[\frac{K_{l-l}(w)}{K_l(w)} \right], \quad (3.42)$$

which can even further be simplified under the WGA using $n_{\text{co}}(\omega) = n_{\text{cl}}(\omega)$, which results in a pure TEM wave. Eq. (3.42) only holds true for certain combinations of the variables k_0 , r_0 , and $n(r, \omega)$, and therefore the characteristic eigenvalue equation (3.42) results in a particular set of transverse field solutions. Note that the LP field solutions are either the electric or magnetic field. For a given l , there exists a finite number of solutions m (0,1,2,3,...). Hence, the LP modes are designated as LP_{lm} modes, and relate to the true field modes as $\text{HE}_{l+1,m}$ and $\text{EH}_{l+1,m}$. for $l \neq 0$. The LP_{lm} is formed by the HE_{2m} , HE_{0m} , and EH_{0m} . The modes HE_{0m} , and EH_{0m} are also often referred to as the transverse-electric (TE) ($\mathcal{E}_z = 0$) and transverse-magnetic (TM) ($\mathcal{H}_z = 0$) modes, respectively. The LP denotation is the grouping result due to the similar propagation constants of the true field modes, and the EH and HE naming convention depends on the largest field in the z -direction. By relying on numerical results, the LP modes formed by the LP field modes are shown in Table 3.1 for the first 7 LP modes [90]. Fig. 3.4 depicts the normalized propagation constant with respect to the normalized frequency for the SI fiber. Note that the V number can be numerically computed for GI fibers too [91], which yields a different normalized propagation constant versus normalized frequency figure as shown in Fig. 3.4.

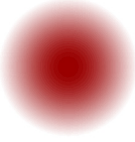
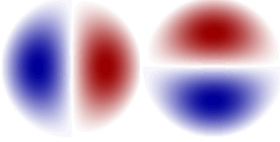
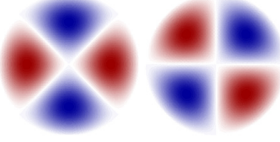

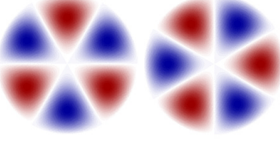
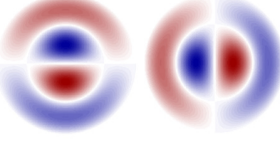
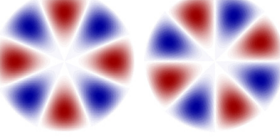
	Spatial LP Mode Distributions	Field modes	Spatial paths (aggregate)
LP ₀₁		HE ₁₁	2 (2)
LP ₁₁		HE ₂₁ , TE ₀₁ , TM ₀₁	4 (6)
LP ₂₁		EH ₁₁ , HE ₃₁	4 (10)
LP ₀₂		HE ₁₂	2 (12)
LP ₃₁		EH ₂₁ , HE ₄₁	4 (16)
LP ₁₂		HE ₂₂ , TE ₀₂ , TM ₀₂	4 (20)
LP ₄₁		EH ₃₁ , HE ₅₁	4 (24)

Table 3.1 First 7 LP modes formed by field modes, where red and blue correspond to the positive and negative phase, respectively. The number of spatial paths includes linear polarizations of the spatial LP modes. The aggregate spatial paths indicate that the higher LP modes require the lower LP modes to be guided.

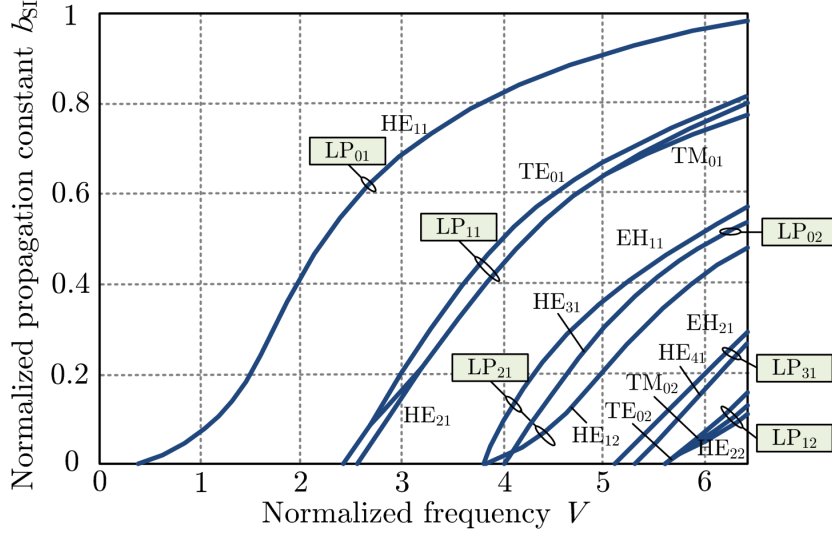


Fig. 3.4 Normalized propagation constant b_{SI} corresponding to a normalized frequency V for a homogeneous SI fiber [92].

As LP fields are assumed, each LP mode contains 2 polarization modes. The 2 polarization modes in the LP transmission case can be proven using the Poynting-vector [93]

$$\mathcal{S} = \mathcal{E} \times \mathcal{H}^*, \quad (3.43)$$

which denotes the directional energy flux density [V A m^{-2}] of an electromagnetic field, and $*$ is the complex conjugate. In other words, it quantifies both the energy density, and the direction of propagation. As Eq. (3.27) indicates that the wave propagation is in the z -direction. For the Poynting vector in the z -direction S_z to be larger than 0, two LP solutions exist, namely

$$\begin{aligned} S_z &= \mathcal{E}_x \times \mathcal{H}_y^*, \\ S_z &= -\mathcal{E}_y \times \mathcal{H}_x^*, \end{aligned} \quad (3.44)$$

where all variables on the right hand side of the equations are assumed positive. Eq. (3.44) corresponds to the X-polarization and Y-polarization case, respectively. Therefore, Eq. (3.44) denotes two π -shifted degenerate solutions in the azimuthal direction with respect to each other. Furthermore, each respective LP_{lm} mode has its own propagation constant β_{lm} . Note that the LP modes are formed by EH and HE modes, which results in a marginal propagation difference between the true field modes. The overlap between the spatial LP modes can be computed using

the spatial mode overlap integral (MOI) in the transverse plane as [94]

$$\text{MOI} = \frac{\left| \iint_A \mathcal{E}_1(r, \varphi) \mathcal{E}_2^*(r, \varphi) dA \right|^2}{\iint_A |\mathcal{E}_1(r, \varphi)|^2 dA \iint_A |\mathcal{E}_2(r, \varphi)|^2 dA}, \quad (3.45)$$

where the subscripts 1 and 2 denote the input and output LP mode distributions, respectively. The result of Eq. (3.45) is 0 when $\mathcal{E}_1(r, \varphi)$ and $\mathcal{E}_2(r, \varphi)$ represent different spatial LP modes, which indicates spatial orthogonality. Therefore, in a perfect optical fiber, there is no coupling between modes. However, in practice there always is coupling to a certain extent, which can be caused by many sources, such as perturbations in the fiber, roughness at the core-cladding interface, refractive index profile variations, and fiber bending [95]. Due to the orthogonality principle in Eq.(3.45), the LP modes can therefore be employed as spatial transmission channels. Hence, the spatial diversity requirement can be satisfied, and a transmission matrix \mathbf{H} with a potentially low condition number is theoretically possible. Therefore, the maximum number of transmittable channels (see Table 3.1) depends on the number of guided LP modes, which is dependent on the cut-off frequency V_C . When only the fundamental LP_{01} mode is allowed to propagate, actually 2 polarizations co-propagate. As the V_C increases, the LP_{01} and LP_{11} modes are allowed to co-propagate. Note that the LP_{11} mode consists of 2 spatial LP_{11} modes, and each spatial mode consists of 2 polarizations. Therefore, a total number of 6 polarization modes can co-propagate.

3.4 Fiber impulse response

In the previous section it is noted that the spatial LP modes are dependent on the chosen refractive index profile $n(r, \omega)$. The primary focus for describing LP modes is based on the constant core refractive index n_{co} and constant cladding refractive index n_{cl} , which represents a SI fiber as shown in Fig. 3.3. To this end, the first generation 3MFs are based on the SI fiber principle, where the core size was increased with respect to a SSMF [96, 97]. In this work, 3 spatial LP modes were allowed to co-propagate, creating a 3MF. By adjusting the core size, the normalized cutoff frequency is engineered. The downside of using a SI fiber is that the propagation constants β_{lm} of the corresponding LP_{lm} modes cannot be manipulated, which is undesired for a transmission system, as is further detailed in section 3.4.1. To this end, GI 3MFs were introduced [73].

3.4.1 Differential mode delay

It has been previously indicated that LP_{lm} modes have corresponding propagation constants. From these propagation constants, the respective group velocities can be determined as

$$vg_{lm}^{-1} = \frac{d\beta_{lm}(\omega)}{d\omega}, \quad (3.46)$$

where vg_{lm} is in $[m\ s^{-1}]$. Therefore, when transmitting a pulse in a particular set of LP modes, the arrival times after a transmission distance for the respective modes will be different. This time difference is known as the differential mode delay (DMD) between modes [98], and is defined as the distance divided by the group velocity. Note that DMD not only exists between LP modes, but also can exist between all spatial solutions within an LP mode. A particular case of DMD occurs between the two polarizations, which is denoted as polarization mode dispersion (PMD). This definition comes from SSMF transmission systems, where the only existing DMD is between polarizations. As polarizations are degenerate solutions with the same propagation constant for an LP mode, PMD is not inherent to the optical fiber but is caused by refractive index perturbations. For simplicity, assume a 2 mode optical fiber as schematically depicted in Fig. 3.5(a), where the modes can be any type of modes, i.e. LP modes, spatial LP solutions, or polarizations. As can be observed from the figure, the transmission system consists of a single

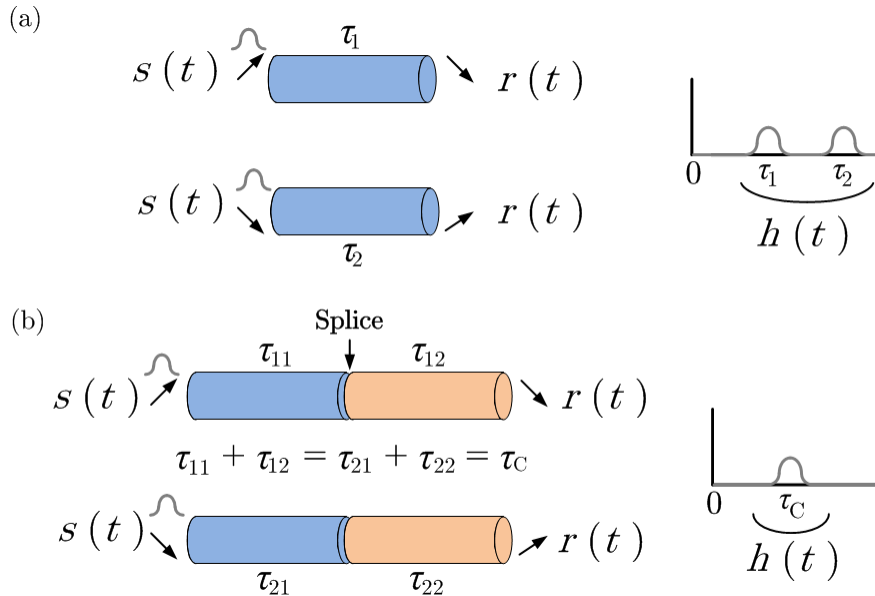


Fig. 3.5 An example two mode transmission system, where the DMD is (a) uncompensated, and (b) compensated.

transmitter and a single receiver. Due to the propagation of the 2 modes in the optical fiber, 2 spatial paths exist. Because of the difference in the respective group velocities, there are two different pulse arrival times. Accordingly, the transmission system impulse response $h(t) = [h_{\tau_1}(t), 0, 0, \dots, 0, 0, h_{\tau_2}(t)]$, where $\tau_2 > \tau_1$. This is an undesirable effect, as the impulse response has to be equalized by the MIMO equalizer. However, it was previously noted that a GI fiber can be engineered to alter the propagation effects. To this end, a second fiber can be engineered which has a DMD with the opposite sign, or negative DMD, of the first fiber. These two fibers are spliced together to form a single transmission link.

3.4.2 Fiber splices

The transmission system in Fig. 3.5(b) is showing an impulse response equal to the original transmitted pulse $s(t)$, where for explanatory reasons both constructively interfere. Hence, $h(t) = h_c(t)$. This transmission system is a DMD managed transmission system, and in this case it is assumed that the splicing point is perfect, i.e. no coupling between distinct modes occurs. Therefore the transmission matrix between the two modes $\mathbf{H}_{\text{splice}} = \mathbf{I}_2$ in this example, where \mathbf{I}_2 is the 2×2 identity matrix. If the splice point is imperfect, $\mathbf{H}_{\text{splice}} \neq \mathbf{I}_2$, mode coupling occurs in the splicing point. This effect causes Rician fading, further detailed in section 3.5.2. The resulting transmission function $h(t)$ will yield 3 pulses as

$$\begin{cases} \tau_{21} + \tau_{22} = \tau_C & \text{mode 1} \\ \tau_{11} + \tau_{12} = \tau_C & \text{mode 2} \\ \tau_{11} + \tau_{22} & \text{crossterm mode 1 to 2} \\ \tau_{21} + \tau_{12} & \text{crossterm mode 2 to 1.} \end{cases}$$

Obviously, fiber splices are of the utmost importance to keep the transmission system impulse response $h(t)$ short. The coupling matrix between the LP modes at the fiber splice can be computed using the mode overlap integral in Eq. (3.45), where $\mathcal{E}_1(r, \varphi)$ represents the respective output LP mode distribution of fiber 1, and $\mathcal{E}_2(r, \varphi)$ represents the respective input LP mode distribution of fiber 2. Accordingly, 2×2 MOIs are to be computed.

Since the RIPs of the two fibers are different to obtain a DMD compensated transmission system, the field modes per optical fiber are slightly different. Therefore, there is always crosstalk between the LP modes in a fiber splice. However, using the WGA, the mode coupling theoretically can be small when the core alignment between both fibers is correct, and the same radius is used. This is confirmed by laboratory experiments in Chapter 8, where the mode coupling was measured to be under -30 dB between the LP_{01} and LP_{11} modes. The measurement

accuracy was limited by the LS channel state information algorithm precision (see section 2.3.1). Note that the two spatial LP₁₁ modes are strongly coupled. In the example case, a simplified model of 2 LP modes is used. In the case of two exactly the same fibers, with perfect alignment, the coupling matrix in the splice can be approximated by the identity matrix. Here, splicing losses are neglected.

Thereby, the example in Fig. 3.5(b) indicates that the two modes have a common group velocity for the combined two-span optical fiber. Previously, for explanatory reasons, it was assumed that these two modes have the exact same arrival time. In reality however, the two modes will not have the exact same arrival time, but have a statistical group delay spread with standard deviation σ_τ . This is the result of the EH and HE group velocity differences, and temporal fluctuations [99, 100]. When transmitting over N_{SEC} fiber sections, the standard deviation grows as $(N_{\text{SEC}})^{1/2} \sigma_\tau$ which was experimentally confirmed for weak coupling mode fibers [101], such as the ones used in the experiments in Chapter 8. This corresponds to strong mode coupling fibers where the group delay spread scales with the square root of the number of fiber sections [102]. As the standard deviation grows with the square root of the transmission distance, the impulse response length of $h(t)$ increases proportionally. As the number of transmitted spatial LP modes increases, DMD management becomes more challenging. At this moment, an area of research is the fiber designs for the transmission of 6 LP modes (10 spatial LP modes) and MMFs.

3.5 Fading channels

This section focuses on frequency selective fading effects that occur when performing SDM. Frequency selective fading, or simply denoted as fading, is the result of constructive and destructive interfering channels in multipath transmission systems. This effect is well known in wireless communications, and similar effects happen in optical MIMO transmission systems. First, flat fading is described, before frequency selective Rician fading is discussed. To overcome frequency selective fading and improve the transmission performance, coding techniques can exploit space and time diversity. This is experimentally demonstrated in Chapter 8 for a 41.7 km 3MF transmission system.

3.5.1 Flat fading

Flat fading is the type of fading in SSMFs, where the transmitted channel has a constant gain and linear phase response over the full bandwidth of the transmitted signal. Hence the frequency response of the fiber medium is flat, and the transmission medium bandwidth is equal to the transmitted signal.

The primary reason SSMF transmission systems are not considered to be a fully flat fading channels, is due to the optical filters inserted in the fiber link. In the core network, these optical filters usually are implemented in the form of reconfigurable optical add-drop multiplexers (ROADMs). A single ROADM can be modeled as a Gaussian filter. Note that multiple ROADMs results in a frequency domain multiplication of the Gaussian filter, which reduces the pass bandwidth.

3.5.2 Rician fading

Within the context of optical MIMO systems, Rician fading is the primary fading type and can originate within an optical fiber through multipath interference [95]. As LP modes are formed by a set of field modes with very similar group velocities, and they are strongly coupled. Thus far, weak intra LP mode coupling is assumed. In this case mode coupling mainly occurs in fiber splices. However, the weak coupling approximation within the fiber is not necessarily true as the refractive index can be modified, and hence, the group velocities of the respective LP modes altered. This causes the LP modes to have similar group velocities, and become strongly coupled. These two cases lead to Rician fading. The experimental results in Chapter 8 are achieved by employing weak coupled LP modes. Therefore, the primary mode coupling points are considered to be originating from the fiber splices.

Consider two N_{MODE} fibers where the modes can either be polarizations, or spatial LP modes. These two fibers are spliced together. Using overlap integrals, the transmission matrix $\mathbf{H}_{\text{splice}}$ in the splice can be computed. Using the WGA, it is safe to assume that the diagonal of $\mathbf{H}_{\text{splice}}$ contains large numbers with respect to the off-diagonal elements. The off-diagonal elements can be considered to be interfering channels. This type of fading is considered to be Rician, and the probability distribution depends largely on the Rician K -factor [103]

$$K_{R,j} = \frac{A_j}{2\sigma_j^2}, \quad (3.47)$$

where A_j is the amplitude of element \mathbf{H}_{jj} , and σ_j represents the variance of the multipath interference. The K -factor denotes the ratio of the diagonal of $\mathbf{H}_{\text{splice}}$, to the crosstalk elements of $\mathbf{H}_{\text{splice}}$, per row. As $K_{R,j}$ increases, the transmission channel becomes more deterministic [52]. The various $K_{R,j}$ are independent. Then, the probability density function (PDF) is given by

$$p(x) = \begin{cases} \frac{x}{\sigma_j^2} \exp\left[-\frac{x^2 + A_j^2}{2\sigma_j^2}\right] J_0\left(\frac{A_j x}{\sigma_j^2}\right) & A_j > 0, x > 0 \\ 0 & x \leq 0 \end{cases}, \quad (3.48)$$

where x represents the possible A_j value, and J_0 is a modified Bessel function. As $K_{R,j} \gg 1$, the Rician distribution can be approximated as the Gaussian PDF [104]. On the other hand, when $K_{R,j} \rightarrow 1$, the Rayleigh fading channel PDF is obtained. The interference results in either a received amplitude gain or reduction, and hence can be seen as a source of MDL [95].

3.6 Propagation effects

By solving the Maxwell equations in section 3.3, it was determined that the field modes propagate as plane waves in the z -direction (Eq. (3.23)). To compute the optical modes, the induced electric current $\mathcal{J}(\mathbf{p}, \omega)$ was assumed to be 0. However, in reality there is a source of induced electric field. This source consists of a linear and a nonlinear component. Therefore, let

$$\mathcal{J}(\mathbf{p}, \omega) = \mathcal{J}_L(\mathbf{p}, \omega) + \mathcal{J}_{NL}(\mathbf{p}, \omega). \quad (3.49)$$

Optical fibers are not prone to induced magnetic fields, hence $\mathcal{K}(\mathbf{p}, \omega)$ remains zero. Eq. (3.49) changes the wave equation obtained in Eq. (3.20) to

$$\begin{aligned} \nabla^2 \mathcal{E}(\mathbf{p}, \omega) &= \omega^2 \mu_0 \varepsilon_0 n^2(\mathbf{p}, \omega) \mathcal{E}(\mathbf{p}, \omega) + \omega^2 \mu_0 \mathcal{J}(\mathbf{p}, \omega) \\ &= \omega^2 c_0^{-1} \mathcal{E}(\mathbf{p}, \omega) + \omega^2 \mu_0 [\mathcal{J}_L(\mathbf{p}, \omega) + \mathcal{J}_{NL}(\mathbf{p}, \omega)]. \end{aligned} \quad (3.50)$$

By taking the induced electric polarization into account, non-linear terms changing the refractive index of the fiber are introduced. The mathematical steps to obtain the non-linear Schrödinger equation (NLSE) from Eq. (3.50) are omitted, as the presented work focuses on the transmission of spatial LP modes and the linear compensation using MIMO processing. In addition, the MIMO DSP primarily allows for optical performance monitoring of linear effects. Furthermore, the conducted experiments in Chapter 8 balanced the linear and nonlinear penalties through adjusting the modal and wavelength channel transmission power. [105] provides a more in-depth analysis for obtaining the NLSE, where the NLSE for a single polarization mode propagating along the optical fiber in the z -direction is

$$\frac{\partial \mathcal{E}}{\partial z} = \underbrace{-\frac{\alpha_{lm}}{2} \mathcal{E}}_{\text{Attenuation}} - \underbrace{j \frac{\beta_{lm,2}}{2} \frac{\partial^2 \mathcal{E}}{\partial T^2}}_{\text{GVD}} + \underbrace{\frac{\beta_{lm,3}}{6} \frac{\partial^3 \mathcal{E}}{\partial T^3}}_{\text{GVD slope}} + \underbrace{j \gamma_{lm} |\mathcal{E}|^2 \mathcal{E}}_{\text{Kerr nonlinearities}} \quad (3.51)$$

where α_{lm} denotes the attenuation of a certain LP_{lm} mode in [dB km⁻¹], $\beta_{lm,i}$ represents the i^{th} -order Taylor series expansion of β_{lm} . Using this expansion, the second derivative and third derivative on the right hand side of Eq. (3.51) denote the GVD and GVD slope, respectively. The variable $T = t - \beta_{lm,1} z$ represents the moving frame of reference, and the nonlinear parameter γ in the Kerr non-

linearity contribution is defined as

$$\gamma_{lm} = \frac{\omega_0 n_{nl}}{c_0 A_{\text{eff}}}, \quad [\text{W}^{-1}\text{km}^{-1}] \quad (3.52)$$

where ω_0 is the carrier frequency, and has been defined in Eq. (3.5). n_{nl} represents the nonlinear refractive index. The most significant Kerr non-linear processes in SMFs are self-phase modulation (SPM), cross-phase modulation (XPM), four-wave mixing (FWM), and cross-polarization mixing. Note that in SDM transmission systems, the spatial dimension is added. In SSMF transmission systems the Kerr non-linearity can be successfully compensated digitally by digital back-propagation (DBP) algorithms [106-108]. Although the OSNR gains are substantial, DBP comes at the cost of very high computational complexity and is currently not considered for real-time implementation. In addition, a key difficulty for the DBP algorithms to work is the required knowledge of all fiber parameters of every fiber span in the transmission link. As optical MIMO transmission systems employ experimental fibers, this poses surmountable difficulties. However, the unknown mode coupling between the consecutive fiber spans results in an unknown set of fiber parameters [109]. Hence, it is currently impossible to perform digital back-propagation in MIMO transmission systems. In Eq. (3.52) the effective area A_{eff} of a particular LP mode is used. A_{eff} can be computed from the electrical field distribution [105]

$$A_{\text{eff}} = \frac{\left[\iint_A |\mathcal{E}_{lm}(r, \varphi)|^2 dA \right]^2}{\iint_A |\mathcal{E}_{lm}(r, \varphi)|^4 dA}. \quad [\text{m}^2] \quad (3.53)$$

For the fundamental LP_{01} mode, the Gaussian distribution approximation is regularly used, which reduces Eq. (3.53) to

$$A_{\text{eff}} = \pi w, \quad (3.54)$$

where w has been defined in Eq. (3.37). By increasing the A_{eff} , the effects of the non-linear processes can be reduced. Currently, research focuses on the characterization of these non-linear processes [37, 110-112].

The nonlinear parameter for SSMFs at 1550 nm is approximately $1.3 \text{ W}^{-1} \text{ km}^{-1}$. To this end, large effective area fibers (LEAFs) are proposed [113], which intentionally increase the effective area and hence increase the nonlinear tolerances of the fiber, but still only guide the fundamental LP mode. On the other hand, the nonlinear coefficient for HC-PBGFs can go up to $640 \text{ W}^{-1} \text{ km}^{-1}$ [79]. It is higher than the γ for SSMFs, as the majority of the light is transported in air. Due to the increased core size, few-mode and multimode fibers also take advantage of the increased nonlinear parameter. However, for MIMO transmission, a higher transmission

power is inserted into the fiber due to the multiple spatial transmission channels. Therefore, the nonlinear interactions between co-propagating LP modes are to be considered. However, this effect is considered to be outside the scope of this thesis.

3.6.1 Attenuation

The optical fiber attenuation α_{lm} introduced in Eq. (3.51) results in an exponential power decrease with the transmitted length Z , and therefore is predictable. Assuming an input power P_{in} , the output power after transmission distance Z becomes [87]

$$P_{out} = P_{in} \exp(-\alpha_{lm}Z). \quad (3.55)$$

Generally in optics, the attenuation α_{lm} is denoted in [dB km⁻¹] as

$$\alpha_{lm,dB} = -\frac{10}{Z} \log_{10} \left(\frac{P_{out}}{P_{in}} \right) \approx 4.343 \cdot \alpha_{lm,dB}. \quad (3.56)$$

The attenuation depends on the transmitted frequency, as shown in Fig. 1.2 for a SSMF. Note that the attenuation per transmitted mode varies. The attenuation difference between polarization modes is denoted as polarization dependent loss (PDL). This definition originates from SSMF transmission systems, where the only attenuation difference occurs between polarizations. A more general term to use for MIMO transmission systems is MDL, where the modes can be any solutions to the wave equation. MDL has been introduced in section 2.4. The attenuation difference in combination with coupling between modes causes Rician fading, detailed in section 3.5.

3.6.2 Amplification

Attenuation compensation is achieved by amplification of the transmitted signal. Preferably, this is performed in the optical domain, as it avoids optical-electronic-optical conversion (OEOC). To this end, one optical amplifier is concatenated with one fiber, creating an attenuation compensated fiber span. There are two optical amplifier types, EDFA and Raman amplification [114, 115]. In this section only the EDFA amplifier is discussed, as the first emerging demonstrations of multi-mode amplifiers are based on EDFA technology, while Raman amplification is also being proposed [116]. Accordingly, these are denoted as multimode EDFAs (MM-EDFAs). The emerging MM-EDFAs further corroborate the experimental nature of the state-of-the-art few-mode and multi-mode fiber transmission systems.

As introduced in Chapter 1, the conventional band (1530-1565 nm) is the preferred transmission wavelength band due to the operating region of the fiber-based low

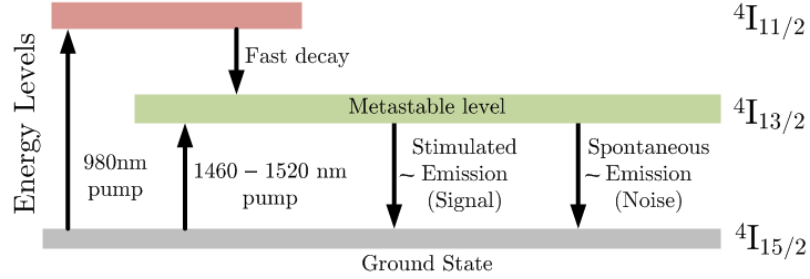


Fig. 3.6 EDFA working principle, where a pump laser increases the Erbium energy level, resulting in stimulated and spontaneous emission [119].

noise EDFA [14, 117]. From Fig. 1.3 it can be observed that the gain spectrum in SMFs is not equal over the entire C-band, resulting in the use of one gain equalizer per EDFA. The gain peak in Fig. 1.3 can be drastically reduced by co-doping the core with aluminum [118]. To this end, it is important to understand the nature of amplification and noise addition originating from EDFAs. The working principle of an EDFA is shown in Fig. 3.6. By using a shorter wavelength (higher frequency) pump laser, usually 980 or 1480 nm for C-band amplification, the Erbium ground-state ions are excited to a higher state. The higher state ions return to the ground state through population inversion, resulting in stimulated emission and amplified spontaneous emission (ASE). Stimulated emission results in amplification of the signal, and ASE results in the addition of noise. The Erbium doping is radially distributed in the optical fiber core, and the amplification corresponds to the modal overlap [119]. For SSMF transmission system the distribution of Erbium is uniform. The ASE noise results in a noise factor, and for a SSMF EDFA is [120]

$$F_{\text{EDFA}} = \frac{\text{SNR}_{\text{in}}}{\text{SNR}_{\text{out}}} = 2\eta_{\text{sp}} \left(1 + \frac{1}{G_{\text{EDFA}}}\right) + \frac{1}{G_{\text{EDFA}}}, \quad (3.57)$$

where SNR and OSNR have been defined in section 2.4, η_{sp} represents the amplified spontaneous emission factor of the EDFA, and G_{EDFA} is the amplifier gain. Accordingly, the OSNR penalty for the lower wavelength regime is higher due to the higher gain and subsequent gain equalization. The corresponding EDFA noise figure (NF) can directly be computed from Eq. (3.57) as

$$\text{NF} = 10 \cdot \log_{10}(F_{\text{EDFA}}) = \text{SNR}_{\text{in,dB}} - \text{SNR}_{\text{out,dB}}. \quad (3.58)$$

Assuming an unlimited gain and perfect spontaneous emission factor $\eta_{\text{sp}} = 1$, the NF theoretical limit is 3 dB. Concatenating multiple attenuation compensated spans, and hence increasing the number of EDFAs, further decreases the OSNR (see section 2.4) figure. For a SMF transmission system, the transmission system

OSNR can be computed as

$$\text{OSNR}_{\text{dB}} = P_{\text{out}} - \alpha(\lambda)L_{\text{SPAN}} - 10\log_{10}(N_{\text{SPAN}}) + 58 \text{ dBm-NF}, \quad (3.59)$$

where P_{out} represents the output power, $\alpha(\lambda)$ the attenuation, L_{SPAN} the span length, N_{SPAN} the number of spans, and $58 \text{ dBm} \approx -10\log_{10}(\frac{hf_0}{B_{\text{ref}}})$. Note that B_{ref} is defined in section 2.4 as the 0.1 nm reference bandwidth (12.5 GHz at $f_0=1550$ nm wavelength), and h denotes Planck's constant.

It was mentioned that the Erbium is uniformly radially distributed in the SMF core for SMF transmission. However, for multimode fibers this is not necessarily true. To balance the spatial gain, there are two methodologies

- The Erbium is uniformly distributed, and a number of pump lasers are used to amplify all spatial LP modes. By adjusting the launch power and launch positions, the spatial LP mode gain difference can be optimized [121, 122].
- One pump laser is used to amplify all spatial LP modes, where the Erbium distribution is chosen to balance the modal gains. One distribution proposed is a ring structure [123, 124].

In addition to the wavelength dependent gain, MM-EDFAs inevitably have a spatial dependent gain. Similarly to the wavelength domain, where GFFs are applied, spatial GFFs can be employed in MM-EDFAs to minimize the modal gain G_{lm} difference. Consequently, multi-mode amplification causes MDL due to the gain difference per spatial LP mode, and has an independent NF per spatial LP mode per wavelength. Furthermore, the MM-EDFA input and output are sources of mode coupling, which occurs in the fiber splice points, as described in section 3.4.2. Therefore, if a large optical DMD is present, it should preferably be compensated per fiber span.

3.6.3 Group velocity dispersion

GVD, in short dispersion, is the frequency dependent group velocity difference with a propagating mode. Remember, the group velocity is defined in Eq. (3.46) as

$$\text{vg}_{lm}^{-1} = \frac{d\beta_{lm}(\omega)}{d\omega}.$$

A frequency dependent $\beta_{lm}(\omega)$ results in a frequency arrival time difference at the receiving end, and hence pulse spreading. Consider a fiber of length L_{fiber} , the arrival time of a pulse would be at $T = L_{\text{fiber}} / \text{vg}_{lm}$. Note that the propagation constant is unknown. To approximate the propagation constant, a Taylor

expansion around ω_0 is employed as

$$\beta_{lm}(\omega) = \beta_{lm}^{(0)} + \beta_{lm}^{(1)}(\omega - \omega_0) + \beta_{lm}^{(2)}(\omega - \omega_0)^2 + \beta_{lm}^{(3)}(\omega - \omega_0)^3 + \dots, \quad (3.60)$$

where

$$\beta_{lm}^{(i)} = \frac{d^i \beta_{lm}(\omega)}{d\omega^i}. \quad (3.61)$$

The first two terms on the right hand side of Eq. (3.60) do not cause pulse spreading [9], and the 3rd term and larger are generally considered to be small. Consequently, the primary pulse spreading contribution is caused by the second derivative of the propagation constant as

$$\Delta T = \frac{dT}{d\omega} \Delta\omega = \frac{d}{d\omega} \left(\frac{L_{\text{fiber}}}{v_{g_{lm}}} \right) \Delta\omega = L \beta_{lm}^{(2)} \Delta\omega. \quad (3.62)$$

Alternatively, an often preferred method in optical transmission systems is writing the pulse spreading in terms of wavelength as [9]

$$\Delta T = \frac{d}{d\lambda} \left(\frac{L_{\text{fiber}}}{v_{g_{lm}}} \right) \Delta\lambda = D(\omega) L \Delta\lambda, \quad (3.63)$$

where the dispersion parameter

$$D(\omega) = -\frac{2\pi c_0}{\lambda^2} \frac{d^2 \beta_{lm}(\omega)}{d\omega^2} = D_M(\omega) + D_W(\omega), \quad [\text{ps nm}^{-1} \text{ km}^{-1}] \quad (3.64)$$

where $D_M(\omega)$ and $D_W(\omega)$ represent the wavelength dependent material and waveguide dispersion, respectively. The dispersion map of a SSMF is shown in Fig. 3.7 [10], which consists of the two wavelength dependent dispersion contributors. Note that the dispersion map depends on the RIP of the optical fiber, and consequently changes when fibers are engineered to be multimode. From Eq. (3.63)

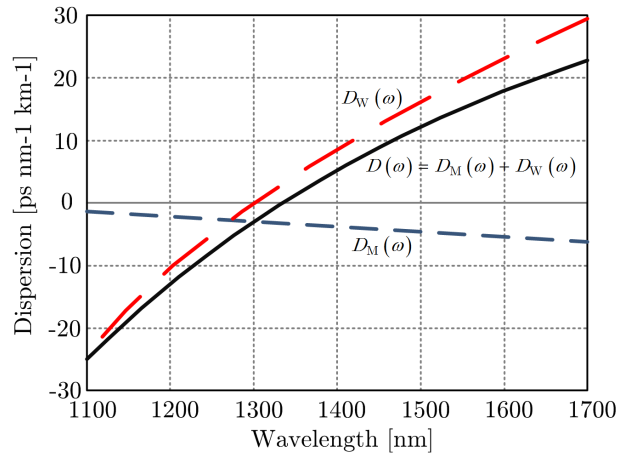


Fig. 3.7 The wavelength dependent dispersion map of a SSMF [10].

can be observed that GVD is an all-pass filter, and hence, it does not degrade the transmitted signal. Accordingly, it is possible to compensate the GVD as discussed in section 5.6. Dispersion compensation can be performed in the optical domain using dispersion compensating fibers (DCFs), or in the digital domain using filters [125]. Digital compensation can be achieved without a penalty with respect to using DCFs, and is performed before MIMO equalization. The advantage of digital compensation over using DCFs is that an equalization filter can be easily adjusted. In addition, GVD estimation can be performed to monitor the optical performance. Frequency domain GVD estimation and compensation is detailed in section 5.6. Note that, spatial LP modes have different propagation constants in the multimode fiber, and hence, different dispersion mappings per LP mode. However, from experiments it is known that the GVD figures per mode are closely related. Accordingly, the bulk of the GVD is compensated using GVD compensation filters, as discussed in section 5.6. The residual dispersion is compensated by the MIMO equalizer, which is further detailed in Chapter 6.

3.7 Scaling using multiple cores

Thus far in this chapter, the propagation effects in a single core have been described. However, as noted in section 3.1, spatially orthogonal cores can also be exploited for SDM transmission. From Eq. (3.41) can be observed that the field distribution is partially outside the core to satisfy the boundary conditions. Therefore, the occurrence of core crosstalk is possible, and depends on the field distributions of the modes co-propagating in the cores. According to the modal field distribution, the inter-core crosstalk can be computed. As the modal field distribution is dependent on the RIP, detailed in section 3.3, low refractive index trenches are regularly applied to increase the confinement of the modal distribution within a core [88]. For multi-core fibers, two cases exist: common multi-core fibers, and coupled-core fibers. Here, coupled-core fibers are multi-core fibers, where the core-to-core pitch is small, resulting in fully coupled cores. In the coupled-core case, MIMO signal processing is mandatory to unravel the mixed transmission channels. In the common multi-core case, only MIMO signal processing per core is required.

As experimentally demonstrated in section 8.3, linear combinations between multimode and multi-core can be made. In this case, inter-core and intra-core crosstalk can be observed. When the inter-core crosstalk is low, it can be neglected. Hence, the MIMO equalizer's computational complexity is reduced with respect to the fully mixed transmission channel case.

3.8 Summary

This chapter established the description of a MIMO transmission channel in an optical fiber medium, where multiple modes can co-propagate and be employed as spatial transmission channels. The modal basis considered is the LP mode basis, which consist of a set of true field modes. For a number of LP modes, where the azimuthal direction is considered a degree of freedom, two spatial LP modes exist. Within each spatial LP mode, two polarizations can co-propagate in the optical fiber medium. All these modes are solutions to the wave equation, obtained from Maxwell's equations, and co-propagate at different group-velocities in the optical fiber medium. Due to the group velocity difference, DMD is introduced. In optical fibers however, the fiber medium can be engineered, and therefore, the DMDs can be compensated by negative DMD fibers. Due to the refractive index profiles of the optical fiber mediums, coupling between modes is introduced in the fiber splices. However, using the weakly guiding approximation, the amount of coupling can be considered to be small. The impact of Rician channel fading is discussed and deduced to be originating from mode coupling within the fiber and fiber splices resulting in MDL.

As all LP modes co-propagate along the optical fiber, key propagation parameters are introduced through the non-linear Schrödinger equation: attenuation, GVD, and Kerr nonlinearities. Each mode is subject to its respective propagation parameters, resulting in different attenuation per mode which requires corresponding amplification for minimizing the impact of MDL. In addition, due to coupling, the GVD cannot be compensated, and residual dispersion needs to be mitigated by the MIMO equalizer.

Chapter 4

DSP aided optical mode multiplexer design and optimization

*For every disciplined effort
there is multiple reward.*

Emanuel James Rohn

In Chapter 2 and Chapter 3 the theoretical MIMO model and the LP mode model are detailed, respectively. However, to employ the LP modes as transmission channels, transmitters need to couple their modulated carriers into the optical fiber. The design of the required optical mode multiplexer and demultiplexer is critical to the launching and hence the propagation characteristics of the signals. This chapter² first describes PDM, the multiplexing method of two polarization modes within the fundamental mode in section 4.1, which is well known in optical transmission systems. This multiplexing method is the fundamental type of SDM. Then, optical LP mode multiplexers are introduced, where CSI estimation techniques described in section 2.3 are critical to the design and alignment. Also, receiver side DSP is important in the processing of the received modes after the demultiplexer, which is further detailed in Chapter 6. In this chapter, first four generations of mode multiplexers are described in chronological order: binary phase plates, spot launchers, three-dimensional waveguides, and currently emerging photonic lanterns. For the first three MMUXs, the experimental performance is further detailed. Key MMUX performance properties are

- Low coupler insertion loss (CIL).
- Low mode dependent loss.
- Polarization independence.
- Supporting all telecom wavelength bands.
- Small footprint.
- Easy handling.
- Potential for scaling to a high number of spatial channels.

² This chapter incorporates results from the author's contributions [r3], [r17], [r26], [r34], and [r36].

4.1 SSMF dual polarization transmission

The term SDM has recently been introduced in optical communications [19]. However, for almost a decade SDM is already a topic in coherent transmission systems [17, 18]. It was merely indicated by a different term, PDM. At that time, SSMFs offered enough bandwidth and were widely employed. Hence, there was a large commercial interest driving research. As only the fundamental LP mode is guided in a SSMF, only two linear solutions to the wave equation are valid: the X and Y-polarization of the LP₀₁ mode, corresponding to the orthogonal \mathcal{E}_x and \mathcal{E}_y linear alignment basis, respectively. The attractiveness of this methodology is that it is fully orthogonal with WDM, and therefore provides a freely available doubling of the available bandwidth in SSMFs.

In Chapter 2 signals exploiting the amplitude and phase components were introduced. Combining the amplitude and phase dimensions with exploiting the two orthogonal polarizations, results in four available dimensions for data to be encoded. Multiplexing this signal into the two LP polarizations is achieved by a cube or fiber polarization beam splitter (PBS) [126]. Alternatively, instead of using two separate discrete components as IQ-modulators, an integrated dual IQ-modulator can be used. Within the photonic integrated circuit (PIC), the polarization multiplexing is performed. In either case, the output is a DP vector signal, conventionally depicted as shown in Fig. 4.1.

At the receiver side, the inversion of the MMUX is performed. Throughout transmission, the two polarizations will rotate and mix. Therefore, 2×2 MIMO signal processing is employed to unravel the two mixed polarizations. MIMO signal processing is further detailed in Chapter 6.

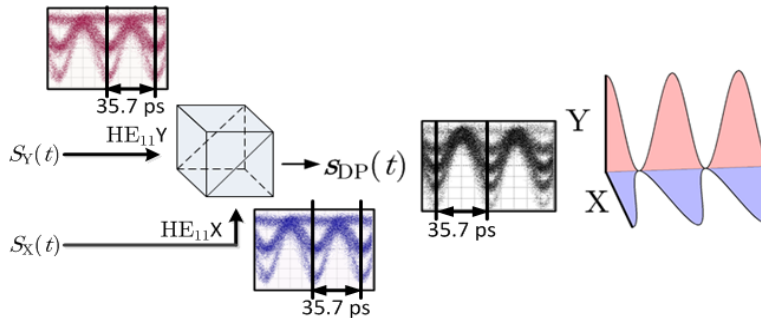


Fig. 4.1 DP vector signal generated from X and Y polarization signals, representing the first SDM in optical transmission systems. Insets: experimental 28 GBaud QPSK optical eyes for single and dual polarization.

4.2 Binary phase plate characterization

As the research community starts nearing the maximum bandwidth available in SSMFs, SDM seems to be the next logical step. Table 3.1 details the increase in available transmission channels when an increased number of LP modes are allowed to co-propagate in a multimode fiber. The contributed work focuses on a 3MF transmission system, allowing the co-propagation of two LP modes, or three spatial LP modes. Hence, a maximum of six polarization modes are available to carry modulated signals. By exploiting the amplitude and phase signal components, a total of twelve real-valued dimensions are available in the 3MF.

4.2.1 Mode conversion

As dual polarization SSMFs were the de facto standard for optical transmission systems, the logical step for increasing the throughput is converting the fundamental mode to the higher order spatial LP modes. Initially, the mode conversion was achieved by inverting the phase of certain spatial areas of the fundamental LP mode in free space using spatial light modulators (SLMs) [127, 128]. Rapidly thereafter, as SLMs are polarization dependent, phase plates were introduced. Due to the phase shifting region, the term binary phase plates is regularly used, and was first proposed in [129]. Phase plates can be based on two different types of materials, either polymethyl methacrylate (PMMA) or quartz can be used. The mode conversion through phase plates is depicted in Fig. 4.2, where the red and blue areas represent a 0 and π phase shift, respectively. It has been experimentally confirmed that the PMMA-based phase plates achieve a higher extinction ratio between LP modes than the quartz-based phase plates. Note that the conversion from higher order LP modes to the fundamental LP mode can be achieved by using the same phase plate types. In section 3.3 it was determined that the LP modes are spatially orthogonal, which can be further confirmed by observing the LP mode phases in Fig. 4.2. By only changing the phase of the fundamental mode, however, the perfect higher order LP mode distribution is not achieved, but approximated, and the conversion efficiency can be computed by using the overlap integral from Eq. (3.45). From Fig. 4.3(a) it can be observed that the 3MF to SMF image ratio is 1, as the same lens is used for the 3MF and SMF. This is due to the similar core diameter of the respective fibers [73]. During the experiments [r26], a conversion loss from the fundamental LP_{01} mode to the LP_{11} mode of approximately 2 dB was found. This is compensated by adjusting the respective launch powers. In addition, as shown in Fig. 4.3(a), the converted modes are spatially multiplexed into the 3MF by beam splitters, where each beam splitter adds 3 dB loss.

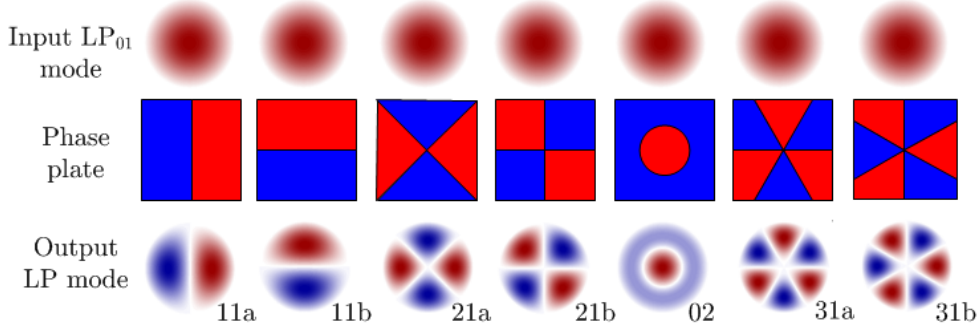


Fig. 4.2 LP_{01} mode conversion to higher order LP modes achieved by phase altering spatial areas of the fundamental LP_{01} mode.

4.2.2 Mode crosstalk

By using binary phase plates, the spatial LP modes are excited individually. Hence, the crosstalk between the modes in the (de)multiplexer is minimized. For a three spatial LP MMUX, where LP_{01} , LP_{11a} , and LP_{11b} are employed, as depicted in Fig. 4.3(a), the complex valued transmission matrix is

$$\mathbf{H}_{\text{MMUX}} = \begin{bmatrix} \mathbf{H}_{\text{LP01}} & \mathbf{0}_{2,4} \\ \mathbf{0}_{4,2} & \mathbf{H}_{\text{LP11}} \end{bmatrix}, \quad (4.1)$$

where \mathbf{H}_{LP01} is a 2×2 matrix (2 polarizations), $\mathbf{0}_{i,u}$ a 0 valued $i \times u$ matrix, and \mathbf{H}_{LP11} a 4×4 matrix (2 polarizations in 2 spatial LP modes). As the crosstalk between LP modes can be neglected, the transmission matrix \mathbf{H}_{MMUX} can be considered as two separate smaller matrices, resulting in a lower computational complexity signal processing requirement than when full mixing is used. This is further detailed in section 6.2.6. Effectively, the transmission can be seen as two separate transmission systems. This shows similarities with employing multiple cores as transmission channels (see section 3.1). However, in the case of cores, mode

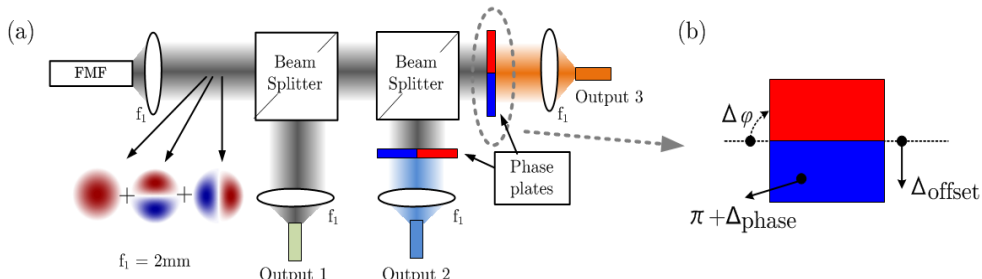


Fig. 4.3 (a) Phase plate based demultiplexer, where the few mode fiber carries 3 spatial modes. (b) Three impairment types of a phase plate, rotation, offset, and phase mismatch.

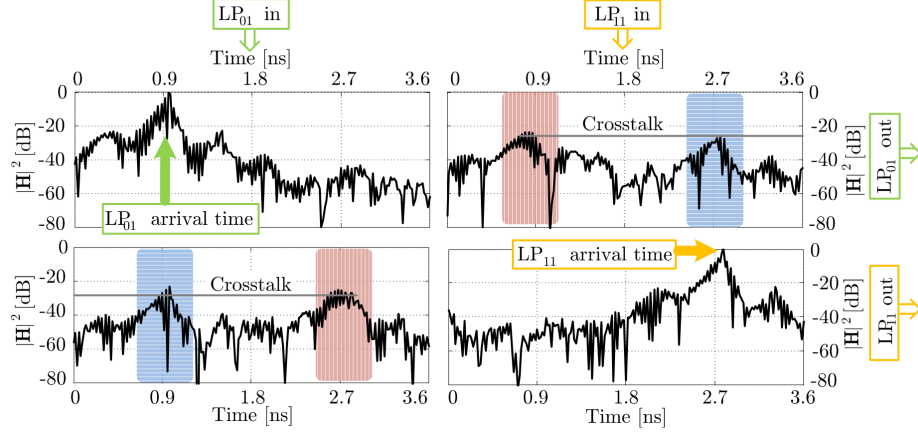


Fig. 4.4 Impulse response measurement using the phase plate MMUX and MDMUX and an 11.8 km 3MF. Blue (horizontally striped) denotes crosstalk at the MMUX, and red (vertically striped) denotes crosstalk at the MDMUX.

coupling is minimized by increasing the distance between cores. Through simulations, the binary phase plates are characterized, and tolerances are investigated [r17]. Here, three impairments on one phase plate are investigated through simulations as shown in Fig. 4.3(a): an azimuthal offset, transversal displacement, and an incorrect phase shifting region. Each of these impairments results in crosstalk and a received power difference in the form of MDL. The crosstalk deficit requires the MIMO equalizer to take all elements of \mathbf{H}_{MMUX} into account, which increases the computational complexity. Fig. 4.4 depicts the MIMO equalizer's response for a two LP mode transmission system [r26], where a crosstalk level better than 26 dB is observed between the two LP modes. Note that Fig. 4.4 only depicts one spatial LP₁₁ mode for simplicity. The LP modal arrival time difference corresponds to the DMD of the fiber. In this case, the DMD is a positive fiber characteristic, as it allows for the independent investigation of the MMUX and MDMUX. Due to the crosstalk, the $\mathbf{0}$ elements in Eq. (4.1) are no longer 0, and can no longer be neglected. The impairment contribution resulting in MDL leads to a channel and system SNR penalty, as shown in Fig. 4.5. For a ≤ 1 dB SNR system penalty, the azimuthal tolerance is approximately 30 degrees. The transverse offset is 0.18 of the e^{-2} mode distribution width, and the phase mismatch tolerance is 45 degrees. All these numbers are high, and therefore it can be concluded that the phase plates can be considered as a mode multiplexer with non-stringent tolerances, as the DSP can unravel the mixed transmission channels. Nevertheless, the primary reasons for the binary phase plates to be superseded with an improved type of MMUX are fourfold: poor scalability to a higher number of transmitted modes due to losses, temporal alignment stability, bulkiness of the

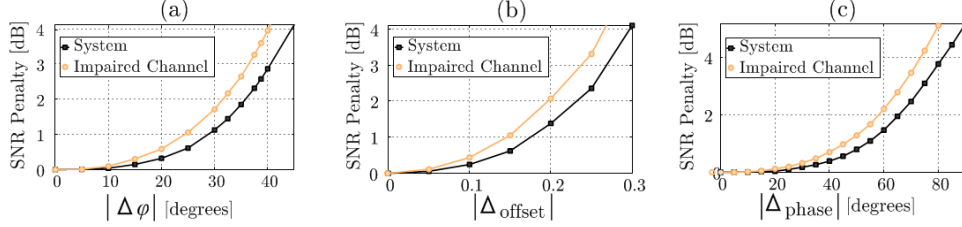


Fig. 4.5 Binary phase plate impairment tolerances for a two LP mode transmission system to (a) azimuthal rotation, (b) transversal offset, and (c) phase shifting region mismatch.

setup, and only exploiting one spatial LP mode as a spatial path. From Fig. 4.3(a) it can be observed that beam splitters are inserted for adding additional modes. Each beam splitter has an inherent insertion loss of 3 dB, and hence is poor in scaling to a high number of modes. The highest insertion loss of the 3 spatial modes was approximately 9 dB. Consequently, by using the phase plates as MMUX and MDMUX, the combined insertion loss is around 18 dB. This loss is the equivalent of 90 km transmission, assuming a fiber attenuation of approximately 0.2 dB km^{-1} . The phase plates were used for C-band transmission, as they may not support all telecom wavelength bands due to the phase shifting region. The broad wavelength range however, is untested. Secondly, the temporal instability leads to a walk-off, and thus an increase in crosstalk. From the results, it is clear that binary phase plate mode (de)multiplexers require regular alignment and tuning which for an experimental setup may be acceptable. Furthermore, the bulkiness renders this system a non-viable solution for integration in a future transmission system when scaling to a high number of spatial channels. Finally, as only a single spatial LP mode is excited per SSMF input, if that particular mode experiences degradation by attenuation, noise addition, or fiber perturbations, the received signal may be severely degraded.

4.3 Spot launching

A different launching approach to the binary phase plate mode multiplexer is performed by free-space spot launching, first reported by R. Ryf in [130]. It is important to realize that equal excitation of all modes maximizes the spatial diversity, and hence the condition number of \mathbf{H}_{MMUX} is minimized [131]. Accordingly, a critical condition is that the characteristics of the spots launched into the fiber, are chosen such that they do not overlap. When \mathbf{H}_{MMUX} is designed as a unitary rotation of the transmitted channels inserted in the fiber, the ultimate channel throughput remains unaffected as the eigenvalues of the transmission matrix are unchanged. The second generation mode multiplexer was employed in [r3] and [r13], and the combination of MDL and insertion loss was optimized by

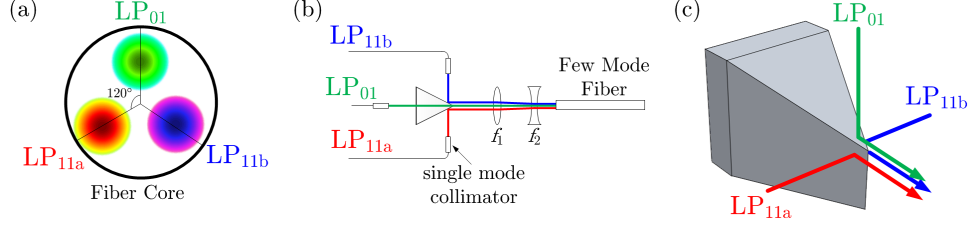


Fig. 4.6 (a) Spot allocation for launching 3 spatial LP modes. (b) The experimental setup allowing the insertion of three DP signals in the few-mode fiber. (c) Three dimensional representation of the 3-facet mirror.

fine-tuning the spot locations. DSP aided in finding the optimum through LS CSI estimation, as detailed in section 2.3. As the inserted channels fully couple into multiple modes, MDL represents the power of a transmitted channel instead of an actual physical polarization of a LP mode. Additionally, a second quality measure variable is introduced for MMUXs as [131]

$$\text{CIL} = \left(\frac{1}{N_r} \sum_{n=1}^{N_r} \sigma_n^2 \right)^{-1}, \quad (4.2)$$

which is the coupler insertion loss, and where N_r represents the number of orthogonal LP modes. The variable σ_n has been previously introduced in Chapter 2 as the singular values of the transmission matrix, obtained through singular value decomposition of the LS or MMSE estimated \mathbf{H}_{MMUX} . Low MDL is obviously desired, however, a low CIL is also advantageous as it indicates the quality of the coupler in terms of insertion losses. Hence, the optimum balance between the two needs to be found.

To obtain the theoretical element values of the spot launcher MMUX transmission matrix \mathbf{H}_{MMUX} , the elements are computed by using the MOI, given in Eq. (3.45). The approximate LP modes in the fiber are known, detailed in Table 3.1. Hence, only the input field distributions need to be chosen. As the spot launcher is based on free-space optics, the inputs are SMFs. The fundamental LP₀₁ free-space mode distribution from a SMF can be approximated by a Gaussian distribution spot [131], which leaves two degrees of freedom, namely the Gaussian beam width, and the spot center location. By altering these variables for a single spot and computing the overlap integral with the respective LP modes, one row in \mathbf{H}_{MMUX} is determined. This process is repeated for all spots to fill the elements of \mathbf{H}_{MMUX} . Note that, to avoid rank deficiency, the spots are chosen such that they cannot overlap. To this end, [131] proposed to divide the azimuthal freedom in three 120 degree regions, where each region represents a respective spot location as depicted

in Fig. 4.6(a). A proposed transmission matrix, where only modes are taken into account, is [132]

$$\mathbf{H}_{\text{MMUX}} = \frac{1}{\sqrt{6}} \begin{bmatrix} \sqrt{2} & \sqrt{2} & \sqrt{2} \\ 0 & \sqrt{3} & -\sqrt{3} \\ 2 & -1 & -1 \end{bmatrix}, \quad (4.3)$$

which satisfies the unitary matrix condition, allocates the channels over the LP modes, and corresponds to the spot distribution shown in Fig. 4.6(a). Note that full rank is achieved, however, the second spot, corresponding to the second row in the transmission matrix \mathbf{H}_{MMUX} , only employs two LP modes. Therefore, the second signal channel is more vulnerable to modal impairments than the other two. Based on this idea, the spot launcher experimental setup is depicted Fig. 4.6(b), where three single mode DP fiber inputs are aligned to imping a single element 3 facet mirror. The 3 facet mirror is detailed in Fig. 4.6(c), where only the very tip of the element is used. This allows for combining the three inputs on the two transverse axes to align in the propagation direction in the fiber. By tuning the position of the SMF inputs, the spot location is changed, and by adjusting the position of the lenses ($f_1 = 150\text{mm}$, $f_2 = 2\text{mm}$) the spot sizes can be modified. The MMUX was optimized for power balance using the LS CSI estimation algorithm detailed in section 2.3, and the channel impulse response is shown in Fig. 4.7. When comparing Fig. 4.7 with Fig. 4.4, it can be observed that the transmitted channel powers are more evenly distributed over the receivers. Again, the difference in modal arrival time is the fiber DMD. The minimum insertion loss was 4 dB, whilst the optimized

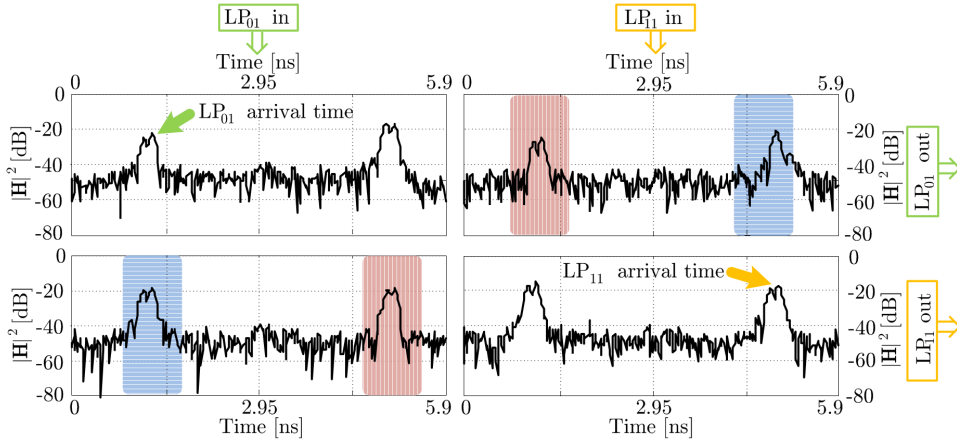


Fig. 4.7 Impulse response measurement using the spot launcher MMUX and MDMUX and a 41.7 km 3MF. Blue (horizontal striped) denotes crosstalk at the MMUX, and red (vertical striped) denotes crosstalk at the MDMUX.

MDL was estimated to be 2 dB. The primary advantage the spot launcher has over the binary phase plates for usage in the laboratory is the temporal stability. In addition, the spot launcher is more tolerable with respect to modal attenuation differences and independent modal impairments. Furthermore, through avoiding phase shifting regions, spot launching supports all used telecom wavelength bands, and a substantially improved insertion loss is achieved in comparison to the phase plate MMUX. Instead of an insertion loss of 9 dB for the binary phase plates, the insertion loss for spot launching was approximately 4-4.5 dB at 1555 nm. Nevertheless, it is always preferred that this number is further reduced to maximize the transmission distance without requiring additional amplification. However, the free-space spot launch MMUX has two major drawbacks shared with the binary phase plates; the free-space spot launcher is bulky and therefore not very viable for future integrated SDM transponders. In addition, scaling spot launching to a higher number of spatial modes results in practical difficulties for a free-space mirror based setup.

4.4 Three dimensional waveguide

These reasons result in the proposal of the third generation MMUX, which is based on the same principle as the spot launcher. However, instead of using a free-space based spot coupler, a 3DW is employed [133, 134]. The designed 3DW depicted in Fig. 4.8(a) was used in [r34] and [r36]. From observing Fig. 4.8(b), it is clear that this MMUX is substantially more compact than any free-space MMUX can offer,

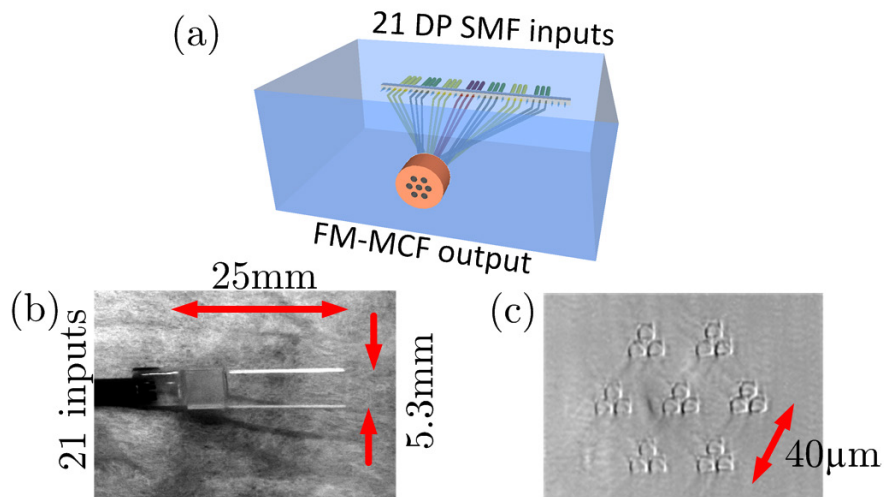


Fig. 4.8 Three dimensional waveguide. (a) top-down perspective indicating size. (b) End facet, which is butt-coupled to the few mode fiber.

where the size of the 3DW is $5.3 \text{ mm} \times 25 \text{ mm}$. In fact, the compactness has been exploited to create 7 sets of 3 triangularly placed spots in a hexagonal arrangement, as depicted in Fig. 4.8(c), which matched the FM-MCF structure. Per core, the triangular arrangement matches the spot allocation positions determined previously in the spot launcher section. The experimental results of the FM-MCF measurement are detailed in Chapter 8.

To this end, 21 SMF inputs are connected to the borosilicate glass substrate of the 3DW on a $127 \text{ }\mu\text{m}$ pitch v-groove. The connecting waveguides in the 3DW were inscribed by direct laser writing using a focused ultrafast femtosecond laser pulses. The inscription technique allows to control sub-surface refractive index modification, producing a three dimensional pattern of transparent waveguides, which are controlled with a precision up to 50 nm . The individual square waveguides have a cross-sectional effective area of $36 \text{ }\mu\text{m}^2$. Again, LS CSI estimation is employed to compute the MDL, which is approximated at 1.5 to 2 dB, and the 3DW loss on average is 1.1 dB across all 21 waveguides (excluding fibers) at 1550 nm . Taking FMF insertion loss into account, the loss over the 3DW is approximately 4 dB, which originates from the air-glass-air interfaces, and matching the fiber field modes. This insertion loss is similar to what was observed for the spot launcher. However, the compact nature of the 3DW allows a highly stable butt-coupled interface to a 3MF or FM-MCF. Note that borosilicate glass supports all key telecom wavelength bands ranging from visible light up to $2.2 \text{ }\mu\text{m}$.

The key downside of this MMUX in regard to the spot launcher is the adjustability of the mode fields. A lens combination can increase or decrease the triangular spot mask image, but not alter the spot locations with respect to each other. Note that, to obtain virtually 0 dB MDL, the insertion loss is very high as is simulated in [131].

4.5 Photonic lantern

This high insertion loss issue with respect to reducing MDL has led to the development of the fourth generation mode multiplexer: the adiabatically tapered photonic lantern. Initial results on the photonic lantern performance are currently emerging [132, 133, 135, 136]. Like the 3DW, the photonic lantern principle is based on the spot launcher, where certain areas of the 3MF are lit up to excite the LP modes. However, in the case of a photonic lantern, this is achieved through a tapering region instead of a discrete conversion step. The three SSMF input is depicted in Fig. 4.9(a). Initially, the SSMFs are placed at a large pitch and hence

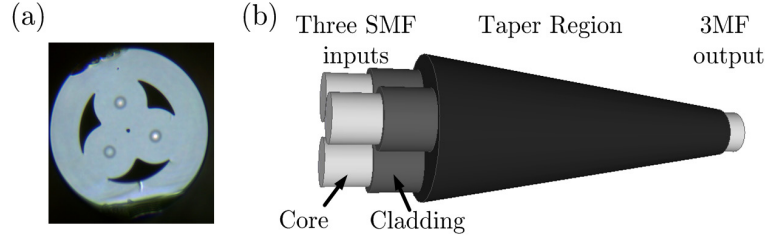


Fig. 4.9 Photonic lantern MMUX. (a) Input facet microscope image (courtesy of R. Amezcua Correa). (b) Schematic photonic lantern tapering.

do not couple. This is generally achieved using SSMF capillaries. As the tapering region progresses, the SSMF pitch decreases and the SSMFs start coupling to the neighboring SSMFs. This continues to the point where they are fully coupled at the output, which is at the 3MF, as shown in Fig. 4.9(b). The primary advantage this MMUX offers is avoiding the glass-air and air-glass conversions. Hence, the bulk of the energy remains in the core of the fibers and losses are greatly reduced. Initial reports indicate an MDL < 0.5 dB [137], and an insertion loss of 2.4 dB. This could be further reduced by optimizing the photonic lantern drawing process.

4.6 Scaling number of multiplexed channels

The four generations of MMUXs provide solutions to guide multiple channels into multimode or multicore fibers. A performance comparison is given in Table 4.1. From Table 4.1, it is clear that the phase plate and spot launcher MMUXs are difficult to scale to a higher number of multiplexed channels, primarily because of the footprint size. In addition, due to individual mode excitation of the phase plates, the MDL is high. The remaining two MMUX solutions have the potential for integration, as the footprint is small, where the 3DW is more limited in scaling the number of inputs than the photonic lantern, as the inscribed waveguide sizes limit the number of inputs per multimode core. Alternatively, a photonic crystal fiber is proposed to be employed as 3DW [138]. Accordingly, it has been shown

MMUX type	Principle	Insertion loss	MDL	Footprint size
Phase plates	Individual excitation	High	High	Large
Spot launcher	Full mixing	Medium	Medium	Large
3DW	Full mixing	Medium	Medium	Small
Photonic lantern	Full mixing	Low	Low	Small

Table 4.1 MMUX characteristics.

that the 3DW has the potential for multicore SDM. The photonic lantern is the ultimate solution, as it has a small footprint, and does not require glass-air and air-glass interfaces. Photonic lanterns are less limited to waveguide sizes, and therefore have the potential to be used for a larger multimode fiber with increased channels [139]. Also, they can be integrated into the fiber medium, as has been proposed in multi-element fibers [140].

4.7 Summary

To create a MIMO transmission system in optical communications, an important component is the MMUX. Through LS channel state information estimation, digital signal processing is a key aid in characterizing the MMUX. The most notable figure to obtain using signal processing is the MDL, as it limits the ultimate transmission system capacity.

Initially, free-space binary phase plates were proposed for optical multiplexing. In this particular setup each launched LP mode represents a DP transmission channel. Three binary phase plate impairment tolerances were investigated, where one phase plate was either moved by an offset, rotated, or the π -phase shifting region was impaired. For a ≤ 1 dB SNR system penalty, the azimuthal tolerance is approximately 30 degrees. The transverse offset is 0.18 of the e^{-2} mode distribution width, and the phase mismatch tolerance is 45 degrees. Additionally, if low crosstalk can be achieved between the LP modes, the computational complexity of MIMO equalization can be greatly reduced as the crosstalk components do not need to be considered.

To improve the insertion loss and make the transmission system more robust, the free-space spot launcher MMUX was introduced. This second generation free-space MMUX distributes the transmission channel's energy over spatial paths, the LP modes. The combined excitation of various LP modes with a single transmission channel is achieved by launching the transmission channel's energy in a particular area in the 3MF. Doing this with multiple inputs, a unitary rotation transmission matrix can be achieved, which does not impact the ultimate transmission system throughput.

As the free-space spot launcher uses a large footprint, the 3DW is introduced as third generation MMUX. It relies on the same principle as the spot launcher, where transmission channels are inserted in the 3MF at particular areas, hence exciting a set of LP modes simultaneously. However, this compactness can be greatly

exploited and accordingly, a FM-MCF 3DW was designed consisting of seven three-spot launchers.

The photonic lantern is the fourth generation optical MMUX, and is seen as the ultimate solution as it can achieve virtually MDL free transmission, and minimize insertion losses. The initial results of this type of MMUXs are currently emerging.

Chapter 5

MIMO receiver front-end

*Adversity reveals genius,
prosperity conceals it.*

Horace

Chapter 4 provided details on the optical MMUX and MDMUX, where the latter forms the input for this chapter³, the MIMO receiver front-end. The MIMO receiver FE is considered to be from the optical MDMUX output to the MIMO equalizer input. Hence, the output of the MIMO receiver FE addresses the processes prior to the input to MIMO Equalization, which is discussed in Chapter 6. Accordingly, the optical quadrature receiver FE is described first in section 5.1, and the generalized quadrature receiver structure is given in 5.1.3. This structure relates to the QAM transmitter structure, detailed in 2.5.1. The optical quadrature receiver forms the basic element for the DP optical FE, and is shown in Fig. 5.1. In the same figure, the structure of this chapter is depicted. The DP optical FE is detailed in section 5.2, and in turn, provides the basic building block for the conventional MIMO receiver optical FE. However, it is clear that scaling the number of received DP channels in laboratory environments is costly, as one DP optical quadrature receiver and corresponding 4-port ADC is required for each transmitted DP signal. In this chapter, a novel optical front-end MIMO receiver scheme is proposed and further detailed in section 5.3. For further study, a complexity scaling analysis for increasing the number of received DP signals up to 20 is outlined and discussed. In addition to the spatial domain, the time domain is exploited to acquire multiple data packets from DP signal inputs. This creates the time-domain multiplexed spatial division multiplexer (TDM-SDM) optical MIMO receiver. In the digital domain, the optically time domain multiplexed signals are parallelized to form the equivalent spatial domain receiver. Then, each optical quadrature FE output signal is optimized by compensating quadrature mixing impairments. These impairments are described in section 5.4. Subsequently, adaptive rate control and skew alignment is performed by an interpolation filter for

³ This chapter incorporates results from the author's contributions [r5], [r7], [r13], and [r37].

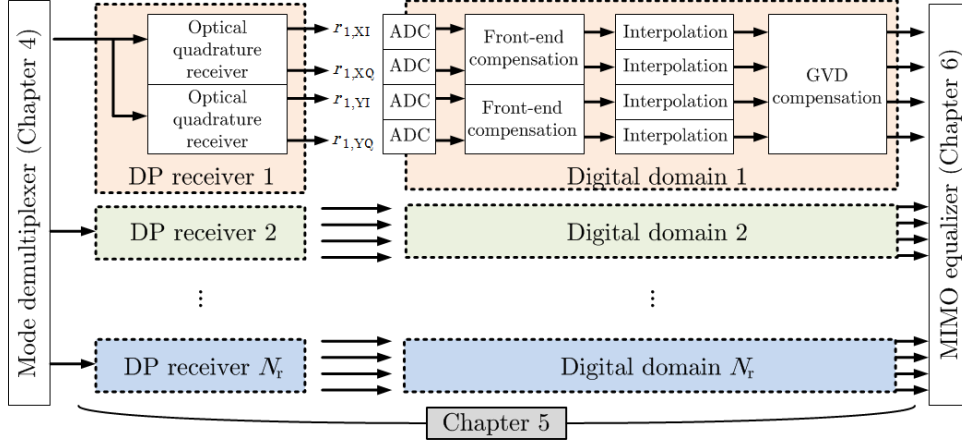


Fig. 5.1 Schematic overview of the MIMO receiver FE discussed in Chapter 5.

all received quadrature signals in the MIMO receiver. The final DSP processing block compensates the effects of group velocity dispersion. GVD is inherent to optical transmission systems, and its origin is described in section 3.6.3. GVD estimation and compensation is detailed in section 5.6, where the outputs form the input of the MIMO equalizer, further described in Chapter 6.

5.1 Optical quadrature receiver

In section 2.5, the generalized QAM symbol generation scheme is introduced. This scheme is converted to the optical domain as discussed in section 2.7, which employs Mach-Zehnder Modulators. When transmitting QAM symbols using a quadrature transmitter, at the receiver side a corresponding quadrature receiver is required. First, the optical mixer is described as it is essential to the operation of the optical quadrature receiver. In addition, the effects arising from the optical to analog conversion and the process taken to mitigate these effects are discussed in the following sections.

5.1.1 Optical mixer

The optical field to electrical current conversion is achieved by a photo detector (PHD), which is a key element in optical receivers. The most commonly used PHD type is a PIN PHD, consisting of three regions: positive doped, intrinsic, and negative doped. After conversion, an analog electrical signal is obtained which can be digitized by an ADC. Thereafter, the digitized signal can be processed using digital signal processing algorithms. To illustrate the coherent receiver reception principle, Fig. 5.2 shows a simple interferometer receiver structure using a balanced

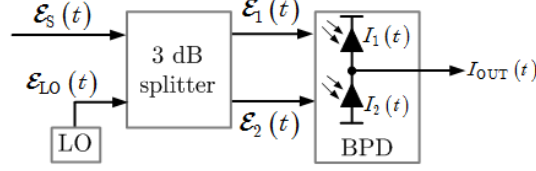


Fig. 5.2 Coherent reception principle, employing an interferometer and a BPHD.

photodetector (BPHD) [72]. The interferometer is a 3 dB power splitter, operating as 180° phase shifter. The BPHD consists of two regular PHDs, functioning in mirrored operation using a positive and negative bias. Let the incoming signal be

$$\mathcal{E}_S(t) = (P_S)^{1/2} \exp\{j[\omega_S t + \varphi_S + \varphi_{NS}(t)]\} s(t) \mathbf{u}_S, \quad (5.1)$$

which is an electric field, and the LO electric field is

$$\mathcal{E}_{LO}(t) = (P_{LO})^{1/2} \exp\{j[\omega_{LO} t + \varphi_{LO} + \varphi_{NLO}(t)]\} \mathbf{u}_{LO}, \quad (5.2)$$

where P_S and P_{LO} represent the continuous wave powers of the incoming signal and LO, respectively. The angular frequencies and initial phases of the signal and LO are ω_S, φ_S and $\omega_{LO}, \varphi_{LO}$, respectively. The unit vectors \mathbf{u}_S and \mathbf{u}_{LO} represent the electric field direction in the transverse plane of the signal and LO, respectively. Note that these signals therefore represent a single polarization. For optimum receiver sensitivity, these unit vectors are assumed to be equal. The type of receiver depicted in Fig. 5.2 is a heterodyne receiver, where the LO comes from a different laser source than the transmitter. Furthermore, the time dependent phase noises of the signal and LO are introduced as $\varphi_{NS}(t)$ and $\varphi_{NLO}(t)$, respectively. The electrical fields impinging the PHDs of the BPHD are

$$\begin{aligned} \mathcal{E}_1(t) &= \sqrt{\frac{1}{2}} [\mathcal{E}_S(t) + j\mathcal{E}_{LO}(t)] \\ \mathcal{E}_2(t) &= \sqrt{\frac{1}{2}} [j\mathcal{E}_S(t) + \mathcal{E}_{LO}(t)], \end{aligned} \quad (5.3)$$

which results in the respective photocurrents

$$\begin{aligned} I_1(t) &= \frac{R_{\text{PHD}}}{2} |\mathcal{E}_S(t) + j\mathcal{E}_{LO}(t)|^2 + I_{\text{sh},1} + I_{\text{th},1} \\ I_2(t) &= \frac{R_{\text{PHD}}}{2} |j\mathcal{E}_S(t) + \mathcal{E}_{LO}(t)|^2 + I_{\text{sh},2} + I_{\text{th},2}. \end{aligned} \quad (5.4)$$

The currents $I_{\text{sh},1}$ and $I_{\text{sh},2}$ are the shot-noise photocurrents from the PHDs, $I_{\text{th},1}$ and $I_{\text{th},2}$ represent the thermal noise currents. For a sufficiently high LO input power, the shot-noise currents become dominant, and the thermal noise currents are neglected [72]. The variable R_{PHD} represents the PHD responsivity and equals

$$R_{\text{PHD}} = \eta \frac{2\pi e_{\text{en}}}{\hbar\omega_s}, \quad (5.5)$$

where η is the quantum efficiency, $e_{\text{en}} = 1.6 \cdot 10^{-19}$ [C] represents the charge per electron and $\hbar\omega_s/(2\pi)$ is the energy per photon, where \hbar is Planck's constant in [Js]. By substituting Eq. (5.1) and Eq. (5.2) in Eq. (5.4), the output current of the BPHD is computed as

$$\begin{aligned} I_{\text{OUT}}(t) &= I_1(t) - I_2(t) \\ &= 2R_{\text{PD}}\sqrt{P_{\text{S}}P_{\text{LO}}}s(t)\sin[\Delta\omega t + \Delta\varphi + \Delta\varphi_{\text{N}}(t)]\mathbf{u}_{\text{S}} \cdot \mathbf{u}_{\text{LO}} + I_{\text{sh}}, \end{aligned} \quad (5.6)$$

where $\Delta\omega = \omega_{\text{S}} - \omega_{\text{LO}}$, $\Delta\varphi = \varphi_{\text{S}} - \varphi_{\text{LO}}$, $\Delta\varphi_{\text{N}}(t) = \varphi_{\text{NS}}(t) - \varphi_{\text{NLO}}(t)$, and $I_{\text{sh}} = I_{\text{sh},1} - I_{\text{sh},2}$. Eq. (5.6) clearly shows that the input signal is multiplied by a sine function. Hence, one arm in the quadrature receiver is satisfied. Note that due to Eq. (5.6), the BPHD output current contains no DC-components. Also, balanced photodetectors have the advantage of removing the ASE-ASE noise beating [72]. If a regular PHD, or only one input of the BPHD is used, the DC term is not removed. Additionally, only using one arm comes at the expensive of receiver sensitivity and relative intensity noise (RIN) [141]. RIN is introduced through the amplitude noise contributions of the signal and LO. However, generally it is assumed that the LO power is substantially higher than the signal power, and therefore is the dominant contributor to RIN. The DC term can easily be removed in the digital domain, as further detailed in section 5.4. The variance of I_{sh} is the summation of the variance of the two shot noise components as

$$\text{var}(I_{\text{sh}}) = \text{var}(I_{\text{sh},1}) + \text{var}(I_{\text{sh},2}), \quad (5.7)$$

and the phase change variance resulting from laser phase noise is

$$\begin{aligned} \text{var}[\Delta\varphi_{\text{N}}(t)] &= 2\pi\Delta\nu_{\text{eff}}|t| \\ &= 2\pi(\Delta\nu_{\text{S}} + \Delta\nu_{\text{LO}})|t|, \end{aligned} \quad (5.8)$$

where $\Delta\nu_{\text{S}}$ and $\Delta\nu_{\text{LO}}$ represent the signal laser and LO laser linewidth, respectively. The laser linewidth becomes increasingly important as the number of constellation points increase [142]. This scheme represents an optical mixer using a BPHD, allowing to down convert the high-frequency carrier and one component of the quadrature receiver.

5.1.2 Optical quadrature receiver

In the previous section, the optical mixer was shown and the BPHD was introduced. A quadrature receiver is in essence structured very similarly, where the key difference is the mixer. From observing Fig. 2.6, a QAM symbol is generated using two separate mixers, representing the inphase and quadrature component, respectively. In section 2.7 the theoretical QAM generator model was converted to the optical domain. Naturally, when two branches are present in the transmitter, at least the same number is required at the receiver side. Accordingly, the 2×4 90°

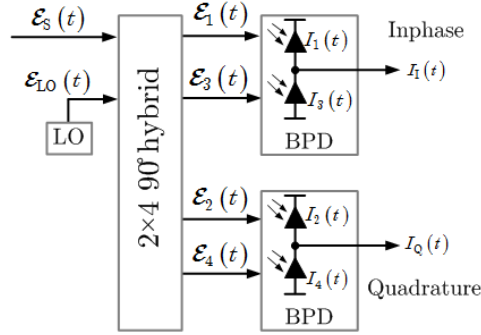


Fig. 5.3 Optical quadrature receiver consisting of 2 BPHDs and one 90° hybrid.

hybrid is introduced as a quadrature mixer, and the quadrature receiver is depicted in Fig. 5.3. The electric field outputs of the 90° hybrid can be described as

$$\begin{bmatrix} \mathcal{E}_1(t) \\ \mathcal{E}_2(t) \\ \mathcal{E}_3(t) \\ \mathcal{E}_4(t) \end{bmatrix} = \begin{bmatrix} 1 \\ 1 \\ 1 \\ 1 \end{bmatrix} \frac{\mathcal{E}_S(t)}{2} + \begin{bmatrix} 1 \\ j \\ -1 \\ -j \end{bmatrix} \frac{\mathcal{E}_{LO}(t)}{2}. \quad (5.9)$$

Note that the signal and LO inputs are still considered to be single polarization and the denominator in Eq. (5.9) is $\sqrt{4}$ due to 4-way power splitting. Following the computational steps in section 5.1.1 for Eq. (5.9), the two solutions

$$\begin{aligned} I_I(t) &= I_1(t) - I_3(t) \\ &= R_{\text{PHD}} \sqrt{P_S P_{LO}} s(t) \cos[\Delta\omega t + \Delta\phi + \Delta\phi_N(t)] \mathbf{u}_S \cdot \mathbf{u}_{LO} + I_{\text{shI}} \end{aligned} \quad (5.10)$$

and

$$\begin{aligned} I_Q(t) &= I_2(t) - I_4(t) \\ &= R_{\text{PHD}} \sqrt{P_S P_{LO}} s(t) \sin[\Delta\omega t + \Delta\phi + \Delta\phi_N(t)] \mathbf{u}_S \cdot \mathbf{u}_{LO} + I_{\text{shQ}} \end{aligned} \quad (5.11)$$

are obtained. These two equations correspond to the sine and cosine branches in the QAM symbol generator, depicted in Fig. 2.6, and hence indicate that the optical quadrature receiver allows for QAM symbol reception.

5.1.3 Generalized quadrature receiver

Clearly, an optical quadrature receiver allows for the reception of transmitted QAM symbols. However, for signal reception optimization, it is important to understand the generalized quadrature receiver, which is shown in Fig. 5.4 [53]. The incoming received signal is equally split into two branches, where each branch is mixed with the LO for frequency down conversion. The down conversion stage is considered to be flat fading and memoryless, and the terms correspond to the sine and cosine functions. This has previously been shown in Eq. (5.10) and Eq. (5.11) for the optical quadrature receiver. However, as can be observed from Fig. 5.4,

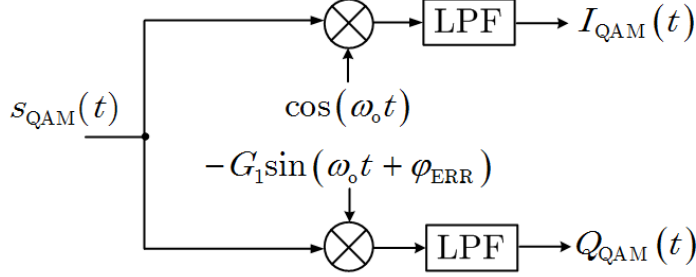


Fig. 5.4 Generalized quadrature receiver structure [53].

these mixing functions may not be fully orthogonal. A phase error φ_{ERR} is introduced in one path with respect to the other. This phase error results in loss of orthogonality, and hence, is the primary source of IQ-imbalance. This imbalance has been introduced in section 2.5 as the transmitter IMRR. Also, one baseband signal is amplified with respect to the other, and both are guided through a LPF, before being converted to the digital domain using an ADC. The amplification difference also results in an IQ-imbalance. The receiver side LO can therefore be described as [143]

$$\begin{aligned} s_{\text{LO}}(t) &= \cos(\omega_{\text{LO}}t) - jG_1 \sin(\omega_{\text{LO}}t + \varphi_{\text{ERR}}) \\ &= K_1 e^{-j\omega_{\text{LO}}t} + K_2 e^{j\omega_{\text{LO}}t}, \end{aligned} \quad (5.12)$$

where the two newly introduced coefficients are

$$K_1 = \frac{1 + G_1 e^{-j\varphi_{\text{ERR}}}}{2} \quad (5.13)$$

and

$$K_2 = \frac{1 - G_1 e^{+j\varphi_{\text{ERR}}}}{2}. \quad (5.14)$$

If IQ imbalance is present in the receiver, the complex valued received signal is

$$r(t) = K_1 s(t) e^{j(\omega_0 - \omega_{\text{LO}})t} + K_2 s^*(t) e^{-j(\omega_0 - \omega_{\text{LO}})t}. \quad (5.15)$$

For simplicity assume $\omega_0 = \omega_{\text{LO}}$. Then, it is clear that in the case of perfect IQ balance $K_2 = 0$ and $\varphi_{\text{ERR}} = 0$. In the digital domain, digital signal processing is employed, and section 5.4 provides further details on signal processing techniques to mitigate the IQ-imbalance.

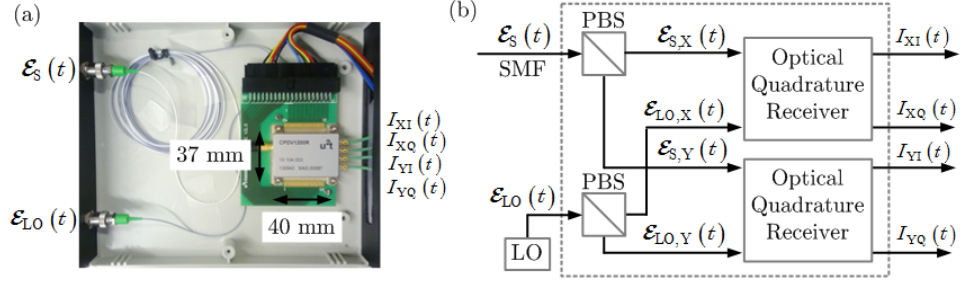


Fig. 5.5 Heterodyne dual polarization coherent receiver [144]. (a) Used receiver in laboratory experiments. (b) Schematic representation.

5.2 Dual-polarization quadrature receiver

Transmitting a dual polarization signal is well known from SMF transmission systems, and the optical MMUX for polarization multiplexing is detailed in section 4.1. Therefore, the dual polarization quadrature receiver input is a single mode fiber. These dual polarization coherent receivers are widely available in an integrated package [144]. The primary advantage of employing integrated receivers is mainly due to footprint and the ease of integration to other sub-systems on a transponder. A coherent receiver employed for work in this thesis is shown in Fig. 5.5(a) [144]. Note that the optical quadrature receiver in the previous section assumed single polarization signals, where the incoming signal and LO were assumed to be aligned. Consequently, for the reception of polarization multiplexed signals, first polarization demultiplexing has to be performed at the receiver side as shown in Fig. 5.5(b). This separates the principle LP mode states into two linear orthogonal components. Any arbitrary rotation of two orthogonal vectors is allowed. For simplicity, the X and Y components are assumed. The LP state of the received signal is random. Hence after separation, each orthogonal component contains a mix of the two polarization states. After polarization demultiplexing has been performed, two optical quadrature receivers are employed. Here, the signal and LO polarization states are matched to maximize efficiency.

5.3 Time-domain multiplexed MIMO receiver

From a theoretical point of view, the MIMO receiver has been schematically shown in Fig. 2.3. In this case, the MIMO receiver consists of N_T dual polarization coherent receivers, where each receiver is coupled to one single mode output of the MDMUX. As such, first the spatial LP modes are separated, before polarization modes. Note that each polarization mode carries mixed signal data from all transmitters and MIMO signal processing is required to unravel the transmitted

channels. This is the straightforward and conventional method of scaling the number of received LP modes in a MIMO receiver. Hence, each transmitted spatial LP mode requires one dual polarization receiver and four corresponding ADCs. In laboratory environments, the ADCs are embedded in high-speed real-time oscilloscopes. Currently, as optical MIMO transmission systems are mainly experimental, offline digital signal processing of captured data is performed. Presently, the focus of the optical MIMO transmission systems in the laboratory is to show that these systems truly are the next generation optical transmission systems, and enable a migration strategy towards real-time products. Therefore, the work in this thesis employs offline DSP. However, as one coherent receiver and corresponding four port oscilloscope per transmitted LP mode is still required, when scaling the number of received spatial LP modes a very costly laboratory setup is required. This has resulted in few research groups in the world having the capability to work in the experimental optical spatial division multiplexing field. In addition, even for these select few research groups, the experimental systems must be cost-effective to be able to scale and investigate higher spatial channel transmission systems. This limitation results in only one research group being able to measure 6 spatial LP modes simultaneously [101], whereas the competing groups are limited to 3 spatial LP modes. As novel fibers continue to emerge [74], rapid progress is required to scale the number of fully mixed MIMO channels that can be received and analyzed. In response to these challenges, a TDM-SDM receiver is proposed and demonstrated with similar performance to the traditional method of scaling the number of ports for the reception of more modes [r13]. The TDM-SDM receiver as currently provisionally patented in [r37] is further discussed in the following subsections.

5.3.1 The TDM-SDM scheme

The proposed TDM-SDM scheme was originally intended for laboratory setups and exploits the space and time dimension, rather than only the spatial dimension for capturing modes. Key to understanding the working of the TDM-SDM scheme is that laboratory setups do not need to acquire data continuously due to the offline mode of processing. Instead, a capture is made of the incoming signal. This capture is time limited and is required to be long enough such that the BER can be accurately estimated. A rule of thumb is that >1000 errors have to be counted per channel. For very low BERs, this means an exceptionally long capture time. To keep transmission systems practically measurable, coherent transmission system research focuses on the upper bound performance of a transmission system. In addition, this upper bound provides a means for the various transmission systems to be comparable to a point of reference and to each other. This upper bound

performance limit is the forward error correcting (FEC) limit, which represents the BER threshold from which error correcting algorithms can achieve error-free transmission. Error-free transmission is generally seen as an output BER $<10^{-16}$. The FEC limit depends on the amount of error correcting overhead used, and the type of error correction scheme employed [145]. Hence, two BERs are to be considered, pre-FEC and post-FEC. This work focuses on pre-FEC BERs, or uncoded BERs, as error correction schemes are considered to be outside the scope of this thesis [146]. In this work, two error FEC limits are of interest: the 6.69% overhead hard-decision (HD) FEC limit [145], and the 20% overhead soft-decision (SD) FEC limit [147]. HD-FEC is based on interleaved blocks which are Reed-Solomon (RS) encoded using RS(255,239), and the FEC-limit for post-FEC error-free transmission corresponds to a BER of 3.8×10^{-3} . [145] SD-FEC employs Low-Density Parity-Check (LDPC) LDPC(9216,7936) as inner FEC and RS(992,956) as outer FEC [147]. The corresponding theoretical BER is 2.4×10^{-2} for post-FEC error-free transmission. Understanding that laboratory systems require a capture window, Fig. 5.6 depicts the functional difference between the conventional and the TDM-SDM schemes. Conventionally, each spatial LP mode is received by one dual polarization coherent receiver and corresponding four port oscilloscope. The TDM-SDM scheme only uses one dual polarization coherent receiver and corresponding four port oscilloscope, whilst being able to acquire multiple spatial LP modes. Note that, as the largest financial investment for a laboratory setup are real-time oscilloscopes, the primary contribution of the TDM-SDM scheme is the significant cost-effective scaling it provides with respect to the conventional MIMO receiver method. In [r33], the TDM-SDM was successfully demonstrated for a three spatial LP mode transmission system, whilst only using two dual polarization coherent receivers and corresponding four port oscilloscopes. Hence, two spatial LP modes are received by a single DP coherent receiver. This setup demonstrates that the TDM-SDM scheme can additionally incorporate the orthogonal spatial dimension

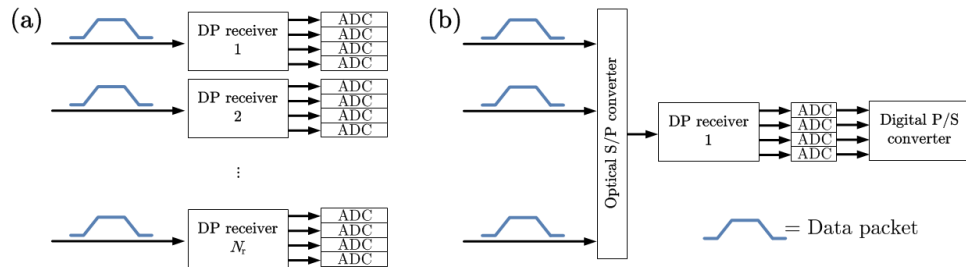


Fig. 5.6 Schematic overview of the (a) conventional spatial multiplexing receiver, and (b) the TDM-SDM.

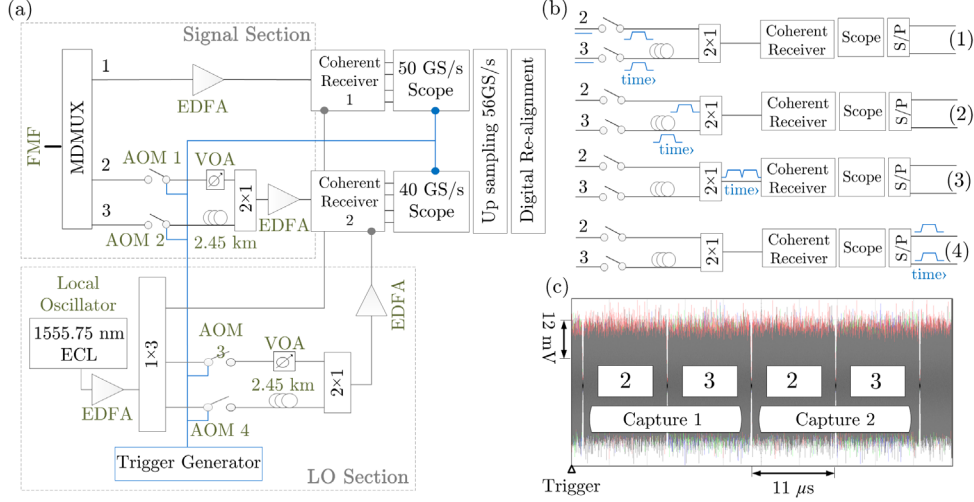


Fig. 5.7 (a) Experimental TDM-SDM receiver for the reception of 3 spatial LP modes.

(b) Schematic description of the data packet alignment in 4 steps. (c) Coherent receiver 2 oscilloscope image [r33].

for further increasing the DP spatial LP modes. For this particular demonstration, the employed TDM-SDM receiver is as depicted in Fig. 5.7(a). For optical MIMO systems, it is mandatory that the received modes are time aligned at the MIMO DSP input. Note that, at the MDMUX output, the signals are also aligned in time. In between these two points, the timing alignment can be freely re-arranged. By using optical delay lines shown in Fig. 5.7(a), and digital domain time re-aligning, both conditions can be satisfied. By employing the following four steps, depicted in Fig. 5.7(b), the number of required four port oscilloscopes can be reduced.

In step (1) each received input signal passes through a shutter or switch, where the (continuous) signal is allowed to pass at selected time slots. The shutters, or switches, open and close simultaneously to create a windowing function. A key requirement for candidate switches/shutters is to minimize the rise and fall times, as the capture window is in the order of μs . Micro-electromechanical systems (MEMS) and piezoelectric switches were initially considered. However, these cannot support the required high speed switching, which leaves only acoustic-optical modulator (AOM) and semiconductor optical amplifier (SOA) switches as potential solutions with a rise/fall time of <1 ns. The major drawback of SOA switches is the ASE noise addition. Hence in this work, low-insertion loss AOM switches are chosen. The AOMs are driven by a 27 MHz sinusoidal RF signal. Consequently, a 27 MHz frequency offset is added to the signal. It is mandatory that all signals experience the same frequency offset for MIMO processing to work. In step (2) one

input is delayed in time with respect to the other in the optical domain. An available fiber in the laboratory was a 2.45 km SMF, and is inserted in the third input path. The delay fiber latency is approximately 11 μ s. This delay equals the AOM open time and defines the capture window. In the second input path, a variable optical attenuator (VOA) is inserted to equal the SMF power loss. Note that the minimum delay fiber length depends on the target BER for error counting, and the maximum length is limited by the memory size of the oscilloscope. In step (3) both the separately received mixed inputs are combined by a 3 dB combiner. The time slotted signal is amplified, and received by coherent receiver 2. Amplifying after the combiner reduces the number of EDFAs required, as otherwise one EDFA per input is needed. Alternatively, amplification can be performed in the 3MF domain before going into the MIMO receiver. Note that the EDFA has to compensate the delay fiber, the power combiner, and the shutter losses. The captured data of input signals 2 and 3 form the input of coherent receiver 2. The respective oscilloscope image is shown in Fig. 5.7(c). Finally, in step (4), the time slotted signal is coherently received and digitized by the ADCs of the 4-port oscilloscope. In the digital domain, the signal is serial to parallel (S/P) converted per input signal block to parallelize the incoming serial data blocks in one time slot.

In Fig. 5.7(a), in the LO section, the previously described signal section is replicated. However, where LP modes are used as inputs in the signal section, one LO acts as source for all the inputs in the LO section. It is critical to match the LO phase such that all inputs beat with a similar LO phase, well within its coherence length. In the perfect case, all inputs have exactly the same LO phase. However, it is particularly difficult to achieve perfect phase matching when employing a 2.45 km SMF. To this end, the 2.45 km SMF delays in the signal and LO section were measured to be within 2 meters of each other using channel state estimation, described in section 2.3. Note that the AOMs in the LO section are also driven by a 27 MHz sinusoidal RF signal, which shifts the LO frequency by 27 MHz. Hence, the frequency offset of the LO with respect to the signal is cancelled.

5.3.2 Scaling the TDM-SDM MIMO receiver

The previous section detailed the function of the TDM-SDM. However, as emerging fiber designs allow the co-propagation of an increased number of spatial channels [74], it is important to understand how the MIMO receiver can be further scaled to continue achieving record throughput MIMO transmission systems. Fig. 5.8 depicts the required number of switches (in this work AOMs) as a scaling function of the number of received DP inputs. Note that there is a limit in reducing the number of required switches when increasing the number of coherent receivers. Large

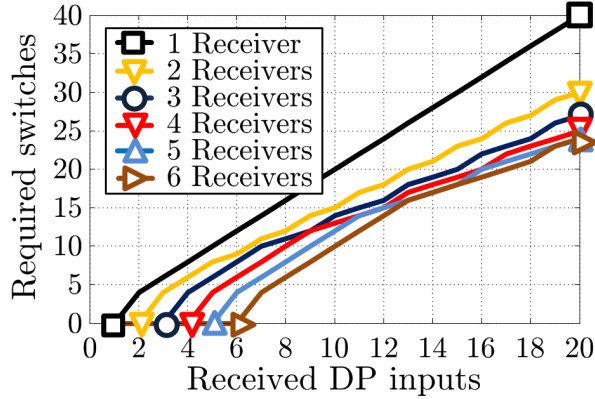


Fig. 5.8 Required AOMs (switches/shutters) for receiving a certain number of modes.

integrated switches exist, and may potentially offer a solution for future MIMO receiver laboratory systems, although these often have high insertion losses.

5.4 Optical front-end impairment compensation

When each real-valued analog received signal is digitized, a DC-offset may be present. For a QAM symbol, there are two real-valued signals, as shown in Fig. 2.6(a). As defined in section 2.1, the transmitted signal $s(t)$ is assumed to be zero-mean, with a variance σ_s^2 . Therefore, the mean value of a data block of $s(t)$ can be taken and subtracted from the signal. Thus, the DC-offset is removed.

However, after DC-offset removal, the IQ imbalance needs to be removed, as it results in a non-optimum IMRR. Performance degradation is caused by the offset angle between the inphase and quadrature components, and the gain imbalance between both branches. The angle offset mainly arises from incorrect optical path lengths in the 90° hybrid, and the gain imbalance mainly originates from the BPHD responsivity differences. Consequently, FE impairment compensation is required in the digital domain for each quadrature receiver separately. Techniques for IMRR reduction are based on non-data-aided signal processing. Such algorithms are Gram Schmidt orthonormalization [148, 149], Löwden orthonormalization [150], and blind moment compensation [151].

5.4.1 Gram-Schmidt orthonormalization

The first orthonormalization method described in this section is Gram-Schmidt orthonormalization. Contrary to the name, the orthonormalization method was earlier proposed by Laplace and Cauchy, but is credited to Jørgen Pedersen Gram

and Erhard Schmidt [152]. First, let the transmitted signal be

$$s_{\text{QAM}} = s_{\text{I}} + js_{\text{Q}}, \quad (5.16)$$

where the dependence on time has been omitted for simplicity. Now, let the received signal be $r = r_{\text{I}} + jr_{\text{Q}}$, where

$$\begin{aligned} r_{\text{I}} &= s_{\text{I}}\cos(\varphi_{\text{ERR}}) + s_{\text{Q}}\sin(\varphi_{\text{ERR}}), \\ r_{\text{Q}} &= s_{\text{I}}\sin(\varphi_{\text{ERR}}) + s_{\text{Q}}\cos(\varphi_{\text{ERR}}), \end{aligned} \quad (5.17)$$

where φ_{ERR} is the angle mismatch, as depicted in Fig. 5.9 [148]. The angle φ_{ERR} can be computed by performing the cross correlation of r_{I} and r_{Q} . The full cross correlation matrix is

$$\mathbf{C}_{\text{IQ}} = \begin{bmatrix} E\{r_{\text{I}}^2\} & E\{r_{\text{I}}r_{\text{Q}}\} \\ E\{r_{\text{I}}r_{\text{Q}}\} & E\{r_{\text{Q}}^2\} \end{bmatrix} = \begin{bmatrix} 1 & \sin(2\varphi_{\text{ERR}}) \\ \sin(2\varphi_{\text{ERR}}) & 1 \end{bmatrix}, \quad (5.18)$$

where unit variance on the diagonal of \mathbf{C}_{IQ} is assumed. Inevitably, the optimum accuracy Gram-Schmidt orthonormalization can achieve is tied to the crosstalk estimation accuracy. Note that both QAM components are assumed to be zero-mean and independent. In the perfect case, $\mathbf{C}_{\text{IQ}} = \mathbf{I}_2$, the 2×2 identity matrix. Since there are only 2 received signals per quadrature receiver, the Gram-Schmidt process is only a two-step process. Therefore, let the inphase component after Gram-Schmidt orthonormalization be

$$g_{\text{I}} = \frac{r_{\text{I}}}{|r_{\text{I}}|}. \quad (5.19)$$

The second step of the Gram-Schmidt process obtains the remaining component as

$$\bar{g}_{\text{Q}} = r_{\text{Q}} - \sin(2\varphi_{\text{ERR}})r_{\text{I}}, \quad (5.20)$$

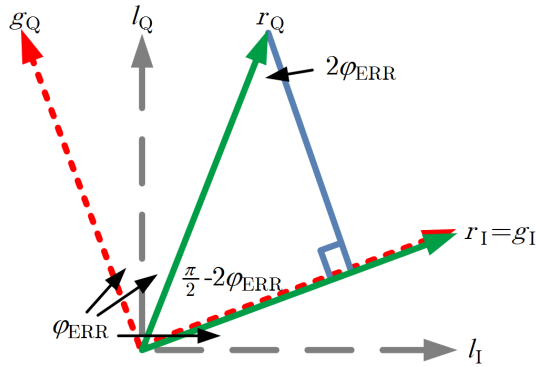


Fig. 5.9 Gram-Schmidt (red short dashed) and Löwdin orthonormalization (grey long dashed) of the received signal r (solid green) [148].

where the second term on the right hand side is the projection of r_Q onto r_I . After normalization of \bar{g}_Q , the orthonormalized quadrature output is obtained using the Pythagorean theorem as

$$g_Q = \frac{\bar{g}_Q}{\cos(2\varphi_{\text{ERR}})}. \quad (5.21)$$

Therefore the Gram-Schmidt matrix multiplication can be described as

$$\begin{bmatrix} g_I \\ g_Q \end{bmatrix} = \begin{bmatrix} 1 & 0 \\ -\tan(2\varphi_{\text{ERR}}) & \sec(2\varphi_{\text{ERR}}) \end{bmatrix} \begin{bmatrix} r_I \\ r_Q \end{bmatrix}. \quad (5.22)$$

5.4.2 Löwdin orthonormalization

The Gram-Schmidt orthonormalization increases the quantization noise impact for the rotated branch [149, 153]. As higher order constellations are more prone to quantization noise distortions, Löwdin orthonormalization is introduced. Löwdin orthonormalization has been discovered by a Swedish chemist, Per-Olov Löwdin, to symmetrically orthogonalize hybrid electron orbitals [154]. Löwdin orthonormalization has the advantage that both the inphase and quadrature components are equally rotated as shown in Fig. 5.9, and thus the quantization impact is balanced between both branches. The optimal Löwdin transformation matrix is [150, 155]

$$\mathbf{L} = \mathbf{C}_{\text{IQ}}^{1/2}, \quad (5.23)$$

and has the relation to the singular value decomposition as [51]

$$\mathbf{L} = \mathbf{U}\mathbf{V}^T. \quad (5.24)$$

The rotation matrices \mathbf{U} and \mathbf{V} have been defined in section 2.4. The Löwdin transformation matrix \mathbf{L} is given as [155]

$$\mathbf{L} = \begin{bmatrix} \frac{\cos(\varphi_{\text{ERR}})}{\cos(2\varphi_{\text{ERR}})} & -\frac{\tan(2\varphi_{\text{ERR}})}{2\cos(\varphi_{\text{ERR}})} \\ -\frac{\tan(2\varphi_{\text{ERR}})}{2\cos(\varphi_{\text{ERR}})} & \frac{\cos(\varphi_{\text{ERR}})}{\cos(2\varphi_{\text{ERR}})} \end{bmatrix}, \quad (5.25)$$

which results in the Löwdin matrix multiplication description

$$\begin{bmatrix} l_I \\ l_Q \end{bmatrix} = \mathbf{L} \begin{bmatrix} r_I \\ r_Q \end{bmatrix}. \quad (5.26)$$

5.4.3 Blind moment estimation

The previous two methods focused on estimating φ_{ERR} , and separately perform the normalization operation. Blind moment estimation however, focuses on optimizing the combination of gains and phase offset simultaneously. By combining these two

effects, the IMRR can be fully optimized. In Eq. (5.15) the mismatched baseband signal was given. If the LO carrier is assumed to be equal to the signal carrier, Eq. (5.15) is simplified to [151]

$$r(t) = K_1 s(t) + K_2 s^*(t), \quad (5.27)$$

where the receiver FE image rejection ratio is [151]

$$\text{IMRR}_{\text{FE}} = \frac{|K_1|^2}{|K_2|^2}, \quad (5.28)$$

and the corresponding IMRR_{FE} in dB is $\text{IMRR}_{\text{FE,dB}} = 10\log_{10}(\text{IMRR}_{\text{FE}})$. To approximate the original transmitted signal,

$$\hat{s}(t) = w_1 r(t) + w_2 r^*(t) \quad (5.29)$$

is introduced. The variables w_1 and w_2 are weight coefficients, which are multiplied by the received signal to approximate the received signal. Note that the goal of the weights is to suppress the complex conjugate term. Therefore, $w_1 K_2 + w_2 K_1^* = 0$ has to be satisfied. Alternatively, this equates to

$$\frac{w_1}{w_2} = -\frac{K_1^*}{K_2}. \quad (5.30)$$

As only the complex conjugate term has to be suppressed, Eq. (5.29) can actually be simplified to

$$\hat{s}(t) = r(t) + w_{\text{OPT}} r^*(t) \quad (5.31)$$

where w_{OPT} represents the optimum weight coefficient for suppressing $r^*(t)$ and is

$$w_{\text{OPT}} = \frac{w_2}{w_1} = -\frac{K_2}{K_1^*} = -\frac{K_1 K_2}{|K_1|^2}. \quad (5.32)$$

Finally, by substituting Eq. (5.32) in Eq. (5.31) the estimated transmitted signal becomes

$$\hat{s}(t) = r(t) - \frac{K_1 K_2}{|K_1|^2} r^*(t) = \left(K_1 - \frac{K_2 K_2^*}{K_1^*} \right) s(t) = \left(\frac{|K_1|^2 - |K_2|^2}{K_1^*} \right) s(t). \quad (5.33)$$

Eq. (5.32) indicates that the optimum weight coefficient results in the suppression of the conjugate term. Therefore, it is important to estimate the required optimum weight coefficient from the incoming signal. By introducing the autocorrelation function (ACF) with lag 0 [151]

$$C_{\text{ss}} = \sigma_s^2 \left(|K_1|^2 + |K_2|^2 \right), \quad (5.34)$$

and the complementary autocorrelation function (CACF)

$$\gamma_s = E \{s(t)^2\} = 2\sigma_s^2 K_1 K_2, \quad (5.35)$$

the values K_1 and K_2 do not need to be estimated directly, but instead the optimum weight coefficient can be directly computed as [151]

$$w_{\text{OPT}} = -\frac{\gamma_s}{C_{\text{ss}} + (C_{\text{ss}}^2 - |\gamma_s|^2)^{1/2}}. \quad (5.36)$$

In theory, this estimator cancels the conjugate term completely. Therefore, the IMRR is in theory infinite. However, in practice it is limited by the effect of sample estimates [151]. Theoretically, this method is the best performing algorithm in this section, and is widely used in wireless transmission systems. However, it was noted in [148] that the other two algorithms suffice for optical transmission systems, and therefore are interesting for implementation. Blind moment estimation has been chosen to be used in the experimental work demonstrated in Chapter 8, as in theory the best performance is achieved. During the experiments, an IMRR lower than -35 dB was noticed per quadrature receiver after compensation, which indicates a good balance between both quadrature components.

5.5 Digital interpolation filters

Interpolation filters are a particularly important filter type, and provide two-fold functionality. Firstly, they allow the compensation of the arrival time differences, or skew, between multiple real-valued inputs, and therefore align them in time. This particular type of functionality is achieved through resampling, where only the sampling time is altered, and the sampling frequency is kept constant. The second functionality of interpolation filters is an adaptive rate converter [156-158]. Here, the sampling rate is changed, and the output sampling rate is generally chosen as two times the transmission signal's baud rate. The term which describes this two-fold functionality as interpolation was first used by G. Ascheid et al. [159]. Two-fold oversampling allows for the $T_{\text{sym}}/2$ (Nyquist rate) fractionally spaced MIMO equalizer implementation, which is further detailed in Chapter 6. To this end, in section 5.5.1 the interpolation filter design considerations are given. Note that a perfect sampling frequency results in perfect timing alignment between both the transmitter and receiver, and a sampling frequency offset results in a timing mismatch. In reality, it is impossible to obtain a perfect sampling frequency. Therefore, timing recovery is key, which minimizes the frequency offset, and is detailed in section 5.5.2.

5.5.1 Interpolation filter design

As analog received signals are digitized, recall the digitized received signal from Eq. (2.3) and the transmission channel description in Eq. (2.5). This results in a received signal $r[k] = r(kT_s)$, where T_s is the receiver sampling rate. The primary task of the interpolation filter is to generate an interpolated signal $y[u] = y(uT_{\text{int}})$, where T_{int} represents the interpolation sample time. Mathematically, classical interpolation filters can be described by Lagrange polynomials, which can be efficiently implemented in offline-processing systems using Neville's method [160]. Such Lagrange polynomials use an even number of ordinates U for a polynomial of odd degree $U - 1$. Obviously, the simplest odd polynomial has a degree of one. This results in linear interpolation between two ordinates. The next polynomial order is a polynomial of order three, and offers cubic interpolation. The Lagrange coefficients for these two interpolation filters are given in [89] by M. Abramowitz and I.A. Stegun. Instead of using Lagrange polynomials, alternative polynomials can also be employed and do not necessarily have to satisfy the odd degree. In this case, the simplest interpolator is the piecewise-quadratic interpolator, and is of order two [161]. As ultimately these algorithms have to be implemented for a real-time system, any of the aforementioned three interpolation filters can be described as [156]

$$y(uT_{\text{int}}) = \sum_k r(kT_s) h_{\text{int}}(uT_{\text{int}} - kT_s). \quad (5.37)$$

Therefore, a filter h_{int} can be designed and employed as interpolation filter. Note that the sample time after the interpolation filter can be adaptively controlled to optimize the receiver performance. To obtain the FIR filter design, Eq. (5.37) can be rewritten in the form

$$y(uT_{\text{int}}) = y[(m_u + \mu_u)T_{\text{int}}] = \sum_{i=I_1}^{I_2} r[(m_u - i)T_s] h_{\text{int}}[(i + \mu_u)T_s]. \quad (5.38)$$

where

$$m_u = \left\lfloor \frac{uT_{\text{int}}}{T_s} \right\rfloor \quad (5.39)$$

is the starting ordinate index and $\lfloor \cdot \rfloor$ represents rounding down to the next integer. The variable

$$i = m_u - k \quad (5.40)$$

is the interpolation filter index, and

$$0 \leq \mu_u = \frac{uT_{\text{int}}}{T_s} - m_u \leq 1 \quad (5.41)$$

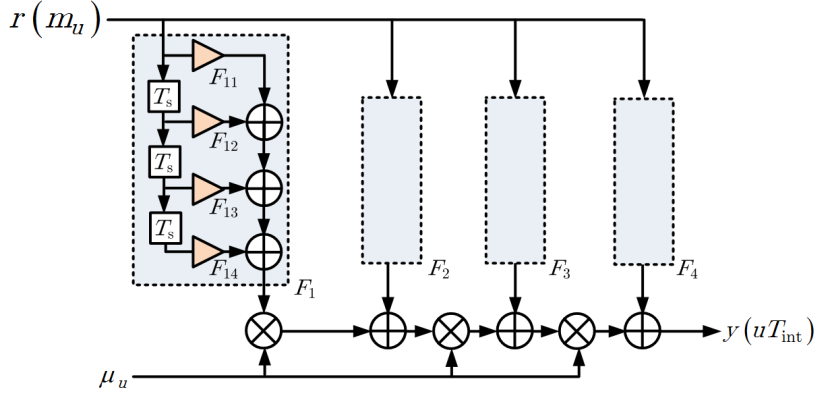


Fig. 5.10 Farrow interpolation filter consisting of 4 filter banks, each comprising 4 taps.

denotes the fractional interval. An alternative FIR filter, optimized for machine implementation, was proposed in 1988 by C.W. Farrow [162]. The Farrow FIR structure is depicted in Fig. 5.10, and is related to Eq. (5.38). It consists of a number of filter banks consisting of 4 taps each, where the Farrow coefficients are given in Table 5.1 and Table 5.2 for the cubic and piecewise-parabolic interpolator, respectively [161]. The linear interpolator is obtained by using the piecewise-parabolic interpolator with $\zeta = 0$.

Unfortunately, when using interpolation filters, a degree of approximation is imminent. This results in degradation of the received signal. [161] notes that the best performing interpolation filter is the piecewise-quadratic interpolator for digital communication systems, which is confirmed to be true for optical transmission systems in [163]. For both these works ζ is chosen as 0.5. Further performance improvement can be obtained by using $\zeta = 0.43$. However, this increases the interpolation filter implementation complexity for real-time systems.

	F_1	F_2	F_3	F_4
F_1	0	-1/6	0	1/6
F_2	0	1	1/2	-1/2
F_3	1	-1/2	-1	1/2
F_4	0	-1/3	1/2	-1/6

Table 5.1 Farrow coefficients for cubic interpolation.

	F_1	F_2	F_3	F_4
F_1	0	$-\zeta$	ζ	0
F_2	0	$\zeta + 1$	$-\zeta$	0
F_3	1	$\zeta - 1$	$-\zeta$	0
F_4	0	$-\zeta$	ζ	0

Table 5.2 Farrow coefficients for piecewise-parabolic interpolation.

5.5.2 Timing recovery

In any digital communications receiver timing recovery and synchronization is critical for optimal reception of the transmitted signal. As the transmitter sampling clock is different from the receiver sampling clock, a mismatch is inevitably present. Under the LTI assumption, the transmission channel $h(t)$ remains the same during a data packet block. However, a clock mismatch results in $h(t)$ linearly shifting in time, as shown in Fig. 5.11 for a simulated channel with a negative frequency offset, i.e. the LO frequency is lower than the transmitter frequency. From Fig. 5.11 can be observed that the impulse response shape of the channel remains very similar. In section 2.1 the impulse response was considered to be a FIR filter. However, in case of a linear time shift, the actual impulse response may shift outside the FIR filter region. In this case, the impulse response can no longer be digitally equalized. When $h(t)$ remains within the equalizer FIR window, the linear time shift can be adaptively tracked. However, this impairment results in an increased error floor as tracking capabilities have to be traded for BER performance. These considerations are further detailed in Chapter 6. To this end, in optical single carrier transmission systems using SMFs, low-complexity timing recovery algorithms are usually implemented [164]. Well-known time domain time recovery algorithms are the early-late algorithm or and the Gardner algorithm [165, 166]. A well-known frequency domain algorithm for timing estimation and recovery is the digital square timing recovery algorithm [167]. However, all these algorithms assume that a pulse shape is present and the original transmitter sampling clock can be recovered. In a single transmission channel, only ISI results in loss of the pulse shape. In a MIMO transmission channel however, both mode channel mixing and ISI can result in loss of a pulse shape. Especially in the case of full mixing,

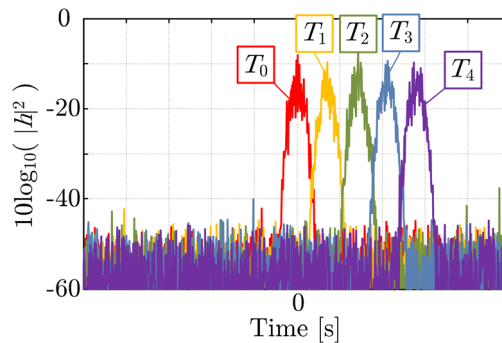


Fig. 5.11 LS estimated channel state information at T_0, \dots, T_5 , where the interpolated sampling frequency has a negative offset (too low).

obtaining a pulse shape, or a strong frequency domain peak at the carrier becomes difficult. Therefore, these algorithms no longer work as intended, and can potentially degrade the receiver performance, rather than improve it. Unfortunately, the issue of timing and synchronization becomes increasingly important for unraveling the mixed transmitted channels as the number of channels increases due to an increased amount of weight taps in the MIMO equalizer. Fortunately, the transmission channel linearly shifts in time and therefore this known effect can be exploited. Where the transmitted channel contains training sequences, a benefit of using training sequences is that the transmission matrix \mathbf{H} can be determined, as detailed in section 2.3. For minimizing the timing recovery complexity, only a single element of \mathbf{H} can be considered. An increased number of elements can be taken into account to increase the accuracy through averaging. However, this is at the detriment of computational complexity. Now, two cases can be made. Case 1: the training sequences are in the header and trailer of the data packets. Case 2: the training sequences are only in the header of the data packets. In the latter case, two consecutive packet headers can be considered, and in both cases, one or multiple elements of \mathbf{H} are estimated. For simplicity assume only element H_{11} . In the perfect LTI transmission system case, $H_{11}(T_1) = H_{11}(T_2)$, where T_1 and T_2 denote the time instances of two consecutive channel estimations. When a linear shift is present, the time shift $T_{\text{shift}} = T_{\text{measured}} - T_2$ can be estimated using the autocorrelation function between both transmission channel response estimations. From this, the correct sampling frequency f_{correct} can be determined from the current sampling rate f_{current} as

$$f_{\text{correct}} = \left(1 + \frac{T_{\text{shift}}}{T_2 - T_1} \right) f_{\text{current}}. \quad (5.42)$$

In the experimental work in Chapter 8, this method was applied where T_1 and T_2 represent the start and end of an oscilloscope capture, respectively, for optimum time synchronization performance. Using the transmission matrix for estimating the sampling offset is denoted as performance monitoring. Note that the electrical sampling mismatch originates from the difference between the transmitter and receiver electrical sampling frequency.

In the transmission case where there are no training sequences present, but blind equalization is performed, the MIMO equalizer weight matrix \mathbf{W} can be exploited. In section 2.3, it is established that there is a strong relation between the transmission matrix \mathbf{H} and the weight matrix \mathbf{W} . Therefore, the exact same aforementioned methodology based on training sequences can be applied. However, instead of \mathbf{H} , the weight matrix \mathbf{W} is used. Further details on the weight matrix \mathbf{W} are given in Chapter 6.

5.6 Group velocity dispersion compensation

GVD is inherent to optical fiber transmission, and its origin has been detailed in section 3.6.3. Additionally, in section 3.6.3 it was noted that GVD is an all-pass filter. Consequently, GVD compensation can be performed at the transmitter or receiver, and the transmitted signal is not degraded by GVD during transmission. However, when the GVD is not compensated, the impulse response becomes lengthy. Note that, in section 3.6.3 it was also noted that the GVD is slightly different for each transmitted LP mode. Therefore, due to mode mixing, residual GVD is inevitably present, even after removing the bulk of the GVD from one mode. This residual GVD is compensated in the MIMO equalizer. In the digital domain, GVD manifests itself as the linear transfer function all pass filter [168]

$$H_{\text{GVD}}(f) = \exp\left(-\frac{jDf^2\lambda_0^2}{c_0}\right), \quad (5.43)$$

where D is the aggregate GVD after transmission in [ps nm⁻¹], and is directly related to Eq. (3.64). In Eq. (5.43) the GVD is assumed to be the same for all transmitted channels. Since LP modes have similar group velocities, and therefore the respective GVD is similar, this is a decent approximation. As all transmission channels undergo the same GVD, GVD can be denoted as a common-mode channel impairment [169]. The GVD originates from the optical fiber refractive index profile design, and therefore it can be considered a static all pass filter [148]. Consequently, GVD can be equalized using a static equalizer. For completeness, first GVD estimation is described, before the final filter is detailed.

5.6.1 GVD estimation

As the GVD can be considered a common-mode impairment, GVD estimation can be applied to a single channel. After estimation, GVD compensation is performed on all DP received signals. Let the digitized complex-valued received signal $r[k]$ be a DP signal, and the corresponding frequency domain transferred signal $r_i[n]$, where i represents the block number. A single block can be used for estimating D . However, for increasing accuracy, the average over multiple frequency domain blocks can be taken. As D can be considered static, a best search window can be generated. Accordingly, in the frequency domain the $r_i[n]$ is element-wise multiplied by [168]

$$\psi_m[n] = \exp\left(-\frac{jD_m n^2 \pi \lambda_0^2}{T_s^2 N_{\text{DFT}}^2 c_0}\right), \quad (5.44)$$

where T_s is the sampling rate, and N_{DFT} the used DFT size to convert the received time domain signal $r[k]$ to the frequency domain. The GVD D under test

$D_m = \{D_{\min}, D_{\min} + \Delta D, D_{\min} + 2\Delta D, \dots, D_{\max}\}$, where the best search step size ΔD is the resolution between the minimum and maximum GVD under investigation. The resulting signal is

$$r_{i,m}[n] = r_i[n] \psi_m[n]. \quad (5.45)$$

Subsequently, the ACF is computed in the frequency domain as

$$C_{rr,i,m}[\Omega] = \sum_f r_{i,m}[n] r_{i,m}^*[n + \Omega], \quad (5.46)$$

where the shift parameter is Ω and the frequency domain samples are represented by f . The transmitted signal clock-tone is located at

$$\Omega_{CT} = \pm N_{DFT} \left(1 - \frac{R}{R_s}\right), \quad (5.47)$$

where R_s is the symbol rate. From Eq. (5.46), two GVD cost functions can be defined as [168]

$$J_{\min}[m] = \sum_i \sum_{\Omega \neq \Omega_{CT}} |C_{rr,i,m}[\Omega]|, \quad (5.48)$$

and

$$J_{\max}[m] = \sum_i |C_{rr,i,m}[\Omega_{CT}]|. \quad (5.49)$$

Clearly, Eq. (5.49) is less computationally complex than Eq. (5.48). Therefore, J_{\max} is used in the experiments in section 8.1 for estimating the joint GVD, and

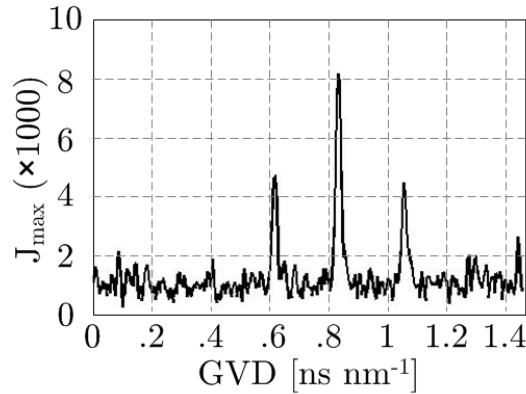


Fig. 5.12 J_{\max} of the LP_{01} mode in a 3 spatial LP mode 41.7 km transmission system, described in section 8.1.1. The main peak corresponds to the estimated GVD. It is unknown where the other two originate from. This effect is also noticeable in SSMF transmission, but not in simulations.

can be used without any boundary conditions as the interpolation filter output is a two-fold oversampled signal. The resulting J_{\max} is shown in Fig. 5.12. The peak around 820 ps nm^{-1} corresponds to the predicted GVD. It is at this time unknown where the other two side peaks originate from. It is not an effect of 3MF transmission, as this effect is also observed in SSMF transmission. It is noteworthy that due to the GVD differences, the estimation algorithm may fail for long lengths of 3MF transmission. This was not noticed for the short transmission distance discussed in Chapter 8. An alternative algorithm for estimating D is based on time domain best search estimation [170]. However, the frequency domain method has a lower computational complexity, and is therefore preferred.

5.6.2 GVD compensation

The aggregate GVD has been estimated in the previous section. The resulting D is applied to all received quadrature inputs separately to compensate the filter function in Eq. (5.43). To this end, the compensation filter is

$$W_{\text{GVD}}(f) = H_{\text{GVD}}^{-1}(f) = \exp\left(\frac{jDf^2\lambda_0^2}{c_0}\right), \quad (5.50)$$

which results in $W_{\text{GVD}}(f)H_{\text{GVD}}(f) = 1$, in the case of perfect GVD estimation. The filter length requirement increases with the square of the baud rate [171], which results in the proposal of implementing sub-band equalization to reduce power dissipation [172].

5.7 Summary

This chapter provided details on the MIMO receiver front-end, which comprises the optical and digital domain. The optical domain of the MIMO receiver consists of a number of optical quadrature receivers, where one optical quadrature receiver is used per transmitted polarization signal. For a large experimental MIMO transmission system, this results in requiring an equal amount of optical quadrature receivers. To this end, the primary contribution in this chapter is the novel TDM-SDM MIMO receiver. This TDM-SDM structure allows for receiving spatial channels in the time domain, and hence a reduced number of optical quadrature receivers and ADCs are required, which results in a cost-effective method of scaling the number of received channels. In the digital domain, the time domain channels are parallelized to form the equivalent spatial domain channels for further processing, which are also found in a SMF transmission system. First, DSP optical FE impairments per optical quadrature receiver are compensated, followed by adaptive rate interpolation. The adaptive rate interpolation filter allows for synchronizing the transmitter and receiver sampling rates. Finally, the GVD is

estimated and compensated by a frequency domain filter. The output of this filter provides the input of the MIMO equalizer, which is further detailed in the next chapter.

Chapter 6

MIMO equalization

*Signal processing: where
physics and mathematics meet*

Simon Haykin

In Chapter 5, subsequently, the received signals were IQ-balanced, two-fold oversampled, and the bulk of the GVD is removed. After FE compensation, these signals form the input of the MIMO equalizer as shown in Fig. 6.1. MIMO equalization is further detailed in this chapter⁴. Modern MIMO equalizers, such as the MMSE time domain equalizer commonly employed for optical single-mode transmission systems evolved from the zero-forcing equalizer (ZF) equalizer. Therefore, ZF equalization is the basis of all MIMO equalizers, and is described in section 6.1. Then, the minimum mean square error time domain equalizer is detailed in section 6.2. The update of the TDE weight matrix is based on the steepest gradient descent algorithm, where three updating algorithms are detailed in particular: the least mean squares algorithm, the decision-directed least squares algorithm, and the constant modulus algorithm. Additionally, the MMSE TDE boundary conditions for convergence are analyzed in section 6.2.2. This chapter addresses the reduction of computational complexity in a number of key algorithms; firstly, the computational complexity can be reduced for the TDE by using only active tap weights of the weight matrix, creating a segmented MIMO equalizer. Segmentation can be performed in either crosstalk elements, or time domain elements, as further discussed in section 6.2.6. Secondly, the proposed use of a varying adaptation gain is employed primarily to reduce the convergence time. At the cost of a minor added computational complexity, the convergence time was significantly reduced as detailed in section 6.2.7.

To further address computational complexity reduction, an MMSE FDE is introduced in section 6.3, which performs block convolutions in the frequency domain. The updating algorithm and convergence properties are detailed in

⁴ This chapter incorporates results from the author's contributions [r11], [r25], [r27], and [r35].

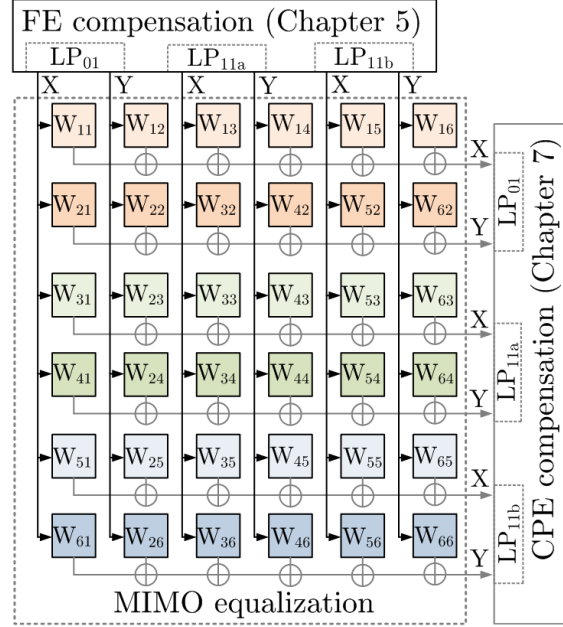


Fig. 6.1 Schematic overview for a 3 spatial LP mode MIMO equalizer, where the FE compensation outputs form the inputs. Either after MIMO equalization CPE is performed [44], or the CPE stage gives feedback to the MIMO equalizer.

sections 6.3.1 and 6.3.2, respectively. Additionally, the varying adaptation gain is implemented for the FDE, to reduce the convergence time in section 6.3.3. The used offline-processing implementation is detailed, which employs a peer-to-peer distributed network of servers to analyse and reduce the processing time for use of the digital signal processing for experimental transmission tests in Chapter 8. However, for SDM transmission systems to become a reality, the potential for hardware-implemented scaling of SDM transmitted channels needs to be investigated. This is started with a discussion on advanced equalization schemes to improve the BER performance in section 6.6.1. Then, in section 6.6.2, the performance of using bit-width reduced floating point operations for MIMO equalization is investigated. This alleviates the stringent implementation constraints for real-time high-speed signal processing in future optical receivers with respect to the commonly used offline-processed 64 bit floating point operations. The implication of bit-width reduction on accuracy is studied in this section. Finally, the scaling of SSMF DSP receivers to accommodate SDM is discussed.

6.1 Zero-forcing equalization

Although zero-forcing equalizers are not used in employed optical transmission systems, it was the earliest equalizer type in MIMO transmission [45]. Therefore, for historic reasons a brief description follows. The basis of the zero-forcing equalizer has been treated in section 2.3, where CSI estimation is used to approximate the transmission channel. Therefore, for this section, the CSI is assumed to be known through LS estimation, where training symbol based headers provide CSI. Fig. 6.2 shows the MIMO transmission packet structure, consisting of a header and payload data. Additionally, the header contains packet overhead. An LTI transmission is assumed, and thus \mathbf{H} is assumed to be constant during the packet transmission. Recall the MIMO transmission system from Eq. (2.10) as

$$\mathbf{R} = \mathbf{H}\mathbf{S} + \mathbf{N}.$$

During transmission, the transmitted signals are mixed according to the transmission matrix \mathbf{H} , and need to be unraveled at the receiver side. To unravel the mixed transmission channels, the received vector can be multiplied by a weight matrix \mathbf{W}_{zf} as

$$\bar{\mathbf{S}} = \mathbf{W}_{zf}\mathbf{R} = \mathbf{W}_{zf}(\mathbf{H}\mathbf{S} + \mathbf{N}), \quad (6.1)$$

where $\bar{\mathbf{S}}$ is the approximated transmission vector. If \mathbf{H} is invertible, a zero-forcing equalizer matrix \mathbf{W}_{zf} exists and can be employed, which is based on linear combinatorial nulling [45]. The weight matrix \mathbf{W}_{zf} is chosen such that any ISI and MIMO transmission channel interference is cancelled. Hence, each transmitted signal can be considered independently, and the remaining transmitted signals are considered to be interferers. This constraint indicates that

$$\mathbf{W}_{zf}\mathbf{H} = \mathbf{I}_{N_t}. \quad (6.2)$$

For nulling the interferers and ISI, a solution to Eq. (6.2) is the left Moore–

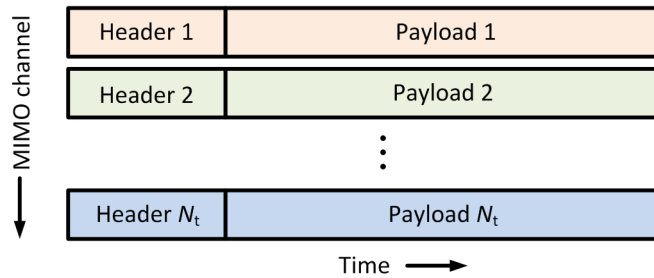


Fig. 6.2 V-BLAST based MIMO transmission, where each transmitted packet consists of a header and payload. In the header, training sequences can be embedded.

Penrose pseudo inverse, which results in

$$\mathbf{W}_{zf} = \mathbf{H}^\dagger = (\mathbf{H}^H \mathbf{H})^{-1} \mathbf{H}^H. \quad (6.3)$$

Initially, Eq. (6.3) was the most common equation used in wireless communications [38, 45], however it is not necessarily the only solution possible. In acoustic systems, often the multiple-input/output inverse theorem (MINT) is used [173]. Both methods provide a solution with similar performance. Previously, the assumption was made that \mathbf{H} has to be invertible, and hence the pseudo inverse exists. Substituting Eq. (6.3) in Eq. (6.1) for a single received signal yields

$$\bar{\mathbf{s}} = \mathbf{s} + \mathbf{W}_{zf} \mathbf{n} = \mathbf{s} + \mathbf{H}^\dagger \mathbf{n}. \quad (6.4)$$

Note that Eq. (6.4) is performed separately for all transmitted channels. From the same equation, it is clear that the noise vector is multiplied by the zero-forcing weight vector. This is the major drawback of using zero-forcing, particularly for transmission matrices with a high condition number, as denoted in Eq. (2.28). The output error after equalization of a single channel can be obtained as

$$\boldsymbol{\varepsilon} = \mathbf{s} - \bar{\mathbf{s}} = -\mathbf{W}_{zf} \mathbf{n} = -\mathbf{H}^\dagger \mathbf{n}. \quad (6.5)$$

Therefore, two cases during transmission can be considered. The first case is during header processing, where the transmission channel is estimated. The second case is payload processing. Here, no channel estimation is performed. However, it was highlighted in section 2.3.1 that the frequency offset between the transmitter laser and local oscillator needs to be estimated. Hence, the channel estimation needs to be performed over a window of possible frequency offsets from $f_{\text{off,min}}$ to $f_{\text{off,max}}$

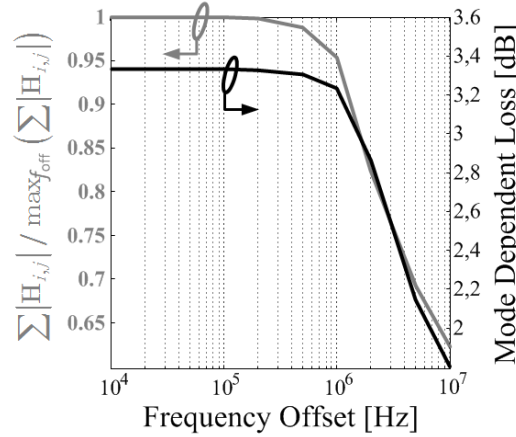


Fig. 6.3 Channel estimation absolute value and MDL of a 3 spatial LP mode 80 km transmission for various frequency offsets. The reference frequency is chosen as the frequency which maximizes the summation of the absolute value of \mathbf{H} [r25].

with a step size of Δf_{off} . The computational complexity increases linearly with the number of investigated frequency offsets. In section 2.3, it was indicated that frequency offset estimation can be performed by LS correlation [r25]. Fig. 6.3 depicts the LS channel estimation absolute value, note that the tolerable frequency offset for channel estimation is < 1 MHz, when a correlation length of 2^{13} is used. The frequency offset makes the zero-forcing equalizer particularly difficult to implement in optical transmission systems, as the transmission laser and LO frequencies vary in the range of 100 MHz on a sub-second time scale [170]. Therefore, a frequency offset window needs to be constantly investigated for correct channel estimation, resulting in an unnecessarily complex estimation block.

6.2 Time domain MMSE equalization

A more stable solution for optimizing the received output of the transmission channel is by employing a TDE, which is based on the MMSE. A weight matrix \mathbf{W}_{mmse} is heuristically updated using a deterministic iterative procedure by means of the cost function \mathbf{J} . In this section three cost function types are described:

- Least mean squares algorithm.
- Constant modulus algorithm.
- Decision-directed LMS (DD-LMS) algorithm.

which each are considered different algorithms. However, all are based on the steepest gradient descent (SGD) method. The SGD method is a one dimensional optimization algorithm for finding a local minimum of a cost function with a gradient descent. The cost function for the LMS algorithm is obtained through training symbols, and therefore LMS is considered to be a data-aided algorithm. The main advantage of LMS is that it converges to the global cost function minimum. The other two algorithms are not data-aided and hence are considered blind algorithms. CMA uses a constant modulus as basis for obtaining the cost function, and DD-LMS exploits the known transmitted constellation points to form a cost function. The downside of these two algorithms is that they converge to a local cost function minimum, which may not be the global minimum. However, the advantage is that no transmission channel training overhead is required. First, the MMSE performance is described, before updating algorithms are discussed. In theory, the optimum performance of all three MMSE algorithms discussed is equal.

Similarly to performing zero-forcing, first the received signal from Eq. (2.10) is multiplied by the weight matrix \mathbf{W}_{mmse} as [40]

$$\bar{\mathbf{S}} = \mathbf{W}_{\text{mmse}} \mathbf{R} = \mathbf{W}_{\text{mmse}} (\mathbf{H}\mathbf{S} + \mathbf{N}). \quad (6.6)$$

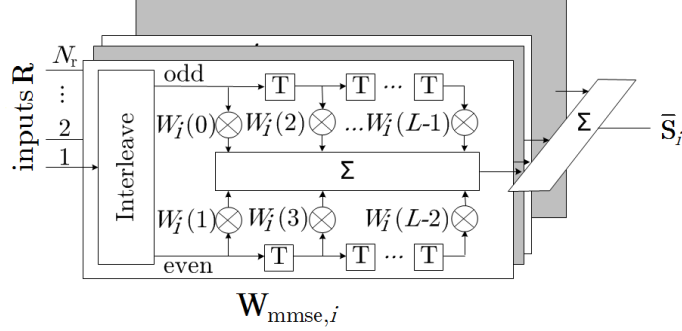


Fig. 6.4 Multiple input single output $\bar{\mathbf{S}}_i = \mathbf{W}_{\text{mmse},i} \mathbf{R}$ implementation.

Note that using a weight matrix \mathbf{W}_{mmse} fully decouples the respective outputs. Therefore, \mathbf{W}_{mmse} in Eq. (6.6) can be seen as N_t row multiplications $\mathbf{W}_{\text{mmse},i}$ of size $[1 \times N_r L]$. The multiplication structure for a single output is shown in Fig. 6.4, where a digital interleaver is used to separate the even and odd samples. This separation results in baud rate spaced multipliers, due to the 2-fold oversampled input obtained through adaptive rate conversion by interpolation, as described in section 5.5. Each multiplication internally consists of a butterfly structure as shown in Fig. 6.5. The outputs after multiplication are fed back through an error, which forms the basis of the cost function. The $[N_t \times 1]$ error vector is

$$\mathbf{e} = \mathbf{d} - \bar{\mathbf{S}} = \mathbf{d} - \mathbf{W}_{\text{mmse}} \mathbf{r}, \tag{6.7}$$

where the vector \mathbf{d} is the $[N_t \times 1]$ desired signal vector. Remember that a correlation matrix between the signal vectors \mathbf{x} and \mathbf{y} is defined as

$$\mathbf{C}_{xy} = E \{ \mathbf{x} \mathbf{y}^H \}, \tag{6.8}$$

and the cost function is the trace of \mathbf{C}_{ee} , which can be readily obtained by

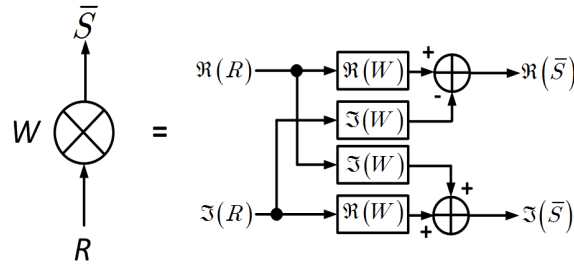


Fig. 6.5 Butterfly structure for each multiplication in Fig. 6.4.

substituting Eq. (6.7) and Eq. (6.6) in Eq. (6.8), which results in [42]

$$\begin{aligned} \mathbf{J}(\mathbf{W}_{\text{mmse}}) &= \text{tr}\left(E\{\mathbf{e}\mathbf{e}^H\}\right) \\ &= \text{tr}\left(E\{(\mathbf{d} - \mathbf{W}_{\text{mmse}}\mathbf{R})(\mathbf{d} - \mathbf{W}_{\text{mmse}}\mathbf{R})^H\}\right) \\ &= \text{tr}\left(\mathbf{C}_{\text{dd}} - \mathbf{C}_{\text{dr}}\mathbf{W}_{\text{mmse}}^H - \mathbf{W}_{\text{mmse}}\mathbf{C}_{\text{rd}} + \mathbf{W}\mathbf{C}_{\text{rr}}\mathbf{W}_{\text{mmse}}^H\right), \end{aligned} \quad (6.9)$$

where \mathbf{e} , \mathbf{r} , and \mathbf{d} still represent the error vector, received signal vector and the desired signal vector. Accordingly, the optimum weight matrix $\mathbf{W}_{\text{mmse,opt}}$ is the matrix which minimizes the cost function, and can be described as [40]

$$\mathbf{W}_{\text{mmse,opt}} = \min_{\mathbf{W}} \{\mathbf{J}(\mathbf{W}_{\text{mmse}})\}. \quad (6.10)$$

To find the \mathbf{W}_{mmse} that minimizes $\mathbf{J}(\mathbf{W}_{\text{mmse}})$, introduce a new matrix \mathbf{A} , which may be regarded as the square root of \mathbf{C}_{rr} as [38, 103]

$$\mathbf{C}_{\text{rr}} = \mathbf{U}^H \Lambda_{\text{rr}} \mathbf{U} = \mathbf{U}^H \Lambda_{\text{rr}}^{1/2} \Lambda_{\text{rr}}^{1/2} \mathbf{U} = (\Lambda_{\text{rr}}^{1/2} \mathbf{U})^H \Lambda_{\text{rr}}^{1/2} \mathbf{U} = \mathbf{A}^H \mathbf{A}. \quad (6.11)$$

In this case, the introduction of \mathbf{A} is allowed as \mathbf{C}_{rr} is symmetric and positive-semidefinite. Then, Eq. (6.9) can be rewritten to obtain the minimum error, where for simplicity, the subscript *mmse* is omitted, as [38]

$$\begin{aligned} \mathbf{J}(\mathbf{W}) &= \text{tr}\left(\mathbf{C}_{\text{dd}} - \mathbf{C}_{\text{dr}}\mathbf{W}^H - \mathbf{W}^H\mathbf{C}_{\text{rd}} + \mathbf{W}\mathbf{C}_{\text{rr}}\mathbf{W}^H\right) \\ &= \text{tr}\left[\mathbf{C}_{\text{dd}} - \mathbf{C}_{\text{dr}}\mathbf{A}^{-1}\mathbf{A}\mathbf{W}^H - \mathbf{W}\mathbf{A}^H(\mathbf{A}^H)^{-1}\mathbf{C}_{\text{rd}} + \mathbf{W}\mathbf{A}^H\mathbf{A}\mathbf{W}^H\right] \\ &= \text{tr}\left[\mathbf{C}_{\text{dd}} - \mathbf{C}_{\text{dr}}\mathbf{A}^{-1}(\mathbf{A}^H)^{-1}\mathbf{C}_{\text{rd}} + \mathbf{C}_{\text{dr}}\mathbf{A}^{-1}(\mathbf{A}^H)^{-1}\mathbf{C}_{\text{rd}}\right. \\ &\quad \left.- \mathbf{C}_{\text{dr}}\mathbf{A}^{-1}\mathbf{A}\mathbf{W}^H - \mathbf{W}\mathbf{A}^H(\mathbf{A}^H)^{-1}\mathbf{C}_{\text{rd}} + \mathbf{W}\mathbf{A}^H\mathbf{A}\mathbf{W}^H\right] \\ &= \text{tr}\left[\mathbf{C}_{\text{dd}} - \mathbf{C}_{\text{dr}}\mathbf{A}^{-1}(\mathbf{A}^H)^{-1}\mathbf{C}_{\text{rd}} + (\mathbf{W}\mathbf{A}^H - \mathbf{C}_{\text{dr}}\mathbf{A}^{-1})(\mathbf{W}\mathbf{A}^H - \mathbf{C}_{\text{dr}}\mathbf{A}^{-1})^H\right]. \end{aligned} \quad (6.12)$$

As the first term on the right hand side of Eq. (6.12) is independent of the weight matrix \mathbf{W}_{mmse} , the optimum weight matrix is obtained when

$$\mathbf{W}_{\text{mmse,opt}}\mathbf{A}^H - \mathbf{C}_{\text{dr}}\mathbf{A}^{-1} = 0. \quad (6.13)$$

Thus, the optimum weight matrix is

$$\mathbf{W}_{\text{mmse,opt}} = \mathbf{C}_{\text{dr}}\mathbf{A}^{-1}(\mathbf{A}^H)^{-1} = \mathbf{C}_{\text{dr}}\mathbf{C}_{\text{rr}}^{-1}, \quad (6.14)$$

which corresponds to the optimum Wiener solution. The MIMO transmission model detailed in section 2.2, the correlation matrices can be obtained as

$$\begin{aligned} \mathbf{C}_{\text{dr}} &= E\{\mathbf{d}\mathbf{r}^H\} = E\{\mathbf{S}(\mathbf{H}\mathbf{S} + \mathbf{N})^H\} = E\{\mathbf{S}\mathbf{S}^H\}\mathbf{H}^H + E\{\mathbf{S}\mathbf{N}^H\} \\ &= \sigma_s^2\mathbf{H}^H, \end{aligned} \quad (6.15)$$

and

$$\begin{aligned}
\mathbf{C}_{\text{rr}} &= E \{ \mathbf{r} \mathbf{r}^{\text{H}} \} = E \{ (\mathbf{H} \mathbf{S} + \mathbf{N})(\mathbf{H} \mathbf{S} + \mathbf{N})^{\text{H}} \} \\
&= E \{ (\mathbf{H} \mathbf{S} + \mathbf{N})(\mathbf{S}^{\text{H}} \mathbf{H}^{\text{H}} + \mathbf{N}^{\text{H}}) \} \\
&= \mathbf{H} E \{ \mathbf{S} \mathbf{S}^{\text{H}} \} \mathbf{H}^{\text{H}} + \mathbf{H} E \{ \mathbf{S} \mathbf{N}^{\text{H}} \} + E \{ \mathbf{N} \mathbf{S}^{\text{H}} \} \mathbf{H}^{\text{H}} + E \{ \mathbf{N} \mathbf{N}^{\text{H}} \} \\
&= \mathbf{H} \sigma_s^2 \mathbf{H}^{\text{H}} + \sigma_n^2 \mathbf{I}_{N_r}.
\end{aligned} \tag{6.16}$$

Substituting Eq. (6.15) and Eq. (6.16) in Eq. (6.14) yields

$$\begin{aligned}
\mathbf{W}_{\text{mmse,opt}} &= \mathbf{C}_{\text{dr}} \mathbf{C}_{\text{rr}}^{-1} \\
&= \sigma_s^2 \mathbf{H}^{\text{H}} (\mathbf{H} \sigma_s^2 \mathbf{H}^{\text{H}} + \sigma_n^2 \mathbf{I}_{N_r})^{-1} \\
&= \mathbf{H}^{\text{H}} \left(\mathbf{H} \mathbf{H}^{\text{H}} + \frac{\sigma_n^2}{\sigma_s^2} \mathbf{I}_{N_r} \right)^{-1}.
\end{aligned} \tag{6.17}$$

In the case where the SNR becomes infinite, Eq. (6.17) equals the zero-forcing solution obtained in Eq. (6.3). This can be observed by rewriting Eq. (6.17) using the binomial inverse theorem as [38]

$$\begin{aligned}
\mathbf{W}_{\text{mmse,opt}} &= \sigma_s^2 \mathbf{H}^{\text{H}} (\mathbf{H} \sigma_s^2 \mathbf{H}^{\text{H}} + \sigma_n^2 \mathbf{I}_{N_r})^{-1} \\
&= \sigma_s^2 \mathbf{H}^{\text{H}} \sigma_n^{-2} - \sigma_s^2 \mathbf{H}^{\text{H}} \sigma_n^{-2} \mathbf{H} (\sigma_s^{-2} + \mathbf{H}^{\text{H}} \sigma_n^{-2} \mathbf{H})^{-1} \mathbf{H}^{\text{H}} \sigma_n^{-2} \\
&= \left[\sigma_s^2 (\sigma_s^{-2} + \mathbf{H}^{\text{H}} \sigma_n^{-2} \mathbf{H}) - \sigma_s^2 \mathbf{H}^{\text{H}} \sigma_n^{-2} \mathbf{H} \right] (\sigma_s^2 + \mathbf{H}^{\text{H}} \sigma_n^{-2} \mathbf{H}) \mathbf{H}^{\text{H}} \sigma_n^{-2} \\
&= (\sigma_s^{-2} \mathbf{I}_{N_r} + \mathbf{H}^{\text{H}} \sigma_n^{-2} \mathbf{H})^{-1} \mathbf{H}^{\text{H}} \sigma_n^{-2} \\
&= \left(\frac{\sigma_n^2}{\sigma_s^2} \mathbf{I}_{N_r} + \mathbf{H}^{\text{H}} \mathbf{H} \right)^{-1} \mathbf{H}^{\text{H}}.
\end{aligned} \tag{6.18}$$

6.2.1 The steepest gradient descent method

The SGD method is commonly used in digital equalizers because of its simplicity and is based on an extension of Cauchy's integral formula. Cauchy's integral formula tries to find the contour of steepest decent of an integral, in one dimension, to a simpler integral which can be analytically solved [174]. The optimum solution is given by the Wiener-Hopf equation [175], and in 1941 A. Kolgorov published the time-discrete equivalent of Wiener-Hopf equation [176]. This resulted in the development of many digital filters and adaptive algorithms, among which the SGD [177]. As previously introduced, an $N_t \times N_r$ transmission system can be seen as N_t single output systems with N_r receivers. To obtain the optimum MMSE weight matrix \mathbf{W} , where for convenience the subscript *mmse* has been omitted, the

deterministic iterative SGD optimization algorithm is introduced as [42]

$$\mathbf{W}(k+1) = \mathbf{W}(k) - \frac{\mu}{2} \nabla_{\mathbf{W}} \mathbf{J}[\mathbf{W}(k)]. \quad (6.19)$$

Here, μ is the adaptation gain, or step size, which is a real-valued positive constant. $\nabla_{\mathbf{W}}$ indicates the performance feedback in the form of the cost function gradient attributed to the change in the weight matrix, and k denotes the symbol sample index as only feedback can be provided on a symbol basis. Accordingly, the weight matrix is updated and optimized heuristically, and the time it takes to reach near optimum performance is the system convergence time. Clearly, the fixed adaptation gain in Eq. (6.19) has a large influence on the convergence time. By taking the derivative of Eq. (6.9), the cost function gradient reads [178]

$$\nabla_{\mathbf{W}} \mathbf{J}[\mathbf{W}(k)] = -2[\mathbf{C}_{\text{dr}}(k) - \mathbf{W}(k)\mathbf{C}_{\text{rr}}(k)], \quad (6.20)$$

and the SGD optimization algorithm in Eq. (6.19) then follows as

$$\mathbf{W}(k+1) = \mathbf{W}(k) - \mu[\mathbf{W}(k)\mathbf{C}_{\text{rr}}(k) - \mathbf{C}_{\text{dr}}(k)]. \quad (6.21)$$

Note that the weight matrix in Eq. (6.21) is written in the complex domain, but can contain real-valued numbers only. In Fig. 6.5, complex numbers were assumed as complex-valued QAM constellations are transmitted. However, it is possible to equalize the inphase and quadrature component separately, as two independent real-valued outputs. The primary benefit of using two independent real-valued outputs in this equalization structure is the capability of compensating residual IQ-imbalance and skew. However, in this particular case, the butterfly structure becomes more complex as four independent weights must be updated instead of two. The convolution stage remains the same in terms of computational complexity. Updating the real-valued or complex weight matrices can both be described by Eq. (6.21), and substituting the correlation matrices results in the updating algorithm as

$$\begin{aligned} \mathbf{W}(k+1) &= \mathbf{W}(k) - \mu[\mathbf{W}(k)\mathbf{r}(k)\mathbf{r}^{\text{H}}(k) - \mathbf{d}(k)\mathbf{r}^{\text{H}}(k)] \\ &= \mathbf{W}(k) - \mu[\mathbf{W}(k)\mathbf{r}(k) - \mathbf{d}(k)]\mathbf{r}^{\text{H}}(k) \\ &= \mathbf{W}(k) + \mu\mathbf{e}(k)\mathbf{r}^{\text{H}}(k). \end{aligned} \quad (6.22)$$

6.2.2 SGD convergence and stability

The heuristic steepest gradient descent update algorithm is given in Eq. (6.21). It is obvious that a convergence time is required before the optimum weight matrix is obtained. This has a clear relation to the adaptation gain μ , and in order to obtain boundary conditions for the adaptation gain value, introduce the weight

coefficient error $\Delta\mathbf{W}$ as [42]

$$\begin{aligned} \mathbf{W}(k+1) &= \mathbf{W}(k) - \mu[\mathbf{W}(k)\mathbf{C}_{\text{rr}}(k) - \mathbf{C}_{\text{dr}}(k)] \\ \mathbf{W}_{\text{mmse,opt}}(k) &= \mathbf{W}_{\text{mmse,opt}}(k) - \mu[\mathbf{W}_{\text{mmse,opt}}(k)\mathbf{C}_{\text{rr}}(k) - \mathbf{C}_{\text{dr}}(k)] - \\ \frac{\Delta\mathbf{W}(k+1)}{\Delta\mathbf{W}(k)} &= \frac{\Delta\mathbf{W}(k) - \mu\Delta\mathbf{W}\mathbf{C}_{\text{rr}}(k)}{\Delta\mathbf{W}(k)[\mathbf{I} - \mu\mathbf{C}_{\text{rr}}(k)]}. \end{aligned} \quad (6.23)$$

The recursion in Eq. (6.23) is stable if and only if the right hand term converges to 0, and hence $|\mathbf{I} - \mu\mathbf{C}_{\text{rr}}(k)| < 1$. Now, let $\mathbf{C}_{\text{rr}}(k) = \mathbf{U}\mathbf{\Lambda}\mathbf{U}^{\text{H}}$ using singular value decomposition. The index k has been omitted as an LTI transmission system is assumed and therefore the optimum remains constant. Then, introduce the parameter

$$\mathbf{v}(k+1) = \mathbf{v}(k)[\mathbf{I} - \mu\mathbf{\Lambda}], \quad (6.24)$$

where

$$\mathbf{v}(k) = \Delta\mathbf{W}(k)\mathbf{U}. \quad (6.25)$$

Finally, the stability can be determined by inspecting one row of \mathbf{v} , as each row is independent due to the diagonal matrices \mathbf{I} and $\mathbf{\Lambda}$ as

$$v_i(k+1) = v_i(k)(1 - \mu\lambda_i), \quad (6.26)$$

where λ_i is the i^{th} eigenvalue of $\mathbf{C}_{\text{rr}}(k)$, and $1 \leq i \leq N_{\text{t}}$. Therefore, the convergence boundary condition is expressed as

$$\begin{aligned} |1 - \mu\lambda_i| &< 1, \\ -1 > 1 - \mu\lambda_i &< 1, \\ 0 \leq \mu &< \frac{2}{\lambda_i}. \end{aligned} \quad (6.27)$$

From Eq. (6.27) it can be observed that the maximum eigenvalue results in the smallest boundary value, and therefore the maximum adaptation gain. If the chosen adaptation gain does not satisfy this condition, the resulting equalization is divergent. Additionally, the convergence time varies for each transmitted channel, and corresponds to the eigenvalue as can be observed in Eq. (6.26). An exponential envelope can be used to describe the convergence of the i^{th} channel as [179]

$$\text{iterations} = \exp\left(-|1 - \mu\lambda_i|^{-1}\right). \quad (6.28)$$

Fig. 6.6 shows the convergence characterization of a 3 spatial LP mode 80 km experimental transmission with various fixed adaptation gains. Note that there is a variation in both the convergence time and the minimum error. A large adaptation gain results in fast convergence with a high error floor, and a small adaptation gain results in slow convergence with a lower error floor. The minimum error is limited by the SNR, which provides a lower bound adaptation gain value which can be

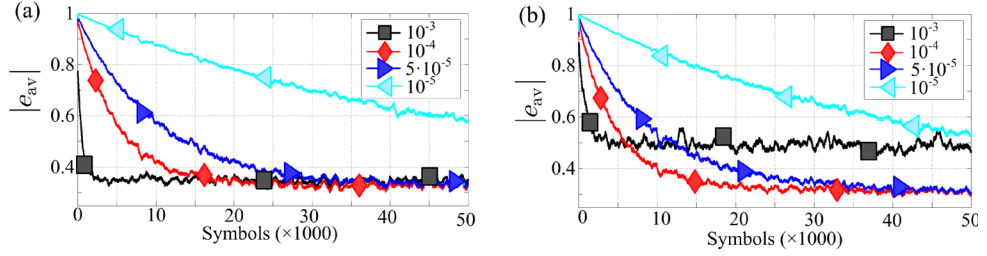


Fig. 6.6 Averaged error over time indicating convergence behavior for a 3 spatial LP mode optical transmission system (a) BTB, and (b) after 80 km.

experimentally obtained. Accordingly, the adaptation gain parameter is to be carefully considered. In addition, B. Widrow and E. Walach noted in [180] that the convergence time increases linearly with the transmitted number of channels.

6.2.3 Least mean squares algorithm

The LMS algorithm is based on the SGD algorithm, where the desired signal \mathbf{d} in Eq. (6.22) is a known transmitted sequence. This sequence is referred to as the training sequence, or learning sequence, and was first proposed in 1960 by B. Widrow and M.E. Hoff Jr. [179]. Accordingly, $\mathbf{d}(k) = \mathbf{s}(k)$ and the training sequence is independent of the constellation type. Also, \mathbf{d} is independent of receiver side symbol estimation, unlike the DD-LMS algorithm described in the next section. The usage of a known training sequence ensures convergence to the global minimum, and hence the weight matrix \mathbf{W} can be initialized arbitrarily. A prudent choice is the $\mathbf{0}$ matrix of size $[N_t \times N_r L]$, or in the case of real-valued outputs a $\mathbf{0}$ matrix of size $[2N_t \times N_r L]$. Note that L denotes the digitized 2-fold oversampled impulse response length.

In Chapter 5 it was noted that there is a frequency offset between the transmitter laser and local oscillator. However, the SGD updating algorithm only compensates linear mixing of channels without any frequency offset. Therefore, a CPE block is inserted in the feedback path of the updating algorithm, and Eq. (6.22) becomes

$$\mathbf{W}(k+1) = \mathbf{W}(k) - \mu \left\{ \bar{\mathbf{S}} \odot \Phi(k) - \mathbf{d}(k) \right\} \odot \Phi^{-1}(k) \mathbf{R}^H(k), \quad (6.29)$$

where $\Phi(k) = [\exp(-j\varphi_1), \dots, \exp(-j\varphi_{N_t})]^T$ is the estimated carrier phase of the current symbol vector of size $[N_t \times 1]$, and \odot is the element-wise multiplication. The phases φ_i are the output phases of the CPE stage described in Chapter 7. Hence, before estimating the symbol error, first the current phase is removed such that the MIMO equalizer only performs linear unraveling of the transmitted channels. The aforementioned formulae denoting the LMS algorithm are graphically shown in Fig. 6.7, for a single output. In the case of real-valued outputs,

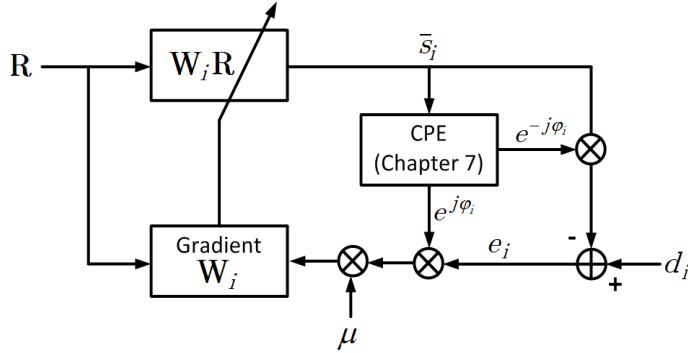


Fig. 6.7 LMS weight updating algorithm including CPE to remove the frequency offset between the transmitter laser and LO.

corresponding inphase and quadrature outputs are combined to form one complex valued CPE input. CPE implementations are further detailed in Chapter 7. Note that Eq. (6.22) can be reduced in computational complexity using an alternative LMS algorithm, the sign LMS algorithm. Using this low-complexity updating algorithm, Eq. (6.22) is altered to

$$\mathbf{W}(k+1) = \mathbf{W}(k) + \mu \text{csign}[\mathbf{e}(k)] \text{csign}[\mathbf{R}^H(k)], \quad (6.30)$$

where csign is the element-wise complex signum function formed by two real-valued signum functions as

$$\text{csign}[\mathbf{a}] = \text{sign}[\Re(\mathbf{a})] + \text{sign}[\Im(\mathbf{a})]. \quad (6.31)$$

The computational complexity reduction advantage comes at the cost of an increased convergence time, which results in reduced tracking capabilities.

6.2.4 Decision-directed least mean squares

The DD-LMS algorithm is closely related to the LMS algorithm, where the main difference is that instead of a known transmitted sequence, either a known transmitted sequence or constellation is used, and hence these two cases can be distinguished. Prerequisite to DD-LMS equalization is a low symbol error rate, and hence, the weight matrix \mathbf{W} has to be initialized close to optimum performance. This results in the DD-LMS algorithm generally being used for optimizing the weight matrix \mathbf{W} during payload transmission, and the weight matrix is initialized by the LMS algorithm to find the global cost function minimum.

As the received signal can have a high error rate, a FEC decoder can be used to minimize the errors. The output of the FEC decoder can be fed back as the desired

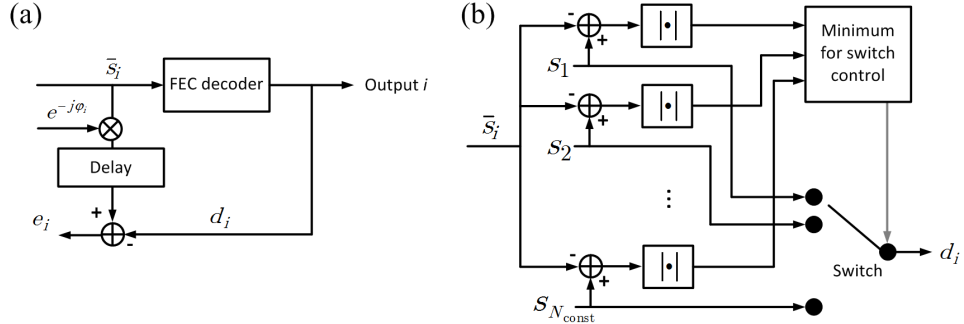


Fig. 6.8 DD-LMS feedback loop employing (a) a FEC decoder, or (b) 2D or 4D maximum likelihood symbols.

signal \mathbf{d} , shown in Fig. 6.8(a). However, FEC decoding is performed on a data block, resulting in the equalizer feedback heavily lagging behind on the actual transmission matrix, which results in performance degradation. Alternatively, a symbol can be directly estimated using a ML estimator. In this work, 2D and 4D symbols have been transmitted. Therefore, the ML estimator delay is substantially smaller than when using a FEC decoder. However, this comes at the costs of a higher error rate, introducing updating errors of the weight matrix. Fig. 6.8(b) depicts the ML estimator which replaces the FEC decoder in Fig. 6.8(a), where N_{const} constellation points are considered in parallel, and the constellation point minimizing the distance between $\bar{s}_i(k)$ with itself is chosen. Note that a high order constellation results in heavy parallelization requirements.

6.2.5 Constant modulus algorithm

The most commonly used blind convergence algorithm is the CMA, which has been originally proposed by D.N. Godard in 1980 [181]. It exploits, as the name indicates, the constant modulus of the transmitted constellation. CMA is primarily designed for phase shift keying signals. However, for square higher order constellations, it can also be used directly [182], or a multi-ring CMA can be employed. The primary advantage over LMS is that no training sequence overhead is required, and hence, a higher throughput can be achieved with the same data rate. Additionally, unlike the DD-LMS algorithm, CMA can converge blindly without a low bit error requirement. These two reasons have resulted in CMA being the predominant MIMO equalization scheme for SSMF transmission systems. The weight matrix update algorithm is [181]

$$\mathbf{W}(k+1) = \mathbf{W}(k) + \mu \mathbf{e}_{\text{CMA},p}(k) \mathbf{R}^H(k), \quad (6.32)$$

where

$$\mathbf{e}_{\text{CMA},p}(k) = \frac{\bar{\mathbf{S}}(k)}{|\bar{\mathbf{S}}(k)|^{p-2}} \odot \left[\gamma_{\text{CMA},p} - |\bar{\mathbf{S}}(k)|^p \right], \quad (6.33)$$

and

$$\gamma_{\text{CMA},p} = \frac{E \left\{ |\bar{\mathbf{S}}(k)|^{2p} \right\}}{E \left\{ |\bar{\mathbf{S}}(k)|^p \right\}}. \quad (6.34)$$

For the reception of QAM constellations in SSMF transmission systems, p is generally chosen to be 2. Clearly, from Eq. (6.33) a second advantage of CMA can be observed with respect to the LMS algorithm: the phase rotation independence. Hence, CPE is performed independently of MIMO equalization, alleviating implementation timing constraints with respect to LMS equalization. However, Eq. (6.33) also indicates the main difficulty of CMA, which is convergence. All outputs can converge to the same transmitted source, as independent outputs are not guaranteed. To this end, many blind source separation algorithms are proposed in acoustic and wireless transmission systems [183]. Thereby, the convergence is dependent on the initialization of the weight matrix \mathbf{W} , and can converge to local optima instead of the global optimum. Theoretically, CMA can achieve the same BER performance as LMS. Due to the optical components currently emerging and in development, the LMS algorithm is the preferred methodology for transmission characterization in this work.

6.2.6 Segmented MIMO equalization

As the transmission matrix can be designed through optical MMUXs, and optical fibers, it is possible that not all MIMO equalizer elements are used. By only employing the interesting (non-zero) elements of \mathbf{W} , results in the MIMO equalizer becoming a segmented MIMO equalizer. Two MIMO segmentation cases exist, namely crosstalk and time segmentation.

For the first case, the crosstalk segmentation case, the transmission system matrix can be denoted as

$$\mathbf{H} = \begin{bmatrix} \mathbf{H}_{\text{LP01}} & \mathbf{0}_{2L \times 4} & \mathbf{0}_{2L \times 4} & \mathbf{0}_{2L \times 2} & \dots \\ \mathbf{0}_{4L \times 2} & \mathbf{H}_{\text{LP11}} & \mathbf{0}_{4L \times 4} & \mathbf{0}_{4L \times 2} & \dots \\ \mathbf{0}_{4L \times 2} & \mathbf{0}_{4L \times 4} & \mathbf{H}_{\text{LP21}} & \mathbf{0}_{4L \times 2} & \dots \\ \mathbf{0}_{2L \times 2} & \mathbf{0}_{4L \times 2} & \mathbf{0}_{4L \times 4} & \mathbf{H}_{\text{LP02}} & \dots \\ \dots & \dots & \dots & \dots & \dots \end{bmatrix}, \quad (6.35)$$

where \mathbf{H}_{LP01} and \mathbf{H}_{LP02} are the intra LP crosstalk transmission matrices of size $[2L \times 2]$. \mathbf{H}_{LP11} and \mathbf{H}_{LP21} are the intra LP crosstalk transmission matrices of size $[4L \times 4]$. These crosstalk matrices correspond to the spatial LP modes denoted in Table 3.1, where L denotes the optical fiber impulse response length. Instead of using LP modes in Eq. (6.35), it can also denote low-crosstalk multi-core transmission, where instead of the LP modes, intra core transmission matrices are placed on the diagonal entries of \mathbf{H} . Although this transmission system minimizes MIMO equalizer computation complexity, the transmission system does not exploit the full spatial diversity the optical fiber offers. Therefore, this case is not preferred for future long haul transmission systems, as MDL degrades the system performance.

Alternatively, to minimize the impact of MDL, full mixing is employed to exploit the spatial diversity. However, the fiber's DMD does not necessarily need to be fully compensated (section 3.4). This results in a transmission matrix

$$\mathbf{H} = \begin{bmatrix} \mathbf{h}_{11} & \mathbf{h}_{11} & \dots \\ \mathbf{h}_{21} & \mathbf{h}_{22} & \dots \\ \dots & \dots & \dots \end{bmatrix}, \quad (6.36)$$

where the elements of \mathbf{H} are $[L \times 1]$ vectors. Due to the optical fiber's DMD, only sections of the L length vectors are non-zero, as shown in Fig. 3.5, such that each element of \mathbf{H} can be defined as multiple short impulse responses as

$$\mathbf{h}_{ij} = [\mathbf{h}_{ij,a}, 0, \dots, 0, \mathbf{h}_{ij,b}, 0, \dots], \quad (6.37)$$

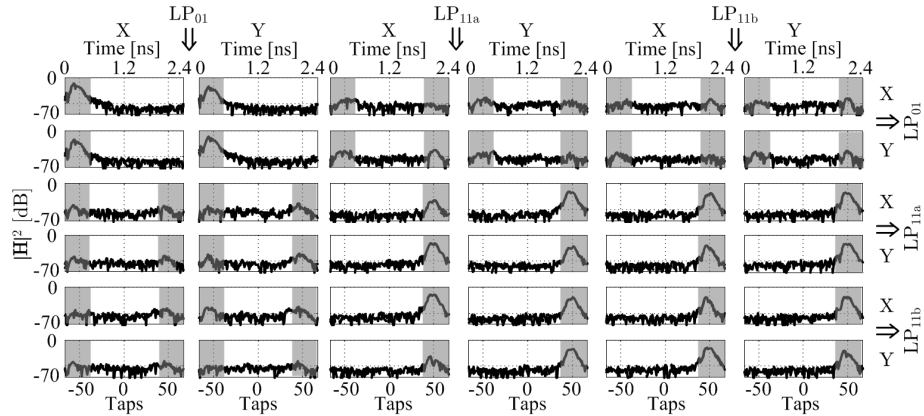


Fig. 6.9 Conventional MIMO equalizer with time segmentation (grey areas) for reducing the computational complexity.

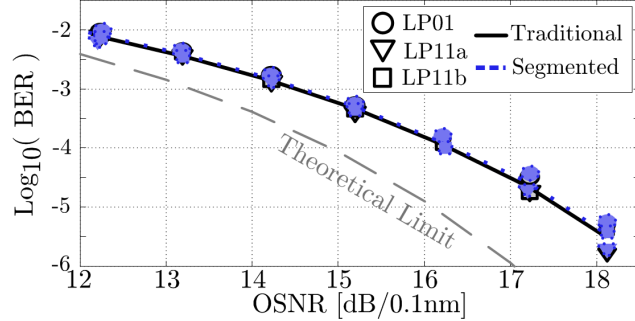


Fig. 6.10 BER performance comparison of the traditional MIMO equalizer with respect to the segmented MIMO equalizer.

which corresponds to a time-segmented MIMO equalizer. The time-segmented equalizer has been experimentally compared to the traditional MIMO equalizer using a 30 km 3 spatial LP mode optical transmission system [r19], in unpublished work. Fig. 6.9 shows the $6 \times 6L$ MIMO equalizer, where $L = 135$, and where the total number of complex multiplications, taps, equals $6 \times 6 \times 135 = 4860$. By time segmenting the MIMO equalizer (grey areas) as shown in Fig. 6.9, the total number of taps is reduced to $2 \times 2 \times 32 + 2 \times 4 \times 64 + 4 \times 2 \times 64 + 4 \times 4 \times 32 = 1280$ taps. Accordingly, the number of taps is reduced by 73.66 %. Fig. 6.10 shows the BER performance for the traditional MIMO equalizer and the time segmented equalizer. It can be observed from Fig. 6.10, that there is no OSNR penalty. Clearly, MIMO equalizer segmentation can be employed without performance loss with respect to the conventional MIMO equalizer, and reduce the MIMO equalizer's computational complexity. However, for long-haul transmission systems full mixing and DMD compensation is mandatory to employ traditional MIMO equalizers, as discussed in section 3.4.

6.2.7 Varying adaptation gain algorithm

Section 6.2.2 focused on the convergence properties of adaptive MIMO equalizers, and it was noted that the key parameter for controlling the convergence properties is the adaptation gain parameter μ . Additionally, it was discussed that a large adaptation gain results in fast convergence, but a high error floor, and a small adaptation gain results in slow convergence, and a lower error floor. The error floor minimum is limited by the SNR. To this end, a look-up table (LUT) based varying adaptation gain (or step size) algorithm is proposed, and its performance experimentally demonstrated [r27]. Note that other MIMO equalization schemes can reduce the convergence time further, at a substantial higher computational complexity, which is further discussed in section 6.4.

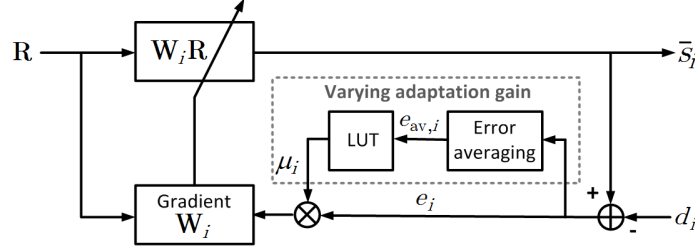


Fig. 6.11 Varying adaptation gain SGD updating algorithm, employing error averaging and a look-up table.

The experimental transmission setup employs 3 spatial modes over 80 km transmission, where QPSK is and phase plate MMUXs are used. The experimental setup is detailed in [r19], as this experimental setup was not original work by the author. As 3 spatial modes are employed, the weight matrix \mathbf{W} is of size $[6 \times 6L]$. As previously noted, this matrix can be subdivided into 6 row vectors, denoted as W_i of size $[1 \times 6L]$, where i denotes the respective output. By subdividing \mathbf{W} , each weight matrix W_i can use its respective adaptation gain μ_i . Therefore, it is possible to adaptively change the adaptation gain independently per output, according to the needs whether it is tracking capabilities, or minimizing the BER performance. The per output basis adaptation scheme is shown in Fig. 6.11. At symbol instance k , a LUT based translation stage is used to map the averaged output error $e_{av,i}(k)$ to a corresponding adaptation gain μ_i . The averaged error of output i is obtained using a 50 symbol averaging window as

$$e_{av,i}(k) = \sum_{j=k-49}^k |e_i(j)|. \quad (6.38)$$

The available adaptation gains in the LUT are logarithmically distributed as $\mu_{\text{LUT}} = [10^{-3}, 9 \cdot 10^{-4}, \dots, 10^{-4}, 9 \cdot 10^{-5}, \dots, 10^{-5}]$, and the corresponding average error level thresholds are $(6L\mu_{\text{LUT}}/2)^{1/2}$. Due to the impulse response length of the fiber, L is chosen as 131. Note that, by increasing the number of entries in the LUT, it is possible to optimize the convergence rate further at the cost of additional complexity. Here, the maximum adaptation gain was limited to 10^{-3} to ensure stable convergence.

The first and foremost comparison between the fixed adaptation gain and the varying adaptation gain is the optimal system BER performance, shown in Fig. 6.12(a). Note that the markers are for identification only, captures were taken every 1 dB OSNR. Fig. 6.12(b) depicts the convergence for the X-Polarization of the LP01 mode for various fixed adaptation gains and the proposed varying

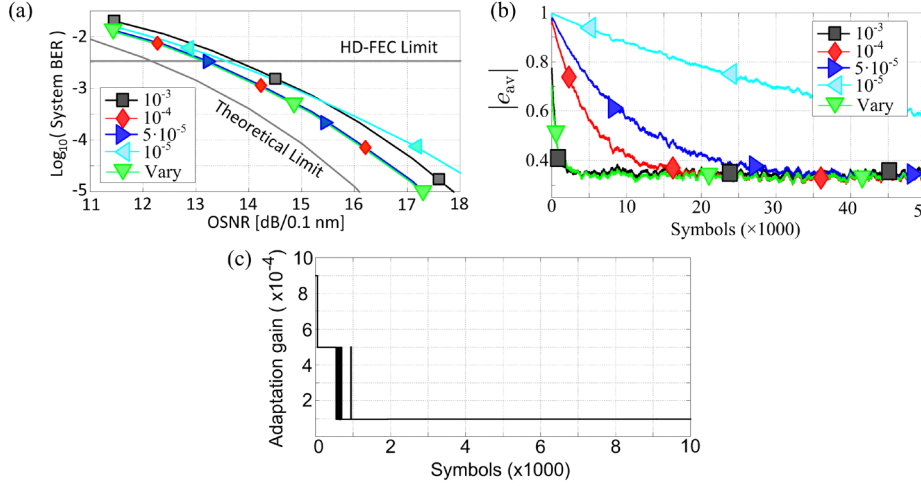


Fig. 6.12 BTB 3 mode QPSK transmission varying adaptation gain performance with respect to fixed adaptation gains. (a) BER performance. (b) Convergence time. (c) Adaptation gain over symbols.

adaptation gain algorithm for the BTB case for an OSNR of 11.4 dB. The fixed adaptation gain convergence time has been shown previously in Fig. 6.6. The convergence performance of the other channels is comparable to the LP01 X-polarization mode. The convergence time of the proposed varying adaptation gain is similar to the fixed 10⁻³ adaptation gain case. However, the BER clearly outperforms the fixed adaptation gain case, as shown in Fig. 6.12(a). Additionally, it outperforms the convergence time of the adaptation gain with the best BER curve. A factor 4 (fixed $\mu = 10^{-4}$) to 10 (fixed $\mu = 5 \cdot 10^{-5}$) times faster convergence is achieved using the varying adaptation gain. The convergence time is denoted as the time for the average error to reach $1.05 \cdot |e_{av,i}(50,000)|$. For completeness of the study, Fig. 6.12(c) shows the varying adaptation gain evolution over the first 10,000 symbols.

As shown in Fig. 6.12(a), the performance for the BTB case is very similar for various adaptation gains. However, the transmission system has an impact on the OSNR performance, as shown in Fig. 6.13(a). Fig. 6.13(b) depicts the convergence characterization for 80 km 3MF transmission for an OSNR of 13.3dB. Accordingly, it can be observed that a large adaptation gain results in an increased high error floor, resulting in degradation of the system performance. The varying adaptation gain allows for the switching to smaller adaptation gain values and hence minimizes the transmission BER. Similarly to BTB performance, the proposed varying adaptation gain outperforms the fixed adaptation gains in terms of convergence

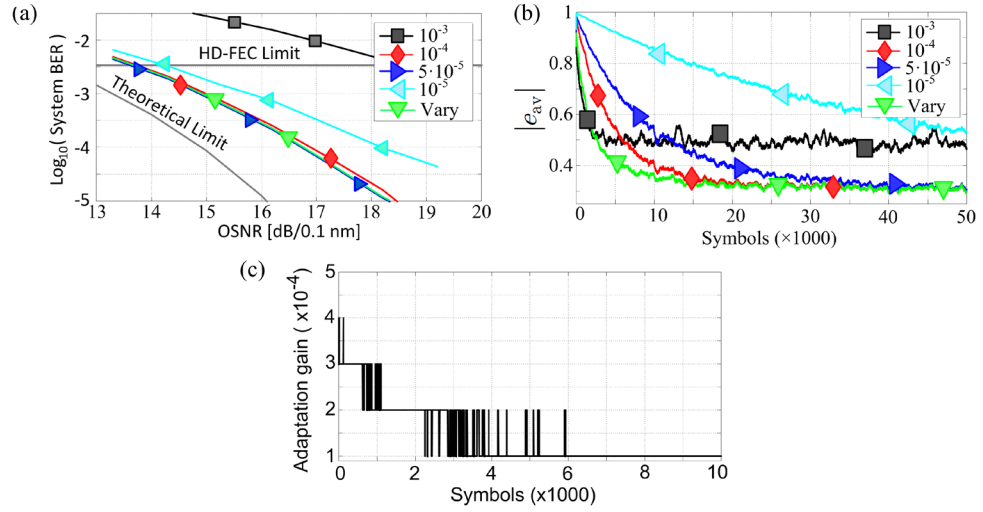


Fig. 6.13 Varying adaptation gain performance for 3 mode QPSK 80 km transmission with respect to fixed adaptation gains. (a) BER performance. (b) Convergence time.

(c) Adaptation gain over symbols.

time. Fig. 6.13(c) shows the evolution of the varying adaptation gain value for the first 10,000 symbols. The switching between adaptation gains is attributed to noise after averaging resulting in threshold crossing error values. This switching effect may be reduced when averaging over a larger number of symbols. However, this results in an increased decision time.

6.3 MMSE frequency domain equalization

In SMF transmission systems, the preferred choice is the time domain MMSE equalizer due to its straightforward implementation, where the computational complexity per output scales linearly with the number of transmitted channels and impulse response length. The computational complexity of the TDE is detailed in section 6.4. In SMF transmission, the number of transmitted channels is limited to 2, and the impulse response length increases with the polarization mode delay. However, in the case of multiple LP mode transmission, impulse responses can become lengthy quickly due to mode propagation differences, and the number of transmitted channels increases ≥ 2 . To reduce the computational complexity requirements, the block LMS algorithm is introduced [42]. This algorithm is also known as the fast LMS algorithm, or the FDE. Unlike the name might suggest, this equalizer does not compensate the frequency spectrum directly, but relies on time domain error estimation consistent with the TDE. The FDE designation is based

on performing the convolution and correlation operations in the digitized frequency domain as

$$\begin{aligned} \mathbf{c}[k] &= \mathbf{a}[k] \otimes \mathbf{b}[k] \\ &= \mathcal{F}^{-1} \left(\mathcal{F} \{a[nk], \dots, a[nk + N_{\text{DFT}} - 1]\} \right. \\ &\quad \left. \odot \mathcal{F} \{b[nk], \dots, b[nk + N_{\text{DFT}} - 1]\} \right) \end{aligned} \quad (6.39)$$

and

$$\begin{aligned} \mathbf{c}[k] &= \text{corr} \{ \mathbf{a}[k], \mathbf{b}[k] \} \\ &= \mathcal{F}^{-1} \left\{ \mathcal{F} \{a[nk], \dots, a[nk + N_{\text{DFT}} - 1]\} \odot \right. \\ &\quad \left. \mathcal{F} \{b^*[nk], \dots, b^*[nk + N_{\text{DFT}} - 1]\} \right\}, \end{aligned} \quad (6.40)$$

respectively. The convolution and correlation operations can be observed from Eq. (6.22). Here, $\mathbf{W}(k)\mathbf{r}(k)$ and $\mathbf{e}(k)\mathbf{r}^H(k)$ correspond to the convolution and correlation operation, respectively, as they are performed for every consecutively received symbol. Accordingly, in the transmission system in Eq. (2.1), the convolution operation is used. In this section, first the algorithm is detailed, before convergence properties are discussed. Finally, the varying adaptation gain proposed in [r12] is also evaluated for the FDE.

6.3.1 Updating algorithm

As noted in section 6.2.7, the $[N_t \times N_r L]$ MIMO equalizer can be split to N_t $[1 \times N_r L]$ MISO equalizers. Hence, in this section one output is considered, and the corresponding equalizer including updating algorithm is shown in Fig. 6.14. The received signals are two-fold oversampled by an adaptive rate interpolator. Therefore, first the received signals are interleaved in even and odd samples and

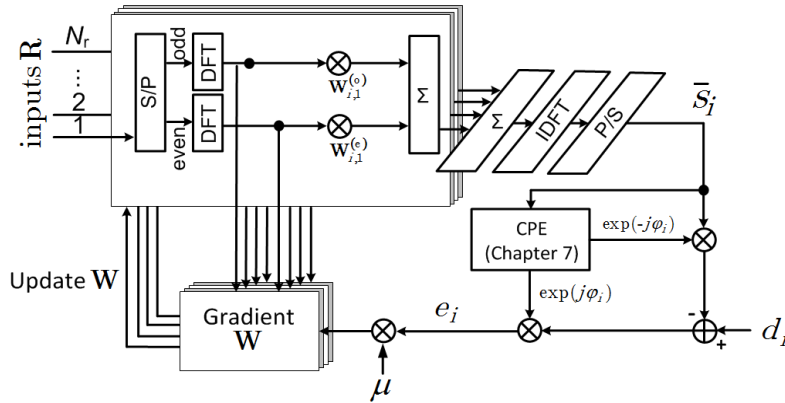


Fig. 6.14 Frequency domain equalizer updating algorithm.

transferred to the frequency domain using an N_{DFT} -point discrete Fourier transform. The interleaving step is necessary as the output is symbol spaced, and was first introduced to optical communications in [184], which in turn is based on [185]. The required N_{DFT} corresponds to the time domain filter length as

$$N_{\text{DFT}} = 2^{\lceil \log_2(L) \rceil}. \quad (6.41)$$

where $\lceil \cdot \rceil$ denotes rounding up to the next integer. DFTs provide a circular convolution, but are being employed to perform a linear convolution. Two methods exist for performing a linear convolution using DFTs, and are the overlap-save and overlap-add method. The former is the most common method, and the most efficient overlap is 50% [186]. If L is a power of 2, the resulting impulse response taken into account is exactly two times L , as can be noted from Eq. (6.41). In this work therefore, the 50% overlap-save method is chosen. Due to the 50% overlap, introduce the new parameter

$$M_{\text{DFT}} = 2^{\lceil \log_2(L) \rceil - 1} = N_{\text{DFT}} / 2. \quad (6.42)$$

Then, the n^{th} block of the j^{th} received input reads

$$\mathbf{R}_j^{(e)}[nM_{\text{DFT}}] = \mathcal{F} \left\{ \overbrace{r_j^{(e)}[(n-1)M_{\text{DFT}}], \dots, r_j^{(e)}[nM_{\text{DFT}}-1]}^{\text{previous block}}, \right. \\ \left. \underbrace{r_j^{(e)}[nM_{\text{DFT}}], \dots, r_j^{(e)}[(n+1)M_{\text{DFT}}-1]}_{\text{current block}} \right\}, \in \mathbf{C} \quad (6.43)$$

and

$$\mathbf{R}_j^{(o)}[nM_{\text{DFT}}] = \mathcal{F} \left\{ \overbrace{r_j^{(o)}[(n-1)M_{\text{DFT}}], \dots, r_j^{(o)}[nM_{\text{DFT}}-1]}^{\text{previous block}}, \right. \\ \left. \underbrace{r_j^{(o)}[nM_{\text{DFT}}], \dots, r_j^{(o)}[(n+1)M_{\text{DFT}}-1]}_{\text{current block}} \right\} \in \mathbf{C} \quad (6.44)$$

where $r_j^{(e)}$ and $r_j^{(o)}$ represent the even and odd input streams of the j^{th} received signal. Remember that the sample allocation is baud rate spaced, and note that in this case the even and odd samples are split. To accommodate residual IQ imbalance and skew compensation, the inphase and quadrature components are also separated [r11]. This comes at the cost of computational complexity, however, it yields the best BER performance. The proposed MIMO equalizer works similarly as the TDE with separated real-valued inphase and quadrature components. The frequency domain inputs $\mathbf{R}_j[n]$ are multiplied by a frequency domain weight vector for the i^{th} output as

$$\mathbf{W}_{i,j}^{(\circ)}[nM_{\text{DFT}}] = \mathcal{F} \left\{ \mathbf{w}_{i,j}^{(\circ)}, \mathbf{0}_{1 \times M_{\text{DFT}}} \right\}, \in \mathbf{C} \quad (6.45)$$

where

$$\mathbf{w}_{i,j}^{(\circ)} = \{w_{i,j}^{(\circ)}[0], \dots, w_{i,j}^{(\circ)}[M_{\text{DFT}} - 1]\}, \in \mathbf{C} \quad (6.46)$$

and (\circ) indicates even or odd. The multiplication then results in the frequency domain estimate of the transmitted signal i^{th} as

$$\begin{aligned} \bar{\mathbf{S}}_i[nM_{\text{DFT}}] &= \sum_{j=1}^{N_i} \mathbf{R}_j^{(\circ)}[nM_{\text{DFT}}] \odot \mathbf{W}_{i,j}^{(\circ)}[nM_{\text{DFT}}] \\ &\quad + \sum_{j=1}^{N_i} \mathbf{R}_j^{(\text{e})}[nM_{\text{DFT}}] \odot \mathbf{W}_{i,j}^{(\text{e})}[nM_{\text{DFT}}], \end{aligned} \in \mathbf{C} \quad (6.47)$$

where the summation is an element-wise summation, and the corresponding time domain output is the inverse Fourier transform of Eq. (6.47) as

$$\bar{\mathbf{s}}'_i[nM_{\text{DFT}}] = \mathcal{F}^{-1}\{\bar{\mathbf{S}}_i[nM_{\text{DFT}}]\}, \in \mathbf{C} \quad (6.48)$$

where the first M_{DFT} samples are discarded due to the circular convolution operation. Hence, the time domain output consist of the last M_{DFT} elements as

$$\bar{\mathbf{s}}_i[nM_{\text{DFT}}] = \{\bar{s}'_{i,M_{\text{DFT}}}[nM_{\text{DFT}}], \dots, \bar{s}'_{i,N_{\text{DFT}}-1}[nM_{\text{DFT}}]\}. \in \mathbf{C} \quad (6.49)$$

Eq. (6.49) therefore is the equivalent of Eq. (6.6) for M_{DFT} consecutive symbols. Following the TDE steps, the error with length M_{DFT} then reads

$$\mathbf{e}_i[nM_{\text{DFT}}] = \mathbf{d}_i[nM_{\text{DFT}}] - \bar{\mathbf{s}}_i[nM_{\text{DFT}}], \in \mathbf{C} \quad (6.50)$$

where \mathbf{d} represents the desired signal block based on the LMS or DD-LMS algorithm. Alternatively, the CMA can be used for estimating the error as well. Subsequently, the error is transferred to the frequency domain as

$$\mathbf{E}_i[nM_{\text{DFT}}] = \mathcal{F}\{\mathbf{0}_{M_{\text{DFT}} \times 1}, \mathbf{e}_i[nM_{\text{DFT}}]\}, \in \mathbf{C} \quad (6.51)$$

and the correlation with the received signal is performed as

$$\Phi_{i,j}^{(\circ)}[nM_{\text{DFT}}] = \mathcal{F}^{-1}\{\mathbf{E}_i[nM_{\text{DFT}}] \odot \mathbf{R}_j^{*(\circ)}[nM_{\text{DFT}}]\}. \in \mathbf{C} \quad (6.52)$$

Finally, the weight update is performed in the time domain as

$$\mathbf{w}_{i,j}^{(\circ)}[nM_{\text{DFT}}] = \mathbf{w}_{i,j}^{(\circ)}[(n-1)M_{\text{DFT}}] + \mu \Phi_{i,j}^{(\circ)}[nM_{\text{DFT}}], \in \mathbf{C} \quad (6.53)$$

where

$$\Phi_{i,j}^{(\circ)}[nM_{\text{DFT}}] = \{\Phi_{i,j,0}^{(\circ)}[nM_{\text{DFT}}], \dots, \Phi_{i,j,M_{\text{DFT}}-1}^{(\circ)}[nM_{\text{DFT}}], \mathbf{0}_{1 \times M_{\text{DFT}}}\}. \in \mathbf{C} \quad (6.54)$$

The time domain weights are transferred to the frequency domain using Eq. (6.45), which completes the updating algorithm loop.

6.3.2 FDE convergence

From observing Eq. (6.51), it is clear that the FDE processes M_{DFT} consecutive symbols per block. Recalling the convergence properties from the SGD algorithm described in section 6.2.2 results in the time domain update algorithm

$$\mathbf{W}(k+1) = \mathbf{W}(k) + \mu M_{\text{DFT}} \mathbf{e}(k) \mathbf{r}^H(k), \quad (6.55)$$

which corresponds to Eq. (6.22) for updating M_{DFT} consecutive symbols. Performing the deriving steps according to section 6.2.2, results in the adaptation gain limit as

$$0 \leq \mu \leq \frac{2}{M_{\text{DFT}} \lambda_i} \quad (6.56)$$

Similar to the TDE convergence stability equation in Eq. (6.27), from Eq. (6.56) can be observed that the largest eigenvalue results in the smallest boundary value, and therefore limits the adaptation gain. Accordingly, the FDE shows the same convergence performance as the TDE when the adaptation gain is bound by Eq. (6.56). However, the TDE has the potential to converge M_{DFT} times faster. In section 6.2.7 it was noted that larger adaptation gains increased the error floor.

6.3.3 Varying adaption gain FDE

The proposed varying adaptation gain described in section 6.2.7 has applied to the FDE in [r11], where the same experimental setup was used. Through OSNR characterization, the varying adaptation gain is compared with the fixed adaptation gain performance. Fig. 6.15 shows the BER of the best performing fixed adaptation gain and varying adaptation gain for the FDE. In addition, for comparison, the optimum adaptation gain TDE has been added. In terms of BER versus OSNR, both the TDE and FDE show the same optimal performance. However, when comparing the convergence performance for the varying adaptation gain of the TDE and FDE with respect to the fixed adaptation gain TDE and

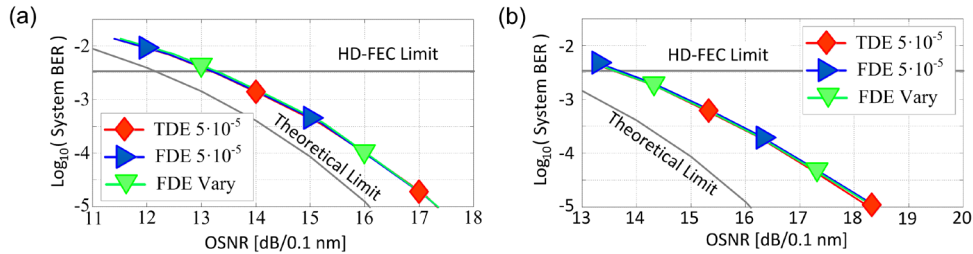


Fig. 6.15 QPSK optimum performance comparison between the TDE, FDE, and FDE with varying adaptation gain for 3 mode (a) BTB, and (b) 80 km transmission.

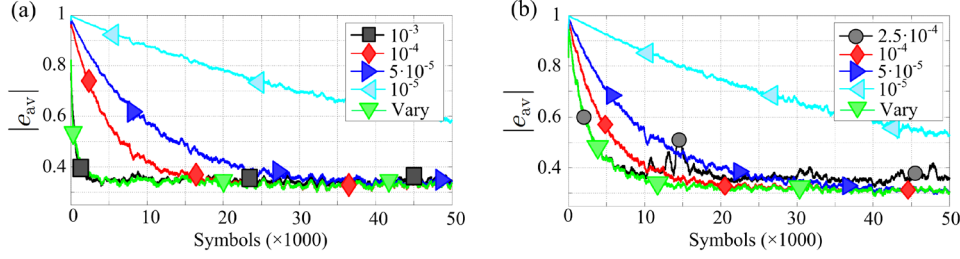


Fig. 6.16 FDE convergence characteristics for various fixed adaptation gains and the varying adaptation gain for 3 mode (a) BTB, and (b) 80 km transmission.

FDE, a difference is observed. Fig. 6.16 depicts the convergence for both the BTB case, as well as the 80 km transmission case. Again, the system convergence time is denoted as the time it takes for the MIMO equalizer to reach an average output error which is within a margin of 5% of the average output error after 50,000 symbols. Note that the TDE with varying adaptation gain outperforms the FDE with varying adaptation gain as the adaptation gain maximum is limited to $2.5 \cdot 10^{-4}$ for the FDE. This result is due to the more stringent maximum adaptation gain for stable convergence, and hence the observed performance complies with Eq. (6.56). Therefore, an increased convergence time reduction can be achieved by the TDE with respect to the FDE, as the maximum stable adaptation gain is M_{DFT} -fold higher.

6.4 MIMO equalizer computational complexity

MMSE equalizers are commonly employed in optical transmission systems, and therefore it is critical that the computational complexity of the TDE and FDE is investigated. The computational complexity of an equalizer is formed by the number of multiplications and additions, where a complex addition (CADD) is described as

$$\begin{aligned} z_1 + z_2 &= [\Re(z_1) + j\Im(z_1)] + [\Re(z_2) + j\Im(z_2)] \\ &= \Re(z_1) + \Re(z_2) + j[\Im(z_1) + \Im(z_2)], \end{aligned} \quad (6.57)$$

where $z_1, z_2 \in \mathbb{C}$, which shows that a complex addition consists of two real additions (RADDs). A complex multiplication (CMUL) can be written by either

$$z_1 z_2 = [\Re(z_1)\Re(z_2) - \Im(z_1)\Im(z_2)] + j[\Im(z_1)\Re(z_2) + \Re(z_1)\Im(z_2)] \quad (6.58)$$

or

$$\begin{aligned} z_1 z_2 &= [\Re(z_1)\Re(z_2) - \Im(z_1)\Im(z_2)] \\ &\quad + j\{[\Re(z_1) + \Im(z_1)][\Re(z_2) + \Im(z_2)] - \Re(z_1)\Re(z_2) - \Im(z_1)\Im(z_2)\}, \end{aligned} \quad (6.59)$$

where Eq. (6.58) uses 4 real multiplications (RMULs) and 2 RADDs [160]. Eq. (6.59) however, has only 3 RMULs and 5 RADDs. The number of operations for Eq. (6.59) is higher than Eq. (6.58), but as multiplications are more costly than additions [186], the computational complexity is lower. Nevertheless, the decisive factor is the latency of a real-time transmission system, and therefore Eq. (6.58) is preferred over Eq. (6.59).

6.4.1 TDE computational complexity

To establish the computational complexity of the TDE, two separate cases are analyzed. First, the computational complexity during the payload is investigated, where only a convolution between data and the weight matrix is performed. The second case is during headers, where additional correlation with the error is performed. Note that MMSE equalization can continue during payload transmission using the DD-LMS algorithm described in section 6.2.4. To compute the complexity of the TDE during payload is very straightforward, and the number of complex multiplications is $N_t N_r L$, and the number of complex additions is $(N_t - 1)(L - 1)N_r$. Note that the number of received bits equals $N_r \log_2(N_{\text{const}})$. During payload processing, the computational complexity is

$$\text{CMUL} = \frac{N_r L}{\log_2(N_{\text{const}})}, \quad (6.60)$$

$$\text{CADD} = \frac{(N_r - 1)(L - 1)}{\log_2(N_{\text{const}})}. \quad (6.61)$$

During headers the complexity increases as the weight matrix is updated. The added complexity from channel estimation is

$$\text{CMUL} = N_t + N_t N_r L, \quad (6.62)$$

$$\text{CADD} = N_t + N_t N_r L, \quad (6.63)$$

and originates from determining the error vector and adding the gradient. Hence, the total complexity during headers is

$$\text{CMUL} = \frac{2N_r L + 1}{\log_2(N_{\text{const}})}, \quad (6.64)$$

$$\text{CADD} = \frac{(N_r - 1)(L - 1) + N_r L + 1}{\log_2(N_{\text{const}})}. \quad (6.65)$$

6.4.2 FDE computational complexity

Eq. (6.41) denotes the relation between the impulse response length and the required DFT size N_{DFT} , where M_{DFT} symbols are processed per block. Again, a distinction is made between payload processing and the header. The computational complexity of an (I)DFT is [186]

$$\text{CMUL} = N_{\text{DFT}} C_{\text{rad}} \log_2(N_{\text{DFT}}), \quad (6.66)$$

$$\text{CADD} = N_{\text{DFT}} \log_2(N_{\text{DFT}}), \quad (6.67)$$

where C_{rad} is 0.5 for a radix-2 DFT, and $3/8$ for a radix-4 DFT. Note that, when a radix-4 DFT is used, N_{DFT} has to be a power of 4. The FDE computational complexity to perform a convolution in the frequency domain when even and odd samples are separated requires $2N_r$ DFTs (received signals), $2N_r N_t N_{\text{DFT}}$ CMULs (frequency domain element-wise multiplications), N_t inverse discrete fourier transformations (IDFTs) (output), and $(2N_r - 1)N_t N_{\text{DFT}}$ CADDs (output summation). The number of transmitted bits processed in one block is $M_{\text{DFT}} N_t \log_2(N_{\text{const}})$, and hence, the computational complexity per bit for payload processing is

$$\text{CMUL} = \frac{2N_r N_t M_{\text{DFT}} + (2N_t + N_r) C_{\text{rad}} N_{\text{DFT}} \log_2(N_{\text{DFT}})}{M_{\text{DFT}} N_t \log_2(N_{\text{const}})}, \quad (6.68)$$

$$\text{CADD} = \frac{N_t (2N_r - 1) N_{\text{DFT}} + (2N_t + N_r) N_{\text{DFT}} \log_2(N_{\text{DFT}})}{M_{\text{DFT}} N_t \log_2(N_{\text{const}})}. \quad (6.69)$$

Similar to the TDE, during headers the computational complexity increases as the weights are updated. The added complexity consists of N_r DFTs (error feedback), $2N_t N_r$ IDFTs (weight update), $2N_t N_r$ DFTs (weight update), $2N_t N_r N_{\text{DFT}}$ CMULs (perform correlation), and $N_r N_{\text{DFT}} / 2$ CMULs (adaptation gain). The complex additions are $N_r N_{\text{DFT}} / 2$, (error estimation) and $2N_t N_r N_{\text{DFT}}$ (weight update). Combined, the added computational complexity is

$$\text{CMUL} = (N_t + 4N_t N_r) C_{\text{rad}} N_{\text{DFT}} \log_2(N_{\text{DFT}}) + 2N_t N_r N_{\text{DFT}} + N_t M_{\text{DFT}}, \quad (6.70)$$

$$\text{CADD} = (N_t + 4N_t N_r) N_{\text{DFT}} \log_2(N_{\text{DFT}}) + 2N_t N_r N_{\text{DFT}} + N_t M_{\text{DFT}}, \quad (6.71)$$

which results in the total computational complexity per bit as

$$\text{CMUL} = \frac{(2N_t + 2N_r + 4N_t N_r) C_{\text{rad}} N_{\text{DFT}} \log_2(N_{\text{DFT}}) + 4N_t N_r N_{\text{DFT}} + N_t M_{\text{DFT}}}{M_{\text{DFT}} N_t \log_2(N_{\text{const}})}, \quad (6.72)$$

$$\begin{aligned} \text{CADD} = & \frac{(2N_t + 2N_r + 4N_t N_r) N_{\text{DFT}} \log_2(N_{\text{DFT}})}{M_{\text{DFT}} N_t \log_2(N_{\text{const}})} \\ & + \frac{N_t (2N_r - 1) N_{\text{DFT}} + 2N_t N_r N_{\text{DFT}} + N_t M_{\text{DFT}}}{M_{\text{DFT}} N_t \log_2(N_{\text{const}})}, \end{aligned} \quad (6.73)$$

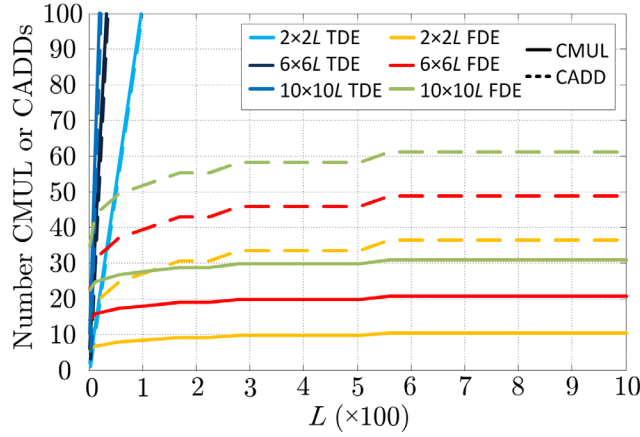


Fig. 6.17 Computational complexity of QPSK transmission with 2.5% training sequence overhead.

6.4.3 Computational complexity comparison

From Fig. 6.17 can be observed that the most commonly used equalizer in SMF transmission systems, the TDE, is clearly not preferable for lengthy impulse responses. Fig. 6.17 assumes QPSK transmission with 2.5% known sequence overhead (header), while during the remainder of the packet the adaptive weights are not updated. Additionally, from the same figure it can be observed that the FDE logarithmic behavior in computational complexity provides a scalable solution for lengthy impulse responses. Hence, when the number of transmitted channels is increased, the computational complexity of the FDE remains limited. Note that L relates to the impulse response length as

$$T_{\text{impulse}} = \frac{LT_{\text{sym}}}{2}, \quad (6.74)$$

for a 2-fold oversampled input signal, i.e. for a 28 GBaud 1000 tap equalizer, the equalizer window spans $1000 \times 35.71 \text{ ps} / 2 = 17.85 \text{ ns}$.

6.5 Offline-processing implementation

It has been previously noted that the experimental results obtained in Chapter 8 use offline-processing. The offline-processing C# code has been implemented on a distributed peer-to-peer server cluster, consisting of Intel Xeon quad-core CPUs. The distributed server cluster allows for simultaneously processing all transmitted channels, where each CPU core allows for processing one MIMO output. This setup was chosen as it minimizes the total processing time. The offline-processing setup is

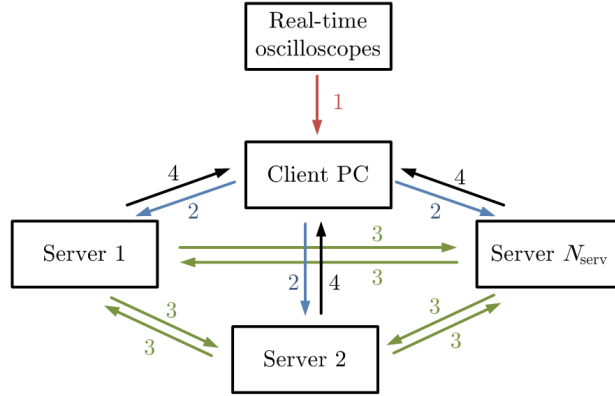


Fig. 6.18 N_{serv} offline-processing distributed peer-to-peer setup.

shown in Fig. 6.18, where one PC acts as client and receives the samples from the real-time oscilloscopes in step 1. Then, in step 2, the captured data is distributed to $N_{\text{serv}} = \lceil N_t / 4 \rceil$ servers, where independently the FE impairments are compensated, adaptive rate conversion is performed, and chromatic dispersion is removed. Subsequently in step 3, the processed data is synchronized amongst the servers, to provide the MIMO equalizer inputs. The implemented MIMO equalizers are the TDE and FDE, as discussed in this chapter. Finally, after MIMO processing, the BER is computed and sent back to the client PC, step 4.

To investigate the time characteristics of increasing the number of transmitted channels, a simulation setup is designed, where the packet length was 310,000 symbols, corresponding to the delay SMF in the TDM-SDM receiver in section 5.3. Three MIMO transmission channel sizes have been investigated, where $N_r = N_t = 6, 12,$ and 24 , which correspond to the co-propagation of 2, 4, and 7 LP modes, as denoted in Table 3.1. For each MIMO transmission channel two cases are studied, namely 25 and 199 taps. 25 taps corresponds to the taps order of magnitude used in SSMF transmission systems, and 199 taps have been chosen to correspond to an order of magnitude larger in computational complexity. The

	25 taps		199 taps		Number of servers
	TDE	FDE	TDE	FDE	
6×6	9.4 sec	8.6 sec	12.3 sec	8.6 sec	2
12×12	14.8 sec	14.9 sec	19.7 sec	15.5 sec	3
24×24	24.7 sec	28.8 sec	40.3 sec	29.4 sec	6

Table 6.1 distributed peer-to-peer offline-processing computation time.

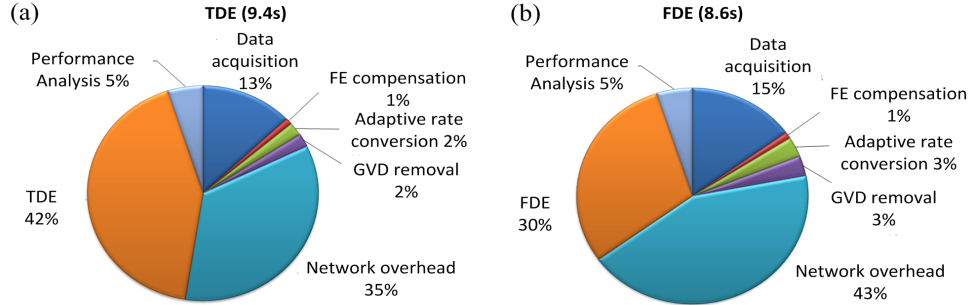


Fig. 6.19 Time per individual processing block for the 6×6 25 tap (a) TDE, and (b) FDE.

processing time is averaged over 10 independent mixed channels, and is shown in Table 6.1. Note that, as N_t increases, for 25 taps, the FDE is slower than the TDE. This is primarily attributed to the DFT library used, and can potentially be further improved by implementing a custom library. When the number of taps increases, the performance is as expected. Additionally, the time difference for the FDE is small when increasing the number of taps, whereas the TDE processing time increase is substantial. Naturally, not only the total processing time is of interest, but also the time spent on performing the individual DSP blocks, which is shown for a 6×6 MIMO transmission of length 310,000 symbols and 25 taps in Fig. 6.19. The processing speed is limited by the combined time spent on server synchronization and MIMO equalization. Note that the CPE is embedded in the MIMO equalization process.

6.6 Towards hardware implementation

For SDM transmission systems to become a reality, offline-processing does not suffice. However, offline-processing can assist in indicating the potential for scaling, and acts as a proof of concept to aid in future SDM implementations. First, advanced equalization schemes are briefly discussed which can improve the BER performance and convergence characteristics. Then, the performance of bit-width reduced floating point operations is investigated. This is mandatory, as offline-processing employs 64-bit floating point operations, which is too high for hardware implementation. Finally, scaling the MIMO DSP is discussed for potential hardware implementation.

6.6.1 Advanced equalization

As the TDE and FDE MMSE equalizers are the general choice for MIMO equalization in optical transmission systems, it is important to note that more advanced equalizers exist which yield an improved BER performance or

convergence properties. Note that the computational complexity of the TDE and FDE is linear and logarithmic, respectively.

The most common algorithms for MIMO equalization in the fields of acoustics and wireless transmission are the recursive least squares (RLS) algorithm [177], and its frequency domain equivalent the fast RLS algorithm, which yield the Wiener-Hopf solution and can have an order of magnitude faster convergence than the LMS algorithm. However, the convergence iteration gain comes at the cost of a much higher computational complexity, as the RLS and fast RLS algorithms scale quadratically and linear in computational complexity [42], and are therefore not relevant for high speed processing.

A second option is to reduce the filter length using infinite impulse response (IIR) filters, which results in a reduction in computational complexity. However, IIR filters require instantaneous feedback, which is difficult to implement in high speed receivers [170]. Another option are distributed feedback equalizers (DFE), which suffer from a similar issue, where in theory an improved BER can be achieved [187]. However, a feedback within a few symbols is required, and therefore DFE are not practical for high speed receiver side implementation.

6.6.2 Bit-width reduced floating point operations

It has been noted previously that results obtained in this thesis use offline processing. In offline-processing, there are virtually unlimited resources and time for processing, and high accuracy arithmetics is used. In modern computers, each value is represented by a 64 bit floating point unit (FPU) number, FPU-64. The FPU-64 is formed according to the IEEE 754 standard by 1 sign bit, 11 exponent bits, and 52 mantissa bits [188]. The decimal value D can be computed from its respective binary value as [189]

$$D = (-1)^S \left(1 + \sum_{m=1}^M b_{M-m} \beta^{-m} \right) \beta^{E-\text{bias}}, \quad (6.75)$$

where S is the value of the sign bit, m the binary value b index of the mantissa with length M , E the exponent value, and β the radix. In this work, $\beta = 2$. Note that in Eq. (6.75), the exponent bias is $\beta^{11-1} - 1$ for FPU-64, which represents the center value. The bias value is related to the exponent width available in the used FPU. However, in reality, implementing FPU-64 in real-time processing chips is difficult [190], as the energy required for computing an output bit is high, the DSP throughput is limited, and the chip footprint is large. Hence, real-time implementations often use fixed point arithmetics, while higher accuracy FPU

	Bit Width	Sign S	Exponent E	Mantissa M	Radix β	Bias
FPU-64	64	1	11	52	2	1023
FPU-32	32	1	8	23	2	255
FPU-16	16	1	6	9	2	63
FPU-12	12	1	6	5	2	63

Table 6.2 The used FP representations consisting of a number of sign, exponent, and mantissa bits. For completeness, the radix has been added.

implementations are becoming more accessible in FPGAs and application-specific integrated circuits (ASICs). Nevertheless, FPU-64 is still too complex [191]. Therefore, the effect of using reduced bit width arithmetics in [r35] for potential future transmission systems is investigated. Additionally, it provides insight in the validity of the experimental work in combination with offline-processing. Accordingly, three bit-width reduced FPU standards, FPU-32, 16, and 12, have been chosen corresponding to the work in [191], and their respective structure is outlined in Table 6.2. These FPUs increase potential throughput for real-time systems, and reduce the energy requirements to perform multiplications and additions, at the cost of computational accuracy.

For the FPU comparison, the experimental setup used is detailed in Chapter 8, where a 41.7 km 3 spatial LP mode transmission system is used. Full mixing is achieved using a spot launcher MMUXs. Fig. 6.20 shows the BER performance for 41.7km 3 mode QPSK, 8, and 16 QAM transmission for the FPU-64, and the investigated bit-width reduced FPU-32, 16, and 12.

In Fig. 6.20(a) the performance for QPSK is detailed. Two performance indicators are used, the HD-FEC and SD-FEC limits. With respect to FPU-64 performance, the penalties are 0.65, 0.75 and 1.1 dB for FPU-32, 16, and 12, respectively, at the HD-FEC limit. At the SD-FEC limit, the respective penalties are 0.1, 0.3 and 0.45 dB for FPU-32, 16, and 12 with respect to FPU-64. Therefore, it is clear that the BER performance of all FPU types for low OSNR converges to the same value. This is attributed to the noise impact becoming substantially higher than the increased round-off error introduced by the FPU bit-width reduction.

Similar behaviour is observed in Fig. 6.20(b) for 8 QAM transmission. However, the respective penalties at the HD-FEC limit have increased to 0.7, 2.7, and 4.1 dB for FPU-32, 16, and 12, with respect to the FPU-64 performance. The penalties at

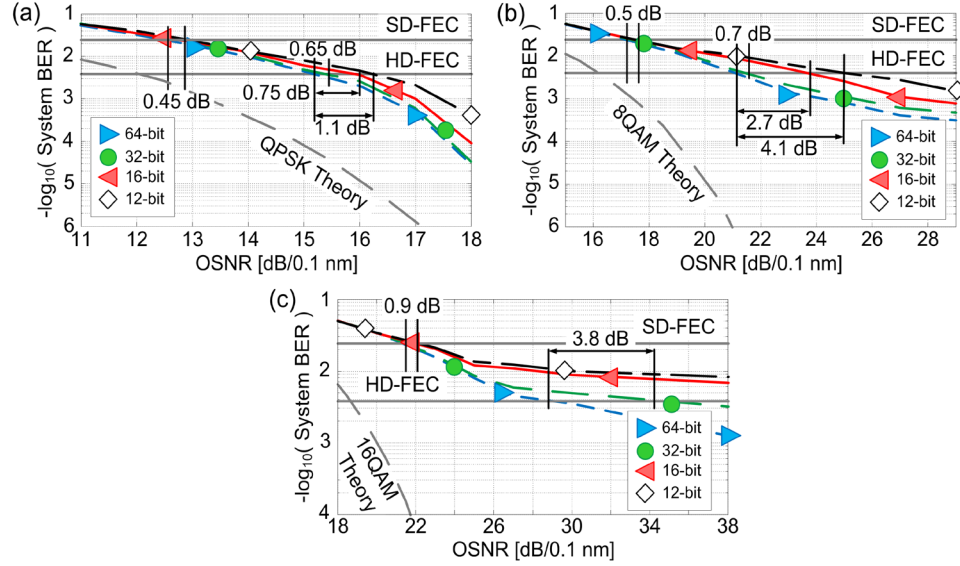


Fig. 6.20 Bit-width reduced floating point BER performance of the TDE MIMO equalizer for 3 mode 41.7 km transmission using spot launching. (a) QPSK. (b) 8 QAM. (c) 16 QAM.

the SD-FEC limit are 0.2, 0.35 and 0.5 dB for FPU-32, 16, and 12 with respect to FPU-64 performance. Also, an increased error floor is observed for high OSNR, which is attributed to the decreased FPU accuracy, as it becomes the predominant source of (quantization) noise.

Finally, the OSNR performance of 16 QAM transmission is shown in Fig. 6.20(c). Again, the penalty at the HD-FEC limit is increased, and is 3.8 dB for FPU-32 with respect to FPU-64. Note that due to the increased error floor, FPU-16 and FPU-12 do not achieve HD-FEC performance. At the SD-FEC limit however, the OSNR penalties are 0.1, 0.8, and 0.9 dB for FPU-32, 16, and 12, with respect to FPU-64. Additionally, from Fig. 6.20(c) it can be observed that the exponent bit reduction has a larger impact than the mantissa bit reduction as the performance of FPU-16 and FPU-12 is similar. From these results it can be noted that similar OSNR performance to offline-processing using FPU-64 can be achieved with a lower number FPU, and therefore indicate the viability of SDM transmission.

6.6.3 MIMO DSP scaling

As the optical medium and components are scaling to accommodate a larger number of transmitted channels, this has an influence on the DSP. Note that for MIMO transmission, the heart of the DSP is the MIMO equalizer, which unravels

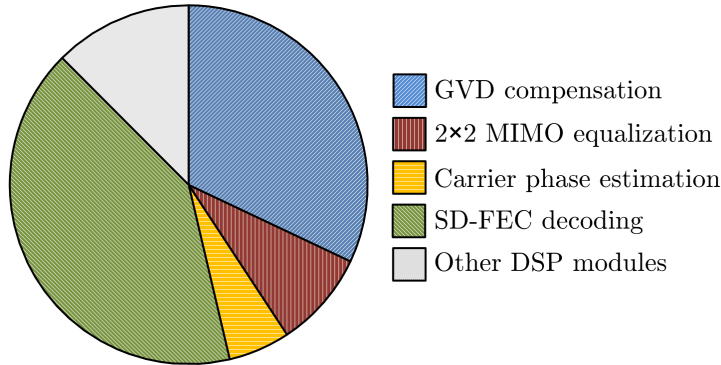


Fig. 6.21 Power dissipation of a conventional SMF-based 100 Gbit s⁻¹ carrier⁻¹ DSP ASIC digital logic core in a line card [172].

the mixed transmission channels. However, the MIMO equalizer is not the most power dissipating module in conventional ASICs. Fig. 6.21 depicts the typical power dissipation distribution of a conventional 100 Gbit s⁻¹ carrier⁻¹ DSP ASIC digital logic core in a line card [172]. From Fig. 6.21 it can be observed that the GVD compensation and SD-FEC modules contribute the lion's share to the aggregate power dissipation of the ASIC. However, the computational complexity of these two modules scales linearly with the number of transmitted channels. The MIMO equalizer scales linearly with the number of transmitted channels, per received channel. Therefore, the number of matrix elements scales quadratically. In a conventional SMF transmission system, the number of elements is $2 \times 2 = 4$. For a 3MF, it is $6 \times 6 = 36$, and a six LP mode fiber $20 \times 20 = 400$ [74]. The latter case corresponds to a 100-fold increase in required computational complexity in the MIMO equalizer. Also note that the impulse response length is longer for SDM transmission systems than conventional SMF transmission systems due to multiple EH and HE modes co-propagating at marginally different group velocities within an LP mode, and similar to SMF propagation, the impulse response length grows with the square root of the transmission distance. However, when an FDE is employed, the computational complexity with respect to the impulse response length remains low, as shown in section 6.4.3. Consequently, the largest contribution to the increase of power dissipation for SDM transmission systems is the increase in number of matrix elements. Therefore, it is unlikely that the number of fully coupled transmission channels scales 2 orders of magnitude, as SDM proposes to achieve [27], as 6 LP mode transmission (10 DP channels) already results in a 100-fold increase in computational complexity. Although, as the ASIC fabrication process continues to advance to smaller transistor sizes, the number of fully mixed transmission channels can be increased beyond what is possible today.

6.7 Summary

This chapter initially addresses the zero-forcing equalizer, which is the first MIMO equalizer used in wireless spatial multiplexing based on the V-BLAST algorithm. The ZF equalizer minimizes the interference between the transmitted channels, but does not take the addition of noise into account. This effect results in zero-forcing not being the predominant equalization method in communication systems, as the noise contribution can be heavily amplified. Instead, the most commonly used MIMO equalizer in currently employed SMF transmission systems is the MMSE TDE, which is based on the SGD algorithm. Accordingly, three SGD based algorithms are described for updating the weight matrix, namely LMS, DD-LMS, and CMA, and convergence properties are given. Based on these convergence properties, a varying adaptation gain is proposed, resulting in greatly improved convergence times, while still achieving the optimum BER performance at the cost of a small added computational complexity. Additionally, bit-width reduced equalization is investigated, as real-time systems cannot employ 64-bit floating point operations used in offline-processed experimental setups. Reducing the bit-width of the floating point operations leads to reducing the computational complexity of the TDE. As the TDE scales linearly in computational complexity, further computational complexity reduction has to be achieved, which led to the introduction of the FDE. This MIMO equalizer is also based on the SGD algorithm. In the FDE, the convolution and correlation multiplications are performed in the frequency domain, which is more computationally efficient than the time domain. Furthermore, the convergence properties of the FDE are detailed, and the varying adaptation gain used for the TDE is also applied to the FDE. Moreover, the FDE is extended to account for residual IQ imbalance and skew, by separating the inphase and quadrature received inputs. This however, comes at the cost of computational complexity, but provides the best optimum performance possible. Subsequently, other MIMO equalizers are discussed which have improved BER or convergence characteristics. However, these alternative equalizers come at either a great increase in computational complexity, or are not suitable for high-speed real-time processing due to practical limitations. Finally, the developed offline-processing peer-to-peer distributed network is described, which supports the experimental activities performed in Chapter 8, and the potential of scaling towards and increased number of mixed channels is discussed.

Chapter 7

Carrier phase estimation

Simplicity is the ultimate sophistication.

Leonardo da Vinci

The CPE stage is the last key DSP block remaining in this thesis. As discussed in Chapter 6, the CPE DSP block is performed during LMS-based MIMO equalization, where feedback is provided to the MIMO equalizer. When the CMA is used for updating the weights of the MIMO equalizer, these two DSP blocks can be considered independent. This chapter⁵ focuses on two types of carrier phase estimation: frequency and phase estimation. Accordingly, first in section 7.1 data-aided frequency offset estimation is discussed. This is based on LS channel estimation, as it has been previously detailed in section 6.1. Frequency offset estimation is usually employed when the frequency offset between the transmitter laser and LO is large with respect to the baud rate. If the frequency offset is small, phase estimation suffices. The two most commonly used phase estimation algorithms are detailed in section 7.2, where first in section 7.2.1 the Viterbi-Viterbi algorithm is detailed. This is an often used method in SMF transmission laboratory experiments. Additionally, the Costas loop is described, which consists of a phase detector and a digital phase locked loop (DPLL). The 2nd order DPLL scheme is detailed in section 7.2.2, and subsequently, three corresponding phase detectors are described. First, in section 7.2.3, the most intuitive phase detector, the multi-dimensional distance phase detector is discussed. An argument-based distance phase detector is detailed in section 7.2.4 which reduces the computational complexity with respect to the multi-dimensional distance phase detector. Further reduction in computational complexity is achieved by the proposed 2×1D phase detector, discussed in section 7.2.5. Furthermore, as all transmitted channels share the same transmitter laser source, and all coherent receivers share the same LO, the laser frequency offset in MIMO transmission systems can be considered a common-mode impairment. This common-mode impairment can be exploited. First a master/slave scheme is introduced, which serves as a performance reference for the argument-based averaging scheme proposed in section 7.3. Both these joint CPE schemes are based on the Costas loop, and the Costas loop is the primary

⁵ This chapter incorporates results from the author's contributions [r7], [r12], and [r21].

CPE scheme used in the experiments in Chapter 8, as it outperforms the V-V phase estimator. The lower performance bound of CPE algorithms is described by the Cramer-Rao bound (CRB), which is the lower bound of the estimator error variance of the deterministic transmission system parameters. As it is particularly difficult to analytically compute the CRB, often in transmission theory the modified CRB (MCRB) is used which was introduced by D' Andrea et. al in 1994 and reads [192]

$$\text{MCRB}_f = \frac{3}{2L_o^3 \pi^2 T_{\text{sym}}^2} \frac{1}{\text{SNR}} \quad (7.1)$$

and

$$\text{MCRB}_\phi = \frac{1}{2L_o} \frac{1}{\text{SNR}}, \quad (7.2)$$

which denote the frequency and phase MCRB, respectively. Note that the frequency estimator is dependent of the symbol duration, and both MCRBs are dependent on L_o , which denotes the number of symbols taken into account. From observing Eq. (7.1) and Eq. (7.2) it is noticeable that the MCRB for frequency and phase scale cubed and linearly with L_o , respectively. Note that in offline-processing systems, there is no system delay, and hence achieves the best possible performance, which is not achievable in real-time systems. To estimate the frequency and phase information, two cases are considered. First, where the frequency offset is large and hence the main performance penalty contributor. The second case is where the frequency offset is small and hence the main performance penalty originates from phase noise.

7.1 Frequency offset estimation

To estimate, and remove, the large frequency offset between the transmitter laser and LO, two main methodologies exists: data-aided, and non-data-aided or blind estimation. For wireless transmission systems, the data-aided method achieves a performance very close to the MCRB, and works independently of channel mixing as it is based on correlation. Hence, this section focuses on data-aided frequency offset estimation, instead of blind frequency offset estimation techniques [165]. Wireless data-aided techniques greatly outperform blind estimation techniques, which was also noticed for optical transmission systems in [193]. For optimum performance, it is assumed that the frequency offset remains constant within the correlation window. If the frequency offset is small, phase estimation per symbol is preferred to track the frequency offset over time as it can provide a lower latency feedback.

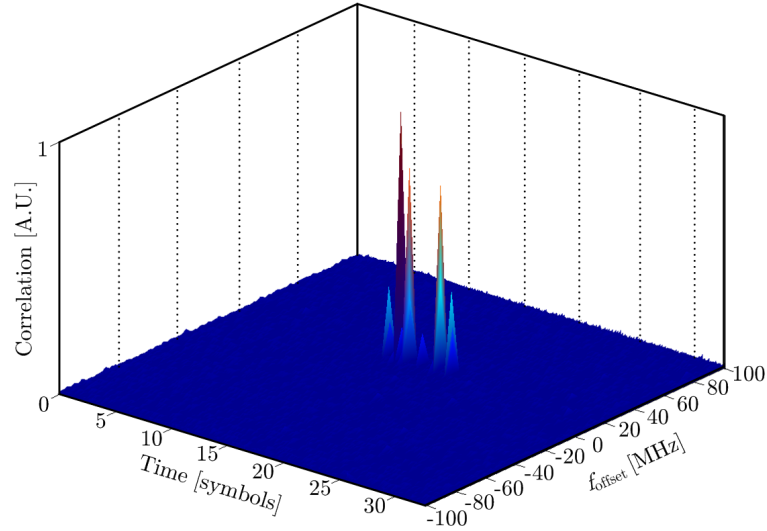


Fig. 7.1 Data-aided frequency offset estimation in the LP_{01} X-polarization through correlation of a 41.7 km 3MF transmission system, where delayed copies are transmitted. The estimated frequency offset between the transmitter laser and LO is ~ 25 MHz.

In section 2.3.1 data-aided LS channel estimation has been performed, and it was noted that finding the frequency offset within a range of frequency offsets is a key difficulty. To investigate the correlation performance, and hence frequency offset, the transmitted channel vector of Eq. (2.16) is multiplied by $\exp(-j2\pi f_{\text{offset}} k T_{\text{int}})$, where $f_{\text{min}} \leq f_{\text{offset}} \leq f_{\text{max}}$. f_{min} and f_{max} represent the minimum and maximum search frequency offset for estimation. The frequency offset estimation results of the 41.7 km 3 spatial LP mode QPSK transmission experiment in section Chapter 8 is shown in Fig. 7.1, where a correlation length of 2^{13} symbols has been used with a frequency step size of 5 MHz. The investigated received channel is the X-polarization of the LP_{01} mode, and the peak height differences are caused by crosstalk differences. From the figure it can be observed that the frequency offset is approximately 25 MHz. The 6 correlation peaks represent the decorrelated polarization modes, as signal copies are used for all transmitted channels where no correlation exists within the MIMO equalizer window.

7.2 Phase offset estimation

Clearly related to frequency offset estimation is phase offset estimation, and due to the high baud rate of the transmitted symbols, phase offset is capable of tracking the frequency offset between the transmitter laser and LO. In optical transmission systems, two main phase estimators are commonly employed: the n^{th} order V-V estimator, and the Costas loop. The Costas loop consists of a phase detector, or Costas detector, and a DPLL. The DPLL scheme outperforms the V-V scheme, as it performs close to the MCRB [192]. However, to achieve this, only a small feedback delay is allowed in the feedback loop. Any delay in the feedback path reduces both the tracking performance, and the lock-in range. Therefore, both carrier phase offset estimators are considered in this section.

7.2.1 n^{th} order Viterbi-Viterbi phase estimator

The n^{th} order V-V phase estimator was originally introduced by A.J. Viterbi and A.M. Viterbi in 1983 [194] for phase shift keyed transmitted signals. The phase estimated output i can be denoted as [187]

$$\varphi_i[k] = \frac{\arg \left\{ \sum_{j=k-L_{\text{VV}}}^{k+L_{\text{VV}}} w_{\text{VV}}(j) \bar{s}_i^n[k+j] \right\}}{n}, \quad (7.3)$$

where n equals N_{const} and w_{VV} is the $2L_{\text{VV}}+1$ FIR filter weight, which allows for a windowing function and can be optimized based on the SNR of the received signal. Note that the argument input $\in \mathbb{C}$ is denoted as

$$-\pi \leq \tan^{-1} \left[\frac{\Im(z)}{\Re(z)} \right] \leq \pi. \quad (7.4)$$

When the received signal has a low OSNR ($\text{BER} \geq 10^{-3}$), a long window is preferred to average the influence of the zero-mean Gaussian noise. On the contrary, when a large phase noise is present, a small window is preferred. Phase noise originates from linear noise sources, which are the transmitter and LO laser linewidths, and a non-linear source, such as SPM [195]. Inherently, by having to

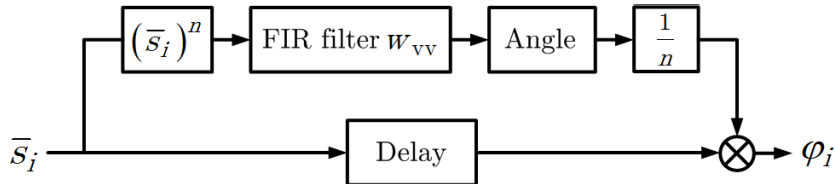


Fig. 7.2 V-V phase estimation algorithm for phase shift keyed transmitted signals.

take the future received signal into account for averaging, a delay is introduced. As the CPE is a part of the LMS-based equalizer, this introduced delay directly affects the MIMO equalizer too. For the CMA, the two DSP blocks operate independently. Eq. (7.3) is graphically shown in Fig. 7.2, where the most commonly used V-V phase estimator in optical transmission systems is the 4th order V-V phase estimator [196], as it relates to the transmission of QPSK symbols.

7.2.2 Costas loop

As previously mentioned, the Costas loop outperforms the V-V phase estimator [192], and performs close to the MCRB when no delays are introduced in the feedback loop [165]. Therefore, Costas loop based carrier recovery has been used in the experiments in Chapter 8. The Costas loop was first introduced by J.P. Costas in 1956 [197, 198], and consists of two components: a phase detector, and a phase locked loop feedback, as shown in Fig. 7.3. It is often implemented in copper-based and wireless transmission systems. The work by J.P. Costas in copper-based transmission was particularly important as it was the first to demonstrate that the offset carrier phase could be reliably removed from the received signal. The Costas loop including the digital phase locked loop and phase detector is shown in Fig. 7.3. Note that a first order phase locked loop can be used, but to avoid steady-state phase errors, generally a second order phase locked loop is employed [165]. In the figure, G_{PD} , G_1 , G_2 , and G_{NCO} represent the phase detector, first, second, and numerically controlled oscillator gains. It is also important to note that a DPLL based implementation has a lock-in range for reliable carrier recovery. Alternatively, in copper-based transmission systems, pilot-symbol assisted modulation is used to increase the lock-in range and reduce the error floor introduced by the Costas loop [165]. The same was effect noticed in optical transmission systems in [199].

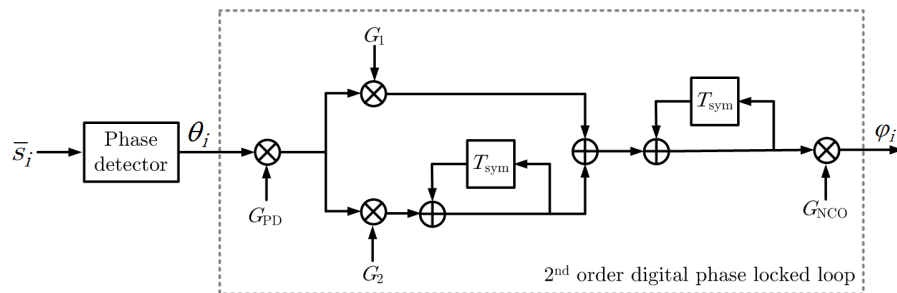


Fig. 7.3 Costas loop consisting of a phase detector and a digital phase locked loop.

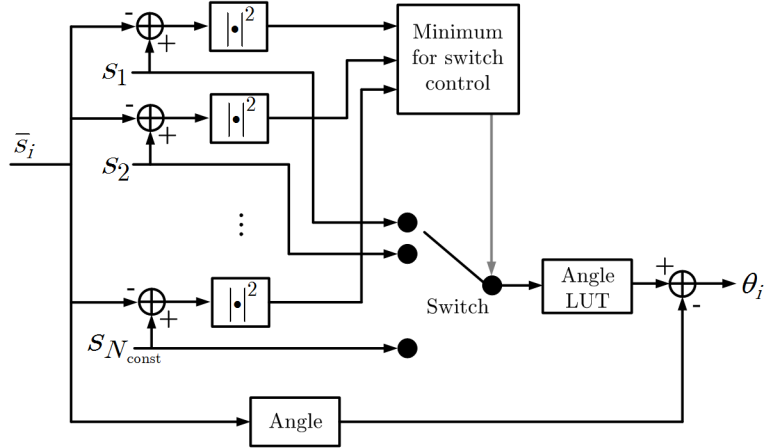


Fig. 7.4 2D maximum likelihood phase detector.

7.2.3 2D maximum-likelihood phase detector

As the phase detector plays a crucial role in phase estimation, it is particularly important to use the correct reference symbol. The reference symbol can be obtained in a data-aided or non-data-aided fashion, which can be changed according to the active MIMO updating algorithm. In the data-aided mode, the reference symbols are part of the training sequence, and during the non-data-aided estimation the reference symbols are maximum likelihood symbols. The most straightforward implementation is shown in Fig. 7.4, where the two dimensional Euclidian distance serves as the maximum likelihood estimator. This implementation is related to Fig. 6.8(b), where also 2D maximum likelihood Euclidian distance estimation was performed for the desired signal of the DD-LMS algorithm. The chosen dimensionality can also be four, which corresponds to the transmitted symbol dimensionality discussed in section 2.5.2. However, this adds an additional symbol delay in the feedback loop. The subtraction of the received symbol argument from the maximum likelihood argument is limited to the range from $-\pi$ to π . The computational complexity of the two dimensional phase detector is $1+4N_{\text{const}}$ RADDs and $2N_{\text{const}}$ RMULs per received symbol, where N_{const} represents the number of constellation points.

7.2.4 Argument-based phase detector

The second maximum likelihood phase detector is the argument-based phase detector, and is shown in Fig. 7.5. This particular phase detector is often used in optical transmission experiments such as in [200]. The computational complexity of the comparison stage is $1+N_{\text{angles}}$ RADDs and no RMULs. N_{angles} is 4, 8, 12, and

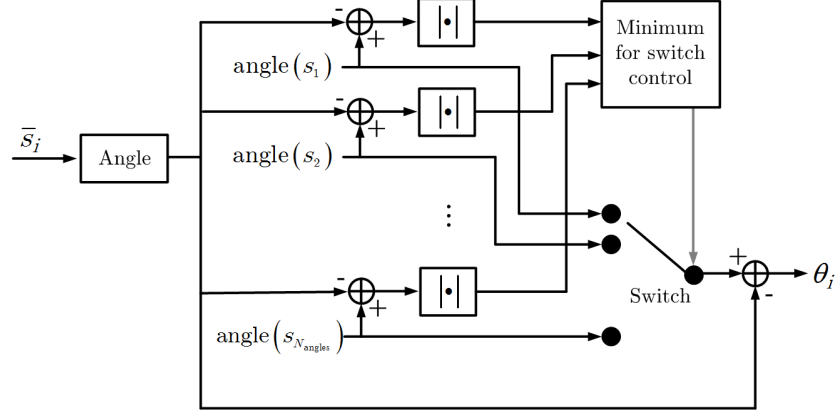


Fig. 7.5 Argument-based phase estimator.

28 for QPSK, 8, 16, and 32 QAM, respectively. Clearly, the computational complexity is lower than for the 2D phase detector, as a few constellation points have the same argument for higher order constellations. Therefore, a reduced number of Euclidian distance comparisons is required with respect to the multi-dimensional phase detector. Additionally, the Euclidian distance computation is only one dimensional, and hence avoids using any multiplications in the Euclidian distance computation. The downside however, is that the amplitude is not taken into account. For higher order symbols this may result in incorrect decisions.

7.2.5 2×1D phase detector

Further computational complexity reduction is achieved by using the 2×1D phase detector, which has been proposed in [r12], and is shown in Fig. 7.6. The comparison values per dimension are

$$\begin{aligned}
 \{-1, 1\}, & \quad \text{QPSK} \\
 \{-0.682, 0, 0.682\}, & \quad \text{8QAM} \\
 \{-1, -\frac{1}{3}, \frac{1}{3}, 1\}, & \quad \text{16QAM} \\
 \{-1, -\frac{3}{5}, -\frac{1}{5}, \frac{1}{5}, \frac{3}{5}, 1\}, & \quad \text{32QAM}
 \end{aligned} \tag{7.5}$$

with $N_{\text{real}} = N_{\text{imag}}$ representing the number of real and imaginary real-valued comparison points, respectively. The corresponding computational complexity per modulation format is $1 + 2N_{\text{real}}$ RADDs, and no multiplications are used. This results in 4, 6, 8, and 12 RADDs for QPSK, 8, 16, and 32 QAM constellations. Hence, the proposed phase detector has a substantial lower computational complexity than the argument-based phase detector, and in addition, takes the amplitude into account. However, using these one dimensional points results in 4,

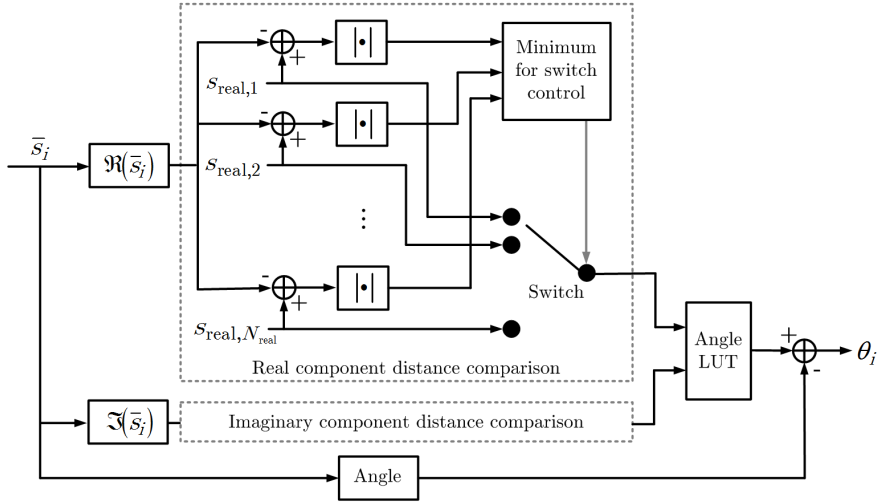


Fig. 7.6 Proposed $2 \times 1D$ phase detector.

9, 16, and 36 possible constellation locations for QPSK, 8, 16, and 32 QAM, respectively. Clearly, the downside of the proposed $2 \times 1D$ phase detector is that for non-square constellations (i.e. 8 and 32 QAM) solutions exist which are not part of the symbol space. When this occurs, the phase locked loop input argument is set to 0. Hence, no carrier phase update is performed. For square constellations this method allows for taking the higher order symbol points into account and therefore being more accurate in determining the maximum likelihood symbol than the argument-based phase detector can. The computational complexity reduction of the proposed $2 \times 1D$ phase detector exploits both one dimensional distance comparisons, as the argument-based phase detector does, and further reduces the number of comparisons with respect to the angular phase detector.

7.3 Joint CPE

As all transmitted channels share the same transmitter laser source, and same LO source, it is clear that the carrier offset is a common-mode impairment. Therefore, this can be exploited to further reduce the computational complexity, and has been reported on in [r7]. The most straightforward implementation of joint CPE is the master/slave (M/S) scheme, where the phase estimation of one master channel is used to compensate all transmitted (slave) channel offsets. It is recommended that the master channel chosen has the largest eigenvalue for optimal SNR performance. The M/S scheme was first proposed for optical communications in [169], and is shown in Fig. 7.7(a). This method achieves the lowest computational complexity possible, however, it is prone to performance degradation caused by phase mismatching between transmitted channels. The phase mismatching can originate

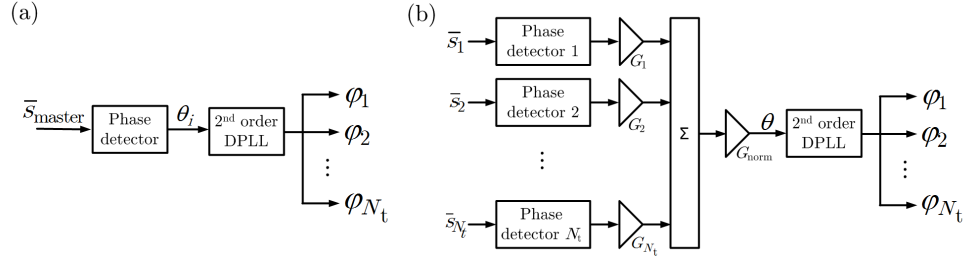


Fig. 7.7 Joint CPE algorithms. (a) Master/slave scheme, where the phase output of one channel controls the phase of all channels. (b) The proposed averaging scheme, a linear transform of all received channels controls the phase of all channels.

at the transmitter or the receiver side. In the perfect case, there is no phase-mismatching. An averaging method in the angular domain is proposed to minimize the phase-mismatching performance degradation is shown in Fig. 7.7(b). Here, either averaging over every channel takes place, or one statically chosen polarization per received mode is used, as two polarizations are generally phase-matched in the integrated receivers. Note that the channel gain G_i can correspond to the eigenvalues of the transmission system, where $G_{\text{norm}} = 1 / \sum G_i$. For simplicity in the presented case in Fig. 7.7(b), the gain for all odd channels is 1, and the gain for all even channels is 0. The computational complexity of the proposed averaging scheme is higher than the M/S scheme, but substantially lower than using one CPE block per received channel.

The CPE performance for the 41.7 km 3 spatial LP mode transmission system described in Chapter 8 is investigated, where due to transmitter side channel decorrelation phase-mismatching is inevitable. The performance comparison is shown in Fig. 7.8 for QPSK, 8, 16, and 32 QAM transmission. The scheme where one DPLL is used per transmitted channel is denoted as the 6-DPLL scheme. Here, 6 corresponds to the number of used polarization channels. Starting with the performance of QPSK transmission, depicted in Fig. 7.8(a), no penalty and 0.3 dB OSNR penalty is noticed at the HD-FEC limit for averaging and M/S, respectively. At the SD-FEC limit all schemes perform the same. The results of 6×8 QAM transmission are shown in Fig. 7.8(b). With respect to the 6-DPLL scheme, an OSNR penalty of 0.1 dB and 0.37 dB is observed at the 7% HD-FEC limit for averaging and M/S, respectively. Again, the averaging method is following the performance trend of the 6 DPLLs. Therefore, from Fig. 7.8(b) it can be observed that higher order constellations pose no issue for a single DPLL with averaging. Note that the M/S method has an increased penalty. Doubling the number of constellation points, and hence adding one additional bit per symbol, results in the

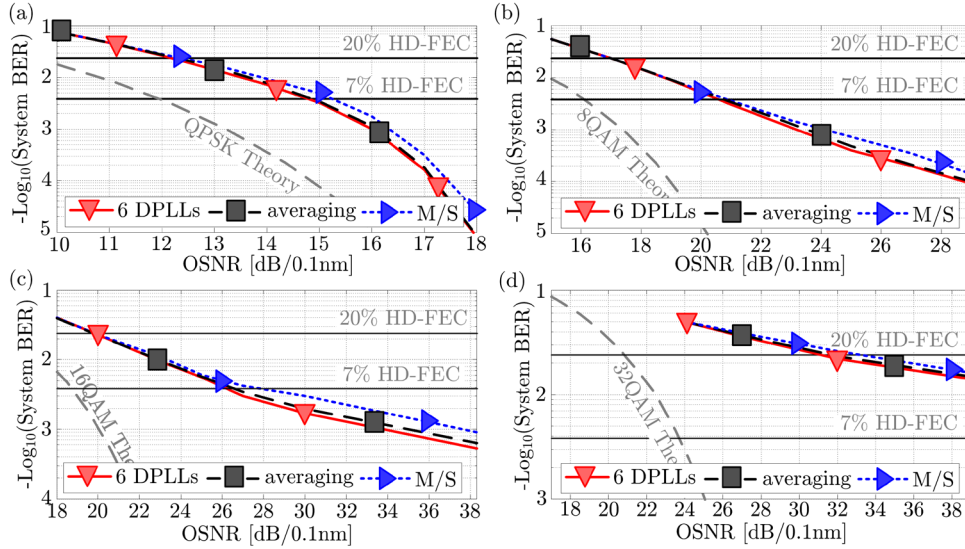


Fig. 7.8 41.7 km 3 spatial LP mode transmission performance of the two joint CPE schemes for (a) QPSK, (b) 8 QAM, (c) 16 QAM, and (d) 32 QAM.

16 QAM constellation, where the BER performance of the 3 methods is shown in Fig. 7.8(c). With respect to the 6-DPLL scheme, a 0.3 dB and 1.6 dB OSNR penalty is observed at the 7% HD-FEC limit for the averaging and M/S scheme, respectively. Clearly, in this case the averaging method is greatly outperforming the M/S scheme. This performance difference is attributed to small variations in the carrier phase offset between the channels, i.e. the common-mode impairment is similar, but not exactly the same for each transmitted polarization mode channel. At the 20% SD-FEC limit, no penalty is observed for either method. Note that the BER floor is slightly increased for both the averaging and M/S schemes with respect to the 6-DPLL setup. Finally, 32 QAM performance is shown in Fig. 7.8(d). As the performance of 32 QAM transmission does not reach the 7% HD-FEC limit, only the 20% SD-FEC limit can serve as a performance indicator. From Fig. 7.8(d) it can be observed that the OSNR penalty is 0.5 dB and 2.1 dB for averaging and M/S schemes, respectively. Again, averaging clearly outperforms the M/S performance, whilst significantly reducing the computational complexity with respect to the 6-DPLL setup. Similar to the 16 QAM OSNR performance, the BER floor is slightly increased for both the averaging and M/S schemes with respect to the 6-DPLL setup.

In addition, it is interesting to quantify the proposed method's tolerance to nonlinearities, which becomes more stringent for higher order modulation formats such as 16 and 32 QAM. As previously indicated, the best performance is achieved

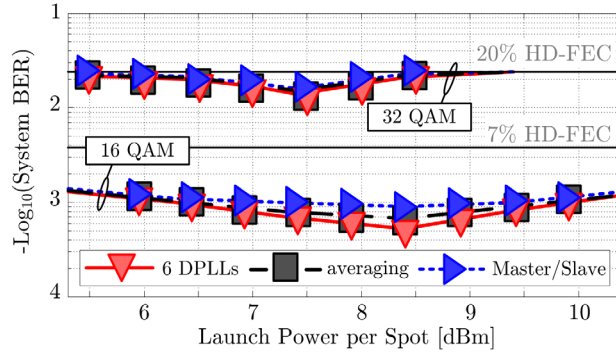


Fig. 7.9 41.7 km 3 spatial LP mode nonlinear transmission performance of the two joint CPE schemes with respect to the conventional one DPLL per transmitted channel.

by the 6-DPLL scheme. However, as Fig. 7.9 shows, the nonlinear performance of both the averaging method and M/S for 16 and 32 QAM transmission closely follows the 6-DPLL performance. With respect to the performance in the non-linear regime, it is possible to conclude that the M/S and particularly the averaging CPE scheme perform similar to the conventional 6-DPLL performance.

The main difficulty of employing a joint CPE scheme is that all MIMO equalizer outputs must be synchronized, which results in an increase in timing constraints when designing the receiver DSP. Therefore, from an implementation point of view, the original multi-DPLL scheme with higher complexity remains attractive.

7.4 Cycle slipping

Over time, the CPE estimate exhibits small random fluctuations around a stable operating point [158], which consists of noise contributions and disturbances. Cycle slipping occurs when the estimate moves away from the stable operating point, into a neighbouring stable point. Accordingly, the CPE stage tracks the carrier phase in that stable point, which results in a continuous series of symbol errors, and hence causes outage. The highest probability of cycle slips occurring is when a burst of errors is received. Note that cycle slipping is a highly non-linear effect and very unpredictable, and the probability of occurrence is a few orders of magnitude smaller than the decision error probability [158]. Consequently, transmission in the low OSNR regime is more prone to cycle slipping [201].

Methods to prevent cycle slipping from occurring are inserting known sequences or differentially encoding symbols [202]. The former method allows for correcting the phase tracking estimate, which results in a maximum of one consecutive data

packet being incorrectly received. This comes at the cost of transmission overhead. By differentially encoding symbols, information is encoded in the differential of two consecutive symbols, rather than encoding the symbol itself. Therefore, when cycle slipping occurs, the relative phase between two consecutive symbols remains correct. The primary issue with differentially encoding symbols is a substantial performance degradation for soft-decision error correcting with respect to conventional symbol encoding [203].

7.5 Summary

This chapter details CPE algorithms which estimate and compensate the frequency offset between the transmitter laser and LO. Furthermore, these algorithms minimize the influence of phase variations over time. In section 7.1 frequency offset estimation has been performed using data-aided LS channel estimation, as it provides the best performance possible which is close to the MCRB. Non-data-aided techniques have been mentioned, however, none can provide the accuracy LS estimation offers. Furthermore, in section 7.2 phase estimation algorithms have been discussed. The most commonly used phase estimators in optical transmission systems are the V-V algorithm, and the Costas loop. The Costas loop consists of a DPLL and a phase detector, where a low computational complexity $2 \times 1D$ PD acts as PD.

In addition, it was noted that the transmitter channels share the same laser source, and the LOs share the same laser source. Therefore, carrier phase offsets can be considered as a common-mode impairment. To this end, two joint CPE schemes have been employed, and compared to the conventional CPE scheme for a 41.7 km 3 spatial mode transmission of QPSK, 8, 16, and 32 QAM symbols. The corresponding conventional scheme is denoted as the 6-DPLL scheme. The joint CPE schemes are the master/slave scheme, and the averaging of the phase detector outputs of multiple channels. Both joint CPE schemes employ only one DPLL. The master/slave scheme has the lowest complexity, and the worst performance. The Averaging scheme performs similarly (0.5 dB OSNR penalty for 32 QAM transmission at the SD-FEC limit) to the conventional 6-DPLL scheme, while being marginally higher in computational complexity than the master/slave scheme. Furthermore, it has been demonstrated that the proposed joint CPE Averaging scheme behaves similarly for nonlinear transmission impairments in comparison to the conventional 6-DPLL CPE scheme.

Chapter 8

Experimental transmission system results

No amount of experimentation can ever prove me right; a single experiment can prove me wrong.

Albert Einstein

In the previous chapters, the theory behind MIMO transmission, the optical transmission medium, and the transmitter and receiver side DSP have been detailed. This chapter⁶ combines all the previous work in an experimental transmission setup, and verifies the operation of the implemented DSP algorithms in combination with the experimental optical subsystems, including optical mode multiplexers, fibers and demultiplexers.

The first experimental fiber investigated is a 41.7 km solid-core GI 3MF, which is based on MMF refractive index profile designs, and for which the optical transmission system is detailed in section 8.1. For this particular fiber, the OSNR performance of conventional 2D constellations has been verified in section 8.1.1 by the transmission of QPSK, 8, 16, and 32 QAM at 28 GBaud. Additionally, 4D constellations have been transmitted in section 8.1.1, which has resulted in the first 6×4D experimental constellation transmission. Note that the 6 denotes the number of mixed independent transmission channels, which correspond to the polarization spatial paths in the optical domain. The 4D constellations are TS-QPSK, 32-SP-QAM, and 128-SP-QAM, which have been detailed in section 2.6. Furthermore, delay-diversity space-time coding (STC) has been applied to the 3MF transmission system in section 8.1.2. This is the first STC MIMO transmission in optical SDM communications. Instead of increasing the maximum throughput, STC increases OSNR tolerances and provides a tradeoff between transmission performance characteristics. This work indicates that 3MFs can achieve the same throughput as SSMFs with increased OSNR tolerances. Finally, a multipoint-to-point transmission system is investigated, where the 3MF's inputs are decorrelated on laser coherence.

⁶ This chapter incorporates results from the author's contributions [r3], [r4], [r14], [r29], [r30], [r34], and [r36].

This work verifies that a future multipoint-to-point system is possible, where in a single location three SSMF inputs from 3 locations can be combined to form a single 3MF transmission system. The second experimental fiber investigated is a 0.95 km 19 cell HC-PBGF, which is not based on any commercially available fiber, and is detailed in section 8.2. The 0.95 km represents the longest HC-PBGF transmission distance reported on for a coherent transmission system. A 32 wavelength carrier single mode transmission is demonstrated with 16 and 32 QAM constellation sequences, achieving a HC-PBGF record distance \times bandwidth product of 8.5 Tbit \cdot km. Finally, to combine both multimode and multi-core aspects of spatial division multiplexing, a 1 km SI 7-core FM-MCF is experimentally verified in section 8.3, where each core allows the co-propagation of 3 spatial LP modes. By employing 50 wavelength carriers, each modulated with a 24.3 GBaud 32 QAM signal, a gross throughput rate of 255 Tbit s⁻¹ was achieved with a gross spectral efficiency of 102 bits s⁻¹ Hz⁻¹.

8.1 Solid-core 3MF transmission

In this section the experimental solid-core 3MF transmission work is described. First, the 3MF transmission setup is detailed, where 2D and 4D transmission constellations have been transmitted [r3]. Then, space-time coding is applied to conventional 2D transmission formats to indicate the potential transmission distance increase by employing 3MFs instead of SSMFs [r29]. Finally, a potential 3MF aggregate network is investigated where three separated transmitter locations are used and received on one receiver site [r30].

8.1.1 41.7 km 3MF transmission setup

The current generation 3MF experimental setups employ GI 3MFs which allow the co-propagation of three spatial LP modes, denoted as the LP₀₁, LP_{11a}, and LP_{11b} mode [129, 204, 205]. By engineering the refractive index profile, the DMD of the 3MF can be controlled, as discussed in section 3.4.1. The experimental setup used is depicted in Fig. 8.1. At the transmitter side, a 1555.75 nm transmitter external cavity laser (ECL) with linewidth < 100 kHz is used. The output is guided through an IQ-modulator, where the laser light is modulated by a 28 GBaud signal. The IQ-modulator is driven by two DACs, which represent the in-phase (real) and quadrature (imaginary) components of the transmitted 2D constellation. The transmitted 2D constellations under investigation are QPSK (2 bits symbol⁻¹), 8 QAM (3 bits symbol⁻¹), and 16 QAM (4 bits symbol⁻¹), and the 4D constellations are TS-QPSK (1.5 bits symbol⁻¹), 32-SP-QAM (2.5 bits symbol⁻¹), and 128-SP-

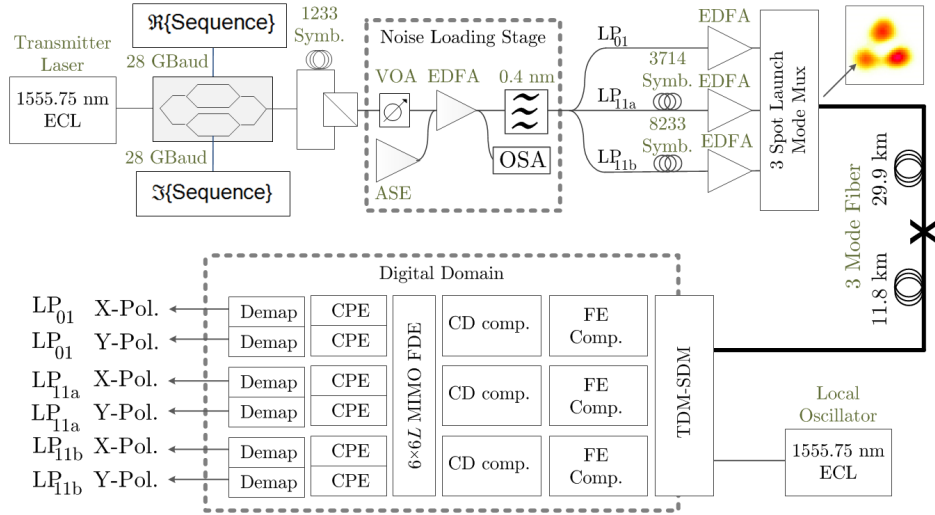


Fig. 8.1 41.7 km 3MF experimental setup. Inset: spot launcher camera image.

QAM (3.5 bits symbol⁻¹). Two consecutive 2D constellations in time are chosen to form a 4D constellation. Hence, when converting the bits per symbol to 2D constellation time-slots, the bits per symbol rate of the 4D formats is reduced by 50%. All transmitted constellations have been described in section 2.5.2. The transmitted sequences are formed in the digital domain by a number of fully uncorrelated PRBSs, each of length 2^{15} , which avoids any correlation within the 2^{15} symbol sequence as described in section 2.6.2. The output of the IQ-modulator is split, and one arm is delayed by 44 ns (1233 symbols) for polarization decorrelation. After recombining the two arms, the DP signal is noise loaded to characterize the optical OSNR system performance. To achieve 3 DP multiplexed mode channels, the noise loaded signal is split into three equal outputs. Two arms are delayed for mode decorrelation by 132 ns (3714 symbols) and 294 ns (8233 symbols), respectively. The signal along each arm is separately amplified before going into the MMUX. The launch power was 8.5 dBm for QPSK, 8, and 16 QAM, and 7.5 dBm for 32 QAM. The optimum launch power is shown in Fig. 7.9 for 16 and 32 QAM. As a MMUX, the single prism spot launcher described in section 4.3

	3MF 1	3MF 2	Unit
Length	29.9	11.8	km
DMD	+2.00	+1.82	ns
GVD LP ₀₁	19.8	19.9	ps nm ⁻¹ km ⁻¹
GVD LP ₁₁	20	20.1	ps nm ⁻¹ km ⁻¹
A _{eff} LP ₀₁	95	96	μm ²
A _{eff} LP ₁₁	95	95	μm ²

Table 8.1 3MF span properties.

is used, which results in the equal excitation of the three LP modes, guaranteeing full mixing. For all inputs, the MMUX insertion losses are approximately 4.5 dB. The transmission link consists of two 3MF spans with respective lengths of 29.9 and 11.8 km, where the 3MF span characteristics are detailed in Table 8.1. At the receiver side, a reciprocal setup of the MMUX comprising a single prism splits the 3MF output into 3 separate fully mixed DP outputs. The insertion loss of the MDUMX is approximately equal to the MMUX with 4.5 dB for each respective output. At the receiver side, the three MDMUX outputs are received using the TDM-SDM receiver described in section 5.3. This receiver acts as 12 (3 spatial LP modes \times 2 polarizations \times 2 real-valued QAM constellation axes) ADCs. The captured data is then post-processed offline, which follows the structure of this work. In the digital domain, first the optical FE impairments are compensated. Then, adaptive rate conversion is applied, and the GVD is removed. To unravel the channels a low computational complexity $6 \times 6L$ MIMO FDE with an DFT size of 256 is used, which corresponds to an equalization window of 4.52 ns, and is larger than the combined 3MF residual DMD. The weight matrix \mathbf{W} of the FDE is heuristically updated using the LMS algorithm during convergence and DD-LMS during data transmission, and is shown in Fig. 8.2 after convergence. From Fig. 8.2 can be observed that the DMD of the combined fiber span is 3.82 ns, which

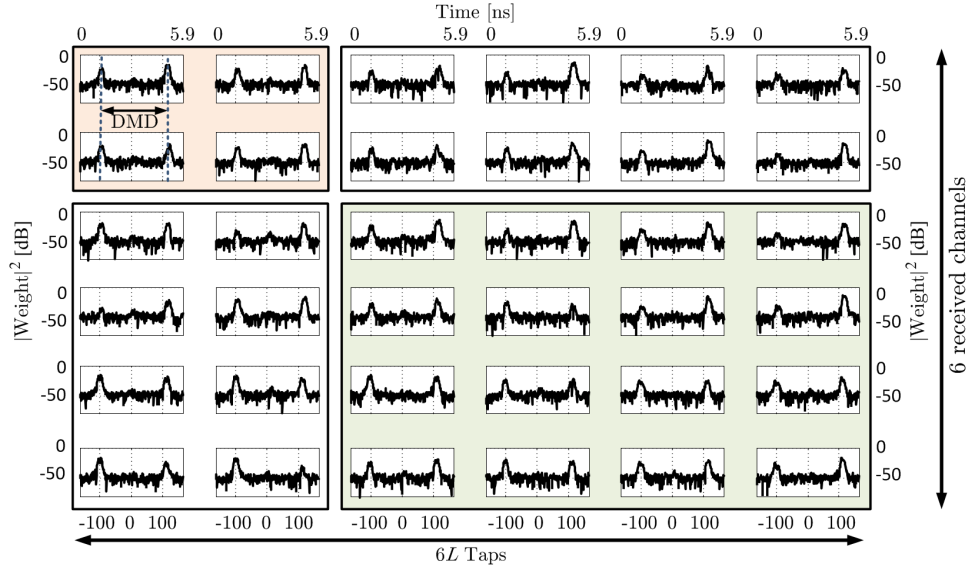


Fig. 8.2 $6 \times 6L$ weight matrix \mathbf{W} after 41.7 km 3MF transmission. Top left sub matrix represents the \mathbf{W}_{LP01} of size $[2 \times 2L]$, and the bottom right sub matrix represents \mathbf{W}_{LP11} of size $[4 \times 4L]$. The remaining sub matrices represent intermodal crosstalk.

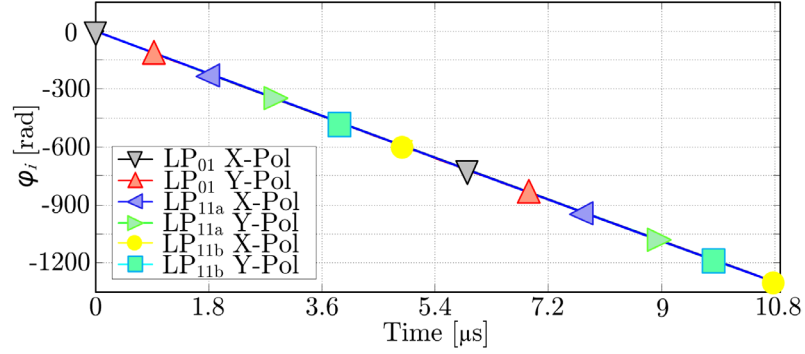


Fig. 8.3 Costas loop phase response over time for 41.7 km 3MF transmission of all 6 received channels.

corresponds to the two peaks in each weight matrix element. This indicates the advantage of employing DSP to accurately characterize the optical transmission system under test.

Since the 4D constellation consists of the concatenation of two 2D constellations, as discussed in section 2.5, the weight updating algorithms are the exactly the same for all formats. In section 6.2, it was shown that the $6 \times 6L$ MIMO equalizer can be rewritten as six independent $1 \times 6L$ equalizers, without affecting the equalizer's complexity. The benefit of coding 4D symbols in time is that only one output is used per 4D-symbol, which reduces the timing alignment complexity between MIMO outputs with respect to coding a 4D-symbol onto two separate outputs. To compensate the frequency offset between the transmitter laser and LO, one Costas loop per transmitted channel is used and the carrier offset tracking over time for all transmitted channels is shown in Fig. 8.3. This figure corroborates the assumptions made in section 7.3, where joint CPE was proposed. After this stage, the received constellations are demapped, and the BER is measured. The presented BER in this section is averaged over 2 captures, where each capture represents 310,000 2D symbols. The first 25,000 symbols are used for convergence, which results in system BER averaging over 3.42 million 2D symbols, or 1.71 (3.41/2) million 4D constellations symbols.

The measurement results for both single mode BTB and 41.7 km 3MF transmission are shown in Fig. 8.4, where the performance of the 2D and 4D constellations is shown in Fig. 8.4(a) and Fig. 8.4(b), respectively. For clarity, the 6×6 few-mode BTB results have been omitted in Fig. 8.4 as the OSNR penalty between 6×6 BTB and 41.7 km few-mode fiber transmission was measured to be under 0.2 dB for 16

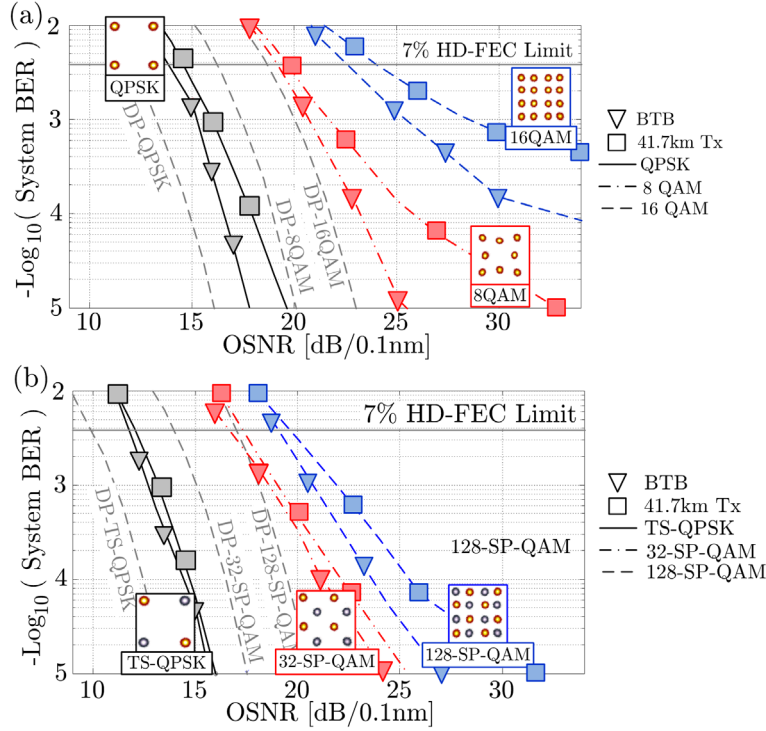


Fig. 8.4 Experimental 41.7 km 3MF transmission performance of (a) 2D constellations, and (b) 4D constellations.

QAM. Here, the HD-FEC limit crossing point is considered to be the primary performance indicator. Accordingly, Table 8.2 denotes the HD-FEC limit OSNR crossing value of all the transmitted constellations for the theoretical limit in the second column. The measured BTB OSNR penalty with respect to the theoretical crossing point is shown in the third column of Table 8.2, where the actual crossing OSNR value is denoted in brackets. To complete the table, in the fourth column, the OSNR penalty after 41.7 km few-mode fiber transmission is denoted. Again, in between brackets the measured OSNR crossing point is given. From the trends

Constellation	Theory OSNR at HD-FEC-limit [dB]	BTB penalty w.r.t theory	6×6 Transmission penalty w.r.t theory
TS-QPSK	9.9	1.9 (11.8)	2.1 (12)
QPSK	12.1	1.9 (14)	2.5 (14.6)
32-SP-QAM	14	2.7 (16.7)	3.3 (17.3)
8 QAM	16.2	2.9 (19.1)	3.5 (19.7)
128-SP-QAM	17	1.8 (18.8)	2.5 (19.5)
16 QAM	18.7	3.9 (22.6)	5.3 (24)

Table 8.2 BTB and 6×6 MIMO transmission OSNR penalties with respect to the theoretical limit. In brackets are the OSNR values for BTB and the 6×6 transmission case at the HD-FEC limit.

shown in Fig. 8.4(a) and Fig. 8.4(b) and outlined in Table 8.2, it is clear that the OSNR penalty substantially increases for the 2D formats when scaling to a higher number of constellation points. However, for the 4D formats, the OSNR penalty marginally increases. Note that the performance with respect to theory for 32-SP-QAM is not as good as the performance of 128-SP-QAM. This issue may be caused by the carrier recovery algorithm, which requires more constellation points to perform optimally. This was also noted in [58], where a similar performance difference was observed in SSMF transmission. Through this, it can be concluded that the optimum 4D constellations are TS-QPSK and 128-SP-QAM. From Fig. 8.4 and Table 8.2, another interesting observation can be made, even though the theoretical limit for 128-SP-QAM is higher than 8 QAM. After transmission, 128-SP-QAM ($28 \times 6 \times 3.5 = 588 \text{ Gb s}^{-1}$ gross throughput rate) outperforms 8 QAM ($28 \times 6 \times 3 = 504 \text{ Gb s}^{-1}$ gross throughput rate), whilst carrying an additional 0.5 bit symbol⁻¹. Finally, from Fig. 8.4 it can be observed that the 4D constellation BER curves after transmission follow the BTB curves closer than the respective 2D constellations.

From the 41.7 km transmission case, it is established that the improved OSNR margin provides a case for 4D constellations to be employed in FMF transmission systems, where the dimensionality could be increased further in the future. As previously noted, a similar OSNR margin improvement was observed for SSMF transmission systems [58], but is more pronounced in 3MF transmission systems. Accordingly, these tolerances indicate that 4D constellations potentially allow more energy efficient data transmission than their respective 2D counterparts [59].

8.1.2 Space-time diversity

In section 8.1.1, it was shown that the 3MF offers a linear increase in transmission throughput. However, the 3MF transmission system can also be used to improve the transmission quality of DP transmission through exploiting STCs [187], as proposed in [r30]. This is the first time STC has been performed for an optical SDM transmission system, which allows for making a trade-off between throughput and performance, potentially managed by software, hence adding an extra dimension to future flex-grid transmission systems. For STC transmission systems, there are three main contenders: space-time trellis codes (STTCs) [206], orthogonal STCs [207], and delay diversity. The latter two are linear space-time block codes (STBCs) and have a lower implementation complexity than trellis codes. Although the STTCs offer improved performance over the linear variants, for high data rate optical transmission systems complexity is a key factor [208]. Therefore, the two linear STBCs are of primary interest, where the orthogonal STBCs are linear codes

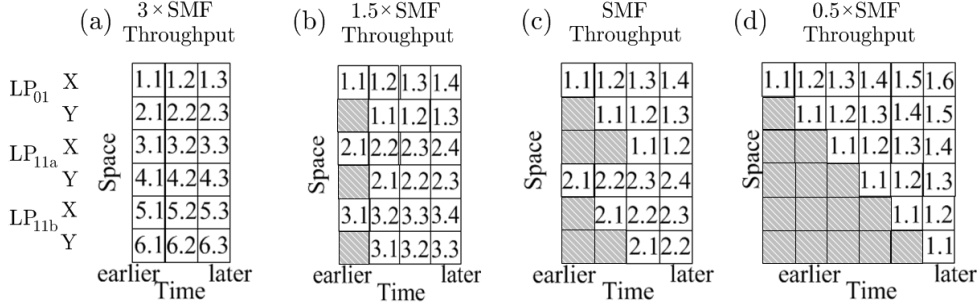


Fig. 8.5 STC block coding where the block notation (i,j) denotes the i^{th} transmission channel of the j^{th} time slot for (a) V-BLAST, (b) 3 channels, (c) 2 channels, and (d) 1 channel. The gray blocks represent data blocks in the past.

from which the data is formed as unitary transmission matrices. The most well-known orthogonal STBCs are Alamouti and Tarokh codes [207, 208]. However, these only exist for certain numbers of transmitters. To this end, we use the simplest STBCs, purely exploiting the space and delay diversity, where delayed signal copies are transmitted over a number of transmitters in certain time slots. This corresponds to the experimental setup detailed in section 8.1.1. Fig. 8.5 depicts four possible cases of the proposed STC scheme, delay-diversity STBCs, where (a) 6, (b) 3, (c) 2, or (d) 1 channel are transmitted. As SSMFs allows two polarizations to co-propagate, case (c) provides the best performance comparison. Note that the block lengths in Fig. 8.5 must be larger than the MIMO equalizer length to fully exploit the space and delay diversity without data correlation. To investigate the performance improvement 3MFs can offer for conventional 2D constellation transmission, the same experimental setup as described in section 8.1.1 is employed. Hence, the transmitter side delays reflect the block time slots in Fig. 8.5. At the receiver side, regular MIMO equalization is performed. Demapping the constellations is performed after MIMO equalization, where respective outputs are delayed and averaged to obtain the received symbol values.

To this end, Fig. 8.6 shows the performance results of the STC 3MF transmission experiment for (a) QPSK, (b) 8, (c) 16, and (d) 32 QAM. As the primary performance indicator, the 7% HD-FEC limit is used. For 41.7 km 3MF QPSK transmission, as shown in Fig. 8.6(a), for threefold throughput increase there is a 0.55 dB OSNR penalty at the HD-FEC limit with respect to SMF BTB performance. Note that the baud rate is kept constant. When applying STBC on two copies for a single channel, the 3MF transmission already outperforms the theoretical SMF performance. However, by doing so, the 3MF transmission throughput is reduced to $1.5 \times$ the SMF throughput. When using a three channel

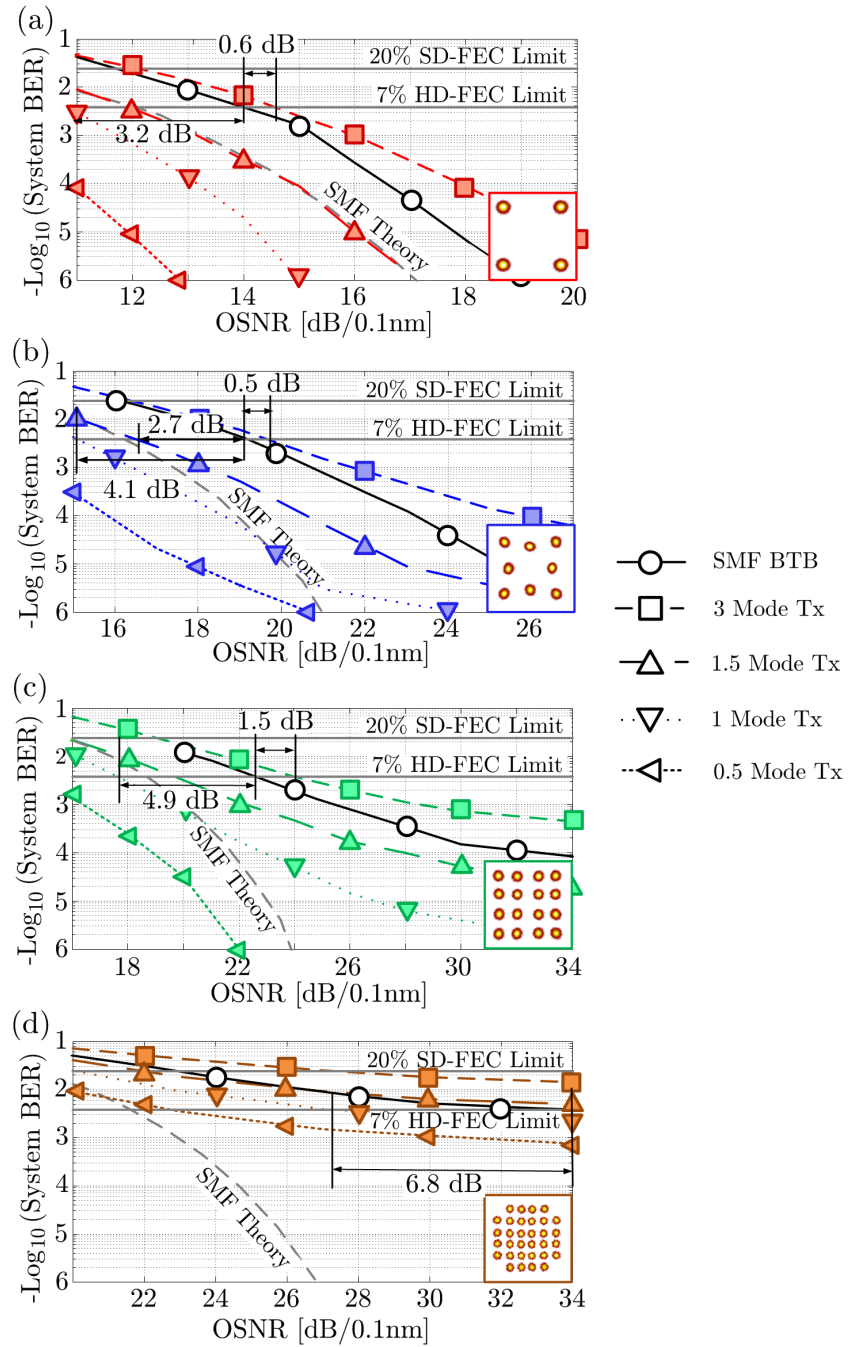


Fig. 8.6 STC with respect to BTB SMF transmission for (a) QPSK, (b) 8 QAM, (c) 16 QAM, and (d) 32 QAM. For the same throughput, 3MFs offer a higher OSNR tolerance than SSMFs theoretically can offer.

STBC, the STC 3MF throughput equals SMF throughput, and the corresponding OSNR gain is approximately 3.2 dB. As for QPSK, the same STBCs can be applied to the 8 QAM 41.7 km 3MF transmission system, and the corresponding performance is shown in Fig. 8.6(b). For threefold throughput increase there is a 0.55 dB OSNR penalty with respect to SMF BTB performance. A performance gain of 2.7 dB and 4.1 dB is observed when comparing the 3MF throughput of $1.5\times$ and $1\times$ SMF throughput to SMF BTB, respectively. Hence, STC can be used to exceed SMF transmission performance. Furthermore, the performance of 16 QAM 41.7 km 3MF transmission is investigated, and the corresponding performance is shown in Fig. 8.6(c). The $3\times$ SMF throughput OSNR penalty with respect to SMF BTB is 1.5 dB. When applying STBCs, and hence reducing the 3MF transmission system throughput to SMF throughput, an OSNR gain of 4.9 dB OSNR is observed. Finally, the 32 QAM 41.7 km 3MF transmission performance is shown in Fig. 8.6(d). Here, for successful 3MF transmission at $3\times$ SMF throughput, SD-FEC is required. Full system throughput does not reach the HD-FEC threshold. However, when STBC transmission is applied, a 6.8 dB OSNR performance gain is observed at the HD-FEC limit with respect to the SMF BTB performance.

For clarity, the OSNR gains at the HD-FEC limit with respect to SMF BTB have been summarized in Table 8.3. Naturally, such enormous OSNR gains come at a cost: DSP complexity and coherent receivers with corresponding ADCs. Instead of using a single DP coherent receiver, now three DP coherent receivers are required. Additionally, for future long-haul transmission, MM-EDFAs are needed. Therefore, high financial investments are required for such transmission systems, which makes STC more interesting for potential flex-grid SDM applications rather than merely for OSNR performance gains. Nevertheless, STCs provide a case for potential SDM flex-grid applications in the future.

Constellation type	HD-FEC limit OSNR gain, with DP capacity multiplier [dB]			
	$3\times$	$1.5\times$	$1\times$	$0.5\times$
QPSK	-0.6	+0.3	+3.2	n/a
8 QAM	-0.5	+2.7	+4.1	n/a
16 QAM	-1.5	+2.9	+4.9	n/a
32 QAM	n/a	n/a	+6.8	+10.1

Table 8.3 OSNR gains for various 2D constellations and capacities.

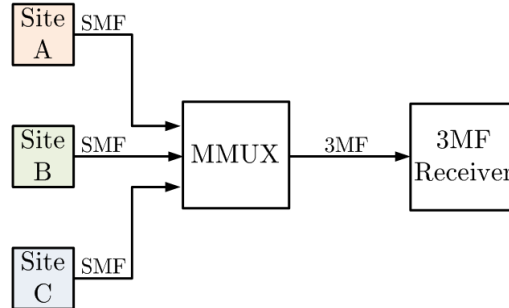


Fig. 8.7 Multipoint-to-point network, where 3 SMFs are combined to one 3MF transmission system using a MMUX.

8.1.3 Multipoint-to-point 3MF aggregate network

Thus far in section 8.1 a point-to-point transmission system has been described. However, when considering a MIMO transmission network, multiple SMF transmitters at various locations can be routed to one single point where they are combined to form a point-to-point SDM transmission system, which is interesting for potential network upgrading scenarios [209]. At the receiver side, all mixed channels have to be unravelled simultaneously, and therefore only a single point is considered. This results in a multipoint-to-point network, as shown in Fig. 8.7. Again, the experimental setup described in section 8.1.1 is used, where the transmitter side decorrelation delays have been changed. The LP_{01} mode remains the reference mode, and 10 and 25 km SMFs have been inserted in the LP_{11a} and LP_{11b} delay paths, respectively. These delays have been chosen on fiber availability in the laboratory and ensure loss of laser coherence, as the employed 100 kHz linewidth ECL coherence length is approximately 1 km. Data-aided LS frequency offset and channel estimation described in section 2.3.1 was used to confirm that all transmitted channels are fully decorrelated signal copies in the MIMO equalizer window. Fig. 8.9 shows the phase response over time of the independently operating Costas loops, detailed in section 7.2.2, indicating phase independence between the transmitted sources. The 41.7 km 3MF multipoint-to-point system transmission performance is shown for QPSK, 8, 16, and 32 QAM in Fig. 8.8 with respect to the conventional 41.7 km point-to-point 3MF performance described in

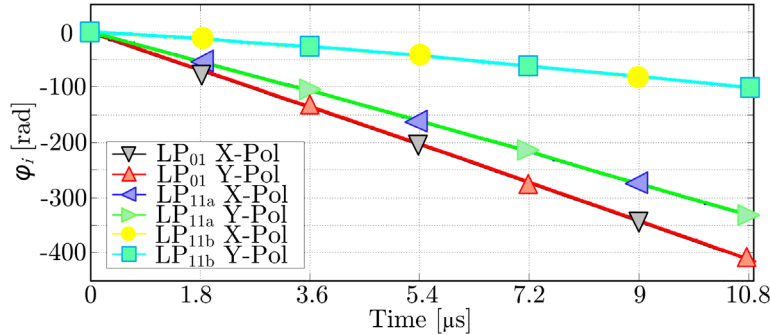


Fig. 8.9 Multipoint-to-point transmission system Costas loop phase response over time for 41.7 km 3MF transmission of all 6 received channels.

section 8.1.1. Due to the laser coherence loss, an OSNR penalty is expected. For QPSK transmission, virtually no OSNR penalty is noticed, whereas an increased error floor for 8 QAM transmission is observed at high OSNR. As the number of constellation points increases, the error floor increase becomes more pronounced. Note that in the experimental setup the same laser source is used, whereas in a real multipoint-to-point network case independent ECLs are used, in which a further increased performance penalty is expected due to the larger differences in carrier frequencies.

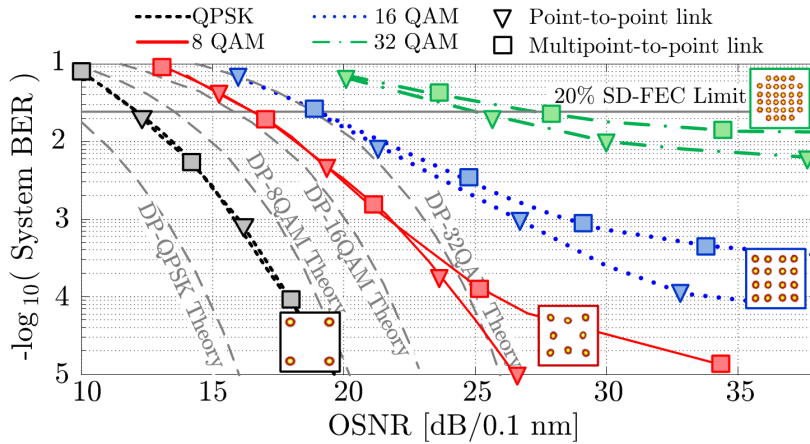


Fig. 8.8 Multipoint-to-point transmission performance, with respect to point-to-point transmission.

8.2 Hollow-core photonic bandgap fiber

The HC-PBGF is the second experimental multimode fiber investigated, and is reported on in [r32]. Unlike the solid-core 3MF, which is based on solid-core designs, the HC-PBGF is not based on any commercially available solid-core fiber. The key interests to study the HC-PBGF for optical transmission systems are

- An ultra-high nonlinear coefficient, 3 orders of magnitude higher than SSMFs [79].
- A group velocity close to speed of light in vacuum. The low-latency property is particularly interesting for gaining a competitive advantage for financial services, where every picosecond counts.
- An optimum attenuation figure below the fundamental limit of fused silica ($\sim 0.148 \text{ dB km}^{-1}$ [210]), with $< 0.1 \text{ dB km}^{-1}$ at the $2 \text{ }\mu\text{m}$ wavelength region [211, 212]. The work in [r32] is focused at 1550 nm transmission, which corresponds to the operating wavelength of conventional components.

Similar to the solid-core based 3MF, DSP can aid in quantitatively investigating the transmission performance of this experimental HC-PBGF. In this particular case, a dual-polarization channel is transmitted over the multimode HC-PBGF, where the DSP allows for characterizing the PDL. In addition, the fiber's impulse response is obtained through LS CSI estimation. The HC-PBGF investigated is a 0.95 km 19 cell HC-PBGF, of which a scanning electron microscope (SEM) image is depicted in the inset of Fig. 8.10(a). The core structure has a diameter of $28.5 \text{ }\mu\text{m}$, and has a micro-structured cladding designed for wavelength operation around $1.5 \text{ }\mu\text{m}$. The average inter hole spacing is around $5 \text{ }\mu\text{m}$, and the relative hole size is approximately 0.97. The 0.95 km transmission distance represents the longest HC-PBGF coherent transmission experiment, where the main limitation of the transmission distance is twofold; the fiber drawing capabilities and corresponding manufacturing costs of the HC-PBGF. The HC-PBGF is formed by a hexagonal structure, periodically arranged in the cladding, to create a photonic bandgap. Currently, as the HC-PBGFs are still very experimental, the attenuation figures are not close to the theoretical limit with low-loss records of approximately 3 dB km^{-1} at 1550 nm , and are being improved. The 19 cell HC-PBGF impulse response, attenuation, and relative diameter deviation, measured over the entire length, are shown in Fig. 8.10(b), (c), and (d), respectively. From Fig. 8.10(c) it can be observed that the minimum loss of 8 dB km^{-1} is at approximately $1.51 \text{ }\mu\text{m}$. The average attenuation in the C-band is 9 dB km^{-1} . This figure can be improved in the future through controlling the scattering surface modes [213], and the development of larger core designs.

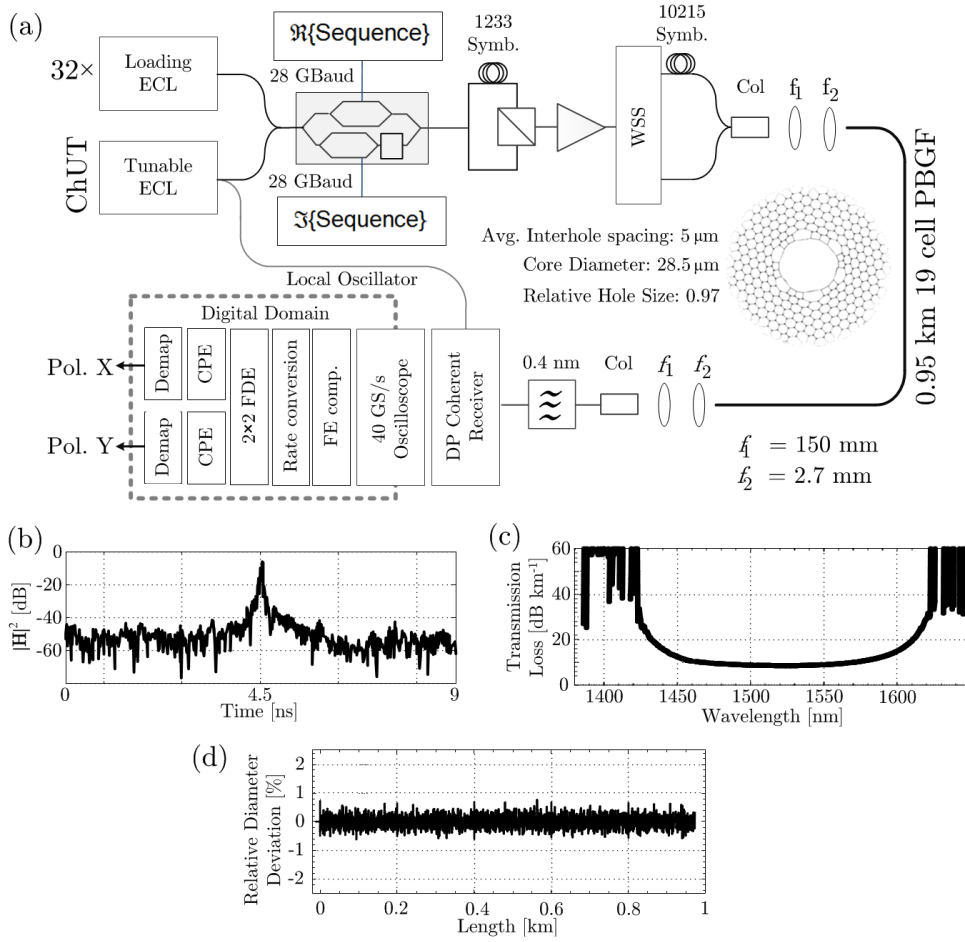


Fig. 8.10 (a) Experimental setup of the 0.95 km 19 cell HC-PBGF, inset HC-PBGF SEM image. (b) Weight matrix impulse response. (c) Measured transmission loss. (d) Measured relative diameter deviation.

The experimental single-mode transmission setup for HC-PBGF transmission verification is shown in Fig. 8.10(a). To cover a large portion of the C-Band, 32 ECLs are placed on a 100 GHz ITU-grid ranging from 1537.4 nm to 1562.23 nm are used as loading channels. A separate ECL, which replaces each of the 32 lasers individually, is used as the channel under test (ChUT). The ChUT laser output is split into two equal tributaries, where one is used as coherent receiver LO. The other acts as the transmitter laser, and is guided through a Lithium Niobate IQ-modulator, where it is modulated by a 28 GBaud signal. The signal generator is the same as described in section 8.1.1, where the IQ-modulator is driven by two DACs, which represent the in-phase (real) and quadrature (imaginary) component of the

transmitted constellations, respectively. The gray coded constellations used are 16 and 32 QAM, and are detailed in section 2.5.2. The transmitted constellation sequences are formed in the digital domain by a number of fully uncorrelated PRBSs, each of length 2^{15} . This minimizes any sequence correlations within the 2^{15} symbol sequence. The output of the IQ-modulator is split into two equal outputs. One arm is delayed by 44 ns (1233 symbols) with respect to the other for decorrelation the two polarization channels. After recombining the two arms, a DP signal is obtained. This DP signal is particularly important to measure the PDL of the HC-PBGF. The corresponding spectral efficiency is 4.48 ($2 \cdot 4 \cdot 28/56$) and 5.6 ($2 \cdot 5 \cdot 28/56$) bit s^{-1} Hz $^{-1}$ for 16 and 32 QAM, respectively. The signals are then guided through a wavelength selective switch (WSS), where the even and odd wavelengths are decorrelated by 364 ns (10215 symbols). The decorrelated output is then launched into the 0.95 km 19 cell HC-PBGF by a collimator (col) and 2 lenses with focal lengths $f_1 = 150$ mm and $f_2 = 2.7$ mm. At the receiver side, a reciprocal setup of the transmitter launcher is used. Then, one DP coherent receiver is employed. A 4-port 40 GS s^{-1} real-time oscilloscope is used as 4 synchronized ADCs. In the digital domain, first the optical FE is compensated before up sampling to 56 GS s^{-1} is performed. A 2×2 MIMO FDE with a DFT size of 128 is used. This equalizer length corresponds to a 9.1 ns equalization window. To minimize the convergence time, the varying adaptation gain algorithm described in section 6.3.1 was used. As the computational complexity of the FDE scales logarithmically with the impulse response length, the computational complexity scaling is minimized. This allows for low-complexity DSP to enable longer transmission over novel HC-PBGFs. The FDE weights are heuristically adapted using the LMS algorithm during initial training sequences, and DD-LMS during payload transmission. Although the transmitter laser and LO are coming from the same laser source, a Costas loop is still required per transmitted channel to compensate for the phase difference. After the CPE stage, the gray-coded constellations are demapped, and the BER is estimated. The BER is estimated over $2 \times 560,000$ symbols per polarization, which results in averaging over 4.48 and 5.6 million bits for 16 and 32 QAM, respectively.

Fig. 8.11(a) shows the single channel BTB and 0.95 km 19c HC-PBGF transmission performance of 16 and 32 QAM. At the SD-FEC limit, for 16 QAM there is no penalty between BTB and after transmission. However, when considering the HD-FEC limit, a 0.5 dB OSNR penalty can be observed. As the 32 QAM is a denser constellation, the OSNR requirements are more stringent. At the SD-FEC limit, a 1.5 dB OSNR penalty is noticed after transmission with respect to BTB

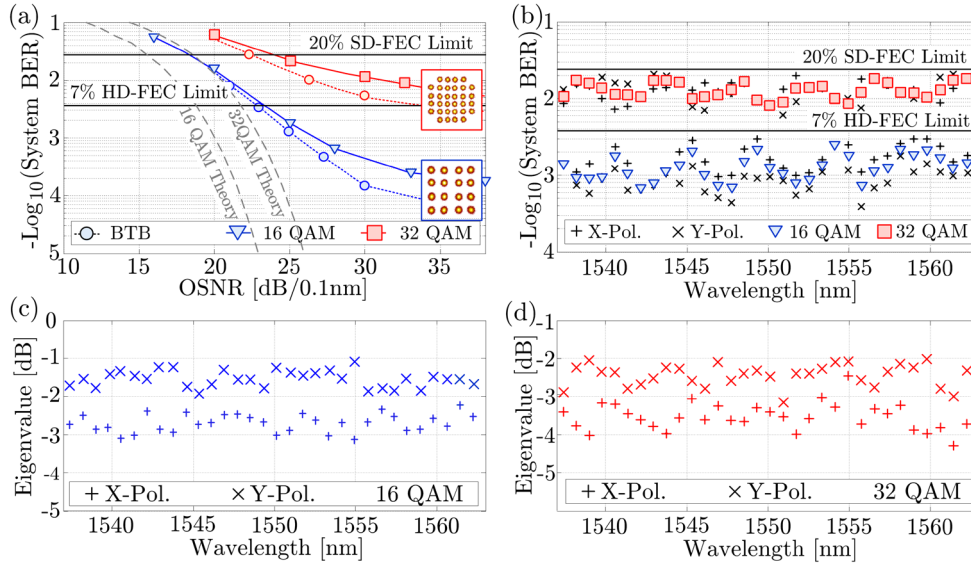


Fig. 8.11 Experimental 16 and 32 QAM transmission results for (a) single channel BTB and 0.95 km HC-PBGF transmission. (b) 32 channel experimental results for 16 and 32 QAM. (c) Eigenvalue decomposition of 16 QAM, and (d) 32 QAM.

performance. When enabling all transmission channels simultaneously, Fig. 8.11(b) shows the successful demonstration of the 100 GHz ITU-grid 32-channel experiment for both 16 and 32 QAM. In this experiment, the aim is to maximize the throughput of the fiber. Obviously, reducing the number of constellation points will improve the BER performance, and hence reduces the required FEC overhead. The 32 channel system BER performance for both 16 and 32 QAM is approximately an order of magnitude higher than the single channel performance, which is depicted in Fig. 8.11(a).

In addition to the 32 channel BER performance, the PDL is investigated for all transmitted wavelength channels. To estimate the PDL, LS channel estimation described in section 2.3.1 is used. This results in two eigenvalues representing each polarization channel per wavelength carrier, which is depicted in dB in Fig. 8.11(c) and Fig. 8.11(d) for 16 and 32 QAM, respectively. The difference between the two eigenvalues is the HC-PBGF's PDL. Ultimately, a low PDL fiber is desired for longer distance transmission. It is clear that the PDL is approximately equal over the entire transmitted wavelength band, and averages at approximately 1.1 dB. The origin of PDL is attributed to small-scale asymmetries over the length of the fiber. However, fiber models indicate that it is not intrinsic to the fiber. Through fabrication improvements, it should be possible to minimize these effects.

8.3 Few-mode multicore fiber

To demonstrate the scalability of SDM, the final transmission experiment is a 1 km hole-assisted SI 7-core FM-MCF transmission system, which has been reported on in [r36] and [r14]. Each core supports the co-propagation of 3 spatial LP modes, and hence the fiber supports an aggregate of 21 conventional SSMF transmission channels. Instead of scaling solely with modes, which requires $42 \times 42L = 1764L$ MIMO equalizer elements, the multi-core approach allows for a $7 \times (6 \times 6L) = 252L$ element equalizer. The benefit of using the multi-core is very clear, as the number of required MIMO elements is reduced by a factor of 7. However, as previously discussed, the MIMO equalizer size is not the only deciding factor for choosing the optimum between scaling in modes and cores. Optical components and fiber nonlinearities are also to be considered. In this experiment, the mode multiplexer described in section 4.4 is employed, and clearly indicates the advantages of a compact multiplexer for simultaneously transmitted channel scaling over a single fiber. The FM-MCF cross-section is shown in Fig. 8.12(a), and receiver side camera images are shown in Fig. 8.12(b) and Fig. 8.12(c). In a conventional single-mode

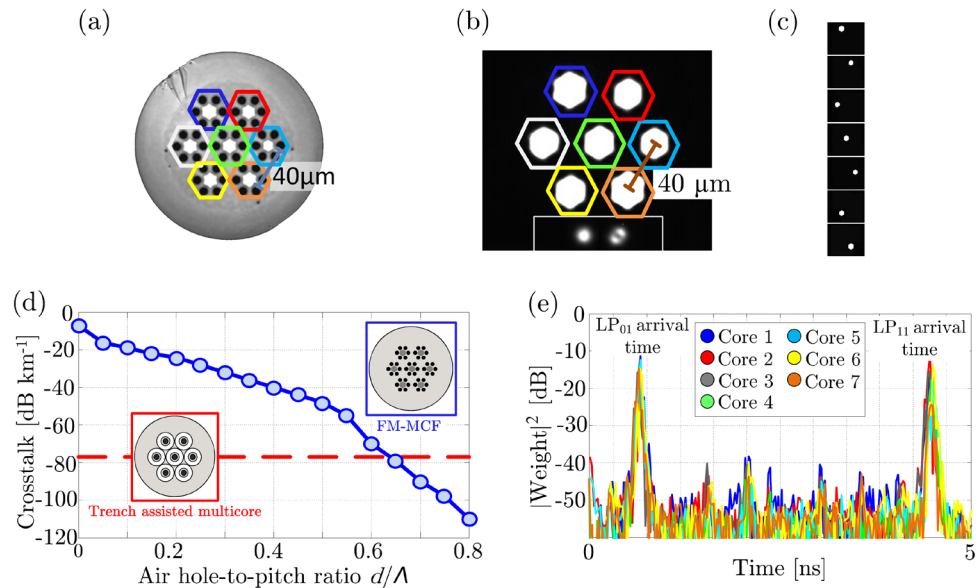


Fig. 8.12 (a) 7-core hole-assisted SI FM-MCF SEM image. (b) Receiver side FM-MCF output camera image with all cores lit up (bottom: individual LP₀₁ and LP₁₁ excitation of the center core). (c) Receiver side FM-MCF output camera image with individual cores lit. (d) Simulated inter-core crosstalk levels with respect to air hole-to-pitch ratio from [214]. (e) Equalizer weight impulse response, indicating uniformity among the 7 cores.

multi-core fiber, modal crosstalk composes of only inter-core crosstalk. However, when designing the FM-MCF, both intra-core (between spatial LP modes) and inter-core crosstalk is to be considered. Intra-core crosstalk is well understood from conventional single core 3MFs as described in section 8.1. Strong coupling between spatial LP modes is inevitable due to imperfections, splices, and proposed few-mode components (e.g. couplers, few-mode amplifiers) along the transmission link. Currently, intra-core crosstalk can be largely mitigated by MIMO equalization as described in Chapter 6. To this end, the FM-MCF design and fabrication focuses on minimizing inter-core crosstalk, to reduce the MIMO equalizer computational complexity. An obvious method to reduce inter-core crosstalk is to fabricate a fiber with a large core pitch, at the detriment of spatial information density. With respect to conventional trench-assisted structures, the hole-assisted structure adopted for the FM-MCF has the potential benefit of improved mode-confinement and minimizes inter-core crosstalk, which is optimized by tuning the air-hole diameter d and air-hole pitch Λ , as simulated in [214] and shown in Fig. 8.12(d) for a core pitch of 40 μm . In effect, this fiber design allows for a type of segmented MIMO equalizer, which has been discussed in section 6.2.6. Accordingly, a novel 1 km hole-assisted SI 7-core FM-MCF within a coating and cladding diameter of 372 μm and 192 μm , respectively, was successfully fabricated.

The individual 3 spatial mode cores have a 13.1 μm diameter, and were placed at a core pitch of 40 μm , arranged on a hexagonal lattice, as shown in Fig. 8.12(a). The air-holes, with $d = 8.2$ μm diameter, were placed $\Lambda = 13.3$ μm apart, creating an air-hole-to-pitch ratio of 0.62, which corresponds to an inter-core crosstalk of -80 dB km^{-1} . The LP_{01} and LP_{11} mode A_{eff} are 112 and 166 μm^2 , respectively, and have a DMD of 4.6 ps m^{-1} . Indicating uniformity among the cores, the DMD shown in Fig. 8.12(e) is estimated by LS channel estimation described in section 2.3. The large DMD is inherent to the step-index cores, as discussed in section 3.4, and can be reduced by employing graded-index cores.

The experimental setup to demonstrate the FM-MCF's throughput capabilities is depicted in Fig. 8.13. 50 ECLs act as loading channels, and are placed on a 50 GHz ITU-grid ranging from 1542.14 to 1561.81 nm. To verify the transmission performance, each of the loading channels is individually replaced by the ChUT ECL (linewidth <100kHz). The ChUT laser output is split into two equal tributaries, where the second output acts as LO. To minimize the impact of the transmitter and receiver laser coherence, a 10 km single mode fiber is inserted in the LO path. This is sufficient as the ECL with <100kHz linewidth has a

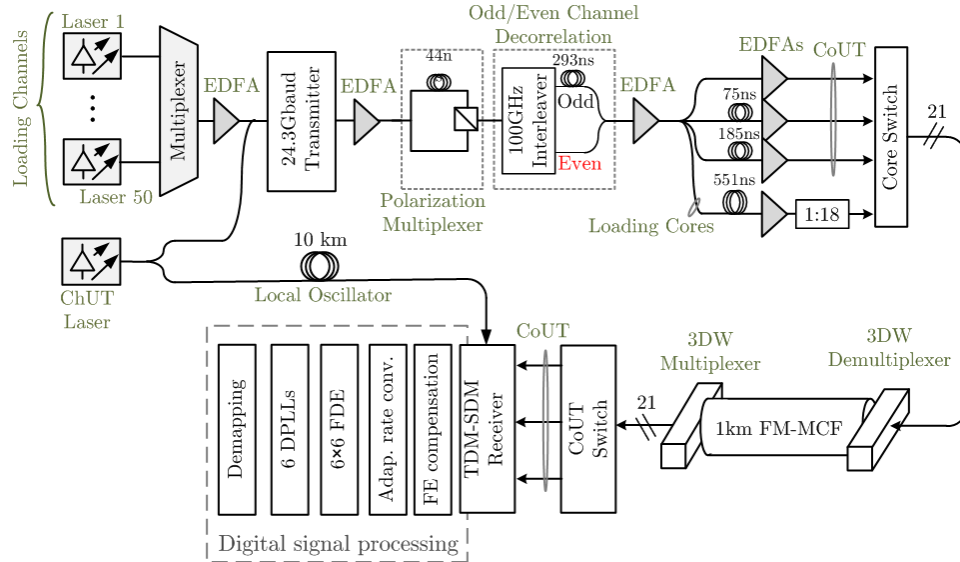


Fig. 8.13 Experimental 1 km SI 7-core FM-MCF performance verification setup.

coherence length of approximately 1 km. Similar to the previous section, 50 signal carriers were guided through a Lithium Niobate (LiNbO_3) IQ-modulator, which was driven by two DACs, representing the in-phase and quadrature components, to generate a 24.3 GBaud 16 or 32 QAM signal. The symbol sequences are generated by independent PRBSs as described in section 2.6. The IQ modulator output is passively split, where one arm is delayed, before being recombined by a PBS, introducing a 44 ns delay (1070 symbols) between the orthogonal polarizations. The DP signal is routed through a WSS, which acts as 100 GHz interleaver to decorrelate the even and odd carrier channels by 293 ns (7120 symbols). The wavelength combined output is split into two tributaries, one represents the core under test (CoUT), and the other the loading cores. The delay between the CoUT and loading cores is 551 ns (13389 symbols), where the loading core output is split 18-fold. Finally, the CoUT signal is split threefold, where two inputs are delayed by 75 (1822 symbols) and 185 ns (4495 symbols), respectively. All signal delays are chosen to achieve fully decorrelated signal copies across the polarizations, neighboring wavelengths, cores, and spatial LP mode channels within the MIMO equalizer window at the receiver (5.27 ns, 128 symbols). The CoUT is varied consecutively over all few-mode cores during the performance investigation. The observed optimum launch power of all 21 inputs was 10 dBm for both constellations. The 3DW MMUX described in section 4.4 is butt-coupled to the FM-MCF, where all 7 cores and corresponding spatial LP modes are simultaneously

excited. The corresponding SE transmitted over the FM-MCF is 81.65 ($7 \times 3 \times 2 \times 4 \times 24.3/56$) and 102.06 ($7 \times 3 \times 2 \times 5 \times 24.3/56$) bit s⁻¹ Hz⁻¹ for 16 and 32 QAM, respectively. These SE figures can be further increased by performing Nyquist pulse shaping, as described in section 2.8. However, the downside of this method is that the carriers are no longer placed on a 50 GHz ITU grid, and hence support of conventional SSMF transmission links is lost. A 1550 nm camera image at the receiver side is shown in Fig. 8.12(b), where the saturated power demonstrates the light confinement achieved by the FM-MCF cores. In Fig. 8.12(c), each core is separately lit. The inset in Fig. 8.12(b) shows selective excitation of the LP₀₁ and LP₁₁ modes of the center core (core 4). At the receiver side, a second 3DW acts as demultiplexer. Here, the respective CoUT spatial LP mode outputs are selected and received by the TDM-SDM receiver, which is also an original contribution, and has been detailed in section 5.3. Successively, in the digital domain, FE impairments, MIMO equalization, and CPE is performed. To unravel the mixed polarization channels, the MIMO FDE with varying adaptation gain is used, with a 128-point DFT size, as it has a lower computational complexity than the conventional TDE and minimizes the convergence time for lengthy impulse responses. The FDE versus TDE computational complexity comparison is detailed in section 6.4.3. The system BER per core is averaged over all transmitted channels, each of length 11 μs (267.000 symbols), resulting in BER averaging over 6.408 and 8.01 million bits for 16 and 32 QAM, respectively.

With all 50 modulated carriers in all 7 cores enabled simultaneously, Fig. 8.14(a) demonstrates the successful 24.3 GBaud 16 QAM transmission over 1 km hole-assisted FM-MCF, where all transmitted channels are well below the 7% HD-FEC. This results in a gross transmission throughput of 4.08 Tbit s⁻¹ carrier⁻¹, and a gross aggregate transmission throughput of 204.12 Tbit s⁻¹. Subtracting a 2.5% training sequence, 20% SD-FEC, and 5% framing overhead results in a net data rate of 3.2 Tbit s⁻¹ carrier⁻¹, and an aggregate rate of 160 Tbit s⁻¹. Additionally, LS channel estimation has been performed on all carrier channels per core to estimate the MDL, which is shown in Fig. 8.14(b). The average MDL for 16 QAM transmission is 3.9 dB, and the MDL differences are attributed to slight misalignments between the cores and MMUX, and wavelength dependent mode field excitation, during the experiment.

The same measurement is repeated for 32 QAM transmission, shown in Fig. 8.14(c), where the gross transmission throughput is 5.1 Tbit s⁻¹ carrier⁻¹, and a gross aggregate transmission throughput of 255 Tbit s⁻¹. After subtracting the

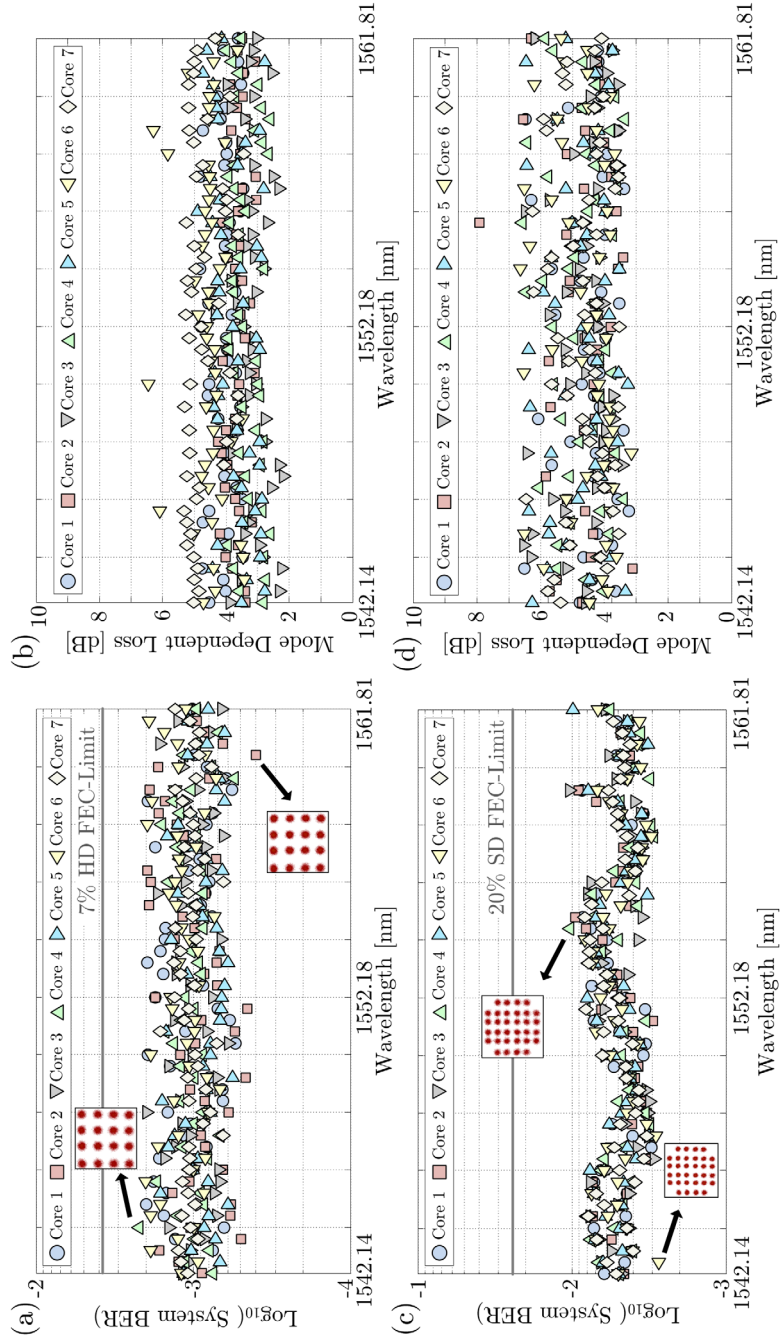


Fig. 8.14 Experimental 16 QAM 50 channel (a) BER and (b) observed MDL transmission performance. Experimental 32 QAM 50 channel (a) BER and (b) observed MDL transmission performance.

transmission overhead, a net data rate of 4 Tbit s⁻¹ carrier⁻¹, and an aggregate net rate of 200 Tbit s⁻¹ is obtained. Again, LS channel estimation has been performed on all carrier channels per core to estimate the MDL figures, which is shown in Fig. 8.14(d), and the average MDL is estimated to be 4.4 dB. This result indicates that the MDL is stable over a longer period of time due to the two measurements, and stable over a large wavelength range. The observed average MDL is within the range of previously reported work for single core few-mode transmission [131], further demonstrating that multicore and multimode SDM can successfully be combined to enable ultra-high density transmission capacity.

8.4 Summary

This chapter combines the sub-systems and algorithms presented in the preceding chapters in an experimental transmission setup, where the transmission performance of three novel fiber types has been investigated. Each of these measurements paves the road to further developing these novel optical fiber types and subsystems, to augment, or replace the SSMF in future optical transmission systems.

The first experimental fiber investigated is the GI solid-core 3MF, which is based on SSMF designs, and allows the co-propagation of 3 spatial LP modes. Accordingly, the potential throughput of this fiber is three times what a SSMF can offer. This has been verified for 2D and 4D constellations, where it was proposed to encode the 4D constellations in two consecutive 2D time slots of one transmission channel to minimize receiver implementation timing synchronization constraints. This is the first experimental work of > 2D constellations in 3MFs. Additionally, the usage of the 3MF accompanied with space-time coding is proposed, based on spatial and delay diversity to achieve better noise tolerance than SSMFs theoretically can offer. This however, comes at the cost of computational complexity and coherent receivers. Nevertheless it indicates that space-time coding can be used for future SDM flex-grid applications. Finally, multipoint-to-point 3MF transmission has been investigated, where three separated sources are combined at the 3MF input. This results in an increased error-floor with respect to point-to-point transmission, as the transmission channels are noise and frequency decorrelated. However, it provides a network upgrade scenario for commercial applications.

The second investigated fiber is not based on any commercially available fiber for optical transmission systems, and is the experimental 0.95 km 19 cell HC-PBGF.

The successful transmission of 32 wavelength carriers spaced on a 100 GHz grid and modulated with 28 GBaud 16 and 32 QAM was demonstrated. This result represents the longest coherent transmission distance over HC-PBGF and the highest distance \times bandwidth product of 8.5 Tbit \cdot km at the moment. The main distance limitation for HC-PBGF transmission is the complexity, skill, and financial investment required to manufacture this highly experimental fiber.

Finally, the last experimental fiber investigated is the 1 km SI 7-core FM-MCF, where each core allows the co-propagation of 3 spatial LP modes. Therefore, this fiber provides the same number of transmission channels as 21 SSMFs, indicating potential for SDM integration into a future transponder. By employing 50 wavelength carriers, each modulated with a 24.3 GBaud 16 or 32 QAM signal, a gross throughput rate of 204.12 and 255 Tbit s⁻¹ was achieved, respectively, with a SE of 81.6 and 102 bits s⁻¹ Hz⁻¹, respectively. Per core, LS channel estimation indicated an average MDL of approximately 4.15 dB, which is similar to previous experimental work using 3MFs. This experimental work demonstrates the state-of-the-art optical communication systems to increase capacity within a single fiber exploiting most available domains: multimode, multicore, WDM, and modulation formats.

Chapter 9

Conclusions and future outlook

The science of today is the technology of tomorrow.

Edward Teller

9.1 Conclusions

Through the ever increasing societal capacity demand, SSMFs in long-haul transmission systems are nearing their theoretical bandwidth limit, which is constrained by the SSMF's linear and non-linear transmission characteristics. Accordingly, an impending capacity crunch is inevitable. A method needs to be exploited to increase the transmission capacity of a single fiber by increasing the spectral efficiency. This method has to be financially more interesting than scaling through employing more SSMFs. SDM is envisioned as the next step in optical transmission systems, by exploiting the spatial domain. In this work, one of the key enablers of SDM transmission systems, digital signal processing is investigated with respect to computational complexity, convergence properties, and scaling the transmitted channels. Other key enablers of SDM transmission systems are novel optical fibers, optical MMUXs, and optical amplifiers. As the author had no access to currently emerging SDM amplifiers, the key enablers for SDM have been investigated and applied to a short haul transmission system. The main contributions are:

- MMUX design and performance investigation, where the performance of these multiplexers has been enabled by LS estimation, and the proposed MMSE CSI estimation algorithm. The OSNR tolerances to an impaired phase-plate based MMUX are investigated. Furthermore, a FM-MCF 3DW MMUX has been designed to demonstrate the viability of scaling the number of transmitted channels through combining multimode with multicore transmission in a single fiber, which has a direct impact on MIMO equalization.
- Proposal and verification of low-complexity MIMO algorithms. To minimize the convergence time, a varying adaptation gain has been applied to the conventional time domain MIMO equalizer. To make a first step towards real-time implementation the offline-processing floating point precision has been reduced from 64 to 12 bits. A FDE has been proposed which allows for the

compensation of IQ-imbalance. Again, to minimize the convergence time, a varying adaptation gain has been applied.

- The proposal and verification of low-complexity CPE algorithms. Here, the laser frequency offset common-mode impairment has been exploited in a joint CPE stage to compensate all transmission channels simultaneously. Furthermore, the usage of a low-complexity phase detector has been proposed.
- The experimental demonstration of using higher order constellations for SDM transmission systems, where the transmission performance of four dimensional constellations has been investigated. It has been shown that four dimensional constellations provide additional throughput values, with respect to conventional two dimensional constellations.
- An SDM coding scheme is proposed based on space-time coding, where multiple spatial channels carry the same information in separate time slots. It is experimentally shown that the 3MF can outperform the theoretical SSMF's transmission performance, at the cost of additional receivers and amplifiers.
- An experimental setup has been constructed, and a distributed offline-processing code implementation has been developed to experimentally demonstrate the above algorithms. Furthermore, this experimental setup is used to characterize three novel fiber types: the 3MF, the HC-PBGF, and the FM-MCF.

9.1.1 Mode multiplexers

The first generation MMUXs, the phase plate based solution (section 4.2), was based on individual mode excitation. This work focused on the transmission of 3 spatial LP modes. Due to the individual excitation nature of the multiplexer, LP modes could be processed independently. Accordingly, 2 independent MIMO equalizers could be used of size 2×2 and 4×4 to process the LP_{01} and LP_{11} (consisting of the LP_{11a} and LP_{11b} mode) modes, respectively. Three worst-case crosstalk scenarios have been investigated, which result in filling the entire transmission matrix, impairing the performance of the phase-plate based MMUX. These scenarios were a rotational misalignment, a lateral offset, and a mismatch in the phase shifting region. A 1 dB SNR penalty was used as performance benchmark. The independent tolerances were 25 degrees rotation mismatch, 0.15 normalized e^{-2} mode radius, and a 45 degree mismatch in the phase shifting region. Accordingly, it is found that the phase plate based MMUX is very tolerant to optimization impairments.

However, using the phase plate MMUX, a single channel does not exploit the spatial diversity available. This results in the transmission system being susceptible to MDL, i.e. the difference in power between transmitted channels arriving at the

receiver. Note that the insertion loss of the phase plate MMUX was approximately 8-9 dB. To minimize the effects of MDL and insertion loss, the second generation MMUX was introduced: the spot launcher. Again, this MMUX was demonstrated for a 3MF transmission system and was characterized using LS channel estimation. This multiplexer provides a unitary rotation in the transmission matrix, allowing for exploiting the spatial diversity and minimizing the impact of MDL. The mixing of the transmission channels results in the usage of a 6×6 MIMO equalizer. The insertion loss of the spot launcher was approximately 4.5 dB, and the MDL was 2 dB. The MDL was characterized using LS CSI estimation and MMSE CSI estimation. For an OSNR regime of 13-19 dB (low OSNR), it was observed that the MDL estimation difference between LS and MMSE CSI estimation was under 0.3 dB, indicating that both methods provide good insight in the transmission channel. It was discussed in section 6.2.1 that the maximum discrepancy between the CSI estimation algorithms occurs when the OSNR performance is low. Note that the spot launcher used bulk optics and has been used in the experimental demonstration of the 3MF.

As a third generation MMUX, the 3DW was proposed. It is based on the same principle as the spot launcher, but minimizes the footprint, allowing for integration into future transponders. This MMUX was designed for the 7-core FM-MCF, demonstrated in section 8.3, where 3 spatial channels per core were launched into the fiber. Consequently, a total of 21 SMF inputs were guided into one FM-MCF. The MMUX size was 5.3×25 mm, and the insertion loss was similar to the spot launcher, approximately 4.5 dB. The estimated MDL was also similar to the performance of the spot launcher, namely 2 dB. Due to the multimode and multicore nature of the launching and fiber, 7 independent MIMO equalizers of size $6 \times 6L$ were used. Here L corresponds to the impulse response length of the fiber.

Currently, the fourth generation MMUX, the photonic lantern, is seen as the ultimate solution as it provides a low insertion loss and allows for fully exploiting the spatial diversity. Photonic lanterns are full in-fiber solutions, and hence no glass-air-glass conversion is required. This solution is scalable to a higher number of modes, multiple cores, or a combination of the two, as shown for the three dimensional waveguide.

9.1.2 MIMO digital signal processing

A key enabler for optical MIMO transmission systems, and a significant part of this work, is performed in the digital domain. Here, the main motivation is computational complexity considerations, and tracking capabilities. A lower computational complexity reduces the required energy per bit for processing, and hence the costs per transmitted bit.

In conventional SMF transmission systems, which exploit polarization division multiplexing, a 2×2 time domain MIMO equalizer is used. This provided a starting point for scaling to multimode transmission, where the focus lied on a 3MF transmission system using a 6×6 time domain equalizer. Initially, the computational complexity of a DMD uncompensated transmission system was reduced by only using the MIMO weights corresponding to the arrival times of the respective modes. To increase the MIMO equalizer's channel tracking capabilities, a varying adaptation gain was proposed for the TDE. It was experimentally demonstrated that the varying adaptation gain is capable of reducing the convergence time by 50% for the 3MF transmission system. Note that all DSP was performed using offline-processing in computers. Computers use 64 bit floating point accuracy, which is impossible for real-time processing using FPGAs and ASICs. Therefore, the effect of bit-width reduction was investigated as a first step towards a potential real-time implementation. The maximum bit-width in modern FPGAs is 16 bits. It was shown that even when using 12 bit floating point processing, <1 dB OSNR penalty was observed at the 20% SD-FEC limit for QPSK, 8, and 16 QAM.

The computational complexity of the TDE scales linearly with the number of transmitted channels, and linearly with the impulse response length. To further reduce the computational complexity in the MIMO equalizer, a low-complexity FDE was proposed, which allows for compensating residual IQ-imbalance. The computational complexity of this equalizer scales linearly with the number of transmitted channels, and logarithmically with the impulse response length. Therefore, it provides a case for equalizing lengthy impulse responses. Similarly to the TDE, the varying adaptation gain was applied and shown to reduce the convergence time by 30%. This improvement is lower than what was observed for the TDE, as the stable convergence properties of the FDE are more constrained.

9.1.3 CPE digital signal processing

As the FDE substantially lowers the computational complexity in the MIMO equalizer with respect to the traditional TDE, other DSP blocks become interesting for lowering the computational complexity too. A key building block is the CPE stage, where the frequency offset between the transmitter and receiver laser is compensated. In MIMO transmission systems, the respective lasers are shared amongst all transmitted channels, which results in a common-mode impairment. A joint CPE scheme based on the Costas loop is proposed, exploiting the common-mode impairment to minimize the computational complexity. In the proposed scheme, the number of digital phase locked loops is reduced by $N_t - 1$, and the number of phase detectors by $N_t / 2$. The maximum observed OSNR penalty was 0.5 dB for 32 QAM transmission at the 20% FEC limit.

Furthermore, a low-complexity 2×1 dimension phase estimator is proposed, which separates the inphase and quadrature components, before independently processing them. A key benefit besides lowering the computational complexity is the potential for parallel processing in real-time processors. No OSNR penalty was observed for constellations up to 32 QAM, with respect to conventional phase estimators.

9.1.4 Higher order modulation formats and coding

After MIMO equalization, residual channel interference is inevitable. To minimize the performance impact caused by this effect, the first experimental demonstration of higher order constellations beyond 2 dimensions in an SDM transmission system was achieved, where two consecutive 2D time slots were occupied by a single 4D symbol. It is shown that the 4D symbols are more robust against residual channel interference than conventional 2D symbols. In addition, it is shown that the four dimensional 128-SP-QAM constellation outperforms the two dimensional 8 QAM constellation at the hard-decision FEC limit, whilst carrying an additional 0.5 bit per symbol more.

Finally, in the digital domain, a space-time coding scheme based on exploiting the spatial and delay diversity was proposed. Accordingly, it is shown that 3MFs offer a better OSNR performance than theoretically possible in SMFs. However, this comes at the cost of additional receivers and energy consumption. With respect to SMF BTB, the OSNR improvements are 3.2, 4.1, 4.9, and 6.8 dB for QPSK, 8, 16, and 32 QAM at the 7% hard-decision FEC limit.

9.1.5 Experimental fiber characterization and DSP validation

To validate the DSP algorithms, and characterize novel fibers for SDM, three experimental fibers were investigated. This performance investigation is enabled by the introduction of a novel TDM-SDM receiver, which allows for the reception of >1 DP spatial LP mode using 1 coherent DP receiver and corresponding 4-port analog-to-digital converter. It is experimentally shown that the transmission performance is similar to conventional MIMO receivers. The transmission performance of the first experimental fiber is investigated using the TDM-SDM receiver, which is the solid-core GI 3MF, which has been predominantly used to validate all proposed DSP algorithms described in the previous sections.

The second experimental fiber investigated is a 0.95 km 19-cell HC-PBGF. Here, due to the experimental nature of the fiber, CSI is applied to investigate the PDL, where an average PDL of 1.1 dB was noticed over a wavelength range from 1537.4 nm to 1562.23 nm. Note that the PDL is not intrinsic to the HC-PBGF, and is attributed to small perturbations in the fiber, and channel estimation accuracy. To obtain a more accurate estimation, longer HC-PBGF transmission is required. This may be reduced in the future. A 32 WDM channel experiment has been performed to demonstrate a gross aggregate throughput of 8.96 Tbit s^{-1} . This result represents the highest capacity \times distance product in HC-PBGFs, and the longest transmission distance over HC-PBGFs, at the time of the experiment.

Finally, the transmission performance of a 1 km 7-core step-index fiber is investigated, where each core allows the co-propagation of 3 spatial modes. Per core, the proposed TDM-SDM receiver was used. The used fiber is denoted as the few mode multicore fiber. Accordingly, 21 SMF channels are guided into the FM-MCF, where $7 \times (6 \times 6L)$ FDE MIMO equalization is employed to equalize the 32 QAM modulated 5.1 Tbit s^{-1} carrier $^{-1}$ spatial superchannels. Combined with 50 wavelength carriers on a 50 GHz grid, a gross aggregate throughput rate of 255 Tbit s^{-1} is demonstrated. The corresponding gross SE is $102 \text{ bits s}^{-1} \text{ Hz}^{-1}$. This work demonstrates the MIMO computational complexity scaling for multimode transmission in combination with multicore transmission. Accordingly, state-of-the-art optical transmission technology has been presented through combining multimode, multicore, and higher order modulation formats.

9.2 Future outlook

In the past four years, a substantial effort has been made towards demonstrating the first experimental SDM transmission systems in laboratory environments by the optical transmission community. However, for long-haul SDM systems to become commercially viable, considerable steps still have to be made. At this moment, it is difficult to determine what the optimum SDM solution is. This choice is currently unknown to everyone, as more knowledge needs to be gained with respect to fiber designs and corresponding DMD mappings, multimode and multicore erbium-doped fiber amplifier designs, and nonlinear propagation effects.

9.2.1 Multimode or multicore for capacity scaling

The 3MF transmission case presented in section 8.1 does not provide a large multiple of SSMF throughput, when considering a CAGR of 40%, it would extend the impending capacity crunch by approximately 3 years, before carriers need to re-upgrade their network again. To really make a substantial impact for a single fiber throughput, at least >50 times SSMF throughput needs to be provided. Assuming a 50-fold increase and a CAGR of 40% per year, this would still only extend the capacity demand by 11 years, before the installed network needs to be upgraded again. In a more optimistic prediction, assuming a 50-fold increase and a CAGR of 25% per year would extend the capacity crunch by approximately 18 years. Therefore, as the MODE-GAP project indicates, preferably a 100-fold increase over SSMF transmission is desired. This many-fold transmission throughput can be achieved either by multimode, multicore, or a combination thereof, as demonstrated for 21-fold increase already in section 8.3.

In single-core multimode transmission, currently the aim is conventional 50 μm core size MMF [137]. Such MMFs allow the co-propagation of >150 spatial LP modes. The downside of exploiting the spatial LP modes in this case is that $\geq 300 \times 300L$ MIMO equalization is required. This corresponds to a 22,500 increase in L -size matrix elements with respect to $2 \times 2L$ SSMF transmission, whilst only increasing the throughput by 150-fold. In addition, it was noted in Chapter 6 that the convergence time linearly increases with the number of transmitted channels. Furthermore, using conventional multimode fibers the DMD needs to be managed to minimize the impulse response length. Alternatively, low DMD MMFs can be employed. However, these low DMD fibers have more stringent non-linear tolerances than their high DMD counterparts. It is currently unknown how the non-linear effects scale with increasing core size and increasing number of transmitted channels.

Alternatively, to limit the MIMO equalizer's size, multicore transmission is of large interest, where the number of cores increases. Furthermore, SMF ribbons are proposed to further minimize fiber manufacturing costs and coupling [215], with a shared multicore amplifier. Accordingly, instead of using a $300 \times 300L$ MIMO equalizer as used in the previous example, $150 \times (2 \times 2L)$ equalizers can be employed. Finally, scaling using multiple cores does not increase the convergence time with respect to SSMF transmission systems. Note that currently fiber bending effects are under investigation for both multimode and multicore fibers, which may limit the scaling in number of modes and cores in a single fiber. Clearly, an optimum of all factors has to be found in the future.

9.2.2 Hollow-core photonic bandgap fibers

HC-PBGFs provide key advantages over solid-core fibers:

- Three orders of magnitude more tolerant to non-linearities.
- Lower latency.
- Lower intrinsic attenuation figure.

Note that the three orders of magnitude non-linear tolerance advantage does not provide three orders of magnitude capacity. In reality, the increase in capacity is small. In addition, the lower attenuation figure is achieved at $2 \mu\text{m}$, where the theoretical Rayleigh scattering is lower than it is at 1550 nm . This implies that all conventional optical components need to be converted to the $2 \mu\text{m}$ regime, which is a major drawback for commercialization. Clearly, the attenuation figure demonstrated at this time needs to become substantially lower, for the HC-PBGFs to make an impact on telecommunication applications. However, if the attenuation figure is to be decreased, it will become interesting in the future. Besides telecom applications, HC-PBGFs are already interesting for sensing, ultra-high power, and ultra-low latency applications [216].

9.2.3 Optical components

Clearly, besides SDM fibers, other key optical components are required to be further developed for future SDM transmission systems. Among these components are MMUXs, where spliced in-fiber solutions are the next step as they provide minimum insertion loss as glass-air-glass interfaces are avoided and low MDL. Additionally, in-fiber solutions support all telecom wavelength bands, and can be manufactured with a small footprint. The second key optical component is the gain equalized multimode and/or multicore optical amplifiers, which provide low MDL, and amplify multiple transmission channels with a shared pump source. Furthermore, the NF should be similar for all amplified modes. One key advantage

MMF transmission has over multicore fiber transmission is the pump amplification efficiency [217], and hence a lower energy consumption. This is due to the overlapping modal areas within the core. Finally, optical spatial filters are necessary for the adding and dropping of spatial superchannels.

9.2.4 Transmission formats and equalization

The first and foremost comparison in optical transmission formats is the choice for OFDM or single-carrier transmission. At this point in time, the optical transmission channel can be considered flat-fading or Rician fading, and therefore the fading type is MDL. Accordingly, there is no need for using OFDM, which also puts a higher constraint on the DAC's ENOB and laser linewidths than single-carrier transmission. However, as research is migrating towards MMFs, OFDM may become interesting in the future, as MMFs have strong multi-path propagation behavior [34, 102].

In the digital domain, higher-order constellation coding schemes are currently becoming more predominant as they can provide substantial OSNR gains at the cost of additional computational complexity. Accordingly, the nonlinear tolerances are increased, and potentially fewer amplifiers are required for the same transmission distance. Especially SDM transmission systems can provide a strong basis for higher-order constellation transmission schemes due to their spatial diversity. Among these higher-order constellations are direct bit mappings, as shown in section 8.1, and Trellis Coded Modulation (TCM). In addition, a key reason for coding schemes being so interesting is that the upgrading for carriers is relatively cheap as only transponder cards need to be replaced.

Furthermore, this work has shown a logarithmic computational complexity scaling with impulse response length using the MIMO FDE, which provides a robust implementation for long impulse response compensation. However, it was noted that convergence, and hence channel tracking capabilities, become slower when the impulse response becomes longer, and as the number of simultaneous transmission channels increases. Therefore, convergence time becomes a limiting factor when increasing the mixed transmission channels. For a TDE this constraint is lower with respect to the FDE, allowing higher channel tracking capabilities. However, the TDE computational complexity scales linearly with the impulse response. This is an undesirable computational complexity scaling. With respect to convergence time, it was noted that using the RLS (or fast RLS) scheme, a lower convergence time can be obtained. However, this MIMO equalization scheme scales particularly poor with the impulse response length in computational complexity. This clearly is

an area of research where further investigation is required for maximizing channel tracking capabilities whilst minimizing the computational complexity. Furthermore, in this work, the updating algorithm was data-aided to convergence to the global minimum, resulting in the optimum BER performance. For future systems, it is preferred that convergence is achieved using blind updating algorithms. This allows for minimizing the required training sequence overhead, and hence increases the throughput of the transmission system.

Bibliography

- [1] J. Hecht, *City of Light: The Story of Fiber Optics*. Oxford University Press (2004).
- [2] T. H. Maiman, "Stimulated Optical Radiation in Ruby," *Nature*, vol. 187, pp. 493-494 (1960).
- [3] R. N. Hall, G. E. Fenner, J. D. Kingsley, T. J. Soltys, and R. O. Carlson, "Coherent Light Emission From GaAs Junctions" *Physical Review Letters*, vol. 9, pp. 366-368 (1962).
- [4] K. C. Kao and G. A. Hockham. (1966, Dielectric-fibre surface waveguides for optical frequencies. *Proceedings of the Institution of Electrical Engineers 113(7)*, 1151-1158.
- [5] H. H. Hopkins and N. S. Kapany, "A flexible fiberscope, using static scanning," *Nature*, pp. 39-41 (1954).
- [6] E. Snitzer and H. Osterberg, "Observed Dielectric Waveguide Modes in the Visible Spectrum," *Journal of the Optical Society of America*, vol. 51, pp. 499-505 (1961).
- [7] D. B. Keck, R. D. Maurer, and P. C. Schultz, "On the ultimate lower limit of attenuation in glass optical waveguides," *Applied Physics Letters*, vol. 22, pp. 307-309 (1973).
- [8] H. Murata and N. Inagaki, "Low-loss single-mode fiber development and splicing research in Japan," *IEEE Journal of Quantum Electronics*, vol. 17, pp. 835-849 (1981).
- [9] G. P. Agrawal, *Fiber-Optic Communication Systems*. Wiley (2012).
- [10] T. s. s. o. ITU. (2009). *G.652 Characteristics of a single-mode optical fibre and cable*
- [11] W. J. Tomlinson and C. Lin, "Optical wavelength-division multiplexer for the 1-1.4 μm spectral region," *Electronics Letters*, vol. 14, pp. 345-347 (1978).
- [12] T. s. s. o. ITU, "G.694.1 Spectral grids for WDM applications: DWDM frequency grid," 2012).
- [13] L. G. Kazovsky, "Phase- and polarization-diversity coherent optical techniques," *Journal of Lightwave Technology*, vol. 7, pp. 279-292 (1989).
- [14] R. J. Mears, L. Reekie, S. B. Poole, and D. N. Payne, "Low-threshold tunable CW and Q-switched fibre laser operating at 1.55 μm ," *Electronics Letters*, vol. 22, pp. 159-160 (1986).
- [15] R. J. Mears, L. Reekie, I. M. Jauncey, and D. N. Payne. (1987, Low-noise erbium-doped fibre amplifier operating at 1.54 μm . *Electronics Letters 23(19)*, 1026-1028.
- [16] P. J. Winzer and R. Essiambre, "Advanced Optical Modulation Formats," *Proceedings of the IEEE*, vol. 94, pp. 952-985 (2006).

-
- [17] M. G. Taylor, "Coherent detection method using DSP for demodulation of signal and subsequent equalization of propagation impairments," *IEEE Photonics Technology Letters*, vol. 16, pp. 674-676 (2004).
- [18] Y. Han and G. Li, "Coherent optical communication using polarization multiple-input-multiple-output," *Optics Express*, vol. 13, pp. 7527-7534 (2005).
- [19] P. J. Winzer, "Optical Transport is Going MIMO," presented at the International Conference on Communications (ICC), (2013).
- [20] Q. Dayou, H. Ming-Fang, E. Ip, H. Yue-Kai, S. Yin, H. Junqiang, and W. Ting, "101.7-Tb/s (370×294-Gb/s) PDM-128QAM-OFDM transmission over 3×55-km SSMF using pilot-based phase noise mitigation," in *Optical Fiber Communication (OFC) Conference*, 2011, pp. 1-3.
- [21] L. Raddatz, I. H. White, D. G. Cunningham, and M. C. Nowell, "An Experimental and Theoretical Study of the Offset Launch Technique for the Enhancement of the Bandwidth of Multimode Fiber Links," *Journal of Lightwave Technology*, vol. 16, p. 324 (1998).
- [22] C. P. Tsekrekos, *Mode group diversity multiplexing in multimode fiber transmission systems* (2008).
- [23] D. C. Kilper, G. Atkinson, S. K. Korotky, S. Goyal, P. Vetter, D. Suvakovic, and O. Blume, "Power Trends in Communication Networks," *IEEE Journal of Selected Topics in Quantum Electronics*, vol. 17, pp. 275-284 (2011).
- [24] Sandvine, "Global Internet Phenomena Report2H," ed, 2013.
- [25] D. J. Richardson, J. M. Fini, and L. E. Nelson, "Space-division multiplexing in optical fibres," *Nature Photonics*, vol. 7, pp. 354-362 (2013).
- [26] P. J. Winzer, "Beyond 100G Ethernet," *IEEE Communications Magazine*, vol. 48, pp. 26-30 (2010).
- [27] E.-U. F. p. MODE-GAP. (2014). Available: www.modegap.eu
- [28] J. Sakaguchi, Y. Awaji, N. Wada, A. Kanno, T. Kawanishi, T. Hayashi, T. Taru, T. Kobayashi, and M. Watanabe, "109-Tb/s (7x97x172-Gb/s SDM/WDM/PDM) QPSK transmission through 16.8-km homogeneous multi-core fiber," in *Optical Fiber Communication (OFC) Conference*, Los Angeles, California, 2011, p. PDPB6.
- [29] J. Sakaguchi, B. J. Puttnam, W. Klaus, Y. Awaji, N. Wada, A. Kanno, T. Kawanishi, K. Imamura, H. Inaba, K. Mukasa, R. Sugizaki, T. Kobayashi, and M. Watanabe, "19-core fiber transmission of 19x100x172-Gb/s SDM-WDM-PDM-QPSK signals at 305Tb/s," in *Optical Fiber Communication (OFC) Conference*, Los Angeles, California, 2012, p. PDP5C.1.
- [30] H. Takara, A. Sano, T. Kobayashi, H. Kubota, H. Kawakami, A. Matsuura, Y. Miyamoto, Y. Abe, H. Ono, K. Shikama, Y. Goto, K. Tsujikawa, Y. Sasaki, I. Ishida, K. Takenaga, S. Matsuo, K. Saitoh, M. Koshiba, and T. Morioka, "1.01-Pb/s (12 SDM/222 WDM/456 Gb/s) Crosstalk-managed Transmission with 91.4-b/s/Hz Aggregate Spectral

-
- Efficiency,” in *European Conference and Exhibition on Optical Communication*, Amsterdam, 2012, p. Th.3.C.1.
- [31] D. Qian, E. Ip, M.-F. Huang, M.-j. Li, A. Dogariu, S. Zhang, Y. Shao, Y.-K. Huang, Y. Zhang, X. Cheng, Y. Tian, P. Ji, A. Collier, Y. Geng, J. Linares, C. Montero, V. Moreno, X. Prieto, and T. Wang, ”1.05Pb/s Transmission with 109b/s/Hz Spectral Efficiency using Hybrid Single- and Few-Mode Cores,” in *Frontiers in Optics 2012/Laser Science XXVIII*, Rochester, New York, 2012, p. FW6C.3.
- [32] S. O. Arik, J. M. Kahn, and H. Keang-Po, ”MIMO Signal Processing for Mode-Division Multiplexing: An overview of channel models and signal processing architectures,” *IEEE Signal Processing Magazine*, vol. 31, pp. 25-34 (2014).
- [33] B. Inan, Y. Jung, V. Sleiffer, M. Kushnerov, L. Gruner-Nielsen, S. Adhikari, S. L. Jansen, D. J. Richardson, S.-u. Alam, B. Spinnler, and N. Hanik, ”Low Computational Complexity Mode Division Multiplexed OFDM Transmission over 130 km of Few Mode Fiber,” in *Optical Fiber Communication (OFC) Conference*, Anaheim, California, 2013, p. OW4F.4.
- [34] N. Cvijetic, E. Ip, N. Prasad, M.-J. Li, and T. Wang, ”Experimental Time and Frequency Domain MIMO Channel Matrix Characterization versus Distance for 6×28Gbaud QPSK Transmission over 40×25km Few Mode Fiber,” in *Optical Fiber Communication (OFC) Conference*, San Francisco, California, 2014, p. Th1J.3.
- [35] P. P. Mitra and J. B. Stark, ”Nonlinear limits to the information capacity of optical fibre communications,” *Nature*, vol. 411, pp. 1027-1030 (2001).
- [36] R. Essiambre, G. Kramer, P. J. Winzer, G. J. Foschini, and B. Goebel, ”Capacity Limits of Optical Fiber Networks,” *Journal of Lightwave Technology*, vol. 28, pp. 662-701 (2010).
- [37] A. D. Ellis, Z. Jian, and D. Cotter, ”Approaching the Non-Linear Shannon Limit,” *Journal of Lightwave Technology*, vol. 28, pp. 423-433 (2010).
- [38] A. van Zelst, *MIMO OFDM for Wireless LANs* (2004).
- [39] C. E. Shannon, ”Communication In The Presence Of Noise,” *Proceedings of the IEEE*, vol. 86, pp. 447-457 (1998).
- [40] J. G. Proakis and D. G. Manolakis, *Digital signal processing*: Pearson Prentice Hall (2007).
- [41] H. Nyquist, ”Certain topics in telegraph transmission theory,” *Proceedings of the IEEE*, vol. 90, pp. 280-305 (2002).
- [42] N. Benvenuto and G. Cherubini, *Algorithms for Communications Systems and Their Applications*: Wiley (2002).
- [43] P. Poggiolini, ”Modeling of Non-Linear Propagation in Uncompensated Coherent Systems,” in *Optical Fiber Communication (OFC) Conference*, Anaheim, California, 2013, p. OTh3G.1.
- [44] S. Randel, A. Sierra, S. Mumtaz, A. Tulino, R. Ryf, P. J. Winzer, C. Schmidt, and R. Essiambre, ”Adaptive MIMO signal processing for mode-

- division multiplexing," in *Optical Fiber Communication (OFC) Conference*, 2012, pp. 1-3.
- [45] G. J. Foschini and M. J. Gans, "On Limits of Wireless Communications in a Fading Environment when Using Multiple Antennas," *Wireless Personal Communications*, vol. 6, pp. 311-335 (1998).
- [46] P. J. Winzer and G. J. Foschini, "MIMO capacities and outage probabilities in spatially multiplexed optical transport systems," *Optics Express*, vol. 19, pp. 16680-16696 (2011).
- [47] G. Strang, *Linear Algebra and Its Applications*: Thomson Brooks/Cole Cengage learning (2006).
- [48] R. M. Gray, *Toeplitz and Circulant Matrices: A Review*: Now Publishers (2006).
- [49] L. N. Trefethen and I. David Bau, *Numerical Linear Algebra*: Society for Industrial and Applied Mathematics (SIAM, 3600 Market Street, Floor 6, Philadelphia, PA 19104) (1997).
- [50] N. Chiurtu, B. Rimoldi, and I. E. Telatar, "On the capacity of multi-antenna Gaussian channels," in *Information Theory, 2001. Proceedings. 2001 IEEE International Symposium on*, 2001, p. 53.
- [51] G. H. Golub and C. F. Van Loan, *Matrix Computations*: Johns Hopkins University Press (2013).
- [52] D. Tse and P. Viswanath, *Fundamentals of Wireless Communication*: Cambridge University Press (2005).
- [53] M. Windisch, *Estimation and Compensation of IQ Imbalance in Broadband Communications Receivers*: Vogt (2007).
- [54] J. K. Cavers and M. W. Liao, "Adaptive compensation for imbalance and offset losses in direct conversion transceivers," *Vehicular Technology, IEEE Transactions on*, vol. 42, pp. 581-588 (1993).
- [55] F. Gray, "Pulse code communication," (1947).
- [56] G. Ungerboeck, "Trellis-coded modulation with redundant signal sets Part II: State of the art," *Communications Magazine, IEEE*, vol. 25, pp. 12-21 (1987).
- [57] S. Betti, F. Curti, G. De Marchis, and E. Iannone, "A novel multilevel coherent optical system: 4-quadrature signaling," *Journal of Lightwave Technology*, vol. 9, pp. 514-523 (1991).
- [58] L. D. Coelho and N. Hanik, "Global optimization of fiber-optic communication systems using four-dimensional modulation formats," in *European Conference on Optical Communications (ECOC)*, 2011, pp. 1-3.
- [59] E. Agrell and M. Karlsson, "Power-Efficient Modulation Formats in Coherent Transmission Systems," *Journal of Lightwave Technology*, vol. 27, pp. 5115-5126 (2009).
- [60] S. Ramachandran, *Fiber Based Dispersion Compensation*: Springer (2007).
- [61] J. G. Proakis, *Digital Communications*: McGraw-Hill Higher Education (2001).

-
- [62] H. J. Zepernick and A. Finger, *Pseudo Random Signal Processing: Theory and Application*: Wiley (2013).
- [63] R. L. Frank, "Polyphase codes with good nonperiodic correlation properties," *Information Theory, IEEE Transactions on*, vol. 9, pp. 43-45 (1963).
- [64] D. Chu, "Polyphase codes with good periodic correlation properties (Corresp.)," *Information Theory, IEEE Transactions on*, vol. 18, pp. 531-532 (1972).
- [65] Xilinx. (1996). *Efficient Shift Registers, LFSR Counters, and Long Pseudo-Random Sequence Generators*.
- [66] E. Grellier, J. C. Antona, and S. Bigo, "Are multilevel pseudorandom sequences really needed to emulate highly dispersive optical transmission systems?," in *European Conference on Optical Communications (ECOC)*, 2010, pp. 1-3.
- [67] M. Goresky and A. Klapper, *Algebraic Shift Register Sequences*: Cambridge University Press (2012).
- [68] "IEEE Standard for Terminology and Test Methods of Digital-to-Analog Converter Devices," *IEEE Std 1658-2011*, pp. 1-126 (2012).
- [69] R. H. Walden, "Analog-to-Digital Converters and Associated IC Technologies," in *Compound Semiconductor Integrated Circuits Symposium, 2008. CSIC '08. IEEE*, 2008, pp. 1-2.
- [70] A. Khilo, S. J. Spector, M. E. Grein, A. H. Nejadmalayeri, C. W. Holzwarth, M. Y. Sander, M. S. Dahlem, M. Y. Peng, M. W. Geis, N. A. DiLello, J. U. Yoon, A. Motamedi, J. S. Orcutt, J. P. Wang, C. M. Sorace-Agaskar, M. A. Popovi, J. Sun, G.-R. Zhou, H. Byun, J. Chen, J. L. Hoyt, H. I. Smith, R. J. Ram, M. Perrott, T. M. Lyszczarz, E. P. Ippen, and F. X. Kärtner, "Photonic ADC: overcoming the bottleneck of electronic jitter," *Optics Express*, vol. 20, pp. 4454-4469 (2012).
- [71] R. Essiambre, "SC327 Modeling and Design of Fiber-Optic Communication Systems," presented at the Optical Fiber Communication (OFC) Conference, San Fransisco, California (2014).
- [72] M. Seimetz, *High-Order Modulation for Optical Fiber Transmission*: Springer (2009).
- [73] L. Gruner-Nielsen, S. Yi, J. W. Nicholson, D. Jakobsen, K. G. Jespersen, R. Lingle, and B. Palsdottir, "Few Mode Transmission Fiber With Low DGD, Low Mode Coupling, and Low Loss," *Journal of Lightwave Technology*, vol. 30, pp. 3693-3698 (2012).
- [74] P. Sillard, D. Molin, M. Bigot-Astruc, H. Maerten, D. van Ras, and F. Achten, "Low-DMGD 6-LP-Mode Fiber," in *Optical Fiber Communication (OFC) Conference*, San Francisco, California, 2014, p. M3F.2.
- [75] T. Mori, T. Sakamoto, M. Wada, T. Yamamoto, and F. Yamamoto, "Six-LP-mode transmission fiber with DMD of less than 70 ps/km over C+L band," in *Optical Fiber Communication (OFC) Conference*, San Francisco, California, 2014, p. M3F.3.

- [76] T. s. s. o. ITU. (2007). *G.651.1: Characteristics of a 50/125 μ m multimode graded index optical fibre cable for the optical access network*.
- [77] K. Igarashi, T. Tsuritani, I. Morita, Y. Tsuchida, K. Maeda, M. Tadakuma, T. Saito, K. Watanabe, K. Imamura, R. Sugizaki, and M. Suzuki, "1.03-Exabit/skm Super-Nyquist-WDM transmission over 7,326-km seven-core fiber," in *European Conference on Optical Communications (ECOC)*, 2013, pp. 1-3.
- [78] R. Ryf, R. J. Essiambre, S. Randel, M. A. Mestre, C. Schmidt, and P. J. Winzer, "Impulse response analysis of coupled-core 3-core fibers," in *European Conference on Optical Communications (ECOC)*, 2012, pp. 1-3.
- [79] D. J. Richardson, K. Furusawa, H. Ebendorff-Heidepriem, P. Petropoulos, V. Finazzi, J. C. Baggett, W. Belardi, T. A. Kogure, J. H. Lee, Z. Yusoff, J. Nilsson, Y. Jeong, J. K. Sahu, and T. M. Monro, "Practical applications of holey optical fibers," in *Optical Fiber Communication (OFC) Conference*, 2004, p. 3 pp. vol.2.
- [80] J. C. Knight, J. Broeng, T. A. Birks, and P. S. J. Russell, "Photonic Band Gap Guidance in Optical Fibers," *Science*, vol. 282, pp. 1476-1478 (1998).
- [81] P. Russell, "Photonic Crystal Fibers," *Science*, vol. 299, pp. 358-362 (2003).
- [82] D. Gloge, "Weakly Guiding Fibers," *Applied Optics*, vol. 10, pp. 2252-2258 (1971).
- [83] E. J. Rothwell and M. J. Cloud, *Electromagnetics*. Taylor & Francis (2001).
- [84] P. Diament, *Wave Transmission and Fiber Optics*. Macmillan Publishing Company (1990).
- [85] A. W. Snyder, "Asymptotic Expressions for Eigenfunctions and Eigenvalues of a Dielectric or Optical Waveguide," *Microwave Theory and Techniques, IEEE Transactions on*, vol. 17, pp. 1130-1138 (1969).
- [86] A. W. Snyder and W. R. Young, "Modes of optical waveguides," *Journal of the Optical Society of America*, vol. 68, pp. 297-309 (1978).
- [87] B. E. A. Saleh and M. C. Teich, *Fundamentals of photonics*. Wiley (1991).
- [88] Draka. (2010). *DrakaElite BendBright-XS Fiber for Patch Cord*.
- [89] M. Abramowitz and I. A. Stegun, *Handbook of Mathematical Functions: With Formulas, Graphs, and Mathematical Tables*. Dover Publications (1972).
- [90] J. Adams, *An Introduction to Optical Waveguides*. John Wiley & Sons (1981).
- [91] R. W. Smit, *Optical fibres Analysis, numerical modelling and optimisation* (2009).
- [92] M. K. Barnoski, *Fundamentals of optical fiber communications*. Academic Press (1981).
- [93] J. H. Poynting, "On the Transfer of Energy in the Electromagnetic Field," *Philosophical Transactions of the Royal Society of London*, vol. 175, pp. 343-361 (1884).

-
- [94] J. A. Buck, *Fundamentals of Optical Fibers*. Wiley (1995).
- [95] H. Keang-Po and J. M. Kahn, "Linear Propagation Effects in Mode-Division Multiplexing Systems," *Journal of Lightwave Technology*, vol. 32, pp. 614-628 (2014).
- [96] L. Gruner-Nielsen, Y. Sun, J. W. Nicholson, D. Jakobsen, R. Lingle, and B. Palsdottir, "Few mode transmission fiber with low DGD, low mode coupling and low loss," in *Optical Fiber Communication (OFC) Conference*, 2012, pp. 1-3.
- [97] V. A. J. M. Sleiffer, Y. Jung, B. Inan, H. Chen, R. G. H. van Uden, M. Kuschnerov, D. van den Borne, S. L. Jansen, V. Veljanovski, A. M. J. Koonen, D. J. Richardson, S. Alam, F. Poletti, J. K. Sahu, A. Dhar, B. Corbett, R. Winfield, A. D. Ellis, and H. de Waardt, "Mode-division-multiplexed 3x112-Gb/s DP-QPSK transmission over 80-km few-mode fiber with inline MM-EDFA and blind DSP," in *European Conference on Optical Communications (ECOC)*, 2012, pp. 1-3.
- [98] R. Pimpinella and A. Brunsting, "Differential Mode Delay (DMD) for Multimode Fiber Types and its Relationship to Measured Performance," in *Optical Fiber Communication (OFC) Conference*, Anaheim, California, 2005, p. NWF2.
- [99] J. M. Kahn, K.-P. Ho, and M. Bagher Shemirani, "Mode coupling effects in multi-mode fibers," in *Optical Fiber Communication Conference*, Los Angeles, California, 2012, p. OW3D.3.
- [100] K.-P. Ho and J. M. Kahn, "Mode-dependent loss and gain: statistics and effect on mode-division multiplexing," *Optics Express*, vol. 19, pp. 16612-16635 (2011).
- [101] R. Ryf, S. Randel, N. K. Fontaine, M. Montoliu, E. Burrows, S. Corteselli, S. Chandrasekhar, A. H. Gnauck, C. Xie, R. J. Essiambre, P. J. Winzer, R. Delbue, P. Pupalakikis, A. Sureka, Y. Sun, L. Gruner-Nielsen, R. V. Jensen, and R. Lingle, "32-bit/s/Hz spectral efficiency WDM transmission over 177-km few-mode fiber," in *Optical Fiber Communication (OFC) Conference*, 2013, pp. 1-3.
- [102] J. M. Kahn and K.-P. Ho, "Mode-Division-Multiplexing Systems: Propagation Effects, Performance and Complexity," in *Optical Fiber Communication (OFC) Conference*, Anaheim, California, 2013, p. OTh4G.1.
- [103] T. S. Rappaport, *Wireless Communications: Principles and Practice*. Dorling Kindersley (2009).
- [104] G. D. Durgin, *Space-time Wireless Channels*. Prentice Hall PTR (2003).
- [105] G. Agrawal, *Nonlinear Fiber Optics*. Elsevier Science (2001).
- [106] E. Ip, "Nonlinear Compensation Using Backpropagation for Polarization-Multiplexed Transmission," *Journal of Lightwave Technology*, vol. 28, pp. 939-951 (2010).
- [107] A. Napoli, Z. Maalej, V. A. J. M. Sleiffer, M. Kuschnerov, D. Rafique, E. Timmers, B. Spinnler, T. Rahman, L. D. Coelho, and N. Hanik, "Reduced

- Complexity Digital Back-Propagation Methods for Optical Communication Systems,” *Journal of Lightwave Technology*, vol. 32, pp. 1351-1362 (2014).
- [108] F. Yaman and L. Guifang, ”Nonlinear Impairment Compensation for Polarization-Division Multiplexed WDM Transmission Using Digital Backward Propagation,” *Photonics Journal, IEEE*, vol. 2, pp. 816-832 (2010).
- [109] G. Rademacher, S. Warm, and K. Petermann, ”Splice induced nonlinear performance penalty in mode-division multiplexed transmission systems,” in *European Conference on Optical Communications (ECOC)*, 2013, pp. 1-3.
- [110] R.-J. Essiambre, R. Ryf, M. A. Mestre, A. H. Gnauck, R. Tkach, A. Chraplyvy, S. Randel, Y. Sun, X. Jiang, and R. Lingle, ”Inter-Modal Nonlinear Interactions Between Well Separated Channels in Spatially-Multiplexed Fiber Transmission,” in *European Conference and Exhibition on Optical Communication*, Amsterdam, 2012, p. Tu.1.C.4.
- [111] K. Y. Song and Y. H. Kim, ”Measurement of Intramodal and Intermodal Brillouin Gain Spectra in a Few-mode Fiber,” in *Optical Fiber Communication (OFC) Conference*, San Francisco, California, 2014, p. W3D.6.
- [112] Y. Xiao, S. Mumtaz, R.-J. Essiambre, and G. P. Agrawal, ”Effect of random linear mode coupling on intermodal four-wave mixing in few-mode fibers,” in *Optical Fiber Communication (OFC) Conference*, San Francisco, California, 2014, p. M3F.5.
- [113] I. Corning. (2012). *Corning LEAF Optical Fiber Product Information*.
- [114] C. Headley and G. P. Agrawal, *Raman Amplification in Fiber Optical Communication Systems*: Elsevier Academic Press (2005).
- [115] M. N. Islam, ”Raman amplifiers for telecommunications,” *Selected Topics in Quantum Electronics, IEEE Journal of*, vol. 8, pp. 548-559 (2002).
- [116] P. M. Krummrich and K. Petermann, ”Evaluation of potential optical amplifier concepts for coherent mode multiplexing,” in *Optical Fiber Communication (OFC) Conference*, 2011, pp. 1-3.
- [117] E. Desurvire, J. R. Simpson, and P. C. Becker, ”High-gain erbium-doped traveling-wave fiber amplifier,” *Optics Letters*, vol. 12, pp. 888-890 (1987).
- [118] B. Wang, G. Pub, R. Osnato, and B. Palsdottir, ”Characterization of gain spectral variation of Erbium-doped fibers codoped with aluminum,” 2004, pp. 161-166.
- [119] C. R. Giles and E. Desurvire, ”Modeling erbium-doped fiber amplifiers,” *Journal of Lightwave Technology*, vol. 9, pp. 271-283 (1991).
- [120] G. P. Agrawal, *Lightwave Technology: Components and Devices*. Wiley (2004).
- [121] Y. Jung, S. Alam, Z. Li, A. Dhar, D. Giles, I. P. Giles, J. K. Sahu, F. Poletti, L. Grüner-Nielsen, and D. J. Richardson, ”First demonstration and detailed characterization of a multimode amplifier for space division

-
- multiplexed transmission systems," *Optics Express*, vol. 19, pp. B952-B957 (2011).
- [122] N. Bai, E. Ip, T. Wang, and G. Li, "Multimode fiber amplifier with tunable modal gain using a reconfigurable multimode pump," *Optics Express*, vol. 19, pp. 16601-16611 (2011).
- [123] Q. Kang, E.-L. Lim, Y. Jung, J. K. Sahu, F. Poletti, C. Baskiotis, S.-u. Alam, and D. J. Richardson, "Accurate modal gain control in a multimode erbium doped fiber amplifier incorporating ring doping and a simple LP01 pump configuration," *Optics Express*, vol. 20, pp. 20835-20843 (2012).
- [124] G. Le Cocq, L. Bigot, A. Le Rouge, M. Bigot-Astruc, P. Sillard, C. Koebele, M. Salsi, and Y. Quiquempois, "Modeling and characterization of a few-mode EDFA supporting four mode groups for mode division multiplexing," *Optics Express*, vol. 20, pp. 27051-27061 (2012).
- [125] M. S. Alfiad, D. Van den Borne, S. L. Jansen, T. Wuth, M. Kuschnerov, G. Grosso, A. Napoli, and H. de Waardt, "A Comparison of Electrical and Optical Dispersion Compensation for 111-Gb/s POLMUX-RZ-DQPSK," *Journal of Lightwave Technology*, vol. 27, pp. 3590-3598 (2009).
- [126] M. F. Weber, C. L. Bruzzone, P. D. Condo, K. M. Hamer, T. J. Hebrink, and W. W. Merrill, "Polarizing beam splitter," ed: Google Patents, 2003.
- [127] M. Salsi, C. Koebele, D. Sperti, P. Tran, H. Mardoyan, P. Brindel, S. Bigo, A. Boutin, F. Verluise, P. Sillard, M. Astruc, L. Provost, and G. Charlet, "Mode-Division Multiplexing of 2x100 Gb/s Channels Using an LCOS-Based Spatial Modulator," *Journal of Lightwave Technology*, vol. 30, pp. 618-623 (2012).
- [128] C. Koebele, M. Salsi, L. Milord, R. Ryf, C. Bolle, P. Sillard, S. Bigo, and G. Charlet, "40km transmission of five mode division multiplexed data streams at 100Gb/s with low MIMO-DSP complexity," in *European Conference on Optical Communications (ECOC)*, 2011, pp. 1-3.
- [129] R. Ryf, S. Randel, A. H. Gnauck, C. Bolle, R. Essiambre, P. J. Winzer, D. W. Peckham, A. McCurdy, and R. Lingle, "Space-division multiplexing over 10 km of three-mode fiber using coherent 6x6 MIMO processing," in *Optical Fiber Communication (OFC) Conference*, 2011, pp. 1-3.
- [130] R. Ryf, N. K. Fontaine, and R. Essiambre, "Spot-based mode coupler for mode-multiplexed transmission in few-mode fiber," in *Photonics Society Summer Topical Meeting Series, 2012 IEEE*, 2012, pp. 199-200.
- [131] R. Ryf, N. K. Fontaine, and R. J. Essiambre, "Spot-Based Mode Couplers for Mode-Multiplexed Transmission in Few-Mode Fiber," *IEEE Photonics Technology Letters*, vol. 24, pp. 1973-1976 (2012).
- [132] R. Ryf, M. A. Mestre, A. Gnauck, S. Randel, C. Schmidt, R. Essiambre, P. Winzer, R. Delbue, P. Pupalaiakis, A. Sureka, Y. Sun, X. Jiang, D. Peckham, A. H. McCurdy, and R. Lingle, "Low-Loss Mode Coupler for Mode-Multiplexed transmission in Few-Mode Fiber," in *National Fiber Optic Engineers Conference*, Los Angeles, California, 2012, p. PDP5B.5.

- [133] N. K. Fontaine and R. Ryf, "Characterization of mode-dependent loss of laser inscribed photonic lanterns for space division multiplexing systems," in *OptoElectronics and Communications Conference held jointly with 2013 International Conference on Photonics in Switching (OECC/PS), 2013 18th*, 2013, pp. 1-2.
- [134] P. Mitchell, G. Brown, R. R. Thomson, N. Psaila, and A. Kar, "57 Channel (19x3) Spatial Multiplexer Fabricated using Direct Laser Inscription," in *Optical Fiber Communication (OFC) Conference*, San Francisco, California, 2014, p. M3K.5.
- [135] S. Yerolatsitis, I. Gris-Sánchez, and T. A. Birks, "Adiabatically-tapered fiber mode multiplexers," *Optics Express*, vol. 22, pp. 608-617 (2014).
- [136] S. G. Leon-Saval, N. K. Fontaine, J. R. Salazar-Gil, B. Ercan, R. Ryf, and J. Bland-Hawthorn, "Mode-selective photonic lanterns for space-division multiplexing," *Optics Express*, vol. 22, pp. 1036-1044 (2014).
- [137] R. Ryf, N. K. Fontaine, H. Chen, B. Guan, S. Randel, N. Sauer, S. J. B. Yoo, A. Koonen, R. Delbue, P. Pupalaiakis, A. Sureka, R. Shubochkin, Y. Sun, and R. Lingle, "23~Tbit/s Transmission over 17-km Conventional 50 um Graded-Index Multimode Fiber," in *Optical Fiber Communication (OFC) Conference*, San Francisco, California, 2014, p. Th5B.1.
- [138] S. Yerolatsitis and T. A. Birks, "Three-mode multiplexer in photonic crystal fibre," in *Optical Communication (ECOC 2013), 39th European Conference and Exhibition on*, 2013, pp. 1-3.
- [139] N. K. Fontaine, R. Ryf, J. Bland-Hawthorn, and S. G. Leon-Saval, "Geometric requirements for photonic lanterns in space division multiplexing," *Optics Express*, vol. 20, pp. 27123-27132 (2012).
- [140] S. Jain, V. J. F. Ranaño, T. C. May-Smith, P. Petropoulos, J. K. Sahu, and D. J. Richardson, "Multi-Element Fiber Technology for Space-Division Multiplexing Applications," *Optics Express*, vol. 22, pp. 3787-3796 (2014).
- [141] C. Wree, D. Becker, D. Mohr, and A. Joshi, "Optical coherent receivers for 2.5 and 5 Gb/s," in *Lasers and Electro-Optics Society, 2005. LEOS 2005. The 18th Annual Meeting of the IEEE*, 2005, pp. 555-556.
- [142] S. Ayotte, F. Costin, G. Brochu, M.-J. Picard, A. Babin, F. Pelletier, S. Chandrasekhar, and X. Liu, "White Noise Filtered C-band Tunable Laser for Coherent Transmission Systems," in *Optical Fiber Communication (OFC) Conference*, Los Angeles, California, 2012, p. OTu1G.5.
- [143] M. Windisch and G. Fettweis, "Standard-independent I/Q imbalance compensation in OFDM direct-conversion receivers," in *In Proc. 9th Intl. OFDM Workshop (InOWo)*, 2004.
- [144] u2t. (2014). *40 GHz, 64 Gbaud, Integrated High-speed Coherent Photodetector*. Available: <http://www.finisar.com/products/optical-components/High-Performance-LW-Detectors/CPDV1200R>
- [145] T. s. s. o. ITU. (2004). *G.975.1 : Forward error correction for high bit-rate DWDM submarine systems*. Available: <http://www.itu.int/rec/T-REC-G.975.1-200402-I/en>

-
- [146] T. K. Moon, *Error Correction Coding: Mathematical Methods and Algorithms*. Wiley (2005).
- [147] T. Mizuochi, Y. Konishi, Y. Miyata, T. Inoue, K. Onohara, S. Kametani, T. Sugihara, K. Kubo, T. Kobayashi, H. Yoshida, and T. Ichikawa, "FPGA based prototyping of next generation forward error correction," in *European Conference on Optical Communications (ECOC)*, 2009, pp. 1-4.
- [148] S. J. Savory, "Digital Coherent Optical Receivers: Algorithms and Subsystems," *Selected Topics in Quantum Electronics, IEEE Journal of*, vol. 16, pp. 1164-1179 (2010).
- [149] C. Sun Hyok, C. Hwan Seok, and K. Kwangjoon, "Impact of Quadrature Imbalance in Optical Coherent QPSK Receiver," *IEEE Photonics Technology Letters*, vol. 21, pp. 709-711 (2009).
- [150] I. Mayer, "On Löwdin's method of symmetric orthogonalization*," *International Journal of Quantum Chemistry*, vol. 90, pp. 63-65 (2002).
- [151] L. Anttila, M. Valkama, and M. Renfors, "Blind Moment Estimation Techniques for I/Q Imbalance Compensation in Quadrature Receivers," in *Personal, Indoor and Mobile Radio Communications, 2006 IEEE 17th International Symposium on*, 2006, pp. 1-5.
- [152] E. W. Cheney and D. R. Kincaid, *Linear Algebra: Theory and Applications*. Jones and Bartlett Publishers (2009).
- [153] I. Fatadin, S. J. Savory, and D. Ives, "Compensation of Quadrature Imbalance in an Optical QPSK Coherent Receiver," *IEEE Photonics Technology Letters*, vol. 20, pp. 1733-1735 (2008).
- [154] P. O. Löwdin, "On the Non-Orthogonality Problem Connected with the Use of Atomic Wave Functions in the Theory of Molecules and Crystals," *The Journal of Chemical Physics*, vol. 18, pp. 365-375 (1950).
- [155] D. F. Scofield, "A note on Löwdin orthogonalization and the square root of a positive self-adjoint matrix," *International Journal of Quantum Chemistry*, vol. 7, pp. 561-568 (1973).
- [156] F. M. Gardner, "Interpolation in digital modems. I. Fundamentals," *Communications, IEEE Transactions on*, vol. 41, pp. 501-507 (1993).
- [157] F. Takahata, M. Yasunaga, Y. Hirata, T. Ohsawa, and J. Namiki, "A PSK Group Modem for Satellite Communications," *Selected Areas in Communications, IEEE Journal on*, vol. 5, pp. 648-661 (1987).
- [158] H. Meyr, M. Moeneclaey, and S. A. Fechtel, *Digital Communication Receivers, Synchronization, Channel Estimation, and Signal Processing*. Wiley (1998).
- [159] G. Ascheid, M. Oerder, J. Stahl, and H. Meyr, "An all digital receiver architecture for bandwidth efficient transmission at high data rates," *Communications, IEEE Transactions on*, vol. 37, pp. 804-813 (1989).
- [160] W. H. Press, *Numerical Recipes 3rd Edition: The Art of Scientific Computing*. Cambridge University Press (2007).

-
- [161] L. Erup, F. M. Gardner, and R. A. Harris, "Interpolation in digital modems. II. Implementation and performance," *Communications, IEEE Transactions on*, vol. 41, pp. 998-1008 (1993).
- [162] C. W. Farrow, "A continuously variable digital delay element," in *Circuits and Systems, 1988., IEEE International Symposium on*, 1988, pp. 2641-2645 vol.3.
- [163] S. H. Chang, H. S. Chung, and K. Kim, "Digital non-data-aided symbol synchronization in optical coherent intradyne reception," *Optics Express*, vol. 16, pp. 15097-15103 (2008).
- [164] M. S. Alfiad, *Multilevel Modulation Formats for Robust Long-Haul High Capacity Transmission* (2011).
- [165] U. Mengali and A. N. D'Andrea, *Synchronization Techniques for Digital Receivers*. Springer (1997).
- [166] F. M. Gardner, "A BPSK/QPSK Timing-Error Detector for Sampled Receivers," *Communications, IEEE Transactions on*, vol. 34, pp. 423-429 (1986).
- [167] M. Oerder and H. Meyr, "Digital filter and square timing recovery," *Communications, IEEE Transactions on*, vol. 36, pp. 605-612 (1988).
- [168] R. A. Soriano, F. N. Hauske, N. G. Gonzalez, Z. Zhuhong, Y. Ye, and I. T. Monroy, "Chromatic Dispersion Estimation in Digital Coherent Receivers," *Journal of Lightwave Technology*, vol. 29, pp. 1627-1637 (2011).
- [169] M. D. Feuer, L. E. Nelson, X. Zhou, S. L. Woodward, R. Isaac, Z. Benyuan, T. F. Taunay, M. Fishteyn, J. M. Fini, and M. F. Yan, "Joint Digital Signal Processing Receivers for Spatial Superchannels," *IEEE Photonics Technology Letters*, vol. 24, pp. 1957-1960 (2012).
- [170] M. Kuschnerov, *Signal Processing for Coherent Optic Receivers*. Köster (2011).
- [171] I. Slim, A. Mezghani, L. G. Baltar, J. Qi, F. N. Hauske, and J. A. Nossek, "Delayed Single-Tap Frequency-Domain Chromatic-Dispersion Compensation," *IEEE Photonics Technology Letters*, vol. 25, pp. 167-170 (2013).
- [172] M. Kuschnerov, T. Bex, and P. Kainzmaier, "Energy Efficient Digital Signal Processing," in *Optical Fiber Communication (OFC) Conference*, San Francisco, California, 2014, p. Th3E.7.
- [173] M. Miyoshi and Y. Kaneda, "Inverse filtering of room acoustics," *Acoustics, Speech and Signal Processing, IEEE Transactions on*, vol. 36, pp. 145-152 (1988).
- [174] A. Erdélyi, *Asymptotic Expansions*. Dover Publications (1956).
- [175] N. Wiener, *Extrapolation, interpolation, and smoothing of stationary time series: with engineering applications*. Technology Press of the Massachusetts Institute of Technology (1964).
- [176] T. Kailath, *Linear least-squares estimation*. Dowden, Hutchinson & Ross (1977).
- [177] S. S. Haykin, *Adaptive filter theory*. Prentice Hall (2002).

-
- [178] Y. Huang, J. Benesty, and J. Chen, *Acoustic MIMO Signal Processing*: Springer (2006).
- [179] B. Widrow and E. Hoff, *Adaptive switching circuits* (1960).
- [180] B. Widrow and E. Walach, *Adaptive Inverse Control, Reissue Edition: A Signal Processing Approach*: Wiley (2008).
- [181] D. Godard, "Self-Recovering Equalization and Carrier Tracking in Two-Dimensional Data Communication Systems," *Communications, IEEE Transactions on*, vol. 28, pp. 1867-1875 (1980).
- [182] P. J. Winzer, A. H. Gnauck, C. R. Doerr, M. Magarini, and L. L. Buhl, "Spectrally Efficient Long-Haul Optical Networking Using 112-Gb/s Polarization-Multiplexed 16-QAM," *Journal of Lightwave Technology*, vol. 28, pp. 547-556 (2010).
- [183] P. Comon and C. Jutten, *Handbook of Blind Source Separation: Independent Component Analysis and Applications*: Elsevier Science (2010).
- [184] M. S. Faruk and K. Kikuchi, "Adaptive frequency-domain equalization in digital coherent optical receivers," *Optics Express*, vol. 19, pp. 12789-12798 (2011).
- [185] J. J. Shynk, "Frequency-domain and multirate adaptive filtering," *Signal Processing Magazine, IEEE*, vol. 9, pp. 14-37 (1992).
- [186] J. Leibrich and W. Rosenkranz, "Frequency Domain Equalization with Minimum Complexity in Coherent Optical Transmission Systems," in *Optical Fiber Communication (OFC) Conference*, San Diego, California, 2010, p. OWV1.
- [187] E. A. Lee and D. G. Messerschmitt, *Digital Communication*: Kluwer Academic Publishers (1994).
- [188] "IEEE Standard for Floating-Point Arithmetic," *IEEE Std 754-2008*, pp. 1-70 (2008).
- [189] R. G. Lyons, *Understanding Digital Signal Processing*: Pearson Education (2010).
- [190] P. Wilson, *Design Recipes for FPGAs: Using Verilog and VHDL*: Elsevier Science (2011).
- [191] Y. Lee, Y. Choi, S.-B. Ko, and M. Ho Lee, "Performance Analysis of Bit-Width Reduced Floating-Point Arithmetic Units in FPGAs: A Case Study of Neural Network-Based Face Detector," *EURASIP Journal on Embedded Systems*, vol. 2009, p. 258921 (2009).
- [192] A. N. D'Andrea, U. Mengali, and R. Reggiannini, "The modified Cramer-Rao bound and its application to synchronization problems," *Communications, IEEE Transactions on*, vol. 42, pp. 1391-1399 (1994).
- [193] K. Piyawanno, M. Kuschnerov, F. N. Hauske, B. Spinnler, E. D. Schmidt, and B. Lankl, "Correlation-Based Carrier Phase Estimation for WDM DP-QPSK Transmission," *IEEE Photonics Technology Letters*, vol. 20, pp. 2090-2092 (2008).

-
- [194] A. Viterbi, "Nonlinear estimation of PSK-modulated carrier phase with application to burst digital transmission," *Information Theory, IEEE Transactions on*, vol. 29, pp. 543-551 (1983).
- [195] T. Pfau, "Carrier Recovery Algorithms and Real-time DSP Implementation for Coherent Receivers," in *Optical Fiber Communication (OFC) Conference*, San Francisco, California, 2014, p. W4K.1.
- [196] D. Van den Borne, *Robust Optical Transmission Systems Modulation and Equalization* (2008).
- [197] J. P. Costas, "Synchronous Communications," *Communications Systems, IRE Transactions on*, vol. 5, pp. 99-105 (1957).
- [198] J. P. Costas, "Synchronous Communications," *Proceedings of the IRE*, vol. 44, pp. 1713-1718 (1956).
- [199] C. Xie and G. Raybon, "Digital PLL Based Frequency Offset Compensation and Carrier Phase Estimation for 16-QAM Coherent Optical Communication Systems," in *European Conference and Exhibition on Optical Communication*, Amsterdam, 2012, p. Mo.1.A.2.
- [200] Z. Xiang, "An Improved Feed-Forward Carrier Recovery Algorithm for Coherent Receivers With M-QAM Modulation Format," *IEEE Photonics Technology Letters*, vol. 22, pp. 1051-1053 (2010).
- [201] C. R. S. Fludger, D. Nuss, and T. Kupfer, "Cycle-slips in 100G DP-QPSK transmission systems," in *Optical Fiber Communication (OFC) Conference*, 2012, pp. 1-3.
- [202] C. Laperle, "Advances in high-speed ADCs, DACs, and DSP for optical transceivers," in *Optical Fiber Communication (OFC) Conference*, 2013, pp. 1-30.
- [203] T. Mizuochi, Y. Miyata, K. Kubo, T. Sugihara, K. Onohara, and H. Yoshida, "Progress in soft-decision FEC," in *Optical Fiber Communication (OFC) Conference*, 2011, p. NWC2.
- [204] E. Ip, M.-j. Li, C. Montero, and Y. Yano, "6x28-Gbaud Few-Mode Recirculating Loop Transmission with Gain-Equalized Inline Few-Mode Fiber Amplifier," in *Optical Fiber Communication (OFC) Conference*, Anaheim, California, 2013, p. OW4F.3.
- [205] V. A. J. M. Sleiffer, Y. Jung, V. Veljanovski, R. G. H. van Uden, M. Kuschnerov, H. Chen, B. Inan, L. G. Nielsen, Y. Sun, D. J. Richardson, S. U. Alam, F. Poletti, J. K. Sahu, A. Dhar, A. M. J. Koonen, B. Corbett, R. Winfield, A. D. Ellis, and H. de Waardt, "73.7 Tb/s (96 x 3 x 256-Gb/s) mode-division-multiplexed DP-16QAM transmission with inline MM-EDFA," *Optics Express*, vol. 20, pp. B428-B438 (2012).
- [206] V. Tarokh, N. Seshadri, and A. R. Calderbank, "Space-time codes for high data rate wireless communication: performance criterion and code construction," *Information Theory, IEEE Transactions on*, vol. 44, pp. 744-765 (1998).

-
- [207] S. Alamouti, "A simple transmit diversity technique for wireless communications," *Selected Areas in Communications, IEEE Journal on*, vol. 16, pp. 1451-1458 (1998).
- [208] V. Tarokh, H. Jafarkhani, and A. R. Calderbank, "Space-time block codes from orthogonal designs," *Information Theory, IEEE Transactions on*, vol. 45, pp. 1456-1467 (1999).
- [209] V. A. J. M. Sleiffer, H. Chen, Y. Jung, P. Leoni, M. Kuschnerov, A. Simperler, H. Fabian, H. Schuh, F. Kub, D. J. Richardson, S. U. Alam, L. Grüner-Nielsen, Y. Sun, A. M. J. Koonen, and H. de Waardt, "Field demonstration of mode-division multiplexing upgrade scenarios on commercial networks," *Optics Express*, vol. 21, pp. 31036-31046 (2013).
- [210] K. Nagayama, M. Kakui, M. Matsui, T. Saitoh, and Y. Chigusa, "Ultra-low-loss (0.1484 dB/km) pure silica core fibre and extension of transmission distance," *Electronics Letters*, vol. 38, pp. 1168-1169 (2002).
- [211] M. N. Petrovich, F. Poletti, J. Wooller, A. Heidt, N. K. Baddela, Z. Li, D. R. Gray, R. Slavík, F. Parmigiani, N. Wheeler, J. Hayes, E. Numkam Fokoua, L. Grüner-Nielsen, B. Pálsdóttir, R. Phelan, B. Kelly, M. Becker, N. MacSuibhne, J. Zhao, F. C. Garcia Gunning, A. Ellis, P. Petropoulos, S.-u. Alam, and D. Richardson, "First Demonstration of 2um Data Transmission in a Low-Loss Hollow Core Photonic Bandgap Fiber," in *European Conference and Exhibition on Optical Communication*, Amsterdam, 2012, p. Th.3.A.5.
- [212] P. J. Roberts, F. Couny, H. Sabert, B. J. Mangan, D. P. Williams, L. Farr, M. W. Mason, A. Tomlinson, T. A. Birks, J. C. Knight, and P. S. J. Russell, "Ultimate low loss of hollow-core photonic crystal fibres," *Optics Express*, vol. 13, pp. 236-244 (2005).
- [213] F. Poletti, V. Finazzi, T. M. Monro, N. G. R. Broderick, V. Tse, and D. J. Richardson, "Inverse design and fabrication tolerances of ultra-flattened dispersion holey fibers," *Optics Express*, vol. 13, pp. 3728-3736 (2005).
- [214] X. Cen, R. Amezcua-Correa, B. Neng, E. Antonio-Lopez, D. M. Arriola, A. Schulzgen, M. Richardson, J. Linares, C. Montero, E. Mateo, Z. Xiang, and L. Guifang, "Hole-Assisted Few-Mode Multicore Fiber for High-Density Space-Division Multiplexing," *IEEE Photonics Technology Letters*, vol. 24, pp. 1914-1917 (2012).
- [215] R. Lingle, "Capacity Constraints, Carrier Economics, and the Limits of Fiber and Cable Design," in *Optical Fiber Communication (OFC) Conference*, Anaheim, California, 2013, p. OM2F.1.
- [216] DARPA. (2013). <http://www.darpa.mil/NewsEvents/Releases/2013/07/17a.aspx>.
- [217] P. M. Krummrich, "Optical amplification and optical filter based signal processing for cost and energy efficient spatial multiplexing," *Optics Express*, vol. 19, pp. 16636-16652 (2011).

List of acronyms

Acronym	Description
3DW	Three dimensional waveguide
3MF	Three mode fiber
ACF	Autocorrelation function
ADC	Analog-to-digital converter
AOM	Acoustic-optical modulator
ASE	Amplified spontaneous emission
AWGN	Additive white Gaussian noise
BER	Bit error rate
BPHD	Balanced photo detector
BTB	Back-to-back
CACF	Complex autocorrelation function
CAGR	Compounded annual growth rate
CAZAC	Constant amplitude zero autocorrelation
ChUT	Channel under test
CIL	Coupler insertion loss
CMA	Constant modulus algorithm
CPE	Carrier phase estimation
CRB	Cramer-Rao bound
CSI	Channel state information
CoUT	Core under test
DAC	Digital-to-analog converter
DBP	Digital back-propagation
DCF	Dispersion compensating fiber
DD-LMS	Decision-directed least mean squares
DFT	Discrete fourier transformation
DMD	Differential mode delay
DP	Dual-polarization
DPLL	Digital phase locked loop
DS	Dispersion-shifted
DSP	Digital signal processing
ECL	External cavity laser
EDFA	Erbium doped fiber amplifier

Acronym	Description
ENOB	Effective number of bits
FDE	Frequency domain equalizer
FDM	Frequency domain multiplexing
FE	Front-end
FEC	Forward error correcting
FIR	Finite impulse response
FM-MCF	Few mode multicore fiber
FMF	Few mode fiber
FWM	Four-wave mixing
GFF	Gain flattening filter
GI	Graded-index
GVD	Group velocity dispersion
HC-PBGF	Hollow-core photonic bandgap fiber
IDFT	Inverse discrete Fourier transformation
IMRR	Image rejection ratio
ISI	Inter symbol interference
ITU	International Telecommunication Union
IQ	Inphase-quadrature
LDPC	Low-density parity-check
LEAF	Large effective area fiber
LFSR	Linear feedback shift register
LMS	Least mean squares
LO	Local oscillator
LP	Linearly polarized
LPF	Low pass filter
LS	Least squares
LTE	Long term evolution
LTI	Linear time invariant
LUT	Look-up table
MCF	Multi-core fiber
MCRB	Modified Cramer-Rao bound
MDL	Mode dependent loss
MDMUX	Mode demultiplexer
MEMS	Micro-electromechanical systems
MIMO	Multiple-input multiple-output

Acronym	Description
ML	Maximum likelihood
MM-EDFA	Multimode erbium doped fiber amplifier
MMF	Multimode fiber
MMSE	Minimum mean squared error
MMUX	Mode multiplexer
MOI	Mode overlap integral
NF	Noise figure
NLSE	Non-linear Schrödinger equation
ODE	Ordinary differential equation
OEOC	Optical-electrical-optical converter
OFDM	Orthogonal frequency domain multiplexing
OSNR	Optical signal to noise ratio
OTDM	Optical time domain multiplexing
PAM	Pulse amplitude modulation
PBS	Polarization beam splitter
PDF	Probability density function
PD	Phase detector
PDL	Polarization dependent loss
PHD	Photo detector
PMD	Polarization mode dispersion
PRBS	Pseudo-random bit sequence
PSK	Phase-shift keying
QAM	Quadrature amplitude modulation
QPSK	Quadrature phase-shift keying
RIN	Relative intensity noise
RIP	Refractive index profile
RLS	Recursive least squares
RS	Reed-Solomon
SD	Soft-decision
SDM	Spatial division multiplexing
SE	Spectral efficiency
SEM	Scanning electron microscope
SGD	Steepest gradient descent
SI	Step-index
SIMO	Single-input multiple-output

Acronym	Description
SMF	Single mode fiber
SNR	Signal to noise ratio
SOA	Semiconductor optical amplifier
SP	Set-partitioned
SPM	Self-phase modulation
STBC	Space time block code
STC	Space time code
STTC	Space-time trellis code
TCM	Trellis coded modulation
TDE	Time domain equalizer
TDM	Time domain multiplexing
TE	Transverse-electric
TEM	Transverse electromagnetic
TM	Transverse-magnetic
TS	Time-shifted
V-BLAST	Vertical-Bell Laboratories Layered Space-Time
V-V	Viterbi-Viterbi
VOA	Variable optical attenuator
VoIP	Voice over internet protocol
WDM	Wavelength division multiplexing
WGA	Weakly guiding approximation
WSS	Wavelength selective switch
XPM	Cross-phase modulation
ZF	Zero-forcing

List of symbols

Symbol	Description
$\mathbf{0}_{i \times j}$	0 matrix of size $i \times j$
α	Fiber attenuation
β	Propagation constant
$\beta^{(0)}$	Zero-order propagation constant
$\beta^{(1)}$	Group velocity
$\beta^{(2)}$	Group velocity dispersion
$\beta^{(3)}$	Group velocity dispersion slope
β_R	Roll-off factor
ε	Absolute permittivity
ε_0	Permittivity in vacuum
ε_r	Relative permittivity
φ	Phase
γ	Kerr non-linearity contribution
γ_s	Complementary autocorrelation function in front-end compensation
η	Quantum efficiency
η_{sp}	Amplified spontaneous emission factor
$\kappa(\bullet)$	Matrix condition number
λ_0	Wavelength
λ_i	Matrix eigenvalue
μ	Adaptation gain
μ_0	Permeability in vacuum
μ_u	Interpolation fractional interval
$\Delta\nu$	Laser linewidth
θ	Polarization rotation angle
\mathbf{p}	Cartesian coordinates
σ_n^2	Noise variance
σ_s^2	Signal variance
σ_τ	Standard deviation impulse response
Σ	Diagonal singular value decomposition matrix
ω	Angular frequency
Ω	Shift parameter
ζ	Farrow coefficient
Φ	Estimated carrier phase

Symbol	Description
ψ	Inverse group velocity dispersion filter
A_{eff}	Effective area
B	Bandwidth
\mathcal{B}	Magnetic flux density
B_{ref}	Reference bandwidth
b	Normalized propagation constant
C	Capacity
C_{IQ}	Correlation between inphase and quadrature
c_0	Speed of light
$d[k]$	Desired signal
\mathcal{D}	Electric flux density
D	Dispersion
D_{M}	Material dispersion
D_{W}	Waveguide dispersion
\mathcal{E}	Electric field
e_{en}	Electron charge
$e[k]$	Error signal
G	Gain
g_{I}	Inphase component Gram-Schmidt orthonormalization
g_{Q}	Quadrature component Gram-Schmidt orthonormalization
f	Frequency
f_0	Carrier frequency
F_{EDFA}	EDFA noise factor
\mathcal{H}	Magnetic field
\hbar	Planck's constant
$h(t)$	Channel impulse response
\mathbf{h}	Channel impulse response vector
\mathbf{H}	Channel impulse response matrix
\mathbf{H}_{LS}	LS channel estimation matrix
\mathbf{H}_{MMSE}	MMSE channel estimation matrix
\mathbf{H}_{MMUX}	Mode multiplexer channel matrix
H_{GVD}	GVD filter function
\mathcal{J}	Induced electric current density
$I(t)$	Current
I_{sh}	Shot noise current
$\mathbf{I}_{i \times j}$	Identity matrix of size $i \times j$
J	Cost function
J_{max}	Cost function maximum

Symbol	Description
J_{\min}	Cost function minimum
\mathbf{J}	Multidimensional cost function
κ	Induced magnetic current density
k	Sample instance
k_0	Wave number in vacuum
\mathcal{K}_R	Rician K-factor
L	Impulse response length
\mathbf{L}	Löwdin orthonormalization matrix
L_{fiber}	Fiber length
L_{SPAN}	Fiber span length
m_u	Interpolation interval
$n(t)$	Noise
\mathbf{N}	Noise vector
$n(\mathbf{p}, \omega)$	Refractive index profile
$n_{\text{co}}(\omega)$	Refractive index of the fiber core
$n_{\text{cl}}(\omega)$	Refractive index of the fiber cladding
N_{CAZAC}	CAZAC sequence length
N_{const}	Number of constellation points
N_{POL}	Number of polarizations
N_r	Number of receivers
N_s	Spatial diversity
N_{SEC}	Number of fiber sections
N_t	Number of transmitters
$P(t)$	Power
Q	Q-factor
$r(t)$	Received signal
\mathbf{R}	Received signal vector
r_0	Core radius
R_{PHD}	Photo detector responsivity
R_T	Total throughput
Δs	Driving voltage difference between two consecutive symbols
\mathcal{S}	Poynting vector
$s(t)$	Transmitted sequence
\mathbf{s}	Transmitted sequence vector
\mathbf{S}	Transmitted sequence vector multiple transmitters
\mathbf{S}_T	Known transmitted sequence
ΔT	Pulse spreading
T_{int}	Interpolated time

Symbol	Description
T_{shift}	Desired time shift
T_{sr}	Receiver sample time
T_{st}	Transmitter sample time
T_{sym}	Symbol time
V	Normalized frequency
V_{π}	Modulator driving voltage for π phase swing
v_g	Group velocity
\mathbf{W}	Weight matrix
\mathbf{W}_{mmse}	MMSE weight matrix
\mathbf{W}_{zf}	Zero-forcing weight matrix
$y(t)$	Interpolated received signal

List of operators

Operator	Description
$\{\cdot\}^*$	Complex conjugate
$\{\cdot\}^\dagger$	Moore–Penrose pseudo inverse
$\{\cdot\}^H$	Hermitian transposition
$\{\cdot\}^T$	Transposition
\otimes	Convolution
\odot	Element-wise multiplication
$\lceil \cdot \rceil$	Round up to the nearest integer
$\lfloor \cdot \rfloor$	Round down to the nearest integer
∇	Gradient operator
∂	Partial derivative
$\arg(\cdot)$	Argument of complex number
$\text{csign}(\cdot)$	Complex signum function
$\text{diag}(\cdot)$	Diagonalization
$E\{\cdot\}$	Expected value
$\text{erfc}(\cdot)$	Complex error function
$\exp(\cdot)$	Exponent
$\mathcal{F}\{\cdot\}$	Discrete Fourier transform
$\mathcal{F}^{-1}\{\cdot\}$	Inverse discrete Fourier transform
$\Im(\cdot)$	Imaginary component of complex number
$\log(\cdot)$	Logarithm
$\max\{\cdot\}$	Maximum value
$\min\{\cdot\}$	Minimum value
$\Re(\cdot)$	Real component of complex number
$\text{rank}\{\cdot\}$	Matrix rank
$\text{sign}(\cdot)$	Signum function
$\text{tr}\{\cdot\}$	Matrix trace
$\text{var}\{\cdot\}$	Variance

List of publications

All publications are listed chronologically per classification.

Invited papers

- [r1] V.A.J.M. Sleiffer, Y. Jung, P. Leoni, M. Kuschnerov, R.G.H. van Uden, V. Veljanovski, L. Grüner-Nielsen, Y. Sun, D.J. Richardson, S.U. Alam, F. Poletti, B. Corbett, R. Winfield, and H. de Waardt, "High capacity multi-mode transmission systems using higher-order modulation formats," in *Proc. OptoElectronics and Communications Conference (OECC)*, paper MR1-1 (2013).
- [r2] C.M. Okonkwo, R.G.H. van Uden, V.A.J.M. Sleiffer, H. Chen, Y. Jung, F.M. Huijskens, M. Kuschnerov, H. de Waardt, and A.M.J. Koonen, "Recent progress within the FP7 project MODEGAP," in *Technical Committee on Extremely Advanced Optical Transmission Technologies (EXAT)* (2013).
- [r3] R.G.H. van Uden, C.M. Okonkwo, H. Chen, H. De Waardt, and A.M.J. Koonen, "6×28GBaud 128-SP-QAM Transmission over 41.7 km Few-Mode Fiber with a 6×6 MIMO FDE," in *Proc. Optical Fiber Communication Conference(OFC)*, paper W4J.4 (2014).
- [r4] R.G.H. van Uden, C.M. Okonkwo, H. Chen, H. De Waardt, and A.M.J. Koonen, "6×6 MIMO Frequency domain equalization of 28GBaud 128-SP-QAM Few-Mode Fiber Transmission," in *Advanced Photonics for Communications*, paper SM2D.2 (2014).
- [r5] A.M.J. Koonen, H. Chen, V.A.J.M. Sleiffer, R.G.H. van Uden, C.M. Okonkwo, "Compact integrated solutions for mode (de-)multiplexing," in *Proc. OptoElectronics and Communications Conference (OECC)*, paper TU3B-4 (2014).

Journals

- [r6] V.A.J.M. Sleiffer, Y. Jung, V. Veljanovski, R.G.H. van Uden, M. Kuschnerov, H. Chen, B. Inan, L. Grüner-Nielsen, Y. Sun, D.J. Richardson, S.U. Alam, F. Poletti, J.K. Sahu, A. Dhar, A.M.J. Koonen, B. Corbett, R. Winfield, A.D. Ellis, and H. de Waardt, "73.7 Tb/s (96 x 3 x 256-Gb/s) mode-division-multiplexed DP-16QAM transmission with inline MM-EDFA," *Optics Express*, vol. 20, no. 26, pp. B428-B438 (2012).
- [r7] R.G.H. van Uden, C.M. Okonkwo, V.A.J.M. Sleiffer, M. Kuschnerov, H. de Waardt, and A.M.J. Koonen, "Single DPLL Joint Carrier Phase Compensation for Few-Mode Fiber Transmission," *IEEE Photonics Technology Letters*, vol. 25, no. 14, pp. 1381-1384 (2013).
- [r8] H. Chen, V.A.J.M. Sleiffer, B. Snyder, M. Kuschnerov, R.G.H. van Uden, Y. Jung, C.M. Okonkwo, O. Raz, P. O'Brien, H. de Waardt, and A.M.J. Koonen, "Demonstration of a photonic integrated mode coupler with MDM and WDM

- transmission," *IEEE Photonics Technology Letters*, vol. 25, no. 21, pp. 2039-2042 (2013).
- [r9] V.A.J.M. Sleiffer, M. Kuschnerov, R.G.H. van Uden, and H. de Waardt, "Differential phase frame synchronization for coherent transponders," *IEEE Photonics Technology Letters*, vol. 25, no. 21, pp. 2137-2140 (2013).
- [r10] H. Chen, V.A.J.M. Sleiffer, F.M. Huijskens, R.G.H. van Uden, C.M. Okonkwo, P. Leoni, M. Kuschnerov, L. Grüner-Nielsen, Y. Sun, H. de Waardt, and A.M.J. Koonen, "Employing prism-based three-spot mode couplers for high capacity MDM/WDM transmission," *IEEE Photonics Technology Letters*, vol. 25, no. 24, pp. 2474-2477 (2013).
- [r11] R.G.H. van Uden, C.M. Okonkwo, V.A.J.M. Sleiffer, H. de Waardt, and A.M.J. Koonen, "MIMO equalization with adaptive step size for few-mode fiber transmission systems," *Optics Express*, vol. 22, no. 1, pp. 119-126 (2014).
- [r12] R.G.H. van Uden, C.M. Okonkwo, H. Chen, H. de Waardt, and A.M.J. Koonen, "28GBaud 32QAM FMF Transmission with Low Complexity Phase Estimators and Single DPLL," *IEEE Photonics Technology Letters*, vol. 26, no. 8, pp. 765 - 768 (2014).
- [r13] R.G.H. van Uden, C.M. Okonkwo, H. Chen, H. de Waardt, and A.M.J. Koonen, "Time domain multiplexed spatial division multiplexing receiver," *Optics Express*, vol. 22, no. 10, pp. 12668-12677 (2014).
- [r14] R.G.H. van Uden, R. Amezcua Correa, E. Antonio Lopez, F.M. Huijskens, C. Xia, G. Li, A. Schülzgen, H. de Waardt, A.M.J. Koonen, and C.M. Okonkwo, "Ultra high-density spatial division multiplexing with a few-mode multi-core fibre," *Nature Photonics* (accepted, 2014).

Reports

- [r15] R.G.H. van Uden, C.M. Okonkwo, H. de Waardt, and A.M.J. Koonen, "Signal processing for optical MIMO transmission systems", www.modegap.eu (2013).

Conferences and symposia

- [r16] R.G.H. van Uden, H. Chen, C.M. Okonkwo, H.P.A. van den Boom, H. de Waardt, and A.M.J. Koonen, "Effects on MIMO-DSP in coherent transmission systems employing few-mode fibers," in *Proc. of the 16th Annual symposium of the IEEE Photonics Benelux Chapter*, pp. 217-220 (2011).
- [r17] R.G.H. van Uden, C.M. Okonkwo, H. de Waardt, and A.M.J. Koonen, "Phase plate tolerances in a tri-mode demultiplexer," Proceedings of the photonics society summer topical meeting series, 216-217 (2012).
- [r18] H. Chen, A.M.J. Koonen, R.G.H. van Uden, H.P.A. van den Boom, and O. Raz, "Integrated mode group division multiplexer and demultiplexer based on 2-dimensional vertical grating couplers," Proc. of the 38th European Conference and Exhibition on Optical Communication (ECOC), paper Th.1.B.2 (2012).

-
- [r19] V.A.J.M. Sleiffer, Y. Jung, B. Inan, H. Chen, R.G.H. van Uden, M. Kuschnerov, D. van den Borne, S.L. Jansen, V. Veljanovski, A.M.J. Koonen, D.J. Richardson, S.U. Alam, F. Poletti, J.K. Sahu, A. Dhar, B. Corbett, R. Winfield, A.D. Ellis, and H. de Waardt, "Mode-division-multiplexed 3x112-Gb/s DP-QPSK transmission over 80-km fewmode fiber with inline MM-EDFA and Blind DSP," Proc. of the 38th European Conference on Optical Communication (ECOC), paper Tu.1.C.2-1 (2012).
- [r20] V.A.J.M. Sleiffer, Y. Jung, V. Veljanovski, R.G.H. van Uden, M. Kuschnerov, Q. Kang, L. Grüner-Nielsen, Y. Sun, D.J. Richardson, S.U. Alam, F. Poletti J.K. Sahu, A. Dhar, H. Chen, B. Inan, A.M.J. Koonen, B. Corbett, R. Winfield, A.D. Ellis, and H. de Waardt, "73.7 Tb/s (96x3x256-Gb/s) mode-division-multiplexed DP-16QAM transmission with inline MM-EDFA," Proceedings of the 38th European Conference on Optical Communication (ECOC), paper Th.3.C.4-1 (2012).
- [r21] R.G.H. van Uden, C.M. Okonkwo, V.A.J.M. Sleiffer, H. Chen, M. Kuschnerov, H. de Waardt, and A.M.J. Koonen, "Employing a single DPLL for joint carrier phase estimation in few-mode fiber transmission," Proceedings of the Optical Fiber Communication Conference and Exposition (OFC) National Fiber Optic Engineers Conference (NFOEC), paper OM2C.1 (2013).
- [r22] V.A.J.M. Sleiffer, Y. Jung, P. Leoni, M. Kuschnerov, N. Wheeler, N. Baddela, R.G.H. van Uden, C.M. Okonkwo, J. Hayes, J. Wooler, E. Numkam, R. Slavik, F. Poletti, M. Petrovich, V. Veljanovski, S.U. Alam, D.J. Richardson, and H. Waardt, "30.7 Tb/s (96x320 Gb/s) DP-32QAM transmission over 19-cell Photonic Band Gap Fiber," Proceedings of the Optical Fiber Communication Conference and Exposition (OFC) National Fiber Optic Engineers Conference (NFOEC), paper OWI1.5 (2013).
- [r23] H. Chen, V.A.J.M. Sleiffer, B. Snyder, M. Kuschnerov, R.G.H. van Uden, Y. Jung, C.M. Okonkwo, P. O'Brien, H. de Waardt, and A.M.J. Koonen, "Demonstration of a photonic integrated mode coupler with 3.072Tb/s MDM and WDM transmission over few-mode fiber," Proceedings Combining the 10th Conference on Lasers and Electro-Optics Pacific Rim (CLEO-PR 2013) and the 18th OptoElectronics and Communications Conference (OECC), paper PD2-5 (2013).
- [r24] H. Chen, V.A.J.M. Sleiffer, R.G.H. van Uden, C.M. Okonkwo, M. Kuschnerov, F.M. Huijskens, L. Grüner-Nielsen, Y. Sun, H. de Waardt, and A.M.J. Koonen, "3 MDMx8 WDMx320 Gb/s DP 32QAM transmission over a 120km few-mode fiber span employing 3-spot mode couplers," Proceedings Combining the 10th Conference on Lasers and Electro-Optics Pacific Rim (CLEO-PR 2013) and the 18th OptoElectronics and Communications Conference (OECC), paper PD3-6 (2013).
- [r25] R.G.H. van Uden, C.M. Okonkwo, V.A.J.M. Sleiffer, H. de Waardt, and A.M.J. Koonen, "Performance comparison of CSI estimation techniques for FMF transmission systems," Proceedings IEEE Photonics Society Summer Topicals Meeting 2013, paper WC4.2 (2013).
- [r26] R.G.H. van Uden, C.M. Okonkwo, H. Chen, F.M. Huijskens, B. Corbett, R. Winfield, H. de Waardt, and A.M.J. Koonen, "2.576Tb/s (23x2x56Gb/s) Mode Division Multiplexed 4PAM over 11.8 km Differential Mode Delay Uncompensated Few-Mode

- Fiber using Direct Detection,” Proceedings of the 39th European Conference on Optical Communication (ECOC 2013), paper We.3.D.2 (2013).
- [r27] R.G.H. van Uden, C.M. Okonkwo, V.A.J.M. Sleiffer, H. de Waardt, and A.M.J. Koonen, “Adaptive step size MIMO equalization for few-mode fiber transmission systems,” Proceedings of the 39th European Conference on Optical Communication (ECOC 2013), paper Th.2.C.2 (2013).
- [r28] H. Chen, R.G.H. van Uden, C.M. Okonkwo, B. Snyder, O. Raz, P. O’Brien, H.P.A. van den Boom, H. de Waardt, and A.M.J. Koonen, “Employing an integrated mode multiplexer on silicon-on-insulator for few-mode fiber transmission,” in *Proc. of the 39th European Conference on Optical Communication (ECOC)*, paper Tu.1.B.4 (2013).
- [r29] R.G.H. van Uden, C.M. Okonkwo, H. Chen, H. de Waardt, and A.M.J. Koonen, “Multipoint-to-Point Few Mode Fiber Performance,” Symposium conducted at International Symposium on extremely advanced transmission technology (EXAT 2013), P12 (2013).
- [r30] R.G.H. van Uden, C.M. Okonkwo, H. Chen, H. de Waardt, and A.M.J. Koonen, “Improving Single Mode Transmission Performance using Few-Mode Fibers and Space-Time Coding,” Proceedings of the 18th Annual Symposium of the IEEE Photonics Society Benelux Chapter, 29-32 (2013).
- [r31] C.M. Okonkwo, R.G.H. van Uden, H. Chen, H. de Waardt, and A.M.J. Koonen, “Towards High-Density Space Division Multiplexed Transmission Systems,” Proceedings of the 18th Annual Symposium of the IEEE Photonics Society Benelux Chapter, 247-250 (2013).
- [r32] R.G.H. van Uden, C.M. Okonkwo, H. Chen, N. Wheeler, F. Poletti, M. Petrovich, D.J. Richardson, H. de Waardt, and A.M.J. Koonen, “8.96Tb/s (32×28GBaud×32QAM) Transmission over 0.95 km 19 cell Hollow-Core Photonic Bandgap Fiber,” Proceedings of the Optical Fiber Communication Conference and Exposition (OFC) (2014).
- [r33] R.G.H. van Uden, C.M. Okonkwo, H. Chen, F.M. Huijskens, H. Waardt, and A.M.J. Koonen, “First Experimental Demonstration of a Time Domain Multiplexed SDM Receiver for MIMO Transmission Systems,” Proc. of the Optical Fiber Communication Conference and Exposition (OFC) (2014).
- [r34] R.G.H. van Uden, R. Amezcua Correa, E. Antonio-Lopez, F.M. Huijskens, G. Li, A. Schülzgen, H. de Waardt, A.M.J. Koonen, and C.M. Okonkwo, “16QAM SDM-WDM Transmission over a Novel Hole-Assisted Few-Mode Multi-Core Fiber,” in *Proc. IEEE Summer Topicals Meeting Series*, paper ME3.2 (2014).
- [r35] R.G.H. van Uden, C.M. Okonkwo, R.H.G. van Uden, H. de Waardt, and A.M.J. Koonen, “The Impact of Bit-Width Reduced MIMO Equalization for Few Mode Fiber Transmission Systems,” in *Proc. of the 40th European Conference on Optical Communication (ECOC)*, paper Tu.3.1.2 (2014).

- [r36] R.G.H. van Uden, R. Amezcua Correa, E. Antonio-Lopez, F.M. Huijskens, G. Li, A. Schulzgen, H. de Waardt, A.M.J. Koonen, and C.M. Okonkwo, "1 km Hole-Assisted Few-Mode Multi-Core Fiber 32QAM WDM Transmission," in *Proc. of the 40th European Conference on Optical Communication (ECOC)*, paper Mo.3.3.4 (2014).

Patents

- [r37] R.G.H. van Uden, C.M. Okonkwo, and A.M.J. Koonen, "Time-Domain Multiplexed (TDM) - Spatial Division Multiplexed (SDM) multi-mode/single-mode converter for optical systems," U.S. provisional patent application no. TUE-147/PROV (2013).

Acknowledgements

I am grateful to my doctoral supervisor prof. ir. Ton Koonen for giving me the opportunity to work in the European Union Framework 7 project MODE-GAP. Also I would like to thank him for his advice and discussions. Furthermore, I would like to express my gratitude to dr. Bas de Hon and dr. Mathé van Stralen (Prysmian Group) for their supervision during my MSc thesis, which has set me on the path to pursuing the doctoral title.

During my work, I was supervised by dr. Chigo Okonkwo, and I would like to thank him for his positive attitude, daily supervision, managing efforts, and critical comments on papers. In addition, I would like to express my thanks to dr. Huug de Waardt for many discussions. Furthermore, I want to thank José Hakkens and Jolanda Levering for helping with the bureaucracy and arranging several mobile air conditioners during the hot summer of 2013 to control the laboratory temperature, after the built-in air conditioners all simultaneously broke down. It would have been impossible to verify the TDM-SDM receiver performance and the proposed algorithms without the help of dr. Haoshuo Chen and Frans Huijskens by setting up and aligning the phase plate based (section 4.2) and spot launcher (section 4.3) based mode (de)multiplexers. In addition, I would like to thank Frans for discussions about the 3D waveguide (section 4.4), and teaching me how to optimize the optical alignment of the multiplexers. I would like to thank dr. Vincent Sleiffer for teaching me how optical SSMF coherent transmission systems work, when I just started, and allowing me to use his experimental 3MF 80 km transmission data. In addition, I would like to thank him and his newly-wed wife Cornélie Westra for making my stays in Munich enjoyable. The peer-to-peer offline-processing distributed server network (section 6.5) was implemented by Roel van Uden and Maikel van de Schans, under supervision of dr. George Exarchakos and dr. Bert Hoeks (Avans Hogeschool, 's-Hertogenbosch), for which I was especially grateful during the 700 FM-MCF measurements.

As my work leading to this thesis has been performed in the European Union project MODE-GAP, there are contributions from several project partners. From Coriant, Munich, I want to thank dr. Maxim Kuschnerov for technical discussions with respect to time segmented equalization (section 6.2.6) and joint CPE (section 7.3). I also would like to thank the students at Coriant for making my stays enjoyable in Munich. The phase plates (section 4.2) were manufactured in Tyndall, Cork, Ireland, where the main contact persons were Brian Corbett, dr. Richard

Winfield, and prof. dr. Andrew Ellis. Clearly, in the field of optical transmission systems where novel experimental fibers are characterized and verified, the fiber manufacturers can not be forgotten. The 3MF (section 8.1) was designed and manufactured at OFS, Brøndby, Denmark, where the primary contact person was dr. Lars Grüner-Nielsen. The 19 cell HC-PBGF (section 8.2) was designed and fabricated in the ORC, Southampton, U.K., where the contact persons were dr. Francesco Poletti, dr. Marco Petrovich, and prof. dr. David Richardson. The 7-core FM-MCF (section 8.3) was designed and manufactured in CREOL, Orlando, U.S.A., where the contact person was Rodrigo Amezcua-Correa. I would also like to thank his twin brother, Adrian Amezcua-Correa (Prysmian Group), for additional discussions and ideas.

Of course, I want to thank all my colleagues in the ECO group, Eindhoven University of Technology, and especially dr. Chigo Okonkwo, dr. Patty Stabile, dr. Cac Tran, Prometheus Dasmahapatra, Wang Miao, and Teng Li, with whom I have shared my office with. Furthermore, a special thanks goes out to Jim Zao, Zizheng Cao, and dr. Nikos Sotiropoulos whom allowed me to borrow components for very lengthy periods of time.

Last but not least, I want to thank my parents, brother, and Yan for their understanding during difficult times under high working pressure, and for always being there for me.

Curriculum Vitae

R.G.H. (Roy) van Uden was born on the 31st of May, 1985, in Oss, the Netherlands. He has received the B.Eng degree in Electrical Engineering from Avans Hogeschool, 's-Hertogenbosch, the Netherlands, in 2006. He received his M.Sc. degree in Electrical Engineering from the Eindhoven University of Technology (TU/e), the Netherlands, in 2010. His M.Sc. thesis was entitled "Improved Reconstruction of Refractive Index Profiles", which was performed in collaboration with Draka Comteq, Eindhoven, the Netherlands. From TU/e, he also completed the specialty master track Broadband Telecommunication Technologies.

In October 2010, he started working towards the Ph.D. degree in the electro-optical communication (ECO) group at TU/e. His research was performed in the European Union framework 7 project MODE-GAP, and his Ph.D. project focuses on digital signal processing techniques and coding schemes for mode division multiplexed optical transmission systems. His main interests are the generation of higher order modulation formats and coding schemes, and mode division multiplexing to achieve high throughput optical transmission systems using novel fiber types.

He has (co-)authored more than 30 publications in top scientific journals and international conferences. He has served as a reviewer for IEEE Photonics Technology Letters, and is a student member of IEEE, and the Optical Society of America.